Gravity Field Recovery from GRACE Satellite Data and Investigation of Sensor, Environment and Processing-Option Influences by Closed Loop Mission Simulation

Vom Fachbereich Produktionstechnik
der
UNIVERSITÄT BREMEN

zur Erlangung des Grades
Doktor-Ingenieur (Dr.-Ing.)
genehmigte

Dissertation
von
M.Sc. Florian Wöske

Gutachter:

Prof. Dr. rer. nat. Claus Lämmerzahl
Center of Applied Space Technology
and Microgravity (ZARM),
University of Bremen

Prof. Dr. rer. nat. Gerhard Heinzel
Max Planck Institute for Gravitational
Physics, (Albert Einstein Institute, AEI),
Hannover

Tag der mündlichen Prüfung: 04. 10. 2021

Gravity Field Recovery from GRACE Satellite Data and Investigation of Sensor, Environment and Processing-Option Influences by Closed Loop Mission Simulation

DISSERTATION
BY
FLORIAN WÖSKE

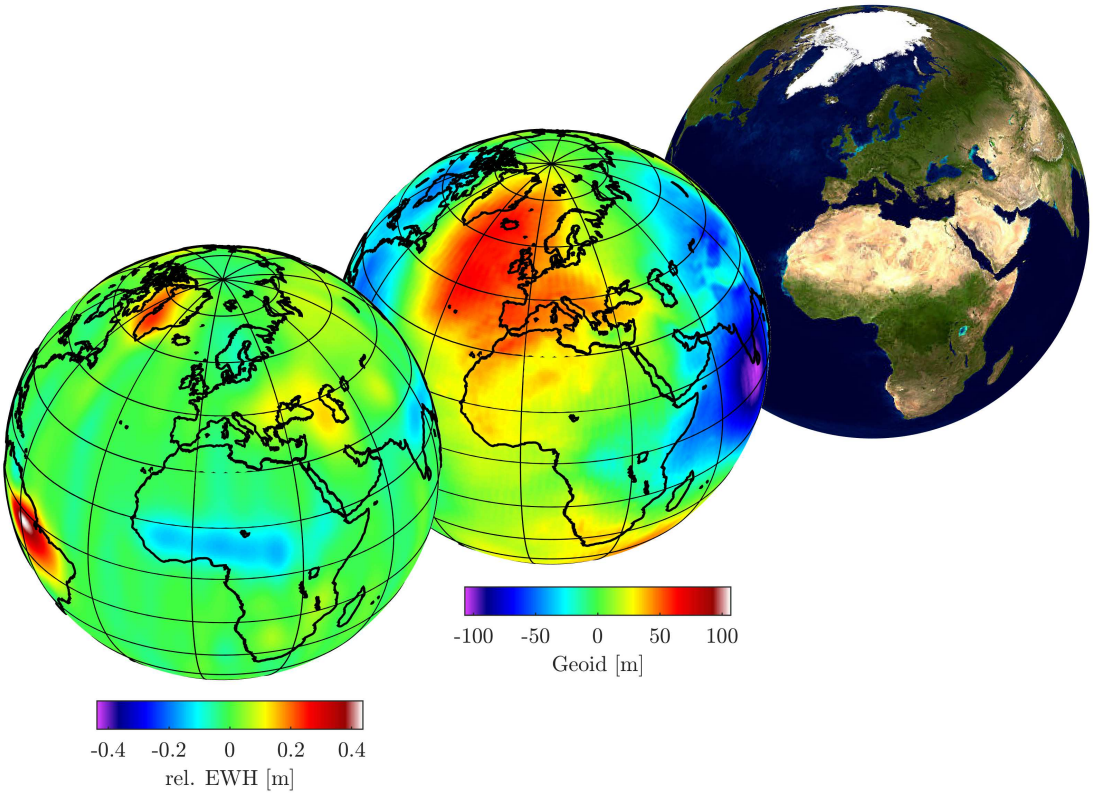

ZARM, University of Bremen
December 2020

PREFACE AND ACKNOWLEDGMENT

Countless hours of lonely pandemic home office writing eventually resulted in this document. Structuring, selecting and writing down the work of five years, I conducted at the ZARM institute of the university of Bremen, have finally come to an end. I guess every PhD agrees, that this is not the most fun part of the scientific work. Therefore I am more than pleased that you are able to hold this thesis in your hands.

For me, as the author, it denotes the end of a big effort and the completion of a long term goal that have been lingering at the horizon for the past years. Sometimes more as a burden, but the next day also as a bright outlook and a motivating goal to achieve.

Nevertheless, a PhD thesis is usually only worked through by a very few people, dealing with that specific topic. In that sense, I hope that this thesis might be a help for some student, PhD student or researcher in the field of gravimetry, orbit and gravity field determination and satellite simulation. The result sections contain lots of plots to hopefully offer an intelligible access to the findings of this thesis. Furthermore, maybe the comprehensively presented background and theory of the beforehand mentioned topics in the first five chapters will be an expedient introduction to people new to that field of research.

I would like to express my sincere gratitude to Prof. Dr. Claus Lämmerzahl, my supervisor and dedicated leader of the diverse space science department at ZARM, for the opportunity to join this group.

I am very pleased for the offered possibility to become a member of the Collaborative Research Center (CRC) geo-Q "Relativistic Geodesy and Gravimetry with Quantum Sensors" in 2015, and thus got introduced to the fascinating topic of satellite gravimetry. Therefore I would like to thank my group leader and colleague Dr. Benny Rievers, as well as Dr. Meike List, who meanwhile moved to the DLR.

I deeply acknowledge your guidance, enabling me to attend conferences around the world, the DAAD exchange to Australia, always arranging a follow-on contract and caring about all the administrative paperwork over the years.

Furthermore I would like to thank all past and present colleagues at ZARM for the good time and all the discussions and events we had, during and after work - I enjoyed the pleasant working atmosphere at the institute with you.

Moreover, I would like to thank Dr. Neda Darbeheshti, by now at AIUB, for our fruitful collaborations and all the discussions we had over the years. I also would like to thank Saniya Behzadpour from TU Graz for answering many questions and the good times we had when we met.

I want to kindly express my appreciation to Prof. Dr. Gerhard Heinzel for reviewing this thesis, thank you!

A special mentioning and thank goes to all people involved in geo-Q's research training group for the organization of all the amazing lecture weeks, giving a broad knowledge of neighboring scientific disciplines, lots of motivation and connecting PhD students

and researchers from all over the world. The financial support by the German Research Foundation (DFG) by funding the CRC (SFB 1128: geo-Q) is gratefully acknowledged.

Last but definitely not least, I am grateful to my parents for all their support and especially to my girlfriend, enduring me for such a long time and always being there for me.

Bremen, December 2020 Florian Wöske

ZUSAMMENFASSUNG IN DEUTSCHER SPRACHE

Die globale Vermessung des Gravitationsfeldes der Erde und dessen zeitliche Veränderung liefert eine einzigartige Messgröße der Erdbeobachtung: Gravitation, und davon abgeleitet Masseverteilung und Massetransport in der oberflächennahen Schicht der Erdkruste. Die Zeitliche Änderung des Gravitationsfeldes liefert Daten, die mittlerweile eine Grundlage für viele Geowissenschagften bilden und eien erheblichen Beitrag zum Verständnis des dynamischen Erdsystems, dessen Wasserkreislauf und des Klimawandels leisten. Die Messung der Gravitation und des Schwerefeldes wird allgemein als Gravimetrie bezeichnet. Sie ermöglicht die quantitative Messung von Masseänderungen, ob sichtbare oder unsichtbar, was durch keine andere Technik möglich ist.

Insbesondere die GRACE (Gravity Recovery And Climate Experiment) Satellitenmission hat seit 2002 zu den großen Erfolgen der Satelliten-Gravimetrie beigetragen. Obwohl der Start der GRACE Satelliten nun schon fast 19 Jahre her ist, und mittlerweile die Nachfolgemission GRACE-FO mit dem selben Messprinzip die Vermessungszeitreihe fortführt, wird die Datenauswertung immer noch kontinuierlich verbessert.

Im Rahmen dieser Arbeit wurde eine Software zur präzisen Orbit und Gravitationsfeld Bestimmung entwickelt. Dabei wird aus den beobachteten Messdaten entlang der Satellitenbahn ein globales Modell des Erd-Gravitationsfeldes in Form von sphärisch-Harmonischen abgeleitet. Dazu wurde in dieser Arbeit der klassische Ansatz der "Variational Equations" implementiert, welcher inzwischen als das Verfahren mit den genausten Ergebnissen betrachtet wird.

Die Arbeit verfolgt zwei Hauptziele. Zuerst wird die GRACE Datenauswertung, also die Bestimmung monatlicher Gravitationsfelder mittels des implementierten Verfahrens untersucht. Ein Hauptaugenmerk ist dabei die Charakterisierung der Auswirkungen verschiedener Parameter und Varianten des Verfahrens auf die Ergebnisse. Des weiteren wird der Einfluss der verschiedenen Sensordaten und dessen Kalibrierung während des Verfahrens analysiert. Vor allem die Akzelerometerdaten, welche nicht-gravitative Beschleunigungen auf die Satelliten messen, werden detailliert studiert. Die größten Einflüsse auf die Ergebnisse haben die Gewichtung der verschiedenen Messdaten, sowie die neben dem Gravitationsfeld bestimmten Parameter. Diese sind hauptsächlich durch die Kalibrierung der Akzelerometer und die Unterteilung der monatlichen Datensätze definiert.

Das zweite Ziel der Arbeit ist die komplette Simulation einer GRACE ähnlichen Satellitenmission samt Datenauswertung. Dazu wurden die beiden Satelliten samt aller relevanten Sensordaten und unter Berücksichtigung von Umwelt- und Sensormodellen simuliert. Mit der Simulation werden Effekte und Einflüsse jedes einzelnen Sensors und dessen Charakteristik, sowie verschiedener Observationsdaten und verschiedener Umwelteinflüsse auf die Ergebnisse untersucht. In der Simulation sind zu jeder Zeit das wahre Gravitationsfeld und die theoretisch perfekten Sensordaten als Referenz bekannt. Zudem bietet die Simulation den großen Vorteil jedes Sensor- und Umweltmodell einzeln ein- und auszuschalten.

Mit dem Vergleich der realen GRACE Datenauswertung und den Ergebnissen der Simulation, werden Rückschlüsse auf die GRACE Daten und die Gravitationsfeldbestimmung gezogen aber andersherum auch die Modellierung validiert.

CONTENTS

1 INTRODUCTION

The scope of this thesis is the investigation of Gravity Field Recovery (GFR) from GRACE (Gravity Recovery And Climate Experiment) satellite observation data. The processing from GRACE instrument data to monthly gravitational field solutions is implemented and analyzed with real GRACE data, as well as with data of a completely simulated GRACE-like mission, including all main observation and satellite data. Through this, different influences and relations between satellite, sensor noise characteristics, environment models and options in the processing chain will be analyzed and revealed. With the simulation approach each effect and its influence on the overall gravitational field solutions can be assessed. Furthermore, the GFR simulation is validated and compared against the real GRACE processing. The whole GFR simulation loop is intended to serve as a testbed for the development of improved and entirely new satellite gravimetry mission concepts in the future.

The idea and objectives of this thesis were developed within the scope of the Collaborative Research Center (CRC) geo-Q "Relativistic Geodesy and Gravimetry with Quantum Sensors". The results, gained expertise and all developed software and tools will be further utilized in the successor CRC TerraQ.

To introduce and motivate this thesis, first a general motivation on satellite gravimetry and its most recent and impressive achievements, with special focus on the GRACE satellite mission, is given in this chapter. It is followed by an introduction of the basic concepts and a historical review of satellite gravimetry. In this context the four most recent gravimetry missions and their measurement concepts are shortly depicted. Subsequently, the research motivation and the resulting main goals and objectives of this thesis are derived. The Introduction concludes with the presentation of the outline of the thesis.

1.1 Motivation

Space-based Earth observation is a prerequisite to globally monitor the dynamic system Earth and thereby improving our understanding of the underlying global processes and interrelations. The measurement of Earth's varying gravitational field, referred to as gravimetry, introduces a completely different and independent measurement quantity: Gravitation, and hence distribution of masses. Changes of Earth's gravitational field are primarily driven by mass redistribution in the near-surface layer of the Earth system, thus the fields of continental hydrology, cryosphere, ocean, atmosphere, and solid Earth are accessed. Water is exchanged between oceans, cryosphere, land and atmosphere within periods from sub-daily to annual and beyond decadal and century scales. Changes in the global water cycle are directly affecting sea level, ocean currents, freshwater resources and weather. The trends may be considered as proxy for global warming

and climate change, natural and or anthropogenic. Hence, in the long term, satellite gravimetry also allows to detect and assess impacts of humankind on the system Earth.

Exceptional contributions have been made in the last two decades by four dedicated satellite gravimetry missions, namely CHAMP (CHAllenging Minisatellite Payload), launched in 2000 (Reigber et al., 2002), GOCE (Gravity field and steady-state Ocean Circulation Explorer), launched in 2009 (Drinkwater et al., 2003) and GRACE (Gravity Recovery And Climate Experiment), launched in 2002 (Tapley et al., 2004a) and not to forget, the recent GRACE successor mission, GRACE-Follow-On (GRACE-FO) (Landerer et al., 2020), launched in mid 2018 to continue the unprecedented successful GRACE measurement time series.

These missions triggered new insights in the understanding of the dynamic Earth system. Today, GRACE monthly gravity field solutions are an indispensable measurement for various science disciplines and for instance essential for IPCC (Intergovernmental Panel on Climate Change) reports.

The GRACE mission provided monthly solutions of Earth's time varying gravitational field for 15 years, which are continued by GRACE-FO with a gap of one year. The annual water cycle results in enormous seasonal water mass redistribution around the globe, measured in the monthly gravitational field solutions (eg. Sec. 7.6 and Fig. 7.46). Furthermore, distinct trends of continental water storage over the mission time are detected and quantified in several regions around the world. A recent summary of detected global trends and their causes is given by Rodell et al. (2018).

Some prominent trends and numbers, detected by GRACE and GRACE-FO, are depicted in the following. The Greenland ice sheet looses on average about 265 Gt mass per year over the GRACE mission period (Forsberg et al., 2017; Tapley et al., 2019). Variations in the year-to-year variability, as well as the annual mass balance may be quite big but the trend is distinct. The biggest annual ice loss was detected in 2019 of about 532 Gt (Sasgen et al., 2020). The situation in Antarctica is more complex, where in western Antarctica and Peninsula the trend is negative, in the eastern regions it is positive. Nevertheless, the overall balance is negative, and the Antarctic ice sheet is losing on average about 100 Gt mass every year over the GRACE mission time period (Forsberg et al., 2017; Shepherd et al., 2020; Tapley et al., 2019). Aside from the redistribution of water, gravitational changes in the polar regions are also caused by Glacier Isostatic Adjustment (GIA), a rebound of the Earth crust due to the decreasing weight of ice sheets since the last glacial period (eg. Caron et al., 2018).

Further cryosphere related trends are detected in the Canadian archipelago, the gulf of Alaska and in Patagonia due to the retreat of ice fields and glaciers. Besides the by far biggest trends of the polar ice sheets, trends over the whole globe can be detected and quantified by the gravitational measurement. For instance due to groundwater depletion and droughts eg. in southern California, the Middle East or northern India (Famiglietti et al., 2011; Voss et al., 2013). Rodell et al. (2018) quantifies the water storage mass losses in terms of annual trends over the GRACE mission time to be 4.2, 32.1 (northern Middle East: eastern Turkey, Syria, Iraq and Iran) and 19.2 Gt/y, respectively. Positive trends due to an increase of precipitation are sensed as well in some regions. Nevertheless, the predominant negative trends of terrestrial water storage result in an increased mass of the oceans, contributing to sea level rise. The average sea level rise per year between 1993 and 2018 is about 3.2 mm (WCRP Global Sea Level Budget Group, 2018), measured by satellite altimetry. It is the sum of mass gain and

expansion due to temperature and salinity changes. The total amount of additional water in the oceans can be distinguished by considering GRACE data of ocean mass change. The mass proportion of the current sea level rise had been calculated to be around two third (eg. Tapley et al., 2019; WCRP Global Sea Level Budget Group, 2018; Feng and Zhong, 2015). Novel, improved data processing by Uebbing et al. (2019) suggests that it is considerably lower.

A recent recap of major advances from GRACE in the various geosciences disciplines with regard to climate change is given by Tapley et al. (2019).

1.2 Satellite Gravimetry

Gravimetry is one of the three pillars of geodesy, with the other two pillars dealing with the shape of the Earth and its orientation in space (eg. Torge and Müller, 2012).

Thereby the term gravimetry is not restricted to satellite measurements, but also ground-based, punctual measurements are enclosed. The enormous advantage of satellite gravimetry is the global coverage with the same instrument in a rather short amount of time, and resulting global gravitational field models. Indeed, these models have to be understood as a mean gravitational model over the time period that was needed to gather enough data for a global model. Due to the quadratic decrease of gravitation with distance, the satellite measurement in an Earth orbit has to suffer a reduced resolution and accuracy compared to ground-based, static instruments.

The general measurement principle of satellite gravimetry is that satellites follow a gravitational trajectory and from its measurement a conclusion on the underlying gravitational field can be drawn. Different concepts are based on the methodology how the satellite's trajectory or orbit is measured. The measurement of a satellite's position or velocity is not possible, directly. Usually just an one-dimensional quantity can be measured. These might be ground-based range, range-rate or angle measurements, furthermore also measurements between satellites, referred to as Satellite-to-Satellite Tracking (SST) are possible. Nevertheless, all these measurements are related to the satellite's position or trajectory, which hence might be determined from it (cf. Ch. 4). Different concepts of implementing and combining these measurement concepts are feasible and conducted by the mentioned CHAMP, GRACE and GOCE satellite missions.

With the three dedicated major satellite gravimetry missions, the beginning of the 21th century was declared as the "Decade of Geopotential Research" (eg. Seeber, 2003). Nevertheless, already with the launch of the first artificial satellite Sputnik in 1957, its signals were used for geodetic measurements to determine the ellipsoidal shape of the Earth. Since then, the satellites Sputnik 2, Explorer and Vanguard were used to determine the flattening and the pear-shape of the Earth (King-Hele and Merson, 1958; O'Keefe et al., 1959). Already before that, the flattening of the Earth was estimated by Laplace from observations of the Moon's nodal precession in 1802 (eg. Seeber, 2003, p. 5).

In the following centuries the number of artificial Earth satellites increased drastically, as well as the tracking and measurement techniques. Furthermore several passive geodetic satellites were launched that were tracked from ground stations, especially SLR (Satellite Laser Ranging) satellites. The motivation was split between the development of more accurate gravitational models of the Earth for more accurate obit propagation and determination, and the geodetic science related to the shape of the Earth and the Geoid

(cf. Sec. 2.3.2 for the definition of the Geoid). With the combination of observations from different satellites more detailed Earth gravitational filed models were developed and published over the centuries like the series of GEM (Goddard Earth Models) (Lerch et al., 1985) and JGM (Joint Gravity Model) (Tapley et al., 1996) models.

The driver for further improvement was the satellite altimetry mission TOPEX/Poseidon, launched in 1992 (Tapley et al., 1994; Nerem et al., 1994). It was concluded, that the largest contributor to the altimeter error budget was to be expected from the orbit accuracy due to uncertainties in the gravitational field model of the Earth (Lemoine et al., 2002). This resulted in the development of the popular EGM96 (Earth Gravity Model) (Lemoine et al., 1998), which is additionally based on satellite altimetry measurements and the first SST measurements between the TOPEX/Poseidon satellite and the GPS (Global Positioning System) constellation. During that time the first ideas for the current gravimetry missions were developed and proposed (Seeber, 2003, p. 469 ff.). For a detailed historic overview of satellite geodesy see eg. Dicati (2017).

The multiply mentioned gravimetry missions CHAMP, GRACE and GOCE have drastically increased the resolution and accuracy of gravitational field models and the realization of the Geoid. It enabled the application of satellite gravimetry to a broad field of geosciences, as introduced in the beginning (Sec. 1.1). Each of the three missions realizes a different main measurement concept of SST, which are especially sensitive to different areas of the gravitational field, meaning the ability to resolve rougher or finer structures. The idea of the different concepts is sketched in Figure 1.1.

Due to the quadratic decrease of the gravitational acceleration with distance, the satellites are in a Low Earth Orbit (LEO), to be more sensitive to the fine structures of Earth's gravitational field. The SST principle can be realized between a LEO satellite and GNSS (Global Navigation Satellite System) satellites like GPS, referred to as high-low (hl)-SST measurement. This concept was first conducted by CHAMP (and is also employed by GRACE and GOCE as additional measurement). The high number of GNSS satellites allows for about seven to 16 measurements at the same time in various directions and thereby the possibility of a kinematic and dynamic absolute position determination of the satellites (cf. Sec. 4.1 for dynamic and kinematic orbits). With this measurement the hl-SST method is especially sensitive to the rougher or large-scale structures of the gravitational field.

The method employed by GRACE is the low-low (ll)-SST between two LEO satellites, separated by about 220 km. With an appropriate measurement device, using dual one-way ranging (cf. Sec. 3.2.1) or even an optical interferometric measurement device (as successfully utilized by GRACE-FO as technology demonstrator Abich et al. (2019)), the relative measurement can be much more accurate than the hl-SST. Nevertheless, the additional hl-SST measurement, which has an accuracy that is orders of magnitude worse, is important to make full use of the accurate ll-SST measurement and to obtain a good overall gravitational field solution. The ll-SST method is most sensitive to the medium to fine structures of the gravitational field. In this range most of the dynamic processes close to the Earth surface take place, which were introduced in Section 1.1.

The GOCE mission used a variant of ll-SST that is referred to as Satellite Gravity Gradiometry (SGG). In one satellite the relative acceleration measurement between six free flying test masses is used to determine the gravitational gradient. This is more or less a ll-SST concept in three spatial directions, condensed in one satellite. The SGG concept is the most sensitive to the fine structures of the gravitational field, but not to the rougher and medium structures. Therefore gravitational fields from GOCE are usually

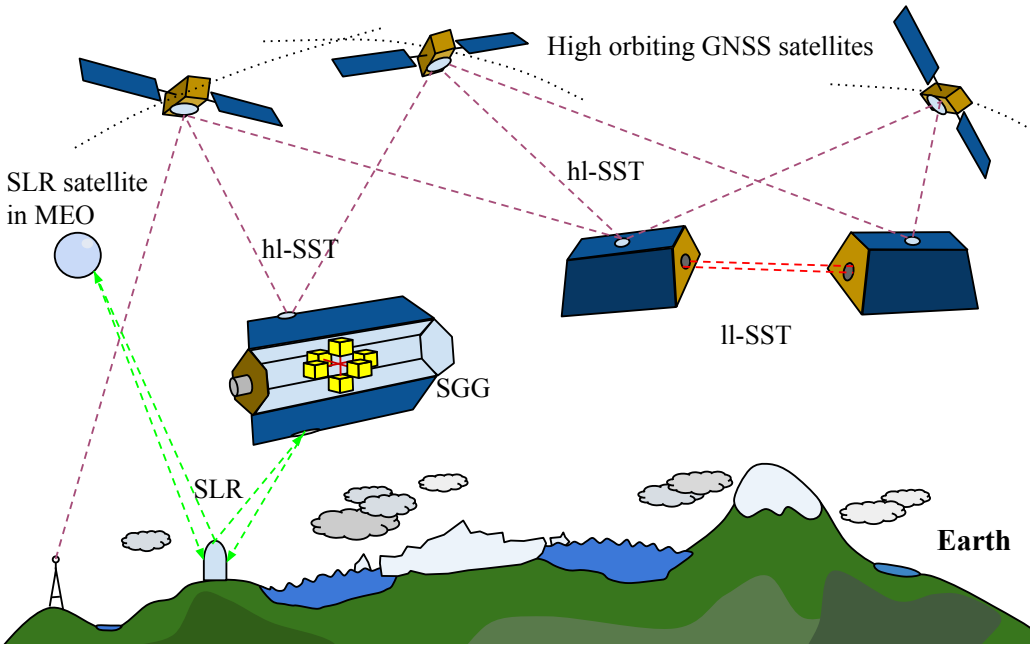

Figure 1.1: Sketch of measurement concepts of satellite gravimetry: High-low Satellite-to-Satellite Tracking (hl-SST) between high orbiting satellites (eg. GNSS) and satellites in LEO, low-low (ll)-SST between two LEO satellites, Satellite Gravity Gradiometry (SGG) measured between six free flying test masses in one satellite, and Satellite Laser Ranging (SLR) to passive MEO satellites or the LEO satellites.

combined with GRACE solutions in the respective resolutions. Dynamic processes on the Earth affecting the finer structures are far below the detectable accuracy. Hence GOCE is related to the static gravitational field of the Earth and provided an unprecedented Geoid accuracy, established as global height reference system (eg. Brockmann et al., 2014).

The most basic structure of the gravitational field, so to say the flattening of the Earth, is still best determined by high orbiting SLR satellites (eg. LAGEOS), tracked from several ground stations. GRACE and GOCE solutions are usually complemented with results or data from SLR satellites for the very basic structure.

For all missions, especially with LEO satellites involved, non-gravitational forces, acting on the satellites or test masses, have to be considered and measured to account for orbit disturbances not based on the gravitational potential. These are mainly caused by drag from the residual atmosphere and Solar and Earth radiation pressure. The measurement of these forces by accelerometers on board the satellites is one limiting factor of the performance of the current missions.

A good overview of satellite geodesy and gravimetry with the different approaches is given eg. by Seeber (2003).

1.3 Research Objectives

The focus of this thesis is satellite gravimetry based on the GRACE ll-SST principle and the Gravity Field Recovery (GFR) from the satellite's measurement data. Since the launch of GRACE in 2002, continuous progress is made to improve the processing of the GRACE data and hence the monthly gravity field solutions. This includes the

officially published instrument data (Level 1B data, with current release number RL06), as well as the processed gravitational fields (Level 2 data). Up to now, the intended pre-launch baseline accuracy of the monthly solutions (Kim, 2000) is still not achieved.

Besides the three official GRACE solutions, from the Center of Space Research at the University of Texas, Austin (UT CSR) (Bettadpur, 2018), the German Research Center for Geosciences Potsdam (GFZ) (Dahle et al., 2018) and the Jet Propulsion Laboratory (JPL) (Yuan, 2018), at least ten more solutions from other groups and institutes are released (for instance distributed by the International Centre for Global Earth Models (ICGEM) Ince et al. (2019), *http://icgem.gfz-potsdam.de/home*), or by the COST-G combination service (Jäggi et al., 2020). Every solution differs to the other ones, even though the same instrument data from the GRACE satellites are used. For the complex inversion from the satellite's measurement data to the monthly gravitational field solutions, different approaches, parameter choices and strategies exist. The three official solutions are compared eg. by Klees et al. (2008); Sakumura et al. (2014); Kvas et al. (2019).

Meanwhile, the classical, variational-equation approach (cf. Sec. 4.2) is considered to be the most accurate and thus the state-of-the-art choice. Gradually the established solutions are approaching each other with updated releases. Nevertheless, with improvements in the modeling and enhanced processing concepts, as well as a better understanding of different error sources, the solutions are still further improved.

Even though no true solution to hold as reference exists, there are several methods to assess the accuracy and quality of a solution for instance by the analysis of error patterns. Especially over the oceans the expected signal in most regions is extremely small, thus a temporal RMS shows mainly error patterns and thus allows to quantify a solution quality. A good example is given in Kvas et al. (2019), comparing the recent ITSG solution from the Institute of Geodesy at TU Graz, which actually can be considered the best, to the three official GRACE solutions.

From these discrepancies, the not completely understood relations in the processing, and the current efforts of designing an improved successor mission for GRACE-FO, the goal of this thesis is derived: **The determination and quantification of various factors and influences on the overall quality of estimated gravitational field solutions**. These factors are mainly different instrument characteristics with respective noise models, different environmental models and conditions, and furthermore options, strategies and parameter choices in the GFR processing, which play a crucial role.

These goals shall be achieved by two parallel approaches, being the main subjects of this thesis. First, **the complete simulation of a GRACE-like satellite gravimetry mission and the subsequent GFR processing of the simulated data**. In the "modeled world", the true gravitational field and all measurements are known and hold as absolute reference. It is possible to switch on and off each instrument and environment model, individually and use perfect observations for other instruments. Different models for each instrument are taken from the literature and are developed for that purpose. Thus, the sensitivity of the overall gravitational field solution with respect to a distinct instrument or noise model can be determined. In the same way also the influence of different options in the GFR processing can be validated, and correlations with respect to instrument and its noise characteristics can be revealed. This is also motivated by the fact, that in the real measurement data it is not possible to distinguish between signal and noise contribution. The same holds for the estimated gravitational field solutions and measurement post-fit residuals because they contain a sum of the noises from all

sensors (inter-satellite ranging, accelerometers, star cameras and GNSS measurements) additionally to modeling errors and errors of the estimation process and the processing of the noisy measurement data. The distinction what relates to which source and how much influence a certain error has is not completely possible.

In parallel, the second objective is **the validation and comparison of the simulated mission and measurement data, as well as the GFR processing against real GRACE data and GRACE GFR processing**. Therefore the developed GFR tool is extended for real GRACE data processing. The obtained results from the GRACE processing verify the developed GFR processing methodology and tools in general. Furthermore, from comparisons between the real and simulated processing, the accuracy and relevance of the simulation is validated. This makes the results and findings obtained with the simulation approach transferable to the real GRACE processing.

For both goals the GFR tool plays a central role. For realistic comparisons and estimates, a state-of-the-art processing needs to be realized. From most GFR processing tools, used for the generation of monthly GRACE solutions, besides general information, not much detail of the implementation and processing is known. The claim of this thesis is that all details of the developed GFR tool are elaborated in depth and not just the final results are shown, but also all kind of intermediate results, that are rarely depicted and mentioned by renowned GRACE processing centers. From the goals of the thesis this of cause includes demonstrating the effects of main GFR processing options on the overall solutions and other parameters. Furthermore, it is intended, that the complete software is published as an open source tool, which is partially already done in a very basic version in Darbeheshti et al. (2018).

The main goals of the thesis may be briefly summarized by:

- Characterization of the influence of options, strategies and parameter choices in the GFR processing on the overall gravitational field solutions and further estimated parameters.
- Determination of the influence and correlations of different sensor characteristics, noise models- and levels on the gravitational field solutions and further estimated parameters.
- Establishing a state-of-the-art GFR software and simulation tool for various investigations of real and simulated satellite data. The software should furthermore serve as a testbed for the development of improved and entirely new gravimetry mission concepts in the future.
- Extension of the GFR tool for real GRACE data processing to validate the GFR-mission simulation loop.

The approach of a complete simulation of a gravimetry mission is not new. Due to the possibility to compare all results with the perfect, initially set parameters and models, this is also referred to as a closed loop GFR-(mission) simulation. For GRACE, the pre-launch study by Kim (2000) investigates the most important relations of the instruments, orbit choices, measurement quantities and data processing for the GRACE mission. A more recent study from Flechtner et al. (2016) estimates outcomes of the GRACE-FO mission and also quantifies to some extend the influence of the different instruments. Nevertheless, the depth of modeling and the connection between different instruments

eg. the effect of the GNSS and SST accuracy on the accelereometer calibration is expandable.

Furthermore, studies and proposals for successor missions of GRACE-FO, commonly referred to as Next-Generation-Gravity-Missions (NGGM) exist, which partly also employ a full closed loop simulation (Panet et al., 2012; Gruber et al., 2014; Baldesarra et al., 2014; Elsaka et al., 2014; Hauk and Pail, 2019; Hauk and Wiese, 2020). The aim of these studies is more on the general mission performance, but not on the specific coherence of different instruments and the processing. Proposed noise models of some prominent studies eg. for the accelerometer are also used and validated here.

A big effort is taken for highly accurate non-gravitational force modeling and the development of the satellites attitude control, which directly influences the non-gravitational forces and furthermore the accelerometer measurement due to intrusions of the attitude thruster firings in the accelerometer measurement. Besides being a benefit for NGGM investigation, these developments and insights impact neighboring disciplines like Precise Orbit Determination (POD) of various satellites, especially with high orbit precision demands, like GNSS and altimetry, and the analysis of Thermospheric density and wind determination. For the letter, satellite accelerometer measurements are reduced by precisely modeled non-gravitational forces to obtain the atmospheric density (Doornbos et al., 2005; Tapley et al., 2007; Doornbos et al., 2010; Doornbos, 2011; Visser et al., 2019). The GRACE mission, with dense orbit and highly accurate accelerometer data, allows a precise validation of the non-gravitational force modeling.

1.4 Outline of the Thesis

In the next Chapter 2, at first the basic reference frames utilized in geodesy and satellite dynamics are introduced. Subsequently, the governing equation of satellite motion and rotation are introduced. In Section 2.3 the background and basic definitions of gravitational theory, as used in geodesy, are given. Furthermore, the modeling of the gravitational field, its relation to the Geoid, and its visualizations are discussed.

Chapter 3 describes the GRACE mission in more detail. Basic mission design, measurement principle, instrumentation of the satellites and its basic functioning, as well as the available sensor data and its pre-processing, is described.

In Chapter 4 the estimation theory of POD and GFR is introduced. After the distinction of dynamic and kinematic orbit determination, the dynamic classical approach, also referred to as variational-equation approach, is derived. Today this is the state-of-the-art method used in gravimetry. The general processing with parallel computation of partitioned arcs, different observations, assessment of error and weighting, as well as the automatic weighting by variance component estimation is described. The theory is applied for the GRACE case, and the form and structure of the main matrices is depicted in detail in Section 4.3.14. Finally the batch algorithm for GRACE GFR is described step by step in Section 4.3.15.

This Chapter is quite detailed, with the intention to hold as mathematical reference for the implemented GFR software tool.

In Chapter 5 the essentials for satellite simulation and propagation are completed. These are, besides the gravitational models (Sec. 2.3), the non-gravitational force modeling and the numeric integration. First, the modeling approach for non-gravitational forces is introduced. The applied and developed models for the different forces related to residual atmosphere and radiation from Sun and Earth, as well as from the satellite itself are described. In the second part a review of numerical integration is given and promising methods in the field of orbital dynamics are evaluated. Therefore an arbitrary precision arithmetic, exceeding the precision limitation of the usually used *double* data type, is investigated and utilized as reference.

Chapter 6 deals with the simulation of the GRACE mission, the satellites, and its instruments. At first, in Section 6.1, the developed non-gravitational force models are applied to the GRACE satellites and extensively validated and compared against the GRACE accelerometer data. Subsequently the implemented attitude control scheme, including star camera, thruster and magnetic torquer models, is described. Results are shown and compared with GRACE data (Sec. 6.2). The different implemented and investigated sensor models or the models for the processed instrument data, are depicted in Section 6.3 for inter-satellite ranging, accelerometer, GNSS based orbit solution, attitude, magnetic torquer and thruster.

Chapter 7 presents the main results from GRACE GFR. The developed GFR tool is investigated in detail, the effects of parameter choices and processing strategies are demonstrated. The major influences are the weighting of the different observations, the accelerometer calibration and the arc length. Furthermore, the pre-processing of the GRACE data is indispensable. Also the sensitivity of the different environmental models is assessed. An analysis of the formal error estimate and the residuals is conducted. Monthly solutions with the most promising parametrization and options are exemplary shown for the year 2006, revealing the annual hydrological signal. Finally, a solution with modeled non-gravitational forces used instead of the accelerometer data is investigated.

In Chapter 8 the results of the closed loop GFR simulation are shown. First, the investigation follows the structure from the previous chapter with the real GRACE data processing. The parametrizaion of the GFR scheme is examined and the results are compared to the real GRACE results. Subsequently, the effects of the different sensor models, introduced in Section 6.3, on the solutions are examined. Thereby a special focus is on the different implemented accelerometer noise models. The characteristics of the different sensors in the gravity field solutions are compared to the real GRACE solutions, as well.

Finally, Chapter 9 gives a summary of the thesis and emphasizes the main scientific findings. It concludes with an outlook, discussing further extensions and applications for the two main parts of the thesis, the GRACE processing and the closed loop GFR simulation.

FUNDAMENTALS 2

The fundamental definitions of geodesy and its defining equations, essential for the topic of this thesis, are introduced in this Chapter. This includes the basic reference frames defining position and orientation of the Earth in space, as well as the definition of Earth's gravity and gravitational potential and its representations and visualizations.

The basic equations of motion for satellites are introduced, which in geodesy is Newtonian or classical mechanics. It may be expanded by considering post Newtonian relativistic corrections. All gravitational models used to describe Earth's static and time dependent gravitational potential are elucidated.

2.1 Reference Frames

A reference system is defined as a set of three mutually perpendicular unit vectors. All systems used here are right hand systems. The notation of the unit vectors throughout the thesis is $\vec{e}_x, \vec{e}_y, \vec{e}_z$, representing the x-, y- and z-axis, respectively.

In literature and theory a strict distinction between a reference system and a reference frame is made. The system is the theoretical definition and a frame the practical realization of it.

2.1.1 Earth-Centered Inertial (ECI)

The Earth-Centered Inertial (ECI) reference frame is an inertial, thus non-accelerated and non-rotating, frame with its origin in the Center of Mass (CoM) of the Earth.

It is based on the International Celestial Reference Frame (ICRF), which is a realization of a quasi inertial frame in the center of the Solar System barycenter. Its axes are defined with respect to distant extragalactic radio objects. To coincide with previous definitions of this system its x-z plane is approximately aligned with the mean equator and the x-axis is pointing towards the vernal equinox at J2000.0. It is maintained by the International Earth Rotation and Reference Systems Service (IERS). For more information see (eg. Seeber, 2003; Torge and Müller, 2012) or the exact definition of the IERS Conventions (2010) (Petit and Luzum, 2010).

For orbit propagation this inertial frame is of high importance, being the basis for the Newtonian mechanics. Hence all equations of motion are formulated in this frame.

2.1.2 Earth-Centered Earth-Fixed (ECEF)

The Earth-Centered Earth-Fixed (ECEF) frame is the other important frame for orbit and celestial mechanics. It is identical with the International Terrestrial Reference Frame (ITRF). Its origin is in the Earth's CoM and it is co-rotating with the Earth. Hence the axes are fixed to the solid Earth. The mean rotation axis of the Earth is defined as

z-axis, while the x-axis is pointing towards the 0° meridian. Its realization is based on different measurements from about 400 stations all over the Earth. It is defined in detail in the IERS conventions (2010) including the considered models for plate tectonics, solid Earth tides, ocean and atmospheric loading effects, polar tides and further regional and local effects (Petit and Luzum, 2010).

All measurements conducted from and on the Earth are made in this frame. Furthermore models of the Earth are defined in an Earth-fixed frame, as well. Therefore the exact determination of this frame or the transformation between the ECEF and the ECI are of the highest importance for nearly all applied space sciences.

The computation of the actual transformation between the ECEF and the ECI is also defined by the IERS conventions (2010) (Petit and Luzum, 2010). Throughout this thesis the transformation matrix is referred to as T_{i2e}. The used models are based on daily Earth Orientation Parameter (EOP), which are computed and published by the IERS based on all available measurements.

2.1.3 Simple Earth Rotation

For the generation of the simulated GRACE data a simple transformation between the ECI and ECEF frame is defined. This makes the computation faster and easy to reproduce by others. The reason for that is, that the complete transformation may be implemented slightly different and different sets of EOPs are published and used, as well.

For the simplified transformation just a constant rotation around the z-axis is assumed. Thus effects like precession, nutation and polar motion are neglected. The transformation matrix is given by

$$\begin{bmatrix} \cos(\nu) & -\sin(\nu) & 0 \\ \sin(\nu) & \cos(\nu) & 0 \\ 0 & 0 & 1 \end{bmatrix}. \tag{2.1}$$

The argument ν is defined with the time in Julian Date as:

$$\nu = (t_{JD} - t_0)\ 86400\ \omega_E - \nu_0. \tag{2.2}$$

with $t_0 = 2453491.5$ (2005-05-01), the angular rate of the Earth $\omega_E = 7.29211514670698 * 10^{-5}\ 1/s$ and $\nu_0 = -2.46276246875459\ rad$. This definition has been introduced for the GRACE Mock-Data challenge in geo-Q (Darbeheshti et al., 2017) and is inherited here.

2.1.4 Satellite Body Frame

A satellite body frame is a satellite fixed frame with its origin in the satellite's CoM. Its axes can be oriented arbitrarily, usually axes are aligned with symmetry axes of the spacecraft.

If the attitude of a satellite is of interest, a body fixed frame is used as reference. Forces which are dependent on attitude or the shape of the satellite, for instance non-gravitational forces, are computed in this frame. Furthermore, it is the computation frame for rotational dynamics of a satellite (cf. Sec. 2.2.2)

For the GRACE satellite's the body frame is called Science Reference Frame (SRF) (Bettadpur, 2012b), for details see the definition in Section 3.3.1.

2.1.5 Orbital Frame

An orbital frame is defined with respect to the orbit of the satellite. Its z-axis is defined to point towards the Earth, thus

$$\vec{e}_z = -\frac{\vec{r}}{|\vec{r}|}, \tag{2.3}$$

the y-axis is in the negative direction of the orbit normal

$$\vec{e}_{y,A} = \frac{\vec{v} \times \vec{r}}{|\vec{v} \times \vec{r}|}, \tag{2.4}$$

and the x-axis completes the right hand system

$$\vec{e}_x = \vec{e}_y \times \vec{e}_z, \tag{2.5}$$

where $\times$ denotes the cross product. For a circular orbit, the x-axis is in the direction of the satellite's velocity $\vec{v}$.

The definition of the orbital frame can vary slightly by different authors, sometimes also the x-axis is defined in velocity direction, and the z-axis follows from the orthogonality.

2.1.6 Other Frames

Throughout this thesis some more reference frames are used. These are rather specific and defined in the context when they are needed. For example to define a reference attitude or pointing, like the Line of Sight (LoS) frame, or just the reference frame of a special instrument like a star camera.

2.2 Equations of Motion

The computation of satellite motion is usually based on Newtonian or classical mechanics. Also all major definitions in geodesy about rotation, shape and gravitational field of the Earth are based on this concept. Nevertheless, usually post-Newtonian relativistic corrections are considered in precise calculations in the classical framework in terms of additional accelerations (cf. Sec. 2.3.6).

With the continuous development of more accurate measurement techniques and devices, approaches for general relativistic definitions are becoming more popular (eg. Philipp et al., 2017). Nevertheless, the realization of these concepts is far from the precision of the ones used in classical geodesy, yet.

The same holds for satellite dynamics. Even easy models of the Earth (and other Planets) give by far better results than possible with general relativistic descriptions, today. Furthermore, the consideration of non-conservative forces in a general relativistic description is troublesome. By the use of post-Newtonian approximations of General Relativity in the Newtonian framework, the small differences cancel out nearly completely, as we have shown for typical Earth-bound satellite orbits in Philipp et al. (2018). Even if the much higher complexity and computational expanse is not considered, the Newtonian approach outweighs the theoretically more correct theory of General Relativity. Hence, there is barely any application of general relativistic satellite dynamics, yet.

2.2.1 Translational Motion

From Newtons second law of motion the equation of motion of a satellite is given by

$$m_{sat}\ \ddot{\vec{r}}^{\,i}_{i,b} = m_{sat}\ \vec{g}^{\,i}_{i,b}(\vec{r}^{\,i}_{i,b}, t) + \vec{F}^{\,i}_{dist} + \vec{F}^{\,i}_{ctrl}, \tag{2.6}$$

which is valid in an inertial frame, with:

m_{sat}	Mass of the satellite.
$\ddot{\vec{r}}^{\,i}_{i,b}$	Acceleration of the satellite relative to the inertial frame, expressed in the inertial frame.
$\vec{g}^{\,i}_{i,b}$	Gravitational acceleration as a function of the satellite's position and time t.
$\vec{F}^{\,i}_{dist}$	Sum of all disturbance forces acting on the satellite.
$\vec{F}^{\,i}_{ctrl}$	Control forces.

Usually the subscripts are omitted for better readability. If all variables are in the same frame, the superscripts may be omitted, as well.

The main acceleration determining a satellite's orbit is the gravitational one $\vec{g}^{\,i}_{i,b}$. Its aspects, modeling and visualization is discussed in detail in Section 2.3. Commonly the disturbing forces are referred to as non-gravitational forces, meaning mainly drag forces due to residual atmosphere and forces due to the radiation of the Sun and Earth (cf. Ch. 5.1). Generally the term may also include magnetic forces caused by the interaction of the satellite with Earth's magnetic field.

2.2.2 Rotational Motion

The rotational motion of the satellite is expressed by the angular velocity of the satellite body frame with respect to the inertial frame, $\vec{\omega}^{\,b}_{i,b}$, expressed in the satellite body frame. The attitude itself is described by the Euler symmetric parameters (quaternions) $\vec{q}^{\,b}_{i}$ or $\vec{q}_{i2b}$, which represent a transformation from inertial frame to the satellite body fixed frame (The use of quaternions to represent rotations is discussed in the Appendix A.1).

The satellite is assumed to be a rigid body. Then the differential equations for the satellites attitude motion is given by Eulers rigid body dynamics:

$$\dot{\vec{\omega}}^{\,b}_{i,b} = \left(I^{b}_{b}\right)^{-1} \left[\vec{T}^{\,b}_{ggt} + \vec{T}^{\,b}_{dist} + \vec{T}^{\,b}_{ctrl} - \vec{\omega}^{\,b}_{i,b} \times \left(I_b\, \vec{\omega}^{\,b}_{i,b}\right)\right], \tag{2.7}$$

$$\dot{\vec{q}}^{\,b}_{i} = \frac{1}{2}\, \vec{q}^{\,b}_{i}\ \underline{\omega}^{\,b}_{i,b}, \tag{2.8}$$

with:

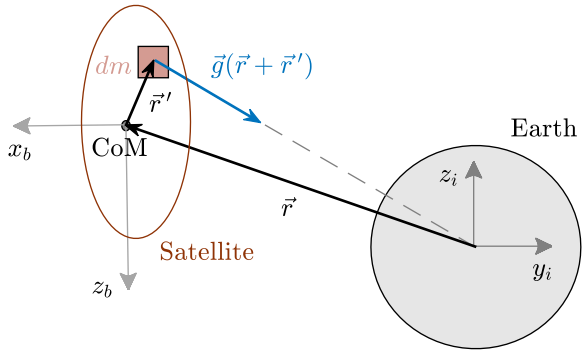

Figure 2.1: Sketch of geometrical conditions and vectors between an extended satellite and a central gravitational body.

$\vec{\omega}^b_{i,b}$	Angular velocity of the satellite body frame with respect to the inertial frame, expressed in satellite body frame.
I^b_b	Moment of Inertia (MoI) matrix of the satellite in body fixed frame.
$\vec{T}^b_{ctrl}$	Control torques applied for attitude control expressed in body fixed frame.
$\vec{T}^b_{\text{dist}}$	Disturbance torques acting on the satellite in body fixed frame.
$\vec{T}^b_{ggt}$	Gravity gradient torque in satellite body fixed frame

The term $\underline{\omega}^b_{i,b}$ is the quaternion representation of the angular velocity $\vec{\omega}^b_{i,b}$ (cf. Appendix A.1.4). The standard quaternion multiplication is applied (cf. Appendix A.1 or eg. Wertz (1978)).

Gravity Gradient Torque

An arbitrarily extended object, eg. a satellite, experiences a gravitational torque in a gravitational field, referred to as Gravity Gradient Torque (GGT). Due to the fact that the gravitational potential is conservative (cf. Sec 2.3), the acceleration at each point of the satellite is slightly different in magnitude and direction. Thus, this will result in a torque around the CoM of the satellite. The GGT is usually the biggest torque acting on Low Earth Orbit (LEO) satellites. The conditions are sketched in Figure 2.1.

Considering an arbitrary gravitational potential (cf. Sec. 2.3.1), the GGT $\vec{T}_{gg}$ can be calculated by (Gottlieb, 1993, p. 19 ff.), (Hughes, 2004, p. 233 ff.)

$$\vec{T}_{gg} = \int \vec{r}' \times G_g \vec{r}' dm, \tag{2.9}$$

with G_g being the gravity gradient matrix in the satellite fixed body frame. The gravity gradient matrix is usually defined in the inertial frame as the derivative (Jacobi matrix) of the gravitational acceleration $\vec{g}$ at the satellite's position $\vec{r}$

$$G^i_g = \frac{\partial \vec{g}}{\partial \vec{r}}. \tag{2.10}$$

Hence it needs to be transformed. With the transformation matrix T_{i2b} from inertial to body frame it is

$$G_g^b = T_{i2b}\, G_g^i\, T_{i2b}^T. \tag{2.11}$$

The GGT is dependent on the attitude with respect to the inertial frame and on the satellites extensions and its mass distribution. It can be shown, that the integral over the satellite's mass distribution results in the components of its MoI matrix I. With the components g_{ij} of the symmetric matrix G_g^b it is

$$\vec{T}_{gg} = \begin{bmatrix} g_{23}(I_{zz} - I_{yy}) - g_{13}I_{xy} + g_{12}I_{xz} + (g_{22} - g_{33})I_{yz} \\ g_{13}(I_{xx} - I_{zz}) + g_{23}I_{xy} - g_{12}I_{yz} + (g_{33} - g_{11})I_{xz} \\ g_{12}(I_{yy} - I_{xx}) - g_{23}I_{xz} + g_{13}I_{yz} + (g_{11} - g_{22})I_{xy} \end{bmatrix}. \tag{2.12}$$

Simplified Computation

An approximation of Equation (2.12) for a simple spherical gravitational potential (cf. Sec. 2.3) and a circular satellite orbit is given by

$$\vec{T}_{gg} = \frac{3\,GM}{|\vec{r}_b|^5}\left(\vec{r}_b \times I\vec{r}_b\right), \tag{2.13}$$

with $\vec{r}_b$ being the satellite's position vector in the satellite body frame and GM the gravitational coefficient of the central body. In Section 6.2 this approximation is used for the attitude controller to approximately assess the actual GGT. The computation of the gravity gradient matrix G_g^i from a realistic gravitational model (cf. Sec. 2.3.1) is computationally demanding. This approximation gives a simple but quite accurate approximation for orbits with low eccentricity.

2.3 Gravitational Potential

The main issue of gravimetry and the central topic of this thesis has been incidentally introduced in Equation (2.6), $\vec{g}_{i,b}^{\,i}(\vec{r}_{i,b}^{\,i}, t)$: The gravitational acceleration of the Earth as a function of position and time. In the following its representation and modeling is elaborated in more detail.

As introduced in Section 2.2, geodesy is based on classical, Newtonian mechanics. Thus gravitation is governed by Newtons law of universal gravitation, stating that every mass in the universe attracts each other with the force $\vec{F}_{grav}$, which is proportional to their product and inversely proportional to the square of their distance $\vec{d}$:

$$\vec{F}_{grav} = -G\frac{m_1\, m_2}{|\vec{d}|^2}\,\frac{\vec{d}}{|\vec{d}|}. \tag{2.14}$$

G is the universal gravitational constant and $\vec{d}$ the vectorial distance between the centers of the masses m_1 and m_2. From Equation (2.14) the gravitational acceleration $\vec{g}$ due to a mass M at the point $\vec{x}$ on an other mass m at the point $\vec{r}$ can be calculated as

$$\vec{g} = -\frac{GM}{|\vec{r} - \vec{x}|^2}\,\frac{\vec{r} - \vec{x}}{|\vec{r} - \vec{x}|} = -\frac{GM}{|\vec{d}|^2}\,\frac{\vec{d}}{|\vec{d}|}, \tag{2.15}$$

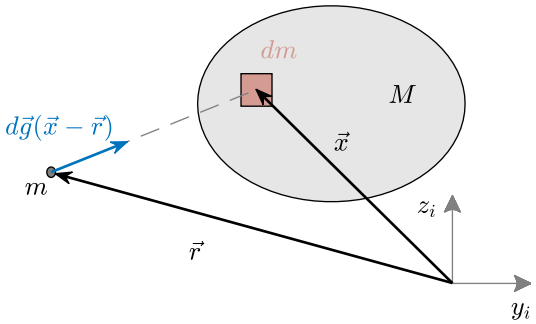

Figure 2.2: Sketch of geometrical conditions for the gravitational acceleration on a small mass m due to an extended mass M.

with $\vec{d} = \vec{r} - \vec{x}$. Assuming that mass M is a celestial body, eg. the Earth, which consists out of infinitesimal mass elements dm with the positions $\vec{x}$, as sketched in Figure 2.2. For an arbitrary mass distribution dm can be written as a density distribution $dm = \rho(\vec{x})\, dV$. The resulting acceleration $\vec{g}$ follows then by the integration over the volume dV

$$\vec{g} = -G \int_V \rho(\vec{x}) \frac{\vec{r} - \vec{x}}{|\vec{r} - \vec{x}|^3}\, dV. \tag{2.16}$$

The vectorial gravitational acceleration field $\vec{g}(\vec{r})$ (Eq. 2.16) can be expressed as the gradient of a scalar potential field $V(\vec{r})$ because it is invariant to rotations $\nabla \times \vec{g} = 0$. The scalar potential field is mathematically easier to handle (eg. Torge and Müller, 2012)

$$\vec{g} = \nabla V(\vec{r}), \tag{2.17}$$

$$V(\vec{r}) = G \int_V \frac{\rho(\vec{x})}{|\vec{r} - \vec{x}|}\, dV. \tag{2.18}$$

With Equation (2.18) the gravitational field of the Earth or an other celestial body is defined. It can be shown (eg. Torge and Müller, 2012, p. 57 ff.), that the gravitational potential, defined by Equation (2.18), satisfies Laplace's differential equation

$$\Delta V(\vec{r}) = 0 \tag{2.19}$$

in the exterior of the gravitating body.

Unfortunately, the density distribution $\rho(\vec{x})$ in Equation (2.18) of the Earth is not adequately known and hard to measure. Thus a sophisticated computation of the potential from Newtons gravitational law is not expedient. This is an important equation because it states a fundamental problem in geodesy. Even if the outer potential $V(\vec{r})$ of a body is known, it is not possible to invert Equation (2.18) to obtain the mass or density distribution $\rho(\vec{x})$: There are infinite mass distributions which result in the same outer potential. More information needs to be known or assumed to restrict this equation.

In general, the English language distinctly distinguishes between gravitation and gravity. The first is the potential, force or acceleration due to the attraction of masses (in the Newtonian perspective). Gravity is the sum of gravitation and the centrifugal

acceleration due to the rotation of a celestial body or the Earth. However, often the terms are used interchangeably. Because satellites do not rotate with the Earth, they do not experience a centrifugal acceleration. Thus gravity does not play a direct role for satellites.

2.3.1 Spherical Harmonic Potential

The gravitational potential outside the Earth can be described as a convergent series expansion, leading to the so called Spherical Harmonic (SH) potential. The SH potential is a special solution of Laplace's equation (Eq. 2.19). A detailed derivation is given by eg. Torge and Müller (2012), p. 69 ff.. Here the notation following Montenbruck and Gill (2005), p. 56 ff., is used. For the spherical geocentric coordinates longitude λ, latitude ϕ and radius r the SH potential is

$$V(\lambda,\phi,r) = \frac{GM}{r}\sum_{n=0}^{\infty}\sum_{m=0}^{n}\left(\frac{R}{r}\right)^n \left(C_{nm}\cos(m\lambda) + S_{nm}\sin(m\lambda)\right) P_{nm}(\sin\phi), \tag{2.20}$$

with degree n and order m. For the lengthy definition of the associated Legendre polynomials P_{nm} of degree n and order m, via Legendre's differential equation and their computations for n and m, the interested reader is referred to the mentioned literature. The coefficients C_{nm} and S_{nm} are the parameters defining the potential. R is a reference radius of the Earth and GM its gravitational coefficient. R and GM are as well parameters of the model. Of cause, in practice the expansion is terminated at a finite degree N. The maximal degree and order is usually abbreviated by d/o. The determination of the C_{nm} and S_{nm} coefficients is the essence of Gravity Field Recovery (GFR). Together with GM and R they make up a static gravitational field model. The number of the SH coefficients C_{nm} and S_{nm} is

$$N_{coef} = N^2 - N_{min}^2 + 2N + 1, \tag{2.21}$$

where N_{min} is the lowest considered degree which is usually two for GFR, see the SH interpretation in Section 2.3.1. The SH coefficients C_{nm} and S_{nm} are also referred to as Stokes Coefficients. They are classified in three groups, zonal ($m = 0$), tesseral ($m < n$) and sectorial ($m = n$). The zonal coefficients with $m = 0$ are not dependent on the longitude (cf. Eq. 2.20) and define the flattening and pear-shape of the Earth.

Spherical Harmonics Interpretation

It is possible to interpret the first few coefficients, physically. For order $m = 0$ the coefficients $S_{n,0}$ always become zero, because $\sin(m\lambda) = 0$ in Equation (2.20), thus the zonal coefficients are just the $C_{n,0}$ coefficients. The degree $n = 0$ coefficient, $C_{0,0}$ is usually set to 1, hence the degree zero potential is $V = GM/r$, what is the representation of a perfect symmetrical sphere, equivalent to a point mass. All other degrees can then be interpreted as disturbances from this ideal case. Therefore, in some notations the first sum in Equation 2.20 is started from $n = 1$ and $C_{0,0} = 1$ is moved in front of the sum.

It can be shown that the coefficients $C_{1,0}$, $C_{1,1}$ and $S_{1,1}$ describe the deviation of the center of mass from the coordinate system origin divided by R in $z-$, $x-$ and $y-$direction, respectively. In an Earth centered coordinate system they are zero by

definition. Furthermore, if the the z-axis is a principle axis of inertia, the coefficients $C_{2,1}$ and $S_{2,1}$ are zero, as well. Neglecting polar motion this is true, and $C_{2,1} = S_{2,1} = 0$ may be applied. This is usually not done for monthly GRACE solutions.

The zonal coefficient $C_{2,0}$ describes the by far biggest deviation from the ideal spherical potential and the main flattening of the Earth due to its rotation. The often used J_2 coefficient is related by $J_2 = -C_{2,0}$. Exact derivation of these interpretations can be found in Torge and Müller (2012), p. 74 - 76 and Montenbruck and Gill (2005), p. 59 - 61.

Usually the SH potential (Eq. 2.20) is given in a normalized notation, with the normalized coefficients $\bar{C}_{nm}$, $\bar{S}_{nm}$ and normalized Legendre polynomials $\bar{P}_{nm}$ (Montenbruck and Gill, 2005, p. 58), making the coefficients more uniform in size. They are barely used in the non-normalized form, therefore the bar is often dropped. In this thesis always the normalized coefficients are used, neglecting the bar, as well. The relations are given by

$$\left\{ \begin{array}{c} \bar{C}_{nm} \\ \bar{S}_{nm} \end{array} \right\} = \sqrt{\frac{(n+m)!}{(2-\delta_{0m})(2n+1)(n-m)!}} \left\{ \begin{array}{c} C_{nm} \\ S_{nm} \end{array} \right\}, \tag{2.22}$$

$$\bar{P}_{nm} = \sqrt{\frac{(2-\delta_{0m})(2n+1)(n-m)}{(n+m)!}} P_{nm}, \tag{2.23}$$

with δ_{0m} being the Kronecker delta.

The SH representation of the gravitational field with different degrees n can be understood as superimposed waves. Therefore, often the term wavelength λ or half wavelength $\lambda/2$ is used to describe features or structures of the gravitational field. At the Earth surface the wavelength in degree is

$$\lambda = \frac{360^\circ}{n}. \tag{2.24}$$

For the maximum degree N of a SH gravitational model, the shortest resolvable wavelength can be determined. Commonly the spatial resolution is given as the half wavelength D in km (Seeber, 2003, p. 470)

$$D = \frac{20000\ km}{N}. \tag{2.25}$$

2.3.2 The Geoid

The Geoid defines the shape of the Earth. It is the reference surface for height measurements and is the scientific definition of the commonly used term "see level". It was first described by C. F. Gauss in 1828 as the "equipotential surface of the Earth's gravity field coinciding with the mean sea level of the oceans" (Gauss, 1828, p. 49). The name Geoid was given later in 1873 by J. B. Listing (Torge and Müller, 2012, p. 76). To fully characterize the Geoid, the gravity potential $W(\lambda, \phi, r)$ and the value W_0 at the mean sea level have to be determined. All gravity accelerations and plumb lines are perpendicular to the equipotential surface of the Geoid. Nevertheless, the magnitude of the gravity is not constant over this surface.

There are several difficulties with that definition due to the fact that the potential is directly influenced by the Sun, Moon and other planets. This causes also indirect

tidal effects, deforming the solid Earth, which in turn changes its gravitational field. Furthermore, the mean sea level is not obvious, too, since it is also affected by tides, but as well by currents, winds, local atmospheric pressure and a general changing water level due to seasonal effects and sea level rise. Therefore a value W_0 is defined by reducing temporal variations of the mean sea level by averaging and referring to an epoch, conventional approaches and values are given in the IERS Conventions (Petit and Luzum, 2010).

Mainly three different approaches to deal with direct and indirect tidal forces exist for a definition of the Geoid:

- **Mean Geoid**: Includes direct third body accelerations, as well as indirect tidal effects due to the deformation of the Earth. It would display an undisturbed mean ocean surface and is hence used in oceanography.
- **Tide-free Geoid**: Excludes all tidal effects, and represents an Earth in an empty universe, which is not periodically deformed by other bodies.
- **Zero-tide Geoid**: Excludes all effects due to time dependent tidal deformation, but keeps permanent effects.

The same terminology needs to be considered for gravitational field models. In GFR usually static models are determined. Tidal effects are added by respective time dependent models. The different effects and its modeling is described in Section 2.3.5. Gravitational field models are usually given in the tide-free or zero-tide system, differing if the permanent contribution is considered by a tide model (tide-free) or is estimated and included in the gravitational field model (zero-tide) (Petit and Luzum, 2010, p. 88 f.). The permanent tidal contribution is mainly affecting the $C_{2,0}$ coefficient and modeled by a solid Earth tide model (cf. Sec. 2.3.5). For the estimated gravitational fields in this thesis the zero-tide representation is used.

Geoid Height

The Geoid can be represented by a SH expansion, like gravitational fields. It is closely connected to the gravitational potential from Equation (2.20) and is determined from it. Hence gravitational fields are often visualized as Geoid, or more exactly as geoid height. The geoid height $N(\lambda, \phi)$ is the common visualization of the Geoid. It is defined as the height difference between the Geoid and a reference ellipsoid, which is best approximating the Geoid. The ellipsoidal gravity potential is defined by $U(\phi, r)$. From the that fact that $U(\phi, r)$ is best approximating the Geoid $W(\lambda, \phi, r)$, it follows that $W_0 = U_0$. For an exact derivation and discussion see eg. Barthelmes (2013). Considering the gravity potential of the ellipsoid $U(\phi, r)$, called normal potential, and the disturbing potential $T(\lambda, \phi, r)$, the gravity potential of the Earth $W(\lambda, \phi, r)$ is

$$W(\lambda, \phi, r) = U(\phi, r) + T(\lambda, \phi, r). \tag{2.26}$$

While W and U contain a centrifugal potential, T is a completely gravitational potential. W and U can be equivalently written as the sum of an gravitational (attractive) potential plus the centrifugal potential Φ

$$U(\phi, r) = U_a(\phi, r) + \Phi(\phi, r). \tag{2.27}$$

The gradient of the normal potential on the ellipsoid

$$\vec{\gamma} = \nabla U \tag{2.28}$$

is referred to as normal gravity vector, and its magnitude γ

$$\gamma = |\nabla U| \tag{2.29}$$

as normal gravity.

Let h be the height above the ellipsoid. Then, according to the popular formula of Bruns (Barthelmes, 2013),(Torge and Müller, 2012, p. 258), the geoid height $N(\lambda, \phi)$ can be approximated to first order (but relatively accurate) by

$$N(\lambda, \phi) = \frac{W(\lambda, \phi, r(h=0)) - U(\phi, r(h=0))}{\gamma(\phi, r(h=0))} = \frac{T(\lambda, \phi, r(h=0))}{\gamma(\phi, r(h=0))}. \tag{2.30}$$

The centrifugal potentials Φ of the Geoid and the ellipsoid are the same and thus vanish in this equation.

For representations in this thesis the attractive ellipsoidal potential U_a is approximated by the constant first even zonal SH coefficients $C_{0,0}$, $C_{2,0}$, $C_{4,0}$, $C_{6,0}$, $C_{8,0}$ of a reference model. With the gravitational potential V (Eq. 2.20), the disturbing potential T in Equation (2.26) can be written as

$$T(\lambda, \phi, r) = V(\lambda, \phi, r) - U_a(\phi, r). \tag{2.31}$$

With both potentials being a SH expansion, the equation (Eq. 2.30) can be written as a SH expansion, as well, with the relative SH coefficients C'_{nm} and S'_{nm}:

$$N(\lambda, \phi) = \frac{1}{\gamma_0} \frac{GM}{r(h=0)} \sum_{n=0}^{N} \sum_{m=0}^{n} \left(\frac{R}{r(h=0)} \right)^n \left(C'_{nm} \cos(m\lambda) + S'_{nm} \sin(m\lambda) \right) P_{nm}(\sin\phi). \tag{2.32}$$

Just the first zonal coefficients of C'_{nm} and S'_{nm} are different from the C_{nm} and S_{nm} coefficients of the gravitational potential V in Equation (2.20).

In Figure 2.3 the geoid height is computed as described before from the GGM05s gravitational field model. The GGM05 model (Ries et al., 2016) is a static SH model computed from ten years of GRACE observations between 2003 and 2013. It is used as a reference throughout this thesis.

A further, very popular simplification of the the geoid height computation exists, used for the visualization of gravitational fields and the computation of degree amplitudes in terms of geoid height (Sec. 2.3.3). It is especially used to compare residual gravitational fields, meaning the difference of two fields. In SH representation (eg. Eq. 2.20), the residual field is the SH expansion with the coefficients ΔC_{nm} and ΔS_{nm}, being the difference of the C_{nm} and S_{nm} coefficients of the two models.

If the normal gravity of the ellipsoid γ_0 is approximated as the one of a sphere with the reference radius R, and furthermore neglecting the much smaller centrifugal potential (it vanishes anyway if a residual field is considered), it can be written as

$$\gamma_0 \approx \frac{GM}{R^2}. \tag{2.33}$$

The relative error of this approximation is about 0.3% (Liu, 2008). Furthermore, the field is evaluated at the reference radius $r = R$. Substituting this in Equation 2.32, the geoid height can be expressed as

$$N(\lambda, \phi) = R \sum_{n=0}^{N} \sum_{m=0}^{n} \left(C_{nm} \cos(m\lambda) + S_{nm} \sin(m\lambda) \right) P_{nm}(\sin\phi). \tag{2.34}$$

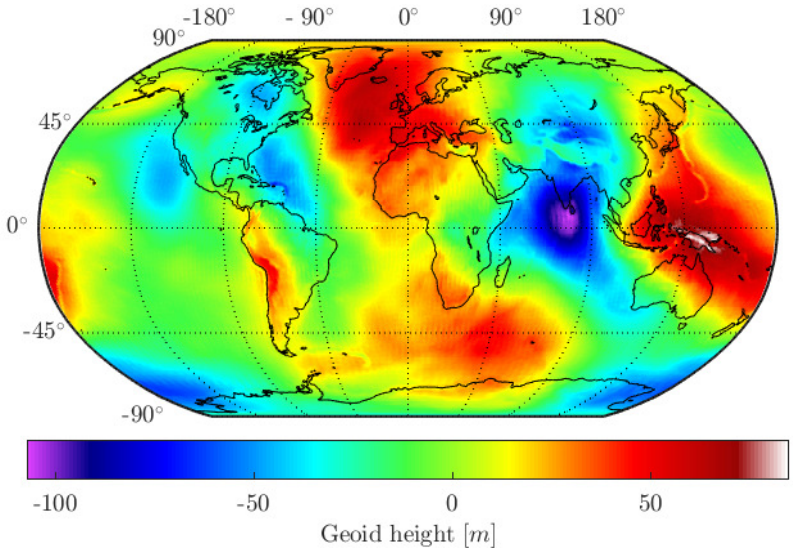

Figure 2.3: Geoid height computed from the GGM05s gravitational field model up to d/o 180.

This is a very common approximation and often used, especially for residual fields.

Mass Change - Equivalent Water Height (EWH)

In the introduction of this section (Sec. 2.3) it has been already mentioned, that it is not possible to obtain the mass distribution from the gravitational field or potential by inversion.

Nevertheless, the actual measured changes of the gravitational field of the Earth are mainly due to changes and the redistribution of water in the near surface layer of the Earth. Therefore it can be assumed that the change of the gravitational potential ΔV or the geoid height ΔN is caused by a thin water layer close to the surface with the density $\rho_w = 1000\ kg/m^3$. Following the derivation by Wahr et al. (1998), the mass change $\Delta\sigma$ is defined as

$$\Delta\sigma(\lambda,\phi) = \int_{thin\ layer} \Delta\rho(\lambda,\phi,r)\ dr, \tag{2.35}$$

with the dimension mass per area. The hydrological processes can be referred to the layer between groundwater and the lower atmosphere, and thus is very small compared to the Earth's radius. The term $\Delta\sigma/\rho_w$ is the change in surface mass expressed as a water column. This is referred to as Equivalent Water Height (EWH). $\Delta\sigma$ is expressed as SH expansion

$$\Delta\sigma(\lambda,\phi) = R\rho_w \sum_{n=0}^{N}\sum_{m=0}^{n} \left(\Delta\check{\mathrm{C}}_{nm}\cos(m\lambda) + \Delta\check{\mathrm{S}}_{nm}\sin(m\lambda)\right) P_{nm}(\sin\phi). \tag{2.36}$$

It can be shown (Wahr et al., 1998), that the correlation between the coefficients $\Delta\check{\mathrm{C}}_{nm}$, $\Delta\check{\mathrm{S}}_{nm}$ and ΔC_{nm}, ΔS_{nm}, is given as a good approximation by

$$\begin{Bmatrix} \Delta\check{\mathrm{C}}_{nm} \\ \Delta\check{\mathrm{S}}_{nm} \end{Bmatrix} = \frac{\rho_{ave}(2n+1)}{3\rho_w(1+k_n)} \begin{Bmatrix} \Delta C_{nm} \\ \Delta S_{nm} \end{Bmatrix} \tag{2.37}$$

with $\rho_{ave} = 5517\ kg/m^3$ being the average Earth density. The term includes the direct effect of the mass change and the indirect effect due to the deformation of the solid

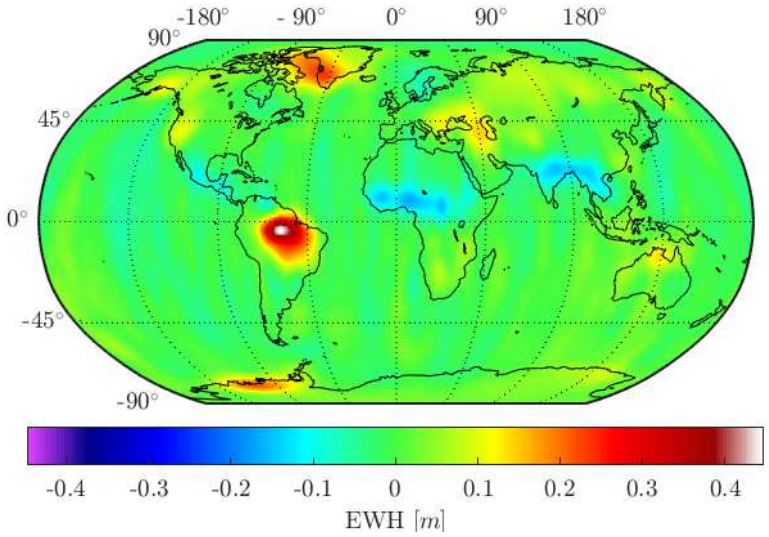

Figure 2.4: EWH with respect to GGM05s from estimated gravitational field of May 2006 from GRACE data, Gaussian filter with 465 km radius applied.

Earth, modeled with the degree dependent load Love numbers k_n (eg. Torge and Müller, 2012, p. 357 ff.).

Exemplary, an estimated gravitational field up to d/o 90 for May 2006 from GRACE data is spatially visualized over the Earth in terms of EWH and ΔN in the Figures 2.4 and 2.5, respectively. In the first figure the relative mass change, expressed as EWH, is shown for the difference of the estimated gravitational field for May 2006 and the mean GGM05s gravitational field model. Around the equator the strong signals mainly relate to mass changes due to seasonal effects of rainy and dry periods compared to the mean GGM05s model. The other strong signals are at the poles where the ice masses seasonally de- and increase. This effect is superimposed by a general mass loss of the polar ice. Thus, even in the summer period in 2006 there is a positive value over the North Pole compared to the ten year (2003 -2013) mean model. A further effect especially in this region is the Glacial Isostatic Adjustment (GIA), but should not be considered in more detail, here.

The same relative field is shown in Figure 2.5 in terms of residual geoid height ΔN. The main signals are visible as well, but it is obvious, that the spatial visualization of the two functionals $\Delta\sigma$, or more exactly EWH, and ΔN over the Earth is slightly different.

2.3.3 Degree Amplitudes

Besides the spatial visualization of the different functionals plotted over the Earth, as shown in the previous sections, the gravitational field parameter C_{nm}, S_{nm} or its differences ΔC_{nm}, ΔS_{nm} are commonly shown and analyzed in a spectral plot over the degree n. The degree amplitude or the spectrum is defined as

$$d_n = \sqrt{\sum_{m=0}^{n} (C_{nm}^2 + S_{nm}^2)}. \tag{2.38}$$

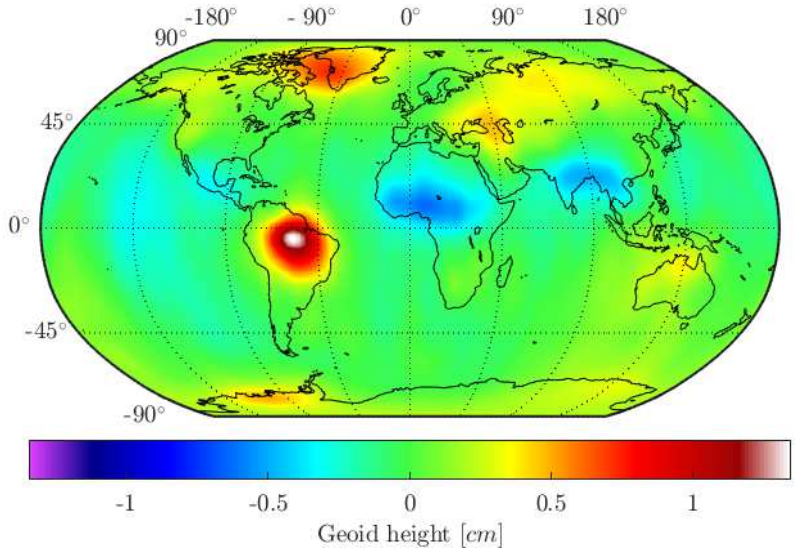

Figure 2.5: Geoid height with respect to GGM05s from estimated gravitational field of May 2006 from GRACE data, Gaussian filter with 465 km radius applied.

If a residual SH field, the error, the variance or the formal error is considered, the spectral plot is referred to as square root of degree difference or square root of degree variance

$$\Delta d_n = \sqrt{\sum_{m=0}^{n} (\Delta C_{nm}^2 + \Delta S_{nm}^2)} \quad \text{or} \quad \sigma_n = \sqrt{\sum_{m=0}^{n} (\sigma_{Cnm}^2 + \sigma_{Snm}^2)}. \tag{2.39}$$

The names of these representations are slightly different from author to author and usually the term "square root" in the name is dropped.

From the comparison of Equation 2.20, defining the SH gravitational potential and 2.34, being the simplified representation of the geoid height (especially used for residual fields), it is obvious that the coefficients just differ by the multiplication of the reference radius R. Therefore degree differences and degree variances are often plotted in terms of geoid height by the multiplication with R giving it the unit of height

$$\Delta d_n(N) = R\, \Delta d_n \qquad \text{or} \qquad \sigma_n(N) = R\, \sigma_n. \tag{2.40}$$

The degree amplitude of an Earth gravitational field model can be approximately described by the so called Kaula rule, stating that the normalized SH coefficients C_{nm} and S_{nm} follow approximately

$$d_n \approx \frac{10^{-5}\sqrt{2n+1}}{n^2}. \tag{2.41}$$

in the degree amplitude plot. The name refers to Kaula (1966).

The degree amplitudes of the GGM05s model and Kaula's rule are plotted in Figure 2.6, together with the degree difference of the monthly solution of May 2006 up to d/o 90 with respect to the GGM05s model (as already shown in the section and figures before).

The differences of the mean GGM05s model and the monthly gravity field solution are quite small and their differences are just visible in the relative plot. The spectral plot reveals different characteristics of the differences over the wavelengths of the field.

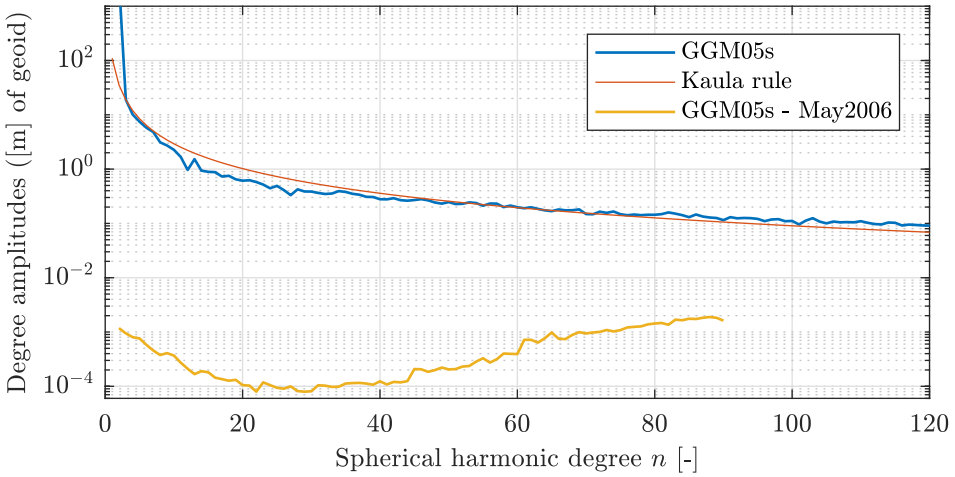

Figure 2.6: Degree amplitudes of the GGM05s model and Kaula's rule plus degree difference of May 2006 solution with respect to GGM05s, all in terms of geoid height.

2.3.4 Filters

Monthly gravity field solutions from GRACE data contain distinct correlated errors resulting in the typical north-south striping pattern in the spatial domain. This aliasing effects are mainly due to the under sampling of tidal effects that are not modeled completely correct and the ground-track pattern of the satellites with the main measurement direction of the inter-satellite ranging in along-track direction.

Many approaches have been developed to remove these errors by smoothing, filtering and decorrelating of the errors see eg. Swenson and Wahr (2006); Kusche (2007). A very popular approach is still the Gaussian filter (Jekeli, 1981). Mainly the higher degree SH coefficients contain a high noise. Therefore a filter needs a gradually decreasing kernel, which is acting as a spatial low-pass filter for the SH coefficients. A typical bell-shaped Gaussian smoothing kernel is used, giving the filter its name. The filtered solution is spatially averaged over the smoothing radius, which can be chosen freely for the Gaussian filter (Sakumura, 2014), (Liu, 2008, p. 225 f.). In this thesis all GRACE solutions are filtered with a Gaussian filter with a filter radius of 465 km.

In Figure 2.7 the estimated gravitational field from May 2006, as shown in the Figures before (eg. Fig. 2.4), is presented in terms of EWH again, but with four different filter radii of the Gaussian filter: (a) no filter is applied, (b) 260 km, (c) 465 km and (d) 720 km. The scale in each plot is different. With no filter (a), the quite strong, unphysical striping is distinctly visible. With increasing filter radius the quality of the solution increases up to a certain point where it is decreasing again. For radii above 700 km the striping is getting more and more pronounced, again.

The optimal filter radius is dependent on the error characteristic of the solution, but furthermore, strongly dependent on the d/o of the estimated field. As reference, a solution with d/o 60 for the same month and apart from the d/o with the same processing options, is shown for four different filter radii in Figure 2.8. The filtered solutions with the same filter radius of r = 465 km are nearly equal. But the unfiltered d/o 90 solution exhibits a striping with an about seven times higher amplitude than the d/o 60 solution. The filter characteristics are also very different. For the lower d/o solution, the filtered solutions are stable over a bigger range of the filter radius. Thus the filter radius of r = 1000 km gives still a reasonable signal (c). This plot illustrates distinctly the smoothing or blurring effect of the spatial filter. Compared to the 465

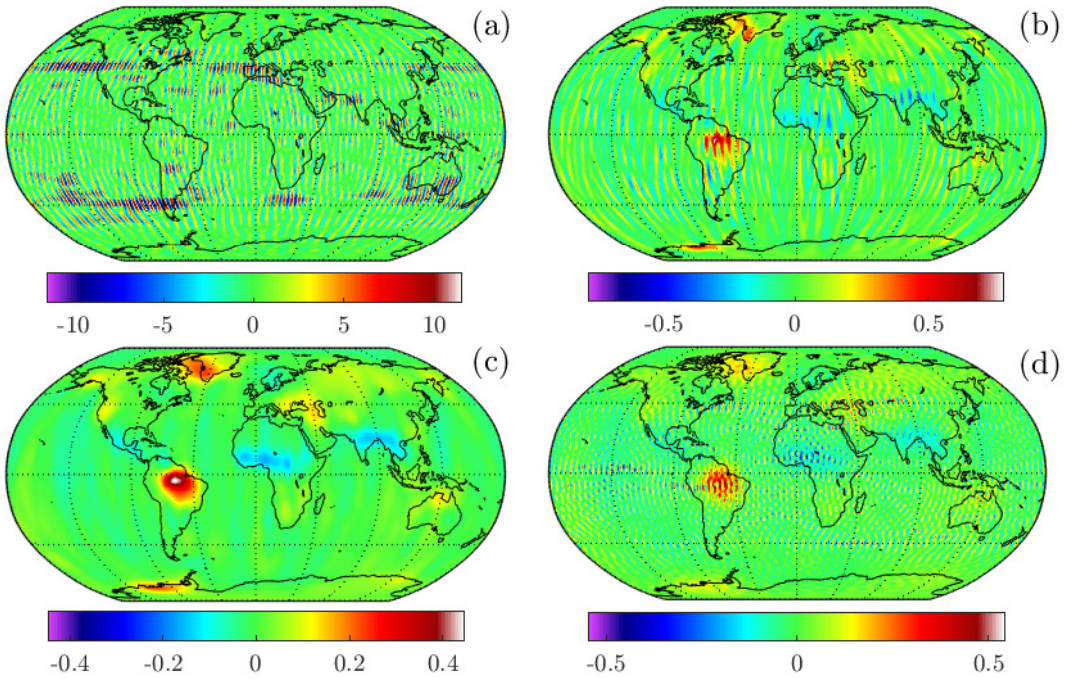

Figure 2.7: EWH [m] with respect to GGM05s from estimated gravitational field of May 2006, d/o 90, filtered with Gaussian filter with different filter radii (a) no filter, (b) r = 260 km, (c) r = 465 km, (d) r = 720 km.

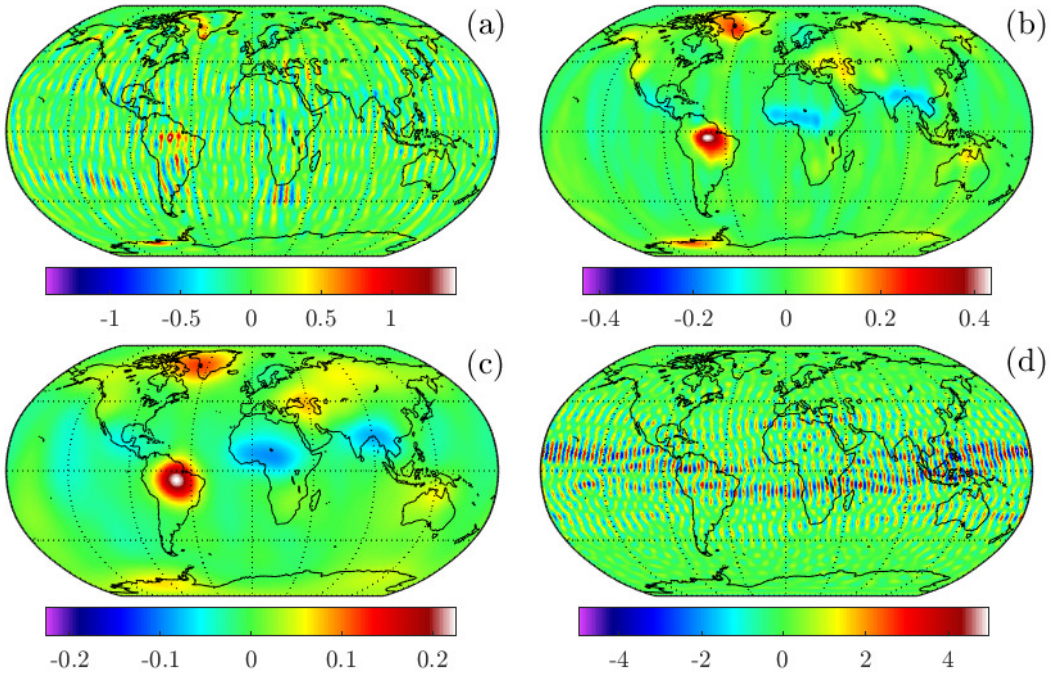

Figure 2.8: EWH [m] with respect to GGM05s from estimated gravitational field of May 2006, d/o 60, filtered with Gaussian filter with different filter radii (a) no filter, (b) r = 465 km, (c) r = 1000 km, (d) r = 1200 km.

km radius (b), the prominent signals are blurred and covering a wider area but with a lower amplitude. This also demonstrates that the filter is an indispensable aid but reduces the precision or resolution and future mission designs should aim to reduce the striping by the measurement concept.

2.3.5 Tidal Forces and Effects

In Section 2.3.2 three different systems to define the Geoid and the gravitational field of the Earth have been introduced. In GFR usually the tide-free system is used because time dependent models of the mostly periodic tidal effects exist. Thus other gravitational effects can be resolved with much better accuracy by a gravitational field model.

Tidal effects are mainly caused by the Moon, the Sun and the rotation of the Earth. Direct and indirect tidal effects are distinguished. The direct effect is the gravitational third body attraction. This attraction deforms the solid Earth and moves the fluid masses, water and the atmosphere, of the Earth. This movement of masses causes the indirect change of Earth's gravitational field.

The change of the gravitational field or potential due to the indirect tides is modeled by SH expansions, as well. Different time dependent SH coefficients are determined considering the periodicity of the effects depending on the position of Sun and Moon.

Third Body Attraction

The gravitational attraction of other celestial bodies than the central one, is also referred to as direct tides in the field of geodesy. For Earth-bound satellites these bodies are so far away, that they are usually considered as point masses. The gravitational acceleration of a point mass, eg. the Sun is described by Equation (2.15). Some care has to be taken, because it refers to an inertial system, but with respect to to the Sun, the Earth is not at rest, but subject to the acceleration

$$\ddot{\vec{r}} = -GM_{Sun}\frac{\vec{r}_{Sun}}{|\vec{r}_{Sun}|^3}. \tag{2.42}$$

Where $\vec{r}_{Sun}$ is the vector pointing from Earth towards the Sun. Thus, the acceleration of the Sun on the satellite r_{sat} in the ECI system is (eg. Montenbruck and Gill, 2005, p. 69)

$$\ddot{\vec{r}}_{sat} = -GM_{Sun}\left(\frac{\vec{r}_{sat}-\vec{r}_{Sun}}{|\vec{r}_{sat}-\vec{r}_{Sun}|^3}+\frac{\vec{r}_{Sun}}{|\vec{r}_{Sun}|^3}\right). \tag{2.43}$$

Solid Earth Tides

The third body accelerations are deforming the solid Earth, leading to mass redistribution, changing its gravitational field. This is the biggest indirect tidal effect. The time dependent SH model up to d/o 4, given in the IERS Conventions 2010 (Petit and Luzum, 2010, p. 81 ff.), is used.

Ocean Tides

The movement of the ocean water masses causes a change of the gravitation, as well as a loading of the solid Earth. Different models exist, here the EOT11a model (Savcenko et al., 2012; Mayer-Gürr et al., 2012) is used, which considers both effects. It is available

up to d/o 120. It is developed from the data of several altimetry satellite missions. It considers several time dependent SH potentials for the different superimposed tidal constituents.

Atmospheric Tides

As the for the ocean tides, the atmosphere is affected by the direct acceleration of Sun and Moon, resulting in changes of the mass distribution and hence the gravitational field. Compared to the ocean tides the models are much simpler. Here the N1 Biancale & Bode model (S1+S2) Biancale and Bode (2006) up to d/o 8 is used. It is based on surface pressure data.

Pole Tides

Polar motion is the movement of Earth's rotational axis with respect to its solid body or the ECEF system. This induces centrifugal forces which affect in turn the mass distribution.

As described in Section 2.3.1 the difference of the principal axis of inertia with respect to the z-axis is described by the coefficients C_{21} and S_{21}. Thus polar motion is modeled by a time dependency of these coefficients. Here the model advertised in the IERS Conventions 2010 (Petit and Luzum, 2010, p. 93 f.) is utilized.

Ocean Pole Tides

The centrifugal forces induced by polar motion also affect the water masses of the Earth. The Desai2002 model (Desai, 2002), advertised in the IERS Conventions 2010 (Petit and Luzum, 2010) estimates the relative gravitaional potential of these effects with a SH model up to d/o 180.

2.3.6 Post-Newtonian Relativistic Corrections

Up to a certain accuracy, general relativistic effects can be represented as correction accelerations in the classical Newtonian framework. These accelerations are referred to as post-Newtonian (pN) corrections. For Earth bound satellites, mainly three terms are considered, as described in the IERS Conventions (Petit and Luzum, 2010). The three effects are a *Schwarzschild* term, representing a relativistic correction for a spherical gravitating central mass, the *Lense-Thirring* term, representing a correction for the rotation of that mass, and the *de Sitter* term, representing a correction for the geodetic or de Sitter effect due to the Sun. For the comparably low gravitation of the Earth and its slow rotation, as well as the velocities in that systems, which are much smaller than the speed of light c, the Schwazschild and Lense-Thirring corrections are very accurate approximations. The de Sitter correction term is already more than 15 orders of magnitude smaller.

Comparisons of simple cases with complete solutions of the general relativistic equations, have shown that the differences with classical solutions considering pN corrections are very small comparing to numerical errors and are just visible when using a data type with a higher precision than the standard *double* data type, as we have analyzed for typical Earth-bound satellite orbits in Philipp et al. (2018).

Magnitude and direction of these correction accelerations are depicted for the GRACE satellites in Section 6.1.3, and are compared to the non-gravitational accelerations acting on the satellites. Furthermore, their influence on the orbit is evaluated and compared, as well.

In the inertial ECI frame, the three pN correction accelerations are (eg. Petit and Luzum, 2010, p. 155 f.)

$$\Delta\ddot{\vec{r}}_{Schw} = \frac{GM_E}{c^2\, r^3}\left[\left(\frac{4GM_E}{r} - \dot{\vec{r}}\cdot\dot{\vec{r}}\right)\vec{r} + 4(\vec{r}\cdot\dot{\vec{r}})\dot{\vec{r}}\right], \tag{2.44}$$

$$\Delta\ddot{\vec{r}}_{LT} = \frac{2GM_E}{c^2\, r^3}\left[\frac{3}{r^2}\left(\vec{r}\times\dot{\vec{r}}\right)\left(\vec{r}\cdot\vec{J}\right) + \left(\dot{\vec{r}}\times\vec{J}\right)\right], \tag{2.45}$$

$$\Delta\ddot{\vec{r}}_{dS} = 3\left[\dot{\vec{r}}_{Sun}\times\left(\frac{-GM_{Sun}\,\vec{r}_{Sun}}{c^2\, r_{Sun}^3}\right)\right]\times\dot{\vec{r}}. \tag{2.46}$$

Therein $\vec{r}$ and $\vec{r}_{Sun}$ are the satellite's and Sun's position in ECI, and r, r_{Sun} their norm, respectively. GM_E and GM_{Sun} are the gravitational coefficients of Earth and Sun, respectively. $\vec{J}$ is the angular momentum per unit mass of the Earth ($|\vec{J}| \approx 9.8*10^8$ m^2/s). The $\cdot$ operator denotes the scalar product and $\times$ the cross product.

THE GRACE MISSION 3

This thesis is dealing with Gravity Field Recovery (GFR) from a GRACE-like mission. Even though, fundamentals, theory and models are generally usable for all kind of satellite missions, measurement principles and observations, the application in this thesis is focused on the GRACE mission. Therefore the GRACE mission, its measurement principle and the satellite's instrumentation is introduced in this chapter.

3.1 Mission Overview

GRACE (Gravity Recovery and Climate Experiment) was a joint satellite mission between the National Aeronautics and Space Administration (NASA) and the German Aerospace Center (DLR). Its primary science purpose was to measure the Earth's gravitational field and its time variability (Tapley et al., 2004a). It was launched in March 2002 and collected science data until June 2017. The exceedingly successful mission is continued by its successor GRACE Follow-On (GRACE-FO) (Landerer et al., 2020) with nearly identical hardware.

The GRACE mission was proposed in 1996 by a scientific consortium of the Center for Space Research at the University of Texas, Austin (UT CSR), the German Research Center for Geosciences Potsdam (GFZ) and the Jet Propulsion Laboratory (JPL). It was selected in 1997 as second mission in NASA's Earth System Science Pathfinder (ESSP) program.

The mission consists of two, basically identical, satellites which are following each other on the same orbit with a slightly varying distance of about 220 km. The two spacecrafts are referred to as GRACE A and B. The nearly polar orbit with an initial altitude of about 500 km assures global coverage of the observations. With an initial mass of about 487 kg at launch they are classified as small satellites. The trapezoid shaped satellites (cf. Fig. 3.2) have the dimensions of about $3.1 \times 1.9 \times 0.7$ m. Detailed satellite information is available in the *Product Specification Document* (Bettadpur, 2012b).

The main and innovative measurement principle of the GRACE mission is the low-low satellite-to-satellite tracking (ll-SST). The inhomogeneous mass distribution of the Earth results in slightly changing gravitational attraction, which in turn results in the change of the satellites distance. From this change, conclusions on the gravitational field can be drawn (cf. Ch. 4). The inter-satellite distance can be measured much more accurately than for example a ground based distance or the absolute position via GNSS (Global Navigation Satellite System). With a microwave ranging system the inter-satellite distance, and especially its change, is measured with an unprecedented accuracy of about 0.1 $\mu m/s$ in a frequency range bigger 1 mHz (just exceeded by the GRACE-FO laser interferometer, (Sheard et al., 2012; Abich et al., 2019).

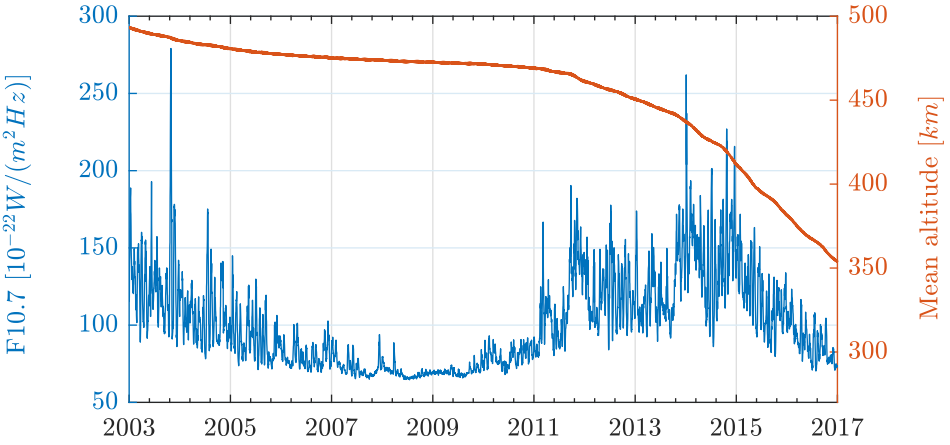

Figure 3.1: Solar radio flux (F10.7) and GRACE mean altitude over the whole mission time period.

The orbit of the satellites is not just determined by gravitational forces, but also influenced by non-gravitational forces (cf. Sec. 5.1), mainly residual atmospheric drag and radiation from Sun and Earth. These forces are measured by electrostatic accelerometers on each satellite to consider them in the analysis.

To refer the measured accelerations to a reference frame, the orientation i.e. the attitude of the satellites needs to be known. Therefore both satellites are equipped with two star cameras. Furthermore, the inter-satellite range is measured between the KBR horns of both satellites but needs to be referred to the satellite's Center of Mass (CoM), therefore the attitude is needed, as well.

Besides the ll-SST, the satellites are equipped with GPS receivers for high-low (hl) SST with the GPS constellation. The GPS measurements are by far less accurate than the ll-SST measurements. Usually, first absolute positions are derived from the GPS observations by POD (sf. Sec. 4.1), which are subsequently also used for GFR. The accuracy of the absolute position is in the range of about 1 - 5 *cm* (Kang et al., 2006; Weinbach and Schön, 2013; Zehentner and Mayer-Gürr, 2016).

The orbit altitude over the mission period is shown in Figure 3.1. Due to atmospheric drag, the altitude is constantly decaying. The main driver therefore is the density of the Thermosphere, for which the Solar radio flux F10.7 is the main proxy. It is shown in the figure, as well. In times with high F10.7, the altitude decay is stronger. Since mid 2011, battery problems limited the data acquisition in times of the longest eclipse transitions. The depletion of fuel and constantly worsen battery conditions resulted in the shut down of the satellites in mid 2017 after tripling the originally planed mission life time. The exponentially increasing density with lower altitude, resulted in the stronger attitude decay at the end of the mission.

3.2 Setup and Instrumentation of the Satellites

A schematic construction of one GRACE satellite is shown in Figure 3.2. The main instruments and components are marked.

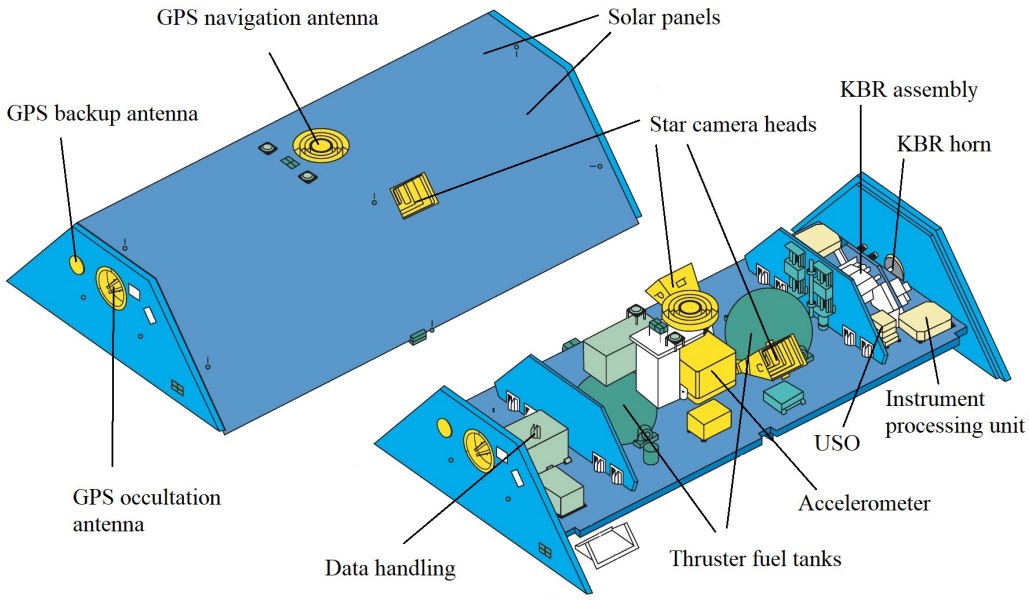

Figure 3.2: Schematic construction of one GRACE satellite with the main instruments, adapted from NASA (2002).

3.2.1 K-Band Ranging System

The K-band microwave ranging system (KBR) is constructed as a dual one-way phase measurement (eg. Kim, 2000). The system consists out of one K-band and one Ka-Band transmitter and receiver, and an Ultra Stable Oscillator (USO) on each satellite. Both satellites transmit and receive signals in the two bands ($\approx$24 and $\approx$32 GHz). The combination of the received and the reference signal, of the same wavelength, give the phase measurement. The transmitted and the reference signal are generated by the same oscillator. Thus, the measured phase at satellite B contains the same oscillator noise as the reference at satellite A. If both measurements are combined, the oscillator noise cancels out. For a separation of 220 km the signal time of travel is about 1 ms and the measured and the reference signal have a small lack. Hence just noise below about 1 kHz can be eliminated by the combination.

The measurement in two frequency bands allows to correct for ionospheric effects on the speed of propagation of the signals. The electron content in the ionosphere causes a decrease of the vacuum speed of light. This decrease is dependent on the signal's frequency. With the combination of both measurements using the "dual band combination algorithm" it is possible to eliminate this effect.

With the speed of light, the phase measurement translates to a distance. Nevertheless, the actual distance between the satellites is not determined by the phase measurement because the total number of phases is unknown. Hence, the measured distance is a biased distance and therefore usually its rate is used as observation. A detailed description of the instrument and the processing can be found in Kim (2000).

The KBR system requires the satellites to point at each other within a narrow band. The Attitude Control System (ACS) is designed to keep this attitude, referred to as "science mode" or "fine pointing mode". The ACS is described in detail in Section 6.2.

3.2.2 Accelerometer

The GRACE satellites are equipped with superSTAR accelerometers manufactured by ONERA (Office National d'Études et de Recherches Aérospatiales) (Touboul et al., 1999, 2004). These are three-axes electrostatic servo-controlled accelerometers, capable of measuring accelerations in all three directions, referred to as linear accelerations, as well as rotational accelerations. The sensor consists of a test mass, which is electrostatically suspended in its housing. By a controller it is kept motionless with respect to the housing and the satellite. In contrast to the satellite, the test mass is protected from non-gravitational forces, thus would follow a pure gravitational orbit. Hence the control forces to maintain the constant distance between housing and test mass are proportional to the non-gravitational forces acting on the housing or the satellite.

The accelerometers are mounted in the CoM of the satellites. This ensures that no inertial forces are measured due to the rotation of the satellites. The GRACE satellites contain movable trim masses to control the satellite's CoM. Occasionally in-orbit calibration maneuvers are conducted to ensure that the CoM of the satellite and the CoM of the test mass coincide.

3.2.3 GPS Receivers

The satellites are equipped with GPS receivers to utilize the hl-SST principle, as well. They are developed by JPL and capable to receive signals from 12 satellites in the L1 and L2 band, simultaneously. This allows 24 distance measurements to 12 GPS satellites. The accuracy of the GPS measurement is much worse than that of the KBR measurement (for general information on GNSS and GPS see eg. Seeber (2003); Montenbruck and Gill (2005)). Nevertheless, the amount of observations to the GPS formation allows an absolute positioning by kinematic or dynamic orbit determination (cf. Sec. 4.1). Usually the GPS observations are first processed and the resulting Kinematic Orbit Solution (KOS) or the dynamic orbit solution (GNV) is subsequently further utilized for GFR. Even though the accuracy of the absolute position is by far less accurate than the relative KBR measurement, it is of high importance for the overall GFR solution (cf. Sec. 4.3.13, 7.1, 7.7). There are mainly two reasons: The lower d/o of the gravity field and the accelerometer calibration are not very sensitive to the relative KBR measurement. Its estimation is highly based on the KOS or GNV observations.

3.2.4 Star Cameras

The satellite's attitude is mainly determined by two star cameras mounted on the side panels of the satellites. The general functional principle is that images of the sky are compared to a star catalog from which the actual attitude can be determined. Star cameras are the most precise attitude sensors available.

Two star cameras are looking in different directions (cf. Fig. 3.2). On the one hand side, with two star cameras the attitude determination precision is improved, furthermore it happens that one camera is blinded by direct light of the Sun, Moon or Earth. Therefore, the GRACE-FO satellites obtained a third star camera mounted on the to panel.

For the real time attitude determination, needed for the ACS, just the raw data of one star camera is used on the satellites (Herman et al., 2004). A post processed solution of the Star Camera Assembly (SCA) is available for the scientific data analysis, see also Section 6.3.4.

3.3 Available Data

The collected science data from all instruments on both GRACE satellites, as well as most housekeeping data are publically available from JPL/NASA at the Physical Oceanography Distributed Active Data Center (PODAAC) and from GFZ's Information System and Data Center (ISDC).

The data are processed in several steps, called levels. Level 0 data are the raw data downloaded from the satellites. The available instrument and satellite data are referred to as Level 1B (L1B) data. Data screening, some instrument calibrations, down-sampling, filtering, transformation to the Science Reference Frame (SRF) and a uniformed time tag are applied. The L1B processing for the different data is described in Wu et al. (2006). Furthermore the *GRACE Level 1B Data Product User Handbook* (Case et al., 2010) and the *Product Specification Document* (Bettadpur, 2012b) list and describe all available data products. Different releases of the L1B data were introduced over the time with ongoing development and improvement of the processing. In this thesis the release RL05 is used.

The main science L1B data for GFR and used in this thesis are:

- **KBR**: Biased-range, range-rate and range-acceleration between the CoM's of the satellites (computed with the SCA attitude data). The biased range is filtered with a digital self-convolution filter (given in Wu et al. (2006)) producing the down-sampled, low-pass filtered, biased range and its derivatives of the L1B data. Just the range-rate is used here for GFR.
- **ACC**: Uncalibrated accelerometer data in SRF. In the L1B processing, for the smoothing and down-sampling, the same filter as for KBR data is used (with different parameters, cf. Wu et al. (2006)). Just the linear accelerations of the ACC L1B data are used in this thesis.
- **GNV**: Dynamic orbit solution, obtained by dynamic POD with the GPS observations and accelerometer data. It contains positions and velocities in ECEF frame.
- **SCA**: Combined estimate of the attitude from the star camera data, given as quaternions (transformation from ECI to SRF).
- **KOS**: Kinematic Orbit Solution. This is not published with the official GRACE data. Here the freely available solution from TU Graz's Institue of Geodesy Zehentner and Mayer-Gürr (2016) is used, providing position data in ECEF by kinematic POD.

KBR, GNV and SCA L1B data are available at a sampling of $1/5\ Hz$, ACC data with $1\ Hz$ and KOS data with $1/10\ Hz$. For the reference orbit integration in the

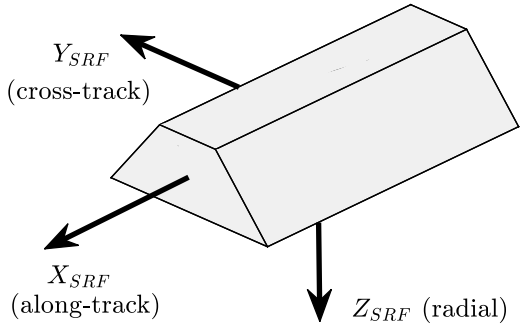

Figure 3.3: Sketch of GRACE satellite with the body fixed Science Reference Frame (SRF)

GFR processing the ACC data are down-sampled to 1/5 Hz using a moving average to avoid loss of information. The lower sampling of the KOS data just results in less KOS observations, which is not a problem for the GFR processing.

3.3.1 Reference Frame

All L1B data are referred to the Science Reference Frame (SRF). It is a body fixed frame with its origin in the satellite's CoM. It is demonstrated in Figure 3.3.

The GRACE orbits are nearly circular, and in the usual "fine pointing" attitude mode, the satellites are pointing onto each other with an accuracy of ≈0.3°. With the satellite's separation, the pitch angle (rotation around the y-axis) is between 0.8° and 2°. Hence the SRF is well aligned with the orbital reference frame (cf. Sec. 2.1.5). Therefore the axes are often considered as along-track, cross-track and radial directions, being rather terms of the orbital frame and not completely identical.

3.4 Data Pre-Processing for GFR

The available L1B data have some inconsistencies that need to be treated before GFR processing. On the first view this are mainly data gaps in the different L1B data, listed before. The length of gaps may vary from some seconds to a whole day and are generally different for the different data products.

While gaps in the observation data (KBR, GNV or KOS) can be stored and missing observations simply skipped in the processing, it is more complicated for the ACC and SCA data. These are not used as observations, but as information to integrate the reference orbit (cf. Sec. 4.3). Thus, these data gaps influence all successive time points of the arc and hence of the whole estimation. Therefore a procedure needs to be defined to fill these gaps or discard these times (complete arcs) where too big data gaps occur.

For the GRACE GFR processing the following criteria were elaborated and used for the results presented in this thesis.

For the ACC data, where the GFR solution is quite sensitive to, gaps shorter than 300 s and smaller than 25 nm/s^2 are interpolated. Arcs for which these conditions are exceeded, are completely discarded from the processing. Furthermore, the accelerometers sense attitude thruster firings, manifesting in sharp peaks (cf. Sec. 6.1.6, 6.3.6). If these peaks in the ACC L1B data are bigger than 300 nm/s^2 the arc is omitted, as well.

For the SCA data the restrictions are not that strong, having a lower influence on the GFR solutions and changing in general more slowly. Data gaps below 2000 s are interpolated using quaternion interpolation.

A further conditions that is checked before GFR processing is unusually high pointing inaccuracy between the two satellites. The pointing, or relative attitude, of the two satellites is described in detail in Section 6.2. If the relative attitude $\vec{\Theta}$ exceeds $\pm$ 0.4°, 0.4°, 0.4° in roll-, pitch- and yaw-axis, respectively, the arc is discarded.

If in one arc more than 50% of the KBR observations are missing the arc is discarded, too.

3.4.1 Pre-Processing by POD

Besides the obvious data gaps a further very important pre-processing needs to be executed to obtain reasonable GFR results for most months. This concerns the KBR data, which contain some rather rare artifacts, but having significant impact on the solutions. The reasons could just be resolved partly during this investigation.

After a gap in the KBR data the instrument does not necessarily continue the time series, but "recalibrates" and continues with a different phase. This results in discontinuous range-rate measurements in the area of around 1 to 15 $\mu m/s$ (eg. Fig. 7.24). Furthermore, after these jumps it might happen that the measurement accuracy is worsen up to an order of magnitude for some time (up to one day). These small effects are not directly visible in the KBR measurement data, which vary with a much higher amplitude, in the range of some m/s, due to the slightly different orbits of both GRACE satellites.

By a POD processing with both GRACE satellites simultaneously, using GNV or KOS data additionally to KBR range-rate data as observations, these effects are visible in the post-fit deviations or residuals. These effects are not visible in the post-fit deviations or residuals of the GFR, because they are affecting and deteriorating the gravitational field and hence the residuals too strong to detect these irregularities.

The POD pre-processing approach is used to detect these outliers and discard affected times (or arcs) for the GFR processing. This problem and its effects on the GFR solution are discussed in detail in Section 7.4 for the whole year 2006.

The presented criteria for discarding arcs from the GFR processing are partly detecting the same times or epochs, and their sensitivity to the GFR solution might not always be very big. Nevertheless, this is not general and especially different for different arcs, epochs and months. However, the POD pre-processing is crucial for the majority of the months and decisive to determine deteriorated measurement data and epochs (cf. Sec. 7.4).

ORBIT DETERMINATION AND GRAVITY FIELD RECOVERY (GFR)

4

The field of orbit determination is closely related to Gravity Field Recovery (GFR). The approach used and developed throughout this thesis, referred to as classical or variational-equation approach is an extension of dynamic orbit determination. Besides the same mathematical heritage of the estimation theory and the same used observations, precise orbits of satellites can be considered as prerequisite for GFR.

In general, orbit determination deals with the estimation of positions or trajectories of celestial bodies. In this context, celestial bodies may be stars, planets, moons, asteroids, comets or artificial satellites. In the context of this thesis the focus is on satellites, but for the theory, the terms are interchangeable.

Historically, the first attempts of "orbit determination" can be dated back to prehistoric times with the discovery of some Solar System planets and attempts to find regularities of their motion. Since Johannes Kepler discovered his three laws of planetary motion and the description of Mars' orbit, orbit determination was based on a mathematical basis in terms of a heliocentric system. Later in the 17th century Isaac Newton laid the theoretical foundation of Kepler's observations, being a result of the two-body problem, governed by his law of gravitation. Around 1800 the methods of orbit determination were significantly enhanced by Carl Friedrich Gauss including the development of the least squares method, which is the basis of most estimation processes, today.

In the middle of the 20th century the orbit determination problem, and estimation theory in general, was linked to modern dynamical system theory. The methodology that is used today dates back to the work of Swerling (1959) and especially Kalman (1960).

Nowadays, often the term Precise Orbit Determination (POD) is used, which is not really delimited from "normal" orbit determination. But generally POD refers to methods based on the mentioned work by Kalman, as presented here in Section 4.3. Typically much more complex orbit models than the Keplerian two-body problem are used, where no analytical solution exists.

4.1 Kinematic and Dynamic Orbits

Two different kind of orbits are distinguished: Kinematic and dynamic orbits. A kinematic orbit is given by positions at discrete time points. It is just based on geometry and no physical model of motion is considered. No information about other time points or velocity and acceleration can be derived from a kinematic orbit, directly. In contrast to that, a dynamic orbit is given by a physical model of motion and initial conditions of the satellite. In the simplest case the model might be a Kepler orbit. But it may also be a more advanced model with no analytical solution, where the orbit is then defined by the force models and an initial condition. Hence, a dynamic orbit is continuous and can be evaluated at any time point, at least by numeric integration.

From these two types of orbits the methods of determining the like are as well distinguished in kinematic and dynamic orbit determination. It should be mentioned here, that both approaches can also be combined in different ways, what is often referred to as reduced-dynamic or reduced-kinematic orbit determination. With GFR being an extension of the dynamic approach, it is the focus in this chapter.

4.1.1 Kinematic Orbit Determination

The idea of kinematic orbit determination is to estimate a solution, i.e. a satellite's position for each time point, independently. Therefore, at least as many observations as parameters need to be available for each time point. The estimation then follows by a "geometrical" best fit of all observations. In reality and applications each point is not completely independent, because clock parameters of the GNSS satellites are estimated over an amount of several time points, as well. Kinematic orbit determination got established and important with the development of GNSS systems. Before that, it was not practical to use it, because usually not enough measurement data were available to determine a position at each measurement time, at least not over a longer time span to make practical use out of it. A general overview of GNSS and related position or orbit determination is eg. given in Hofmann-Wellenhof et al. (2007).

The basic method usually used for kinematic orbit determination of satellites is referred to as Precise Point Positioning (PPP) (eg. Witchayangkoon, 2000). Recent implementations are eg. given by Zehentner and Mayer-Gürr (2016).

The advantage of kinematic orbit determination is that no force models for the motion of the satellites are utilized. Therefore the resulting orbits are independent from any force models. When the determined orbit is further used as observations for GFR this is favorable because no prior dependencies of the observations is introduced. Kinematic orbit determination is not further discussed in this thesis and the interested reader is referred to the mentioned literature.

4.1.2 Dynamic Orbit Determination

Dynamic orbit determination means to estimate a "best fitting" mathematical model to a set of observations. "Best fitting" is usually defined in the sense of least squares and will be defined later, exactly. The mathematical model is thereby adjusted by the estimation of model parameters. For a simple Keplerian orbit model, parameters would be the Keplerian orbit elements or equivalently the initial position and velocity. In more realistic models, additional to the initial position and velocity, parameters can be force model coefficients like the gravitational coefficient GM of the central body or a drag coefficient to model residual atmospheric effects. As observation any measure that can be physically related to the parameters, can be used. Depending on the estimation parameters, some observations are more sensitive to a specific parameter than others. Furthermore, every measurement has an error influencing the accuracy of the estimated parameters and hence the determined orbit.

The classical approach for GFR directly evolves from the dynamic orbit determination. In the previous paragraph the analogy was already mentioned indirectly: Force model parameters include of cause gravitational parameters, as well. Thus the estimated parameters may include all parameters of the gravitational model, like spherical harmonic (SH) coefficients.

4.2 Gravity Field Recovery

There are several methods for Gravity Field Recovery (GFR) from satellite data. Here the gravitational field is represented by a SH potential. The aim of the approaches is to determine global SH coefficients from the available satellite observations. Classically the approaches are distinguished in timewise and spacewise methods (Rummel et al., 1998).

Spacewise methods relate the in-situ observations, made at certain spatial positions, to the gravitational potential, or any of its functionals. Usually spacewise approaches are utilized in two steps. First the observations are collected along the orbit at the measurement positions and connected to the gravitational potential. In a second step the systems is solved in terms of least squares to determine the SH coefficients. The Acceleration approach (Weigelt, 2017) and the Energy Balance approach (Jekeli, 2017) are the most popular representatives of spacewise approaches.

On the other hand, timewise methods tread the observations as time series with the goal to represent them as best as possible by a dynamic model. From the differences between the observations and the modeled observations, parameters of the dynamic model can be estimated. Therefore variational equations for the motion of the satellite(s) and the observation equation(s) are solved. Thus not only the gravitational field is estimated but also the satellite's trajectories. The solution usually consists of a numeric integration of the equation of motion and the state transition matrix. Because the highly nonlinear system is linearized to utilize least squares estimation theory, the whole approach needs to be iterated.

Timewise approaches are referred to as classical or variational-equation approach. Variants of this are the Celestial Mechanics Approach (CMA) developed by Beutler et al. (2010); Jäggi (2006) and the Short Arc arc approach by Mayer-Gürr (2006).

All methods are based on Newtonian mechanics and in the perfect case should give the same results. Due to the handling of different erroneous observation data, parameter choices in the processing and the error propagation through the processing chains, in reality the results differ for each approach and also for each implementation.

Throughout this thesis the classical, variational-equations approach is utilized. It is rather complex and computationally the most demanding, but also the most fertile and powerful. It has evolved to the state-of-the-art approach and is used by all major GRACE processing centers, like JPL, GFZ, CSR or TU Graz.

In general, the classical theory is not only applicable for celestial applications, but as well for all kind of parameter estimation problems, where parameter of a model (usually given as a system of ordinary differential equation) should be adjusted with respect to measurement data.

Here it should be mentioned, that a further representation of the gravitational field, especially employed and developed more recently for the GRACE data processing by the JPL, is investigated and used. It is referred to as mascons (from mass concentration). Thereby the gravitational field is modeled as spatially distributed mass elements, serving as gravitational sources. Recent developments for GRACE are given by eg. Watkins et al. (2015); Wiese et al. (2016, 2018). This representation is not considered and further discussed in this thesis.

4.3 The Classical Approach for POD and GFR

The notation in the following sections is generally based on Tapley et al. (2004b), McCullough (2017) and our description in Darbeheshti et al. (2018). A slightly different notation of the same concept is often based on (Montenbruck and Gill, 2005, Ch. 7,8).

The methodology of the approach is based on a mathematical model of the satellites motion. With the model, which is usually a set of differential equations, it is possible to determine the state of the satellite $\vec{X}(t)$ at each time t. Applying general system theory, the model is transformed to a system of first order Ordinary Differential Equations (ODE) (cf. Sec. 5.2) and thus the state needs to contain at least the position $\vec{r}$ and the velocity $\vec{v}$, for translational motion. If attitude is of concern, it may also contain the quaternion and angular rate for rotational motion (cf. Eq. 2.7). Generally the ODE system can be expressed as

$$\dot{\vec{X}}(t) = F(\vec{X}(t), t), \tag{4.1}$$

where F may be an arbitrary nonlinear function. The task in orbit determination is to estimate the unknown n-dimensional state vector $\vec{X}(t_0)$. For a given ODE with given initial state $\vec{X}(t = t_0) = \vec{X_0}$, the state $\vec{X}(t)$ at every time $t > t_0$ is determined, and can be computed, at least by numerical integration of the ODE system. Thus just one initial state vector needs to be estimated. In orbit determination and parameter estimation in general, the state vector usually contains all parameters to be estimated, not only the satellites' state. It is therefore also called extended state vector.

The p-dimensional observations $\vec{Y_i}$, at the times t_i, with i: 1, ... l, shall be used for the estimation of $\vec{X}(t_0)$. It was mentioned before, that observations need to be related to the parameters to be estimated. This means that the observations $\vec{Y_i}$ can be expressed with the state vector $\vec{X}(t)$ and a suitable function G

$$\vec{Y_i} = G(\vec{X}(t_i), t_i) + \vec{\epsilon_i}, \qquad i : 1, ...l \tag{4.2}$$

where $\vec{\epsilon_i}$ represents observation errors.

A short remark on the dimensions of the different instances: There are n parameters that are to be estimated, for example the satellite's initial state and model parameters. Observations $\vec{Y_i}$ are available at l time points. The dimension p of a set of observations $\vec{Y_i}$ at one time (eg. ranges, angles or 3d-positions) is usually smaller than n (this is an important difference to kinematic orbit determination, where this is not the case). For reasonable results of the dynamic approach, the number of observations $m = p * l$ usually must be much bigger than n.

4.3.1 Linearization

For orbital mechanics the function F from Equation (4.1) is highly nonlinear. For most observations the same holds for the observation equation (Eq. 4.2) and the function G. The nonlinear estimation problem is linearized to make use of the well established theory and tools for linear system. The linearization of the problem makes it necessary to determine a solution iteratively.

The equations of dynamics and observation models (Eq. 4.1 and 4.2) are linearized via Taylor expansion. To do so, a reference point for the linearization needs to be set. This is called nominal or reference trajectory and needs to be known or guessed up to a certain accuracy to allow convergence over the iterations. The closer the initial guess for

the parameters to be estimated and hence the reference trajectory, the fewer iterations are needed. The absolute variables $\vec{X}(t)$ and $\vec{Y}(t)$ are replaced by the relative deviation between true and reference values.

$$\vec{x}(t) = \vec{X}(t) - \vec{X}^*(t) \tag{4.3}$$

$$\vec{y}(t) = \vec{Y}(t) - \vec{Y}^*(t) \tag{4.4}$$

Where the $()^*$ denotes the reference values. Under the assumption that the reference trajectory is within close proximity to the truth, the Taylor expansion of $\dot{\vec{X}}(t)$ around $\vec{X}^*(t)$ is given by

$$\begin{aligned}\dot{\vec{X}}(t) = F(\vec{X}, t) = F(\vec{X}^*, t) + \left[\frac{\partial F(\vec{X}, t)}{\partial \vec{X}}\right]_{\vec{X}=\vec{X}^*} (\vec{X} - \vec{X}^*) \\ + O(\vec{X} - \vec{X}^*)^2.\end{aligned} \tag{4.5}$$

By defining the partial derivative matrix A

$$A(t) = \left[\frac{\partial F(\vec{X}, t)}{\partial \vec{X}}\right]_{\vec{X}=\vec{X}^*} \tag{4.6}$$

and using the state deviation $\vec{x}(t)$ (Eq. 4.3) and omitting the higher order terms, this results in the linearized dynamics equation

$$\dot{\vec{x}}(t) = A(t)\vec{x}(t). \tag{4.7}$$

Equivalently, the observation equation $\vec{Y}_i$ (Eq. 4.2) is expanded

$$\begin{aligned}\vec{Y}_i = G(\vec{X}_i, t_i) + \vec{\epsilon}_i = G(\vec{X}_i^*, t_i) + \left[\frac{\partial G(\vec{X}_i, t_i)}{\partial \vec{X}}\right]_{\vec{X}_i=\vec{X}_i^*} (\vec{X}_i - \vec{X}_i^*) \\ + O(\vec{X}_i - \vec{X}_i^*)^2 + \vec{\epsilon}_i.\end{aligned} \tag{4.8}$$

The partial derivative matrix is defined by $\widetilde{H}$ and called mapping matrix

$$\widetilde{H}(t_i) = \left[\frac{\partial G(\vec{X}_i, t_i)}{\partial \vec{X}}\right]_{\vec{X}_i=\vec{X}_i^*}. \tag{4.9}$$

Using the observation deviation $\vec{y}(t)$ (Eq. 4.4) and again omitting higher order terms, the linear observation equation is obtained

$$\vec{y}(t_i) = \widetilde{H}(t_i)\vec{x}(t_i) + \vec{\epsilon}_i. \tag{4.10}$$

In this Equation, the error $\vec{\epsilon}_i$, which was introduced as observation errors (Eq. 4.2), now also contains linearization errors.

With the Equations (4.7) and (4.10) the nonlinear estimation problem is transformed to a linear one. Nevertheless, it is not possible to solve for the desired parameter deviation $\vec{x}(t_0)$ with Equation (4.10), yet. The reason is, that the vector $\vec{x}(t_i)$ contains n unknown parameter at each time point i. As mentioned before, it is not necessary to solve for a state vector at all times, just one is sufficient. The state at all other times is then defined by the dynamic model. Thus, each row in Equation (4.10) needs to be related to the state at $\vec{x}_0$ for one time t_0. This can be done by the state transition matrix.

4.3.2 The State Transition Matrix

Equation (4.7) is the linearized dynamics model. The general solution to such linear ODE system is given by

$$\vec{x}(t) = \Phi(t, t_0)\vec{x}(t_0) \tag{4.11}$$

where t_0 is some specified (initial) time and Φ is called the state transition matrix. It satisfies the following conditions

$$\dot{\Phi}(t, t_0) = A(t)\Phi(t, t_0), \quad \Phi(t_0, t_0) = I. \tag{4.12}$$

The state transition matrix maps deviations in the state vector from a time t_0 to t. Hence, if $\Phi(t, t_0)$ is known at the time t, the state deviation $\vec{x}(t)$ can be computed with the initial state $\vec{x}_0$.

With a given matrix $A(t)$, the differential equation for $\Phi(t, t_0)$ (Eq. 4.12) can be solved, at least numerically, and $\Phi(t, t_0)$ can be computed for every time t_i.

4.3.3 Relating Observations to One Time

With the state transition matrix at hand, it is possible to relate all observations in Equation (4.10) to one time t_0. Substituting the state transition matrix (Eq. 4.11) into Equation (4.10) gives the expression

$$\vec{y}(t_i) = \widetilde{H}(t_i)\Phi(t_i, t_0)\vec{x}(t_0) + \vec{\epsilon}_i. \tag{4.13}$$

Accumulating all time points i like demonstrated in the following gives the final linear system.

$$\begin{bmatrix} \vec{y}_1 \\ \vec{y}_2 \\ \vdots \\ \vec{y}_l \end{bmatrix} = \begin{bmatrix} \widetilde{H}_1\Phi(t_1, t_0) \\ \widetilde{H}_2\Phi(t_2, t_0) \\ \vdots \\ \widetilde{H}_l\Phi(t_l, t_0) \end{bmatrix} \vec{x}_0 + \begin{bmatrix} \vec{\epsilon}_1 \\ \vec{\epsilon}_2 \\ \vdots \\ \vec{\epsilon}_l \end{bmatrix}. \tag{4.14}$$

The matrix $H(t_i)$ is defined as

$$H(t_i) = \widetilde{H}(t_i)\Phi(t_i, t_0), \tag{4.15}$$

and substituted into Equation (4.13). With that the linear system can be written as

$$\vec{y} = H\vec{x} + \vec{\epsilon}. \tag{4.16}$$

The subscripts and time dependencies are dropped here in the notation for convenience and better readability in the following sections. This linear system can be used to determine the desired parameter deviations $\vec{x}$ in an optimal sense, for example using the concept of least squares as demonstrated in Section 4.3.4. In estimation theory the H matrix is usually referred to as design matrix.

The errors $\vec{\epsilon}$ in Equation 4.16 are not only measurement errors any more. Due to the linearization and the combination of dynamical and observation model, it also contains linearization errors, model errors and numerical integration errors, as well.

4.3.4 Least Squares Adjustment

Usually the number of equations of the linear system (Eq. 4.16), or equivalently speaking, the number of observations, is much bigger than the number of parameters in the $\vec{x}$ vector. Systems with equal, or even less, numbers of equations are not of interest in the field of orbit determination or GFR, where lots of data are necessary to determine reasonable results. The basic linear model was derived in the section before (Eq. 4.16). The $\vec{x}$ vector contains $n \times 1$ unknown parameters, the observation deviation $\vec{y}$ is a $m \times 1$ vector and the design matrix H or observation equation matrix is of size $m \times n$. The error vector $\vec{\epsilon}$ is as well of size $m \times 1$. As mentioned before, it contains errors in the measurement data, but as well errors of the analysis, like truncation errors from the linearization, modeling errors or numerical integration errors.

To solve such overdetermined system, the method of least squares is utilized, which was first proposed by Gauss in 1809. The idea is to minimize the sum of the squares of the difference between the calculated (by the linear model) and observed quantities. The difference or the error is obtained by rearranging Equation (4.16)

$$\vec{\epsilon} = \vec{y} - H\vec{x}. \tag{4.17}$$

The performance index of the squared differences is then defined by

$$J(\vec{x}) = \vec{\epsilon}^T \vec{\epsilon}. \tag{4.18}$$

Additionally, a weighting of each observation, or equivalently speaking of each equation of the linear system (Eq. 4.16), can be considered. Thus, it is to find the minimum of the weighted, squared differences. Therefore, in the performance index a weighting matrix W can be added

$$J(\vec{x}) = \vec{\epsilon}^T W \vec{\epsilon}. \tag{4.19}$$

The weighting and the weighting matrix is further discussed in the next Section 4.3.5 in more detail. In the case no weighting is considered, the weighting matrix is a $m \times m$ identity matrix, and can be dropped. Minimizing the performance index is done by taking its first derivative which should equal 0

$$\frac{\partial J(\vec{x})}{\partial \vec{x}} = \frac{\partial}{\partial \vec{x}} (\vec{y} - H\vec{x})^T W (\vec{y} - H\vec{x}) = 0. \tag{4.20}$$

With the relation $\partial / \partial \vec{x}(B^T B) = 2(B^T \partial / \partial \vec{x}(B))$ and considering that W is symmetric, thus $W = W^T$, it follows

$$\frac{\partial J(\vec{x})}{\partial \vec{x}} = 0 = -2(\vec{y} - H\vec{x})^T W H = -2H^T W (\vec{y} - H\vec{x}). \tag{4.21}$$

This yields the optimal estimate (in terms of least squares) for the parameters $\vec{x}$

$$\hat{\vec{x}} = (H^T W H)^{-1} H^T W \vec{y}. \tag{4.22}$$

Estimated quantities are denoted by a hat $\hat{\cdot}$. Equation (4.22) is often written as

$$N\hat{\vec{x}} = \vec{n}, \qquad \text{with} \quad N = H^T W H, \qquad \vec{n} = H^T W \vec{y} \tag{4.23}$$

and commonly referred to as normal equations with the normal matrix N and the right hand side vector $\vec{n}$. The equation can be slightly rewritten as

$$\hat{\vec{x}} = L\vec{y}, \qquad \text{with} \quad L = (H^T W H)^{-1} H^T W, \tag{4.24}$$

showing explicitly the linearity of the system.

With the estimate $\hat{\vec{x}}$, the error estimate $\hat{\vec{\epsilon}}$ from Eq. (4.17) can be determined

$$\hat{\vec{\epsilon}} = \vec{y} - H\hat{\vec{x}}. \tag{4.25}$$

It is referred to as the residuals or post-fit residuals. Again, the $\hat{}$ denotes an estimated quantity, the real errors are still unknown.

In general, and especially in this thesis, there is a difference between residuals and observation deviations. Residuals are generally speaking the difference between the observations and the estimated observations computed with the model and the estimated parameters $\hat{\vec{x}}$. Thus they are obtained with the linear system. The estimated parameters $\hat{\vec{X}}$ can be used as well with the original model to compute the observations $\vec{Y}_i = G(\hat{\vec{X}}, t_i)$ (Eq. 4.2) eg. by numerical integration, the differences between those and the observations are referred to as (observation) deviations. With sufficient iterations residuals and deviations should become similar. Using the observation deviations instead of residuals has the big advantage, that the design matrix H does not need to be saved, which might be quite big and unnecessary (cf. Sec. 4.3.7).

4.3.5 Statistical Errors and Weighting

The derived least squares approach does not consider any statistical information of the errors in the observations. A different approach to determine a performance index or an estimator is the minimum variance estimate. Under some conditions, it will yield the same result than the weighted least squares approach (Eq. 4.22), but with a formal consideration of statistical errors. For a complete derivation and discussion, the interested reader is for example referred to Tapley et al. (2004b) or Kusche and Springer (2017), while here just the results are summarized.

The two assumptions of this approach are that 1. the errors $\vec{\epsilon}$ are random, and their expectation $E[\,]$ is zero, meaning averaging an infinite number should yield zero

$$E[\,\vec{\epsilon}\,] = 0. \tag{4.26}$$

The errors do not have to be distributed normally. And 2. the variance-covariance matrix $C_{\epsilon\epsilon}$ of the observations is known up to the factor σ^2

$$E[\,\vec{\epsilon}^T\vec{\epsilon}\,] = C_{\epsilon\epsilon} = \sigma^2\bar{C}_{\epsilon\epsilon} = \sigma^2\begin{bmatrix} \sigma_1^2 & \sigma_{12} & \cdots & \sigma_{1m} \\ \sigma_{21} & \sigma_2^2 & \cdots & \sigma_{2m} \\ \vdots & \vdots & \ddots & \vdots \\ \sigma_{m1} & \sigma_{m2} & \cdots & \sigma_m^2 \end{bmatrix}. \tag{4.27}$$

With the conditions that the estimate should be the best linear, unbiased, minimum variance estimate, also referred to as Best Linear Unbiased Estimate (BLUE), it can be shown, that the solution for $\hat{\vec{x}}$ is given by (e.g. Tapley et al., 2004b)

$$\hat{\vec{x}} = (H^T C_{\epsilon\epsilon}^{-1} H)^{-1} H^T C_{\epsilon\epsilon}^{-1}\vec{y}. \tag{4.28}$$

Comparing the solutions of the least squares principle (Eq. 4.22) and the minimum variance approach (Eq. 4.28), it is obvious, that for

$$W = C_{\epsilon\epsilon}^{-1} = \frac{1}{\sigma^2}\bar{C}_{\epsilon\epsilon}^{-1} \tag{4.29}$$

both solutions agree. Using the inverse of the observation variance-covariance matrix $C_{\epsilon\epsilon}^{-1}$ as weighting is a very popular strategy in least squares estimation.

Because the variance factor σ^2 often cancels out or is separately determined and just $\bar{C}_{\epsilon\epsilon}^{-1}$ is needed, it is substituted by $\bar{W}$ making succeeding equations a little easier to read

$$\bar{W} = \bar{C}_{\epsilon\epsilon}^{-1}. \tag{4.30}$$

A full variance-covariance matrix means, that observation errors are time correlated. Often the simplification is used, that errors are assumed to be not correlated. Thus the variance-covariance matrix will be a diagonal matrix with the variances σ_m^2 of each observation i on its diagonal. If all observations are of the same kind, the variance factor is the same for all. Thus the variance matrix reduces to $\sigma^2 I$ and cancels out in the normal equations (Eq. 4.28), completely.

4.3.6 Formal Error

From the residuals of an estimate, an information on the accuracy of the estimated parameters $\hat{\vec{x}}$ can be drawn. The variance factor σ^2 can be determined from the residuals $\hat{\vec{\epsilon}}$, more exactly the square sum of the residuals, under the assumption that it is an unbiased estimate, meaning $E[\,\hat{\sigma}^2\,] = \sigma^2$ (Kusche and Springer, 2017)

$$\hat{\sigma}^2 = \frac{\hat{\vec{\epsilon}}^T \bar{W} \hat{\vec{\epsilon}}}{m-n} = \frac{(\vec{y} - H\hat{\vec{x}})^T \bar{W} (\vec{y} - H\hat{\vec{x}})}{m-n}. \tag{4.31}$$

With m and n being again the number of observations and number of estimated parameters, respectively.

Using the slightly alternated form of the normal equation $\hat{\vec{x}} = L\vec{y}$ (Eq. 4.24), the error covariance matrix of the estimated parameters can be computed by

$$C_{\hat{x}} = L\, C_{\epsilon\epsilon}\, L^T = (H^T W H)^{-1} H^T W\, C_{\epsilon\epsilon}\, W^T H (H^T W^T H)^{-1}. \tag{4.32}$$

Using $W = \frac{1}{\sigma^2}\bar{C}_{\epsilon\epsilon}^{-1} = \frac{1}{\sigma^2}\bar{W}$ (Eq. 4.29), after some rearranging this transforms to

$$C_{\hat{x}} = (H^T W H)^{-1} = \sigma^2 (H^T \bar{C}_{\epsilon\epsilon}^{-1} H)^{-1} = \sigma^2 (H^T \bar{W} H)^{-1}. \tag{4.33}$$

Substituting the normal matrix N (Eq. 4.23), this can be simply expressed by

$$C_{\hat{x}} = \sigma^2 N^{-1}. \tag{4.34}$$

With the estimate of $\hat{\sigma}^2$ from Eq. (4.31) an estimate for the parameter covariance matrix can be computed

$$\hat{C}_{\hat{x}} = \hat{\sigma}^2 N^{-1}. \tag{4.35}$$

Thus the diagonal of $\hat{C}_{\hat{x}}$ is giving an estimate for the variances $\hat{\sigma}^2$, or the standard deviation $\hat{\sigma}$, of each estimated parameter in $\hat{\vec{x}}$. In Geodesy or GFR these standard deviation $\hat{\sigma}$ are commonly referred to as formal errors. Among others, they can be used to assess the quality of a solution. Nevertheless, the formal errors need to be interpreted with caution. The estimate of $\hat{C}_{\hat{x}}$ and $\hat{\sigma}^2$ is just as good as the error variance covariance matrix $\bar{C}_{\epsilon\epsilon}$ of the data is known. Thus for a reliable estimate of $\hat{C}_{\hat{x}}$ the correlations of the data errors need to be known or modeled precisely.

4.3.7 Solving the Normal Equations

In the sections before it was shown that the least squares and the minimum variance approach arrive at the linear system, referred to as the normal equations (Eq. 4.23).

In the case of POD and especially GFR, lots of parameters are estimated and thus the normal matrix is quite big. To solve such system, it is preferable to avoided the computation of the inverse of the normal matrix N^{-1}, which is computationally heavy and might be inaccurate, too. Matrix decomposition methods like Cholesky-, QR-, LU- or LUL-decomposition are often used (eg. Tapley et al., 2004b; McCullough, 2017). Also iterative methods, which generate approximate solutions of the system, like Preconditioned Conjugate Gradient (PCG) methods, are used (eg. Mayer-Gürr, 2006). PCG methods have the advantage to reduce matrix operations and especially avoiding to build the normal matrix, explicitly. In case of high order gravity fields this might be of interest to avoid storing big matrices.

To get an idea on the dimensions of the normal matrix, two examples are shortly discussed: For a gravity field of d/o 60, 3717 SH coefficients need to be estimated (cf. Eq. 2.21). Thus the normal matrix has 3717×3717 elements. Assuming *double* data type, this matrix needs a memory of about 0.11 GB. A gravity field with d/o 250 has 62617 coefficients and the normal matrix needs a memory of 31.37 GB. The latter case justifies the use of the more complicated PCG methods.

In this thesis the issue of solving the linear system is not addressed in detail. Compared to the computational effort for the assembly of the design matrix H, solving the normal equations is negligible. The size of the normal matrix for the investigated gravity fields can be handled easily by average clusters. In the implementation MATLAB's linear system solver is used, which uses different matrix-decomposition methods depending on the conditions of the given matrix.

4.3.8 Arcs and Partitioned Normal Equations

Usually the orbit determination or GFR problem is separated into different arcs. This has several reasons and advantages, which will be shortly discussed. By an arc, a part of a satellite's trajectory, or an arbitrary time span of observation data is meant. Arc lengths may vary from 30 minutes over days to month and years, depending on the problem, the used method and models. For low Earth orbits, arcs are normally not longer than one day.

Splitting the available data into different arcs means that the model, with its parameters and initial condition, is estimated and valid just for a certain time span. This allows to estimate more parameters over time, eg. for each arc. Using the technique of partitioning, it is also possible to define and estimate certain parameters that are valid over more arcs.

Due to the introduction of arcs, the influence of model inaccuracies and numerical errors can be reduced. Furthermore, it allows the parallel computation of different arcs. Also the sizes of the different matrices can be reduced, easing the requirements on the computer hardware.

For the GFR case, the situation is a little bit more complicated. The amount of parameters to estimate for a gravitational field model may require observation data of weeks to a month (GRACE) or months to years (GOCE) to compute reasonable results. Such arc length for low Earth orbits are not possible considering the dynamic models, linearization and numeric integration. Fortunately, as already hinted, this is

not necessary.

The normal equations, as derived in Equation (4.23), are given by

$$N\hat{\vec{x}} = \vec{n}, \qquad \text{with} \quad N = H^T W H, \qquad \vec{n} = H^T W \vec{y}. \tag{4.36}$$

Under the condition that the weighting matrix W is block diagonal, mathematically it is equivalent to split this into the following sum

$$N = \sum_{k=1}^{a} H_k^T W_k H_k, \qquad \text{and} \qquad \vec{n} = \sum_{k=1}^{a} H_k^T W_k \vec{y}_k. \tag{4.37}$$

With a being the number of arcs, which may be an arbitrary number smaller or equal to m, the number of observations. A block diagonal weighting matrix is given by

$$W = \begin{bmatrix} W_1 & & & \\ & W_2 & & \\ & & \ddots & \\ & & & W_a \end{bmatrix}. \tag{4.38}$$

Practically, a block diagonal weighting matrix means that observation errors of different arcs k are not correlated, and correlation stops at the arc borders. Especially for GFR this is a necessary assumption to handle the amount of data. But considering that good results are obtained even with diagonal weighting matrices, this is a feasible assumption. Splitting the normal matrices into arcs allows a parallel accumulation of the H_k matrices, determining at least a set of initial conditions for each arc k.

The form of Equation (4.37) opens different strategies for the implementation, with several advantages and disadvantages. It is possible to build the normal Matrix N_i after processing each time point i and summing it up over all times. The other extreme is accumulating the complete design matrix H with all times first and just building N once. In the first case, for each time point, the $n \times n$ normal matrix needs to be build. However, no memory is needed to store the H matrix. In the second case a huge memory may be needed to store the $m \times n$ H matrix for all time points, but the normal matrix is just build once. Depending on the dimensions of n and m and an assessment towards computation time and memory consumption needs to be conducted to find an appropriate way.

When defining arcs, the parameters are separated or partitioned into different groups, or levels depending on their validity for all arcs or only one arc:

- Local: Parameters that are valid for only one arc, like initial position and velocity
- Global: Parameters that are valid across all arcs, like gravity field coefficients

The groups could be also arbitrarily expanded to parameters that are valid for several arcs. In the following the method is demonstrated just for these two groups of parameters.

The parameter vector $\vec{x}$ is expanded to a generalized parameter vector $\vec{z}$, containing local parameters $\vec{x}$ and global parameters $\vec{c}$. Thus the design matrix H and generalized state vector $\vec{z}$ for one arc can be written as

$$\vec{z} = \begin{bmatrix} \vec{x} \\ \vec{c} \end{bmatrix}, \qquad H_z = [H_x \quad H_c] \tag{4.39}$$

Building the normal equations based on this partitioning (substituting Eq. 4.39 in Eq. 4.36), the following linear system is made.

$$\begin{bmatrix} H_x^T W H_x & H_x^T W H_c \\ H_c^T W H_x & H_c^T W H_c \end{bmatrix} \begin{bmatrix} \hat{\vec{x}} \\ \hat{\vec{c}} \end{bmatrix} = \begin{bmatrix} H_x^T W \vec{y} \\ H_c^T W \vec{y} \end{bmatrix} \tag{4.40}$$

The sub-matrices and -vectors in there are defined as

$$M_{xx} = H_x^T W H_x \tag{4.41}$$

$$M_{xc} = H_x^T W H_c$$
$$M_{cx} = M_{xc}^T$$
$$M_{cc} = H_c^T W H_c$$
$$\vec{m}_x = H_x^T W \vec{y}$$
$$\vec{m}_c = H_c^T W \vec{y}.$$

Substituting these abbreviations, results in the partitioned normal equation for one arc

$$\begin{bmatrix} M_{xx} & M_{xc} \\ M_{cx} & M_{cc} \end{bmatrix} \begin{bmatrix} \hat{\vec{x}} \\ \hat{\vec{c}} \end{bmatrix} = \begin{bmatrix} \vec{m}_x \\ \vec{m}_c \end{bmatrix}. \tag{4.42}$$

Multiplying out the above equations, results in

$$M_{xx}\hat{\vec{x}} + M_{xc}\hat{\vec{c}} = \vec{m}_x, \tag{4.43}$$
$$M_{cx}\hat{\vec{x}} + M_{cc}\hat{\vec{c}} = \vec{m}_c. \tag{4.44}$$

Solving for $\hat{x}$ in Equation (4.43)

$$\hat{\vec{x}} = M_{xx}^{-1}\vec{m}_x - M_{xx}^{-1}M_{xc}\hat{\vec{c}}, \tag{4.45}$$

and inserting this result into Equation (4.44) gives an expression for the global parameters $\hat{\vec{c}}$

$$\hat{\vec{c}} = \left(M_{cc} - M_{cx}M_{xx}^{-1}M_{xc}\right)^{-1}\left(\vec{m}_c - M_{cx}M_{xx}^{-1}\vec{m}_x\right). \tag{4.46}$$

With the solution for $\hat{\vec{c}}$, $\hat{\vec{x}}$ can be computed with Equation (4.43) by back-substitution. This can be understood as elimination of parameters as called by other authors Mayer-Gürr (2006) or Wu (2017).

Nevertheless, the previous is just applied to a single arc, thus $\hat{\vec{c}}$ can not be considered as a global parameter, yet. But it is not difficult to extend the idea to incorporate any number of arcs, each with its own set of local parameters $\vec{x}_k$. By expanding Equation (4.39) for k arcs, $\vec{z}$ and H_z transforms to

$$\vec{z} = \begin{bmatrix} \vec{x}_1 \\ \vec{x}_2 \\ \vdots \\ \vec{c} \end{bmatrix}, \qquad H_z = \begin{bmatrix} (H_x)_1 & 0 & \cdots & 0 & (H_c)_1 \\ 0 & (H_x)_2 & \cdots & 0 & (H_c)_2 \\ \vdots & \vdots & \ddots & \vdots & \vdots \\ 0 & 0 & \cdots & (H_x)_k & (H_c)_k \end{bmatrix}. \tag{4.47}$$

Again, the normal equations can be build based on this partitioning (substituting Eq. (4.47) in Eq. (4.36)). This results in the linear system for the generalized partitioned normal equations

$$\begin{bmatrix} (H_x^T W H_x)_1 & 0 & \cdots & 0 & (H_x^T W H_c)_1 \\ 0 & (H_x^T W H_x)_2 & \cdots & 0 & (H_x^T W H_c)_2 \\ \vdots & \vdots & \ddots & \vdots & \vdots \\ 0 & 0 & \cdots & (H_x^T W H_x)_k & (H_x^T W H_c)_k \\ (H_c^T W H_x)_1 & (H_c^T W H_x)_2 & \cdots & (H_c^T W H_x)_k & \sum_k (H_c^T W H_c)_k \end{bmatrix} \begin{bmatrix} \hat{\vec{x}}_1 \\ \hat{\vec{x}}_2 \\ \vdots \\ \hat{\vec{x}}_k \\ \hat{\vec{c}} \end{bmatrix} = \begin{bmatrix} (H_x^T W \vec{y})_1 \\ (H_x^T W \vec{y})_2 \\ \vdots \\ (H_x^T W \vec{y})_k \\ \sum_k (H_c^T W \vec{y})_k \end{bmatrix}. \tag{4.48}$$

The local parameters are independent of each other, explaining their contribution located on the diagonal of the normal matrix. All local parameters contribute to the global parameters, the last row and column of the matrix are fully populated.

This system can be arranged in a similar fashion as in the single arc case, with the substitutions for the sub-matrices and -vectors from Equations (4.41). Multiplying out the upper rows gives expressions for the local parameters $\hat{\vec{x}}_k$ for each arc

$$\hat{\vec{x}}_k = (M_{xx})_k^{-1} (\vec{m}_x)_k - (M_{xx})_k^{-1} (M_{xc})_k \hat{\vec{c}}. \tag{4.49}$$

From the last row of the system (Eq. 4.48), with substitution of the local parameters $\hat{\vec{x}}_k$ from the previous equation (Eq. 4.49), an expression for the global parameters follows

$$\hat{\vec{c}} = \Big(\sum_k (M_{cc})_k - \sum_k (M_{cx} M_{xx}^{-1} M_{xc})_k \Big)^{-1} \Big(\sum_k (\vec{m}_c)_k - \sum_k (M_{cx} M_{xx}^{-1} \vec{m}_x)_k \Big). \tag{4.50}$$

Again, with the solution for the global parameters $\hat{\vec{c}}$, the local parameters for each arc $\hat{\vec{x}}_k$ can be computed with Equation (4.49) by back-substitution.

The residuals $\hat{\vec{\epsilon}}_k$ for the partitioned case, can be computed using the definition (Eq. 4.25) and inserting the partitioning (Eq. 4.39)

$$\hat{\vec{\epsilon}}_k = \vec{y}_k - (H_x)_k \hat{\vec{x}}_k - (H_c)_k \hat{\vec{c}}. \tag{4.51}$$

4.3.9 Combination of Different Observations

Often different types of observations are available to be used for the estimation. To combine different kind of observations it is reasonable to weight observations according to their accuracy. Even if just one kind of observation is used, it might be reasonable to introduce a weighting of different data arcs. The accuracy of satellite observations in orbit determination is often dependent on environmental conditions and thus not constant. This might be due to the orbit constellation, space weather, satellite and instrument temperatures and so on. Observations of different satellites or in the case of GFR also ground based measurements may be combined, as well.

Mathematically there is no difference weather different kind of observations or different data arcs are weighted separately, thus it is not explicitly mentioned in the following.

It is assumed, that correlations of the observation errors are known or are neglected, meaning the variance-covariance matrix $\bar{C}_{\epsilon\epsilon}$ is known or is the identity matrix I, respectively. Furthermore, the accumulated design matrix H contains measurements of different accuracies σ_v^2. The subscript v counts the different weighted observation groups, which may also be different arcs.

Under this conditions σ^2 does not cancel out in Equation (4.28). Nevertheless, regarding Equation (4.37), where the normal equations were summed over each arc k, it is possible to arrange the normal equations in the same fashion, that all observations of the same group v are lumped together. For each observation group, its variance σ_v^2 can be extracted, and the whole normal equations can be written as

$$N\hat{\vec{x}} = \vec{n} \qquad \text{with} \qquad N = \sum_v \frac{1}{\sigma_v^2} H_v^T (\bar{W})_v H_v, \quad \vec{n} = \sum_v \frac{1}{\sigma_v^2} H_v^T (\bar{W})_v \vec{y}_v. \tag{4.52}$$

Compared to Equation (4.37), no more arc k appears explicitly. Each arc may be weighted separately, but the sum over v may also include a sum over the arcs k with observations of the same variance σ_v^2. This means that, additional to each arc, observations of the same kind or group can be accumulated separately. This is important for the concept of variance component estimation (VCE), as described in the following section.

The definitions of the sub matrices M and $\vec{m}$ in Equation (4.41) includes the weighting matrix W, when isolating the σ_v^2 terms, these substitutions are equivalently used with $\bar{W}$ ($\bar{W} = \sigma_v^2 W$, Eq. 4.29, 4.30) in the next sections.

4.3.10 Variance Component Estimation (VCE)

The variance factors σ_v^2 of different observations or their evolution over time are usually not known with high certainty. Nevertheless, the weighting factors have a crucial influence on the solution.

In Section 4.3.6 it has been shown, that in case of only one kind of observation group, the variance factor σ^2 can be estimated from the square sum of the residuals after solving the normal equations. In case of more than one observation this is not possible any more, because the solution of the normal equations is dependent on the weighting factors σ_v^2 itself. Variance component estimation (VCE) is a technique to determine the variance factors σ_v^2 of different observation groups during the solution of the normal equations iteratively, based on the residuals and the formal errors from the normal equations. VCE is used and described here in the way it was introduced by Koch and Kusche (2001) and especially utilized for GFR by Mayer-Gürr (2006). In the following it is shown without considering arcs and partitioning as described in Mayer-Gürr (2006). In Section 4.3.11 it is generally expanded for the case of partitioned normal equations with an arbitrary number of variance factors and arcs.

The form of the normal equations from Equation (4.52) can be summarized as

$$N\hat{\vec{x}} = \vec{n} \qquad \text{with} \qquad N = \sum_v \frac{1}{\hat{\sigma}_v^2} N_v, \qquad \vec{n} = \sum_v \frac{1}{\hat{\sigma}_v^2} \vec{n}_v. \tag{4.53}$$

In there, the variance is denoted with a $\hat{\cdot}$ because it is to be estimated by the VCE method. The variances are defined referring to the case with just one observation group (Eq. 4.31), but now for v observation groups

$$\hat{\sigma}_v^2 = \frac{\hat{\vec{\epsilon}}_v^T \bar{W} \hat{\vec{\epsilon}}_v}{r_v} = \frac{(\vec{y}_v - H_v\hat{\vec{x}})^T \bar{W} (\vec{y}_v - H_v\hat{\vec{x}})}{r_v}, \tag{4.54}$$

with

$$r_v = m_v - \frac{1}{\hat{\sigma}_v^2} trace(N_v N^{-1}), \tag{4.55}$$

where $\sum_v r_v = m - n$ as in the single observation group case. For the computation of the residuals $\hat{\vec{\epsilon}}$, the solution $\hat{\vec{x}}$ must be know, for which $\hat{\sigma}_v^2$ must be known. Thus, as already mentioned, this problem can only be solved iteratively. Therefore an initial guess for the variances $\hat{\sigma}_v^2$ is needed. Fortunately, convergence is usually obtained quite fast (after one to three iterations).

The computation of the residuals $\hat{\vec{\epsilon}}_v$ in Equation 4.54 requires the design matrices H_v. In many implementations the design matrices are not saved to reduce memory demands. Nevertheless, with some matrix algebra the computation of the square sum of the residuals in Equation (4.54) can be transformed to

$$\begin{aligned} \hat{\vec{\epsilon}}_v^T \bar{W} \hat{\vec{\epsilon}}_v &= (\vec{y}_v - H_v \hat{\vec{x}})^T \bar{W} (\vec{y}_v - H_v \hat{\vec{x}}) \\ &= \hat{\vec{x}}^T N_v \hat{\vec{x}} - 2\hat{\vec{x}}^T \vec{n}_v + \vec{y}_v^T \bar{W} \vec{y}_v, \end{aligned} \tag{4.56}$$

avoiding the use of the design matrix H_v explicitly. For the use of PCG methods, this can also be arranged without explicit use of the normal matrices N_v like demonstrated in eg. Mayer-Gürr (2006).

4.3.11 Partitioned VCE

The concept of VCE is derived in this section for the partitioned normal equations with v observation groups and k arcs.

The starting point are the partitioned normal equations (Eq. 4.48), where for each arc k, here additionally v observation groups are introduced. The derivation follows the same way as before, but with the aim to separate the $1/\hat{\sigma}_v^2$ terms and bring the equation to the form of Equation (4.53) to apply the VCE concept. By multiplying out the upper rows of the matrix Equation (4.48) and considering $\hat{\sigma}_v^2$ observation groups, the following expression for the local parameters is obtained

$$\hat{\vec{x}}_k = \Big(\sum_v \frac{1}{\hat{\sigma}_v^2}(M_{xx})_v\Big)_k^{-1} \Big(\sum_v \frac{1}{\hat{\sigma}_v^2}(\vec{m}_x)_v\Big)_k - \Big(\sum_v \frac{1}{\hat{\sigma}_v^2}(M_{xx})_v\Big)_k^{-1} \Big(\sum_v \frac{1}{\hat{\sigma}_v^2}(M_{xc})_v\Big)_k \hat{\vec{c}}. \tag{4.57}$$

The last row of the system gives

$$\sum_k \left[\Big(\sum_v \frac{1}{\hat{\sigma}_v^2}(M_{cx})_v\Big)_k \hat{\vec{x}}_k\right] + \sum_v \frac{1}{\hat{\sigma}_v^2}\Big(\sum_k (M_{cc})_k\Big)_v \hat{\vec{c}} = \sum_v \frac{1}{\hat{\sigma}_v^2}\Big(\sum_k (\vec{m}_c)_k\Big)_v. \tag{4.58}$$

In order to reach the desired form, the different sums need to be arranged in the same order. For the first sum of the previous equation the summation can be switched, it applies

$$\sum_k \left[\Big(\sum_v \frac{1}{\hat{\sigma}_v^2}(M_{cx})_v\Big)_k \hat{\vec{x}}_k\right] = \sum_v \frac{1}{\hat{\sigma}_v^2}\Big(\sum_k (M_{cx})_k \hat{\vec{x}}_k\Big)_v. \tag{4.59}$$

Again, Equation (4.57) is substituted into Equation (4.58). According to Equation (4.59), sums over the same index can be combined. Hence the equation can be transformed to

$$\begin{aligned} &\sum_v \frac{1}{\hat{\sigma}_v^2}\Big(\sum_k \Big[(M_{cc})_k - (M_{cx})_k \Big(\sum_v \frac{1}{\hat{\sigma}_v^2}(M_{xx})_v\Big)_k^{-1} \Big(\sum_v \frac{1}{\hat{\sigma}_v^2}(M_{xc})_v\Big)_k\Big] \hat{\vec{c}}\Big)_v \\ &\quad = \sum_v \frac{1}{\hat{\sigma}_v^2}\Big(\sum_k \Big[(\vec{m}_c)_k - (M_{cx})_k \Big(\sum_v \frac{1}{\hat{\sigma}_v^2}(M_{xx})_v\Big)_k^{-1} \Big(\sum_v \frac{1}{\hat{\sigma}_v^2}(\vec{m}_x)_v\Big)_k\Big]\Big)_v \end{aligned} \tag{4.60}$$

By substituting the matrix L_v and the vector $\vec{l}_v$, the system from the previous equation (Eq. 4.60) can be reduced to

$$\sum_v \frac{1}{\hat{\sigma}_v^2} L_v \hat{\vec{c}} = \sum_v \frac{1}{\hat{\sigma}_v^2} \vec{l}_v, \tag{4.61}$$

which is the form needed for VCE (see Eq. 4.53). However, it is not possible to isolate the variance factor $1/\hat{\sigma}_v^2$ and the sum over v completely, L_v and $\vec{l}_v$ still contain $\hat{\sigma}_v^2$. Thus, the concept of the "elimination of parameters" as described in eg. Mayer-Gürr (2006) or Wu (2017) is mathematically not possible in the partitioned case.

Since the VCE procedure is an iterative process already, this is not a problem and solved iteratively together. Nevertheless, the summed matrices over k are not constant during the VCE iteration.

For the VCE iteration the square sum of the residuals for each observation group v needs to be computed. The residuals $\hat{\vec{\epsilon}}$ for the partitioned case are defined in Equation (4.51). Thus it follows for one observation group v

$$\hat{\vec{\epsilon}}_v^T (\bar{W})_v \hat{\vec{\epsilon}}_v = \left(\vec{y}_v^T - \hat{\vec{x}}^T (H_x^T)_v - \hat{\vec{c}}^T (H_c^T)_v\right) (\bar{W})_v \left(\vec{y}_v - (H_x)_v \hat{\vec{x}} - (H_c)_v \hat{\vec{c}}\right). \tag{4.62}$$

By multiplying out the expression, using $\hat{\vec{x}}^T (H_x^T)_v \vec{y}_v = \vec{y}_v^T (H_x)_v \hat{\vec{x}}$, the symmetry of $\bar{W}$ ($\bar{W} = \bar{W}^T$) and substituting the sub matrices as defined in Equation (4.41), Equation (4.62) can be transformed to

$$\begin{aligned}\hat{\vec{\epsilon}}_v^T (\bar{W})_v \hat{\vec{\epsilon}}_v = {} & \hat{\vec{x}}^T (M_{xx})_v \hat{\vec{x}} + \hat{\vec{x}}^T (M_{xc})_v \hat{\vec{c}} + \hat{\vec{c}}^T (M_{cx})_v \hat{\vec{x}} + \hat{\vec{c}}^T (M_{cc})_v \hat{\vec{c}} \\ & - 2\hat{\vec{x}}^T (\vec{m}_x)_v - 2\hat{\vec{c}}^T (\vec{m}_c)_v + \vec{y}_v^T (\bar{W})_v \vec{y}_v.\end{aligned} \tag{4.63}$$

Again it is possible to compute the square sum of the residuals without using the design matrix H, explicitly. In here, the different arcs k are not considered, yet. Nevertheless, for Equation (4.54) it is necessary to build the residual square sum over all arcs. Thus Equation (4.63) needs to be set up and summed over all arcs k. With the summed overall residuals $(\hat{\vec{\epsilon}}_s)_v$ being

$$(\hat{\vec{\epsilon}}_s)_v = \sum_k \left((\vec{y}^T)_{k,v} - \hat{\vec{x}}_k^T (H_x^T)_{k,v} - \hat{\vec{c}}^T (H_c^T)_{k,v}\right), \tag{4.64}$$

the total squared residuals can be build in the same way as before, and after some transformation one obtains

$$\begin{aligned}(\hat{\vec{\epsilon}}_s)_v^T (\bar{W})_v (\hat{\vec{\epsilon}}_s)_v = {} & \sum_k \left(\hat{\vec{x}}_k^T (M_{xx})_{k,v} \hat{\vec{x}}_k\right) + \sum_k \left(\hat{\vec{x}}_k^T (M_{xc})_{k,v} \hat{\vec{c}}\right) \\ & + \sum_k \left(\hat{\vec{c}}^T (M_{cx})_{k,v} \hat{\vec{x}}_k\right) + \sum_k \left(\hat{\vec{c}}^T (M_{cc})_{k,v} \hat{\vec{c}}\right) \\ & - \sum_k \left(2\hat{\vec{x}}_k^T (\vec{m}_x)_{k,v}\right) - \sum_k \left(2\hat{\vec{c}}^T (\vec{m}_c)_{k,v}\right) - \sum_k \left((\vec{y})_{k,v}^T (\bar{W})_v (\vec{y})_{k,v}\right).\end{aligned} \tag{4.65}$$

Each sum in there can be rearranged, like

$$\sum_k \left(\hat{\vec{c}}^T (M_{cc})_{k,v}\, \hat{\vec{c}}\right) = \hat{\vec{c}}^T \sum_k (M_{cc})_{k,v}\, \hat{\vec{c}}. \tag{4.66}$$

Thus the sums over the arcs k of all sub matrices can be build once and used in all VCE iterations.

For the VCE algorithm the inverse of the normal matrix N needs to be build (see Eq. 4.55). Again there are methods that avoid the explicit inversion of the matrix (eg. Mayer-Gürr, 2006). In our implementation we do not bother with that problem because compared to the accumulation of the normal equations this is computationally completely neglectable, as described for the solution of the normal equations (Sec. 4.3.7). The MATLAB standard library is used to compute the inverse by decomposition methods, here as well.

4.3.12 Formal Error with Partitioning and Combined Observations

The formal error was defined in Section 4.3.6 for the simple case without partitioning and just one observation group. The formal error is derived for the partitioned case with more than one weighted observation group in the following in two steps. For practical applications this is usually the case and especially, the determination of the covariance matrix of the estimated global parameters $\hat{C}_{\hat{c}}$ is of interest to plot the degree variance of a solution (cf. Sec. 2.3.3).

First, the formal error is defined for the partitioned case (cf. Sec. 4.3.8). $\hat{C}_{\hat{c}}$ is given in Equation (4.35) with $\hat{\sigma}^2$ defined in Equation (4.31). For the global parameters $\hat{\vec{c}}$ it is given by

$$\hat{C}_{\hat{c}} = \hat{\sigma}^2 \Big(\sum_k (M_{cc})_k \Big)^{-1}. \tag{4.67}$$

Subsequently the formal error of the local parameters can be determined by back-substitution for the local parameters of the arc k by

$$\hat{C}_{\hat{x}_k} = \hat{\sigma}^2 \Big[(M_{xx})_k^{-1} + (M_{xx})_k^{-1} (M_{xc})_k \Big(\sum_k (M_{cc})_k \Big)^{-1} (M_{cx})_k (M_{xx})_k^{-1} \Big]. \tag{4.68}$$

Secondly, the formal error is expanded for v different weighted observation groups. The estimated variance $\hat{\sigma}^2$ in Equations (4.67) and (4.68) needs to be defined as an overall variance factor $\hat{\sigma}^2_{ges}$, considering the variances $\hat{\sigma}^2_v$ of all observation groups

$$\hat{\sigma}^2_{ges} = \frac{\sum_v \frac{1}{\sigma_v^2} \vec{\epsilon}_v^T \bar{W}_v \vec{\epsilon}_v}{m - n}. \tag{4.69}$$

This variance is not an absolute quantity anymore, because it is multiplied with the weighting factors $1/\sigma_v^2$ of each observation group. Therefore it just can be compared relatively. The covariance of the global parameters is then

$$\hat{C}_{\hat{c}} = \hat{\sigma}^2_{ges} \Big[\sum_v \frac{1}{\sigma_v^2} \Big(\sum_k (M_{cc})_k \Big)_v \Big]^{-1}. \tag{4.70}$$

The inverse of the summed normal matrix includes the weighting factors $1/\sigma_v^2$ as well, making the covariance matrix an absolute quantity again. Building the square root of the diagonal gives the standard deviation σ_{Cnm} and σ_{Snm} of each SH coefficient. This can be used to plot the degree variance of a GFR solution (cf. Eq. 2.39).

The covariance of the local parameters follows from Equation (4.68) when adding the sums over the observation groups v with their corresponding weighting $1/\sigma_v^2$ and using the overall variance factor $\hat{\sigma}^2_{ges}$.

4.3.13 Regularization

Regularization is not used for all results presented in this thesis. Nevertheless, the option is implemented in the GFR software and the frequently addressed topic is just shortly discussed for completeness in this subsection.

Regularization is a technique used in least squares analysis especially if a system is ill-conditioned. An ill-conditioned system means that a small change of the input (noisy observations) has a big effect on the results. In other words, the variance of the estimated parameters is high. In the normal matrix this is reflected in the fact that its rows are nearly linear combinations of each other. The cause of that is that a measurement is not sensitive to the estimated parameters, or the noise level is too high.

Both has usually an implication for GFR. The gravitational signal is attenuated at the height of the satellites (regarding Newtons gravitational potential by $1/r$). Additionally, in the spherical harmonic potential the factor $(R/r)^n$ (cf. Eq. 2.20) makes the effect even wavelength (or degree) dependent. Thus the higher the degree of the spherical harmonic coefficients, the lower is the signal to noise ratio. Furthermore, the KRB range and range-rate measurement is not sensitive to the absolute position and velocity and also not so much to accelerometer calibration parameters. The second point may be compensated by adding additional GNSS observations.

By regularization additional information is added to the system, also called pseudo-observations, making the whole system more stable. Therefore, regularization is also referred to as stabilization.

In the normal equations (Eq. 4.22) a regularization matrix R is added

$$\hat{\vec{x}} = (H^T W H + \alpha R)^{-1} H^T W \vec{y}, \tag{4.71}$$

with the regularization parameter α. This is also referred to as Tikhonov regularization. With regard to Equation (4.37) and (4.53) it is obvious, that the regularization matrix R is mathematically a normal matrix of a further observation and the regularization parameter α is the weighting factor of that added information.

The matrix R needs to be known from prior information or experience. Often the identity matrix or a diagonal matrix is used and just α is determined. For the determination of the regularization parameter α different methods and criteria exist, the interested reader is refereed to eg. Save (2009) or Wu (2017), Ch. 2. It may be determined in an optimal sense using VCE, as well.

In GFR Kaula regularization is very popular. It refers to Kaula (1966), who stated that the degree amplitude spectrum of Earth's SH gravity potential can be approximated by a function $10^{-5}\sqrt{2 * n + 1}/n^2$, where n is the SH degree (cf. Sec. 2.3.3 and Fig. 2.6). With this information R can be build. For the precision of GRACE observations this kind of regularization is not useful, at least for degrees below 100. In the developed GFR software this kind of regularization is not used and therefore not further elaborated. Regularization can be used to stabilize the estimation of the local parameters, especially when only KBR range-rates are used as observations. This is not part of this thesis, but results with just range-rate observations and this kind of regularization have been published in (Darbeheshti et al., 2020).

With the partitioned normal equations (Sec. 4.3.8), and a diagonal regularization matrix R it is easy to separate the regularization of local and global parameters. The R matrix is partitioned in R_{xx} and R_{cc} as well and simply added to M_{xx} and M_{cc} with α_x and α_c, respectively.

4.3.14 Form and Components of the Matrices for the GRACE Case

In this section the main matrices of the estimation procedure A, Φ and $\widetilde{H}$ shall be presented in their matrix form in more detail. Their assembly and components are demonstrated for the GRACE type mission. It demonstrates that the concept is easily expandable and applicable to any other satellite mission and set of parameters.

The GRACE mission is especially characterized by the realization of the inter-satellite ranging system (KBR) between the two satellites and the use of accelerometers to measure non-gravitational forces acting on the satellites. Additionally a 3d-position solution from the GPS receivers is available. Usually not the range between the satellites is used as observation, but the range-rate (cf Sec. 3.2.1). Due to the KBR observation equation, both satellites are coupled and hence the determination process needs to be conducted for both satellites simultaneously. A combination of the normal matrices for the gravity field coefficients can not be realized, as it would be possible when having two independent satellites.

Matrix A: State Partials

The extended state vector $\vec{X}$ contains the set of unknown parameters to be estimated, as defined in Section 4.3 and Equation (4.1). For two satellites (A and B) $\vec{X}$ and its derivative $\dot{\vec{X}}$ are

$$\vec{X} = \begin{bmatrix} \vec{r}_A \\ \dot{\vec{r}}_A \\ \vec{r}_B \\ \dot{\vec{r}}_B \\ \vec{p} \end{bmatrix}, \qquad \dot{\vec{X}} = \begin{bmatrix} \dot{\vec{r}}_A \\ \ddot{\vec{r}}_A \\ \dot{\vec{r}}_B \\ \ddot{\vec{r}}_B \\ \dot{\vec{p}} \end{bmatrix} = \begin{bmatrix} \dot{\vec{r}}_A \\ \ddot{\vec{r}}_A \\ \dot{\vec{r}}_B \\ \ddot{\vec{r}}_B \\ 0 \end{bmatrix}. \tag{4.72}$$

In there $\vec{r}$, $\dot{\vec{r}}$ and $\ddot{\vec{r}}$ are the satellites position, velocity and acceleration, respectively. The vector $\vec{p}$ contains all additional model parameters that are to be estimated, as well. The estimated parameters are constant over the time period they are estimated, thus its derivatives are zero. Here, for GRACE, the parameter vector $\vec{p}$ contains the SH coefficients of the gravitational model, referred to as $\vec{K}_{nm}$ and calibration parameters for both accelerometers. Usually the three accelerometer axis are calibrated at least with a constant bias $\vec{b}$. Here additionally a linear drift $\vec{d}$ and a scale factor $\vec{s}$ are considered

$$\vec{p} = \begin{bmatrix} \vec{b}_A & \vec{d}_A & \vec{s}_A & \vec{b}_B & \vec{d}_B & \vec{s}_B & \vec{K}_{nm} \end{bmatrix}^T. \tag{4.73}$$

The A matrix is defined in Equation (4.6), for the assumed conditions it is

$$A = \left[\frac{\partial \dot{\vec{X}}}{\partial \vec{X}}\right]_{\vec{X}=\vec{X}^*} =$$

$$\begin{bmatrix} \frac{\partial \dot{\vec{r}}_A}{\partial \vec{r}_A} & \frac{\partial \dot{\vec{r}}_A}{\partial \dot{\vec{r}}_A} & \frac{\partial \dot{\vec{r}}_A}{\partial \vec{r}_B} & \frac{\partial \dot{\vec{r}}_A}{\partial \dot{\vec{r}}_B} & \frac{\partial \dot{\vec{r}}_A}{\partial \vec{p}} \\ \frac{\partial \ddot{\vec{r}}_A}{\partial \vec{r}_A} & \frac{\partial \ddot{\vec{r}}_A}{\partial \dot{\vec{r}}_A} & \frac{\partial \ddot{\vec{r}}_A}{\partial \vec{r}_B} & \frac{\partial \ddot{\vec{r}}_A}{\partial \dot{\vec{r}}_B} & \frac{\partial \ddot{\vec{r}}_A}{\partial \vec{p}} \\ \frac{\partial \dot{\vec{r}}_B}{\partial \vec{r}_A} & \frac{\partial \dot{\vec{r}}_B}{\partial \dot{\vec{r}}_A} & \frac{\partial \dot{\vec{r}}_B}{\partial \vec{r}_B} & \frac{\partial \dot{\vec{r}}_B}{\partial \dot{\vec{r}}_B} & \frac{\partial \dot{\vec{r}}_B}{\partial \vec{p}} \\ \frac{\partial \ddot{\vec{r}}_B}{\partial \vec{r}_A} & \frac{\partial \ddot{\vec{r}}_B}{\partial \dot{\vec{r}}_A} & \frac{\partial \ddot{\vec{r}}_B}{\partial \vec{r}_B} & \frac{\partial \ddot{\vec{r}}_B}{\partial \dot{\vec{r}}_B} & \frac{\partial \ddot{\vec{r}}_B}{\partial \vec{p}} \\ \frac{\partial \dot{\vec{p}}}{\partial \vec{r}_A} & \frac{\partial \dot{\vec{p}}}{\partial \dot{\vec{r}}_A} & \frac{\partial \dot{\vec{p}}}{\partial \vec{r}_B} & \frac{\partial \dot{\vec{p}}}{\partial \dot{\vec{r}}_B} & \frac{\partial \dot{\vec{p}}}{\partial \vec{p}} \end{bmatrix}_{\vec{X}=\vec{X}^*} = \begin{bmatrix} 0_{3\times3} & I_{3\times3} & 0_{3\times3} & 0_{3\times3} & 0_{3\times\bar{n}} \\ \frac{\partial \ddot{\vec{r}}_A}{\partial \vec{r}_A} & \frac{\partial \ddot{\vec{r}}_A}{\partial \dot{\vec{r}}_A} & 0_{3\times3} & 0_{3\times3} & \frac{\partial \ddot{\vec{r}}_A}{\partial \vec{p}} \\ 0_{3\times3} & 0_{3\times3} & 0_{3\times3} & I_{3\times3} & 0_{3\times\bar{n}} \\ 0_{3\times3} & 0_{3\times3} & \frac{\partial \ddot{\vec{r}}_B}{\partial \vec{r}_B} & \frac{\partial \ddot{\vec{r}}_B}{\partial \dot{\vec{r}}_B} & \frac{\partial \ddot{\vec{r}}_B}{\partial \vec{p}} \\ 0_{\bar{n}\times3} & 0_{\bar{n}\times3} & 0_{\bar{n}\times3} & 0_{\bar{n}\times3} & 0_{\bar{n}\times\bar{n}} \end{bmatrix}_{\vec{X}=\vec{X}^*}, \tag{4.74}$$

where $\bar{n}$ is the number of the additional parameters (excluding the 12 initial conditions $\bar{n} = n - 12$) and evaluated on the reference trajectory $\vec{X}^*$. Many of the partials are zero by definition. The expressions for the partial derivatives $\partial\dot{\vec{r}}/\partial\vec{r} = 0_{3\times3}$ or $\partial\vec{r}/\partial\dot{\vec{r}} = 0_{3\times3}$ sometimes cause some confusion, stating that position and velocity are not dependent on each other, whereas you can think of an example (eg. a free falling mass) where it is easily possible to write down an equation $\dot{\vec{r}}(\vec{r})$ or vice versa. Therefore a general comment on that: Position $\vec{r}$ and velocity $\dot{\vec{r}}$ are mathematically two variables (or states) of the differential system of equations, which both depend explicitly just on the independent variable time t. For a unique solution, for position and velocity initial conditions are required, where a mass can be at any position $\vec{r}$, completely independent of its velocity $\dot{\vec{r}}$, and vice versa. Of cause, when one solution of the differential system of equations is determined, by rearranging of the equations, a function $t(\vec{r})$ may be written down in some special cases, and substituted into the equation for the velocity, giving $\dot{\vec{r}}(t(\vec{r}))$. Nevertheless, this notation already implies that $\vec{r}$ and $\dot{\vec{r}}$ are not directly dependent on each other, but just indirect via the time t. Thus their partial derivative is zero. Vividly this can be understood, that if the velocity changes, the time changes, and due to that change in time, the position changes, as well.

In the implementation the A matrix should not be saved completely because the lower part contains always $n \times \bar{n}$ zeros.

The accelerations that need to be considered for satellites are gravitational and non-gravitational ones. The partials from different contributions can be split arbitrarily like

$$\frac{\partial \ddot{\vec{r}}}{\partial \vec{r}} = \frac{\partial \ddot{\vec{r}}_{grav}}{\partial \vec{r}} + \frac{\partial \ddot{\vec{r}}_{ng}}{\partial \vec{r}} + \frac{\partial \ddot{\vec{r}}_{other}}{\partial \vec{r}}. \tag{4.75}$$

The computation of the partials can be done by numerical differentiation, but for many accelerations, especially the gravitational ones, an analytical formulation exists. A numerical differentiation can be realized by evaluating the models at slightly different points (positions or velocities) and building the difference quotient in all three directions

to determine the nine elements of the partial derivative matrix $\partial\ddot{\vec{r}}/\partial\vec{r}$. There may also be the case that no model for an acceleration exists, because measurements or other time series are used, like the accelerator measurements used as non-gravitational accelerations. In that case a numeric differentiation can be realized by using the data on the reference trajectory for the actual and previous points and building a difference quotient with non-equidistant bases.

In the following the partial derivatives of the acceleration with respect to the different variables are discussed in detail.

Derivatives with respect to Position The gravitational part of the partial, $\partial\ddot{\vec{r}}_{grav}/\partial\vec{r}$ known as the gravity gradient matrix, can be computed analytically. It consists of an contribution from the SH models (which usually include a static gravitational field and tidal models) and one from third body perturbations. The derivative of the SH acceleration follows from its definition (Eq. 2.20 and 2.17) and is quite lengthy. The interested reader is referred to eg. Montenbruck and Gill (2005), Ch. 7. The relativistic corrections could be considered here as well, but are so small, that they are neglected for the A matrix.

For realistic non-gravitational models no analytic form of the derivatives exists and they need to be computed numerically. Building the partials for atmospheric drag (Sec. 5.1.6 and Eq. 5.20 requires the derivative of the density, which is usually also not possible analytically.

Nevertheless, the contributions of the non-gravitational accelerations are orders of magnitudes smaller than the gravitational ones. It was found, that neglecting these terms in the A matrix does not have any influence on the results or the convergence of the POD or GFR procedure.

Derivatives with respect to Velocity The only velocity dependent acceleration for satellites is usually atmospheric drag. It can be computed analytically from Equation (5.20). It is usually orders of magnitudes smaller than the gravitational accelerations, as well. Also this partial can be neglected without any influence on the results.

Derivatives with respect to Accelerometer Calibration The calibration equation for the accelerometers can be written as

$$\ddot{\vec{r}}_{acc,b} = \vec{s} * ACC + \vec{b} + \vec{d} * t \tag{4.76}$$

where ACC is the measured acceleration vector in the SRF- or body-frame for one satellite and time t. However, the desired partial derivatives need to be computed in the inertial ECI frame. Thus Equation (4.76) needs to be transformed

$$\ddot{\vec{r}}_{acc,i} = T_{b2i}(\vec{s} * ACC + \vec{b} + \vec{d} * t). \tag{4.77}$$

From this equation the partials with respect to $\vec{b}$, $\vec{d}$ and $\vec{s}$ directly follow as

$$\begin{aligned} \frac{\partial\ddot{\vec{r}}}{\partial\vec{b}} &= \frac{\partial\ddot{\vec{r}}_{ACC}}{\partial\vec{b}} = T_{i2b}, \\ \frac{\partial\ddot{\vec{r}}}{\partial\vec{d}} &= T_{i2b}\, t, \\ \frac{\partial\ddot{\vec{r}}}{\partial\vec{s}} &= T_{i2b}\, ACC. \end{aligned} \tag{4.78}$$

Derivatives with respect to SH Coefficients $\vec{K}_{nm}$ The derivatives $\partial\ddot{\vec{r}}/\partial\vec{K}_{nm}$ can be computed from the definition of the SH gravitational field model (Eq. 2.20 and 2.17) analytically. Written down they may fill pages. Again, the interested reader is referred to eg. Montenbruck and Gill (2005), Ch. 7. The actual computation, especially for reasonable d/o, is one of the most time consuming steps of the GFR procedure.

Matrix Φ: State Transition Matrix

The state transition matrix, as defined in Section 4.3.2 and Equation (4.12), for two satellites A and B is

$$\Phi(t,t_0) = \left[\frac{\partial \vec{X}(t)}{\partial \vec{X}(t_0)}\right] =$$

$$\begin{bmatrix}
\frac{\partial \vec{r}_A(t)}{\partial \vec{r}_A(t_0)} & \frac{\partial \vec{r}_A(t)}{\partial \dot{\vec{r}}_A(t_0)} & \frac{\partial \vec{r}_A(t)}{\partial \vec{r}_B(t_0)} & \frac{\partial \vec{r}_A(t)}{\partial \dot{\vec{r}}_B(t_0)} & \frac{\partial \vec{r}_A(t)}{\partial \vec{p}(t_0)} \\
\frac{\partial \dot{\vec{r}}_A(t)}{\partial \vec{r}_A(t_0)} & \frac{\partial \dot{\vec{r}}_A(t)}{\partial \dot{\vec{r}}_A(t_0)} & \frac{\partial \dot{\vec{r}}_A(t)}{\partial \vec{r}_B(t_0)} & \frac{\partial \dot{\vec{r}}_A(t)}{\partial \dot{\vec{r}}_B(t_0)} & \frac{\partial \dot{\vec{r}}_A(t)}{\partial \vec{p}(t_0)} \\
\frac{\partial \vec{r}_B(t)}{\partial \vec{r}_A(t_0)} & \frac{\partial \vec{r}_B(t)}{\partial \dot{\vec{r}}_A(t_0)} & \frac{\partial \vec{r}_B(t)}{\partial \vec{r}_B(t_0)} & \frac{\partial \vec{r}_B(t)}{\partial \dot{\vec{r}}_B(t_0)} & \frac{\partial \vec{r}_B(t)}{\partial \vec{p}(t_0)} \\
\frac{\partial \dot{\vec{r}}_B(t)}{\partial \vec{r}_A(t_0)} & \frac{\partial \dot{\vec{r}}_B(t)}{\partial \dot{\vec{r}}_A(t_0)} & \frac{\partial \dot{\vec{r}}_B(t)}{\partial \vec{r}_B(t_0)} & \frac{\partial \dot{\vec{r}}_B(t)}{\partial \dot{\vec{r}}_B(t_0)} & \frac{\partial \dot{\vec{r}}_B(t)}{\partial \vec{p}(t_0)} \\
\frac{\partial \vec{p}(t)}{\partial \vec{r}_A(t_0)} & \frac{\partial \vec{p}(t)}{\partial \dot{\vec{r}}_A(t_0)} & \frac{\partial \vec{p}(t)}{\partial \vec{r}_B(t_0)} & \frac{\partial \vec{p}(t)}{\partial \dot{\vec{r}}_B(t_0)} & \frac{\partial \vec{p}(t)}{\partial \vec{p}(t_0)}
\end{bmatrix} =
\begin{bmatrix}
\frac{\partial \vec{r}_A(t)}{\partial \vec{r}_A(t_0)} & \frac{\partial \vec{r}_A(t)}{\partial \dot{\vec{r}}_A(t_0)} & 0_{3\times3} & 0_{3\times3} & \frac{\partial \vec{r}_A(t)}{\partial \vec{p}(t_0)} \\
\frac{\partial \dot{\vec{r}}_A(t)}{\partial \vec{r}_A(t_0)} & \frac{\partial \dot{\vec{r}}_A(t)}{\partial \dot{\vec{r}}_A(t_0)} & 0_{3\times3} & 0_{3\times3} & \frac{\partial \dot{\vec{r}}_A(t)}{\partial \vec{p}(t_0)} \\
0_{3\times3} & 0_{3\times3} & \frac{\partial \vec{r}_B(t)}{\partial \vec{r}_B(t_0)} & \frac{\partial \vec{r}_B(t)}{\partial \dot{\vec{r}}_B(t_0)} & \frac{\partial \vec{r}_B(t)}{\partial \vec{p}(t_0)} \\
0_{3\times3} & 0_{3\times3} & \frac{\partial \dot{\vec{r}}_B(t)}{\partial \vec{r}_B(t_0)} & \frac{\partial \dot{\vec{r}}_B(t)}{\partial \dot{\vec{r}}_B(t_0)} & \frac{\partial \dot{\vec{r}}_B(t)}{\partial \vec{p}(t_0)} \\
0_{\bar{n}\times3} & 0_{\bar{n}\times3} & 0_{\bar{n}\times3} & 0_{\bar{n}\times3} & I_{\bar{n}\times\bar{n}}
\end{bmatrix} \tag{4.79}$$

It can not be formed analytically, in general. For the Keplerian two-body problem it is possible to build it with some simplifications (Goodyear, 1965). For POD and GFR it needs to be integrated numerically using the A matrix (Eq. 4.12). This is commonly done together with the reference orbit.

Matrix $\widetilde{H}$: Observation Partials

The $\widetilde{H}$ matrix is defined as the partial derivative of the observations with respect to the state (Eq. 4.9). Written-out for 3d-position observations $\vec{r}_A$, $\vec{r}_B$ for satellite A and B, respectively and a scalar range-rate observation $\dot{\rho}$ it is

$$\widetilde{H} = \left[\frac{\partial G}{\partial \vec{X}}\right] = \begin{bmatrix}
\frac{\partial \vec{r}_A}{\partial \vec{r}_A} & \frac{\partial \vec{r}_A}{\partial \dot{\vec{r}}_A} & \frac{\partial \vec{r}_A}{\partial \vec{r}_B} & \frac{\partial \vec{r}_A}{\partial \dot{\vec{r}}_B} & \frac{\partial \vec{r}_A}{\partial \vec{p}} \\
\frac{\partial \vec{r}_B}{\partial \vec{r}_A} & \frac{\partial \vec{r}_B}{\partial \dot{\vec{r}}_A} & \frac{\partial \vec{r}_B}{\partial \vec{r}_B} & \frac{\partial \vec{r}_B}{\partial \dot{\vec{r}}_B} & \frac{\partial \vec{r}_B}{\partial \vec{p}} \\
\frac{\partial \dot{\rho}}{\partial \vec{r}_A} & \frac{\partial \dot{\rho}}{\partial \dot{\vec{r}}_A} & \frac{\partial \dot{\rho}}{\partial \vec{r}_B} & \frac{\partial \dot{\rho}}{\partial \dot{\vec{r}}_B} & \frac{\partial \dot{\rho}}{\partial \vec{p}}
\end{bmatrix} = \begin{bmatrix}
I_{3\times3} & 0_{3\times3} & 0_{3\times3} & 0_{3\times3} & \frac{\partial \vec{r}_A}{\partial \vec{p}} \\
0_{3\times3} & 0_{3\times3} & I_{3\times3} & 0_{3\times3} & \frac{\partial \vec{r}_B}{\partial \vec{p}} \\
\frac{\partial \dot{\rho}}{\partial \vec{r}_A} & \frac{\partial \dot{\rho}}{\partial \dot{\vec{r}}_A} & \frac{\partial \dot{\rho}}{\partial \vec{r}_B} & \frac{\partial \dot{\rho}}{\partial \dot{\vec{r}}_B} & \frac{\partial \dot{\rho}}{\partial \vec{p}}
\end{bmatrix}. \tag{4.80}$$

The partial derivatives $\partial\vec{r}_A/\partial\vec{p}$ and $\partial\vec{r}_B/\partial\vec{p}$ are components of the state transition matrix (see Eq. 4.79) and are used from there. The 3d-position observation partials $\partial\vec{r}_A/\partial\vec{r}_A$ and $\partial\vec{r}_B/\partial\vec{r}_B$ simply reduce to the identity matrix I.

For the partials of range-rate, first the range ρ and range-rate $\dot{\rho}$ are mathematically defined in the following.

Relative position and velocity of satellite A and B are defined as

$$\begin{aligned}\vec{r}_{AB} &= \vec{r}_B - \vec{r}_A,\\ \dot{\vec{r}}_{AB} &= \dot{\vec{r}}_B - \dot{\vec{r}}_A.\end{aligned} \tag{4.81}$$

Range and range-rate are then given by

$$\rho = \sqrt{\vec{r}_{AB}\cdot\vec{r}_{AB}}, \tag{4.82}$$

$$\dot{\rho} = \frac{\vec{r}_{AB}}{\rho}\cdot\dot{\vec{r}}_{AB} = \vec{e}_{AB}\cdot\dot{\vec{r}}_{AB}, \tag{4.83}$$

where $\cdot$ is the vector dot product and $\vec{e}_{AB}$ is the line of sight unit vector of the two satellites. Accordingly, the partials of the leading satellite (A) can be computed for range and range-rate measurements by derivation. Utilizing product and chain rule, this gives

$$\frac{\partial\rho}{\partial\vec{r}_A} = -\vec{e}_{AB}, \tag{4.84}$$

$$\frac{\partial\dot{\rho}}{\partial\vec{r}_A} = -\frac{1}{\rho}(\dot{\vec{r}}_{AB} - \dot{\rho}\vec{e}_{AB}), \tag{4.85}$$

$$\frac{\partial\dot{\rho}}{\partial\dot{\vec{r}}_A} = -\vec{e}_{AB}. \tag{4.86}$$

For the trailing satellite (B) the partials are the same as for the leading one, but with opposite sign. The partials with respect to the line of sight vector $\vec{r}_{AB}$ are quite similar:

$$\frac{\partial\rho}{\partial\vec{r}_{AB}} = \vec{e}_{AB}, \tag{4.87}$$

$$\frac{\partial\dot{\rho}}{\partial\vec{r}_{AB}} = \frac{1}{\rho}(\dot{\vec{r}}_{AB} - \dot{\rho}\vec{e}_{AB}), \tag{4.88}$$

$$\frac{\partial\dot{\rho}}{\partial\dot{\vec{r}}_{AB}} = \vec{e}_{AB}. \tag{4.89}$$

For the partials with respect to the parameters $\partial\dot{\rho}/\partial\vec{p}$ the range-rate partial needs to be related to the partials of the positions of the two satellites $\partial\vec{r}_A/\partial\vec{p}$ and $\partial\vec{r}_B/\partial\vec{p}$, which are known from the state transition matrix Φ (eg. Eq. 4.79).

Therefore, the partial is build with respect to the relative position vector $\vec{r}_{AB}$. It follows under consideration of the chain rule: $\partial/\partial x f(g(x)) = \partial f/\partial g\ \partial g/\partial x$. For completeness, first the range partial with $\rho = \rho(\vec{r}_{AB}(\vec{p}))$ is given by

$$\frac{\partial\rho}{\partial\vec{p}} = \frac{\partial\rho}{\partial\vec{r}_{AB}}\frac{\partial\vec{r}_{AB}}{\partial\vec{p}}. \tag{4.90}$$

And the range-rate partial with $\dot{\rho} = \dot{\rho}(\vec{r}_{AB}(\vec{p}), \dot{\vec{r}}_{AB}(\vec{p}))$ is

$$\frac{\partial\dot{\rho}}{\partial\vec{p}} = \frac{\partial\dot{\rho}}{\partial\vec{r}_{AB}}\frac{\partial\vec{r}_{AB}}{\partial\vec{p}} + \frac{\partial\dot{\rho}}{\partial\dot{\vec{r}}_{AB}}\frac{\partial\dot{\vec{r}}_{AB}}{\partial\vec{p}}. \tag{4.91}$$

Using the relations from the previous Equations (4.88), (4.89) and multiplying out, it transforms to

$$\frac{\partial \dot{\rho}}{\partial \vec{p}} = \frac{(\dot{\vec{r}}_B - \dot{\vec{r}}_A)^T}{\rho}\Big[\frac{\partial \vec{r}_B}{\partial \vec{p}} - \frac{\partial \vec{r}_A}{\partial \vec{p}} + \vec{e}_{AB}\vec{e}_{AB}^T\Big(\frac{\partial \vec{r}_A}{\partial \vec{p}} - \frac{\partial \vec{r}_B}{\partial \vec{p}}\Big)\Big] + \vec{e}_{AB}^T\frac{\partial \dot{\vec{r}}_B}{\partial \vec{p}} - \vec{e}_{AB}^T\frac{\partial \dot{\vec{r}}_A}{\partial \vec{p}}, \quad (4.92)$$

as also given in eg. McCullough (2017) without derivation. All remaining partials in this equation are components of the state transition matrix Φ. Hence, for building the observation partials $\tilde{H}$, the state transition matrix plays another important role.

4.3.15 Implementation of the Batch Processor Algorithm

In the following the GFR batch algorithm is described step by step, considering important points of the implementation and handling of data. It follows more or less the theoretical descriptions in this chapter.

1. Pre-processing of satellite data
   - In case real satellite data are used, usually a pre-processing is needed. For GRACE L1B data the implemented pre-processing is described in detail in Section 3.4. Times with missing observation data (KBR, GNV, KOS) are saved as well as arcs with too bad and missing ACC or SCA data or too high thruster firings.
   - All GRACE L1B data except ACC data are sampled with 1/5 Hz. Because five seconds are a good integration step size for LEO using the Adams-Bashforth-Moulton (ABM) numerical integration method (cf. Sec. 5.2), it is used as step size for the integration, as well. Therefore the ACC data are down-sampled to 5 s. To avoid loss of information, a moving average is used.
2. Initialization
   - The models to compute the reference orbit need to be defined. These are mainly the background gravity models (tides and the higher d/o of the static gravity field which are not estimated).
   - Definition of the parametrization (arc length, instrument calibration parameters)
   - Definition of processing options. For example: Number of iterations, weighting of observations, estimate C_{20} or use a given value, computation of residuals or deviations for which iterations, save matrices for error analysis.
   - The initial values for the parameters to be estimated need to be set to integrate the reference orbits $()^*$. These are the local parameters like initial position and velocity for all arcs of the satellites, ACC calibration parameters and the global SH gravitational field coefficients up to the desired d/o. Furthermore the initial value of the state transition matrix $\Phi(t_0, t_0) = I$ is set.
3. Loop over all observation times i of one arc
   - The reference orbit and the state transition matrix are integrated for the current time point of the observations i. Thus the integrator needs to be supplied with

$$\begin{bmatrix} \dot{\vec{r}}_A & \ddot{\vec{r}}_A & \dot{\vec{r}}_B & \ddot{\vec{r}}_B & \vec{\Phi} \end{bmatrix}^T. \quad (4.93)$$

- Therefore, the accelerations $\ddot{\vec{r}}_A$ and $\ddot{\vec{r}}_B$ are calculated and $A(t)$ needs to be build do compute $\dot{\Phi}(t, t_0)$ (Eq. 4.12).
- All partials of $A(t)$ are build on the reference orbit (see Sec. 4.3.14) not the 3d-position observations are used for that!
- The star camera quaternions from SCA data are used to build the transformation matrix T_{i2b}, which is subsequently used to generate the ACC calibration partials (Eq. 4.77) and to compute the non-gravitational accelerations.
- With the integration results, the observation deviation $\vec{y}_i$ is computed on the reference orbit with the function G (Eq. 4.81 - 4.83)

$$\vec{y}_i = \vec{Y}_i - G(\vec{X}_i^*, t_i). \tag{4.94}$$

- Finally, the p rows of the design matrix H_i with the processed observations of time point i are assembled by (cf. Eq. 4.14)

$$H_i = \widetilde{H}_i \Phi. \tag{4.95}$$

- The design matrix is partitioned and saved for local and global parameters $(H_x)_v$ and $(H_c)_v$, for each observation group v.
- Time points i with no observation data are simply skipped.
- After all time points i of the arc are processed, the partitioned normal matrices for each observation group v are build (Eq. 4.41): $(M_{xx})_v$, $(M_{cc})_v$, $(M_{xc})_v$, $(\vec{m}_x)_v$ and $(\vec{m}_c)_v$. As discussed in Section 4.3.8 and 4.3.7, the trade-off between computation time and memory consumption at which stage the normal matrices are build is usually set to the end of the arc. This works well for the used shorter arc length and gravity fields up to d/o 100. An implementation where the matrices are build after a certain amount of observations are processed can be utilized, as well.
- If the residuals $(\hat{\vec{\epsilon}})_k$ (Eq. 4.51) should be computed, the design matrices $(H_x)_v$ and $(H_c)_v$ must be saved.

4. Solving for the parameters $(\hat{\vec{x}})_k$ and $\hat{\vec{c}}$

- The previous step (3.) is done for all arcs (in parallel). Arcs that are discarded from the pre-processing are simply skipped.
- The normal matrices form all arcs are combined to compute the global solution. If a constant weighting is used, the global parameters $\hat{\vec{c}}$ follow from either of the Equations (4.58) or (4.60).
- With $\hat{\vec{c}}$ determined, the local parameters $(\hat{\vec{x}})_k$ can be computed for each arc k with Equation (4.57). As discussed in Section 4.3.7, the system is solved using MATLAB's solver.
- If VCE is used, the two previous steps are iterated, starting with the initial, or last weighting. The standard deviation $\hat{\sigma}_v^2$ of each group is determined by Equation 4.54 and 4.55, where $\hat{\vec{\epsilon}}_v^T (\bar{W})_v \hat{\vec{\epsilon}}_v$ is build according to Equation (4.65) with the determined local and global parameters $(\hat{\vec{x}})_k$, $\hat{\vec{c}}$. Usually two VCE iterations are sufficient. However, the influence of the VCE iterations on the overall computation time is marginal.

- The residuals $\hat{\vec{\epsilon}}_k$ may be computed with the design matrices $(H_x)_v$ and $(H_c)_v$ and estimated parameters $(\hat{\vec{x}})_k$ and $\hat{\vec{c}}$ according to Equation (4.51).
- The observation deviations $\vec{y}$ may be saved (see Sec. 4.3.4). They are computed from the reference orbit, which was integrated with the parameters from the previous iteration. For the actual deviations, the reference orbit would need to be integrated again with the determined parameters. This is done in the next iteration anyway, and thus the deviations are saved then and are always "delayed" by one iteration.

5. Iteration: The steps (3.) and (4.) are iterated until convergence or an accepted tolerance is achieved
   - Remember, the estimated parameter $(\hat{\vec{x}})_k$ and $\hat{\vec{c}}$ from the previous step are just the deviations between the true and the reference values (Eq. 4.3). The estimated local parameter $(\hat{\vec{X}}_0^*)_k$ need to be computed by

     $$(\hat{\vec{X}}_0^*)_k = (\vec{X}_0^*)_k + (\hat{\vec{x}})_k, \tag{4.96}$$

     and the global gravity field coefficients

     $$\hat{\vec{K}}_{nm}^* = \vec{K}_{nm}^* + \hat{\vec{c}}. \tag{4.97}$$

   - The estimated parameters $(\hat{\vec{X}}_0^*)_k$ and $\hat{\vec{K}}_{nm}^*$ are set as initial conditions and model parameters for the next iteration to integrate the reference orbit.
6. End
   - If the observation deviations should be computed, the reference orbit is integrated one last time with the last estimated parameters $(\hat{\vec{X}}_0^*)_k$, $\hat{\vec{K}}_{nm}^*$ to compute $\vec{y}$ (the state transition matrix Φ does not need to be integrated).
   - If desired, the position overlap of consecutive arcs can be computed. Therefore the last integration for the computation of the deviations is extended for one more time step and thus overlapping with the next arc.
   - All desired results are saved.

SIMULATION ENVIRONMENT BACKGROUND

5

The accurate simulation of satellite orbits is fundamental for Precise Orbit Determination (POD) and Gravity Field Recovery (GFR). Dynamic POD and GFR fits a model with certain parameters to the measured observations. Therefore the overall quality of the results is determined to a large extend by the model's quality and its numeric propagation. The computation of the reference orbit is the basis for the whole estimation process (cf. Ch. 4).

In contrast to the modeling of gravitational accelerations, shown in detail in Chapter 2.3, the non-gravitational accelerations are much smaller, but crucial for resolving the higher harmonics of the gravitational field and hence the hydrological signal measured by GRACE observations. Thus in this chapter the approaches and models for non-gravitational accelerations are presented. The models are validated in detail in Chapter 6.1 for the GRACE satellites.

No analytic solution for the the equations of motion exist when going beyond the Keplerian two-body problem. Thus a numeric propagation is needed. With the increasing accuracy of the measurement devices and sensors, the demands on the numerical precision for POD and GFR increases, as well. Mainly two numerical integration methods were adapted within the scope of this thesis. The validation concerning accuracy and efficiency are conducted for the simple Keplerian case with an analytical solution as reference and for more realistic cases with a spherical harmonic gravitational model. In both cases an arbitrary precision arithmetic, exceeding the precision limitation of the usually used *double* data type, is investigated and utilized as reference.

5.1 Non-Gravitational Force Models

The precise modeling and knowledge of non-gravitational forces acting on satellites is of high interest for gravimetry and many other missions and scientific tasks.

Detailed knowledge or force models are a prerequisite for accurate orbit propagation and orbit determination. Dynamic POD techniques to obtain the most accurate satellite orbits rely on the quality of the utilized force models or measured forces. Therefore the knowledge of the non-gravitational forces, and thus sophisticated models, are of high importance for a variety of tasks related to accurate measurements from satellites. Examples are GNSS, satellite altimetry, surveying and satellite gravimetry, where accurate positions of satellites are required.

Dedicated gravimetry missions like GRACE carry accelerometers to measure the non-gravitational accelerations acting on the satellite, thus the modeling is not of the highest priority for these missions. Nevertheless, the accelerometer measurement is not absolute. All accelerometer measurements need to be calibrated. Bias, drift and scale factors have to be regularly estimated. Thus a modeled reference is of interest. With

regard to GRACE-FO where the accelerometer on one satellite suffered a malfunction this is even more true.

Nevertheless, the number of satellite missions equipped with accelerometers can be counted on the fingers of one hand. Satellites equipped with GNSS receivers to deliver valuable measurements for gravimetric science are numerous. With the right approach to do deal with the non-gravitational forces this offers potential for much broader gravimetric research eg. Weigelt et al. (2013).

For this thesis and the analysis of the influence of different sensors by full simulation it is necessary to have sophisticated models for the non-gravitational forces to generate realistic simulated accelerometer data.

Non-gravitational forces summarizes all forces acting on a satellite not related to gravitation. For satellites and other objects in space mainly three kind of forces may be considered: Radiative forces, drag forces due to residual atmosphere and magnetic forces due to interaction of magnetic/electric devices with Earth's magnetic field. Usually, for satellites, the last category can be neglected.

In this thesis the following radiative forces are considered: Solar Radiation Pressure (SRP), albedo radiation from the Earth (ALB), Infrared Radiation from the Earth (IR) and Thermal Radiation Pressure (TRP) from the satellite itself. SRP is the force due to the direct radiation from the Sun. ALB is the force due to radiation from the Sun, that is reflected by the Earth. Furthermore the Earth surface and atmosphere is radiating itself in the infrared spectrum, referred to as thermal radiation, being the origin of the IR force. The effect of irradiation is twofold. The direct radiation (SRP, ALB and IR) exerts direct forces and torques on a satellite. The secondary effect is a thermal heating of the satellite surfaces due to the absorbed radiation. This results in a thermal radiation from those surfaces, according to the Stefan-Boltzmann law. This force is called TRP.

The atmosphere of the Earth is not vanishing at a certain altitude but its density is slowly diluting while its composition is changing. Therefore also satellites in in an 1000 km orbit are decelerated by atmospheric drag. The lower the orbit is, the higher is the density and hence the drag force. The composition and density of the Thermosphere is highly variable and changing with the Sun radiation. The Sun activity has an immense influence on the Thermosphere (see eg. Fig. 3.1 in Chapter 3).

The magnitude of all these forces is dependent on the satellite's shape, surfaces, its properties with respect to radiation of different wavelength and interaction with the rarefied atmospheric particles and of cause on its position and attitude. Therefore the non-gravitational forces are also called surface forces. In contrast to the gravitational forces they are referred to as non-conservative forces, as well.

The models used in this thesis are based on the HPS simulation software, developed at ZARM since 2002 (Theil, 2002; Bremer et al., 2013). Now it is a cooperation between ZARM and the DLR Institute of Space Systems, Bremen. The sophisticated FEM approach including a shadowing algorithm for SRP and TRP was developed in this framework by Rievers and Lämmerzahl (2011); Rievers et al. (2012); List et al. (2015); Bremer (2018). In the course of this thesis and within the CRC geo-Q, the HPS software was fundamentally revised under the Name XHPS (Wöske et al., 2016, 2019). Models for ALB and IR were developed in the same framework and the TRP modeling (Rievers et al., 2016) was extended with all radiation sources and for conductive and transient temperature calculation for the GRACE satellites (Wöske et al., 2019).

5.1.1 Modeling Approach: Finite Elements and Pre-Processing

A sophisticated model for non-gravitational forces needs to consider the geometry of the satellite and orientation of each surface. Therefore state-of-the-art models utilize a Finite Element Model (FEM) of a satellite to compute non-gravitational forces. Shadowing of surfaces by others can make it necessary to use fine FE models of a satellite.

The general principle is that all forces are calculated for each element of the FEM and are summed subsequently. Therefore for each element all necessary properties need to be assigned and stored. These are orientation and position of each element. A satellite fixed frame is used for that, referred to as the mechanical frame. That frame is usually used to build the FEM, and does not necessarily coincide with the Center of Mass (CoM) of the satellite. Furthermore the nodes of each element need to be stored to keep track which elements adjoin each other. This is of importance for the shadowing computation. For the radiative interaction optical properties of each element need to be assigned, as well. The algorithm considers the well known effects of absorption, emission, specular and diffuse reflection (eg. Knocke et al., 1988; Rievers et al., 2012).

Detailed FEMs may contain some thousand elements for accurate geometry and shadowing conditions. In an integration loop, where the non-gravitational models are called at least every integration step, this is computationally not acceptable. The workaround is a pre-processing of normalized force and torque coefficient look-up tables for a grid of specified incident perturbation directions. the normalized coefficient contain all information on the satellite's geometry, and material properties, which are not dependent on the actual satellite's position, attitude or incoming radiation. The enormous potential of that is demonstrated in the next subsections in the equations of the models. Perturbation directions may be the Sun for SRP, or a cell on the Earth for ALB. When calling the force model with a given incident disturbance direction, e.g. the Sun direction, the values are interpolated in the look-up tables. Once the look-up tables are computed for one satellite, this approach allows fast computation of very complex satellite and perturbation models independent of the level of detail of the satellite FEM.

The incident disturbance direction is described in polar coordinates in a satellite body frame with polar angle θ reaching from 0 to π and azimuth angle ϕ from 0 to 2π. This is demonstrated in Figure 5.1 for an exemplary GRACE satellite. The unit vector of the incident direction in satellite body frame $\vec{e}_{inc}$ is given by

$$\vec{e}_{inc} = [\sin(\theta)\cos(\phi), \sin(\theta)\sin(\phi), \cos(\theta)]^T. \tag{5.1}$$

In the pre-processing the incident direction $\vec{e}_{inc}$ is rotated around the satellite in arbitrary, discrete steps of the angles θ and ϕ.

The optical properties of the surfaces, namely absorption coefficient α, specular reflection coefficient γ_s, diffuse reflection coefficient γ_d and emissivity ε are in general dependent on the wavelength. Usually they are averaged over different ranges or assumed to be constant over a range. Commonly material properties are given for visible light and infrared (eg. for GRACE in Bettadpur, 2012b). Therefore the look-up tables for IR radiation are in general different from the ones used for SRP and ALB.

Nevertheless, the following applies for coefficients of the same wavelength for a non-transparent surface:

$$\alpha + \gamma_s + \gamma_d = 1 \tag{5.2}$$

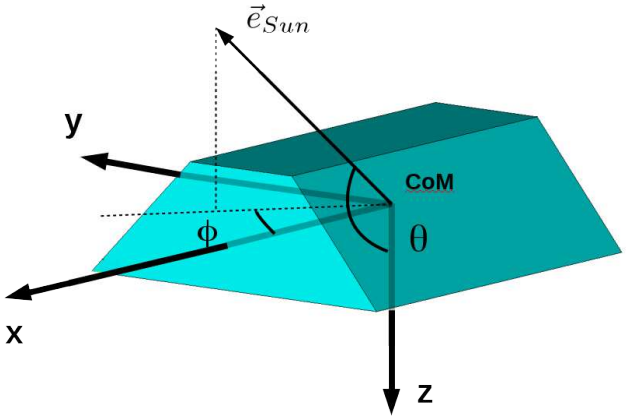

Figure 5.1: Definition of polar and azimuth angles θ, ϕ for an exemplary incident direction of the Sun $\vec{e}_{Sun}$ in a satellites fixed body frame.

and from Kirchhoff's law of thermal radiation

$$\alpha = \varepsilon. \tag{5.3}$$

For the second equation it is important to be aware of, that the absorption is usually at a different wavelength than the emission and thus the coefficients are not equal.

5.1.2 Solar Radiation Pressure (SRP)

SRP is the force due to the impulse of the Sun's light. The resulting force of the light can be computed with the speed of light c and the incoming radiation power or the flux. Here the incoming radiation flux is referred to as q_{in}. In this context the term "flux" is used as a flux density with the unit W/m^2 throughout this thesis.

For one element k with the area A_k and the optical properties α_k, $\gamma_{s,k}$, $\gamma_{d,k}$, the force is given by

$$\vec{F}_{SRP,k} = -\frac{q_{in}}{c}\, f_{shadow,k}\, A_k\, \vec{e}_{inc} \cdot \vec{e}_{N,k} \left[(\alpha_i + \gamma_{d,k})\vec{e}_{inc} + 2\left\{ \frac{\gamma_{d,k}}{3} + \gamma_{s,k}\, \vec{e}_{inc} \cdot \vec{e}_{N,k} \right\} \vec{e}_{N,k} \right]. \tag{5.4}$$

The $\cdot$ denotes the vector dot product and $\vec{e}_{N,k}$ is the unit normal vector of the element k expressed in the satellite body frame. The binary factor $f_{shadow,k}$ indicates if an element is shadowed by another one. A shadowed element is not further considered. The shadowing conditions are computed by employing the ray-tracing method. This is demonstrated in detail in Bremer et al. (2013); Bremer (2018).

In Equation (5.4) q_{in}/c is the only term that is not just dependent on satellite properties and the satellite's orientation (θ, ϕ). Therefore everything else can be evaluated in a pre-processing. From Equation (5.4) the total force is obtained by the sum over all elements k, disregarding the factor q_{in}/c we define

$$\vec{\Gamma}(\theta, \phi) = \sum_k -f_{shadow,k}\, A_k\, \vec{e}_{inc} \cdot \vec{e}_{N,k} \left[(\alpha_i + \gamma_{d,k})\vec{e}_{inc} + 2\left\{ \frac{\gamma_{d,k}}{3} + \gamma_{s,k}\, \vec{e}_{inc} \cdot \vec{e}_{N,k} \right\} \vec{e}_{N,k} \right]. \tag{5.5}$$

In the pre-processing $\vec{\Gamma}$ is evaluated for all desired irradiation directions $\vec{e}_{inc}$. Usually a resolution of some degrees for θ and ϕ is sufficient. The results are then saved for each body frame axis as two dimensional look-up table.

When the model is called for a given incident direction (θ and ϕ), q_{in}/c is multiplied after interpolation of $\vec{\Gamma}$ from the look-up tables, resulting in the actual force

$$\vec{F}_{SRP} = \frac{q_{in}}{c}\ \vec{\Gamma}(\theta, \phi). \tag{5.6}$$

The terms summarized in the lookup tables ($\vec{\Gamma}(\theta, \phi)$), are not unique for SRP, but for general incoming radiation. Therefore, the same look-up tables can be used for ALB radiation, as well. For IR the optical coefficients are different and the tables need to be recomputed.

For SRP q_{in} is the solar flux which is dependent on the satellite's and Sun's position. The solar flux at the distance of one astronomical unit (AU) is referred to as the solar constant $q_\odot$ with a value of about 1367 W/m^2. The solar constant is not completely constant but its fluctuation is less than 0.1%.

With the solar constant $q_\odot$ at the desired time and the Sun position $\vec{r}_{Sun}$, the incident flux at the satellite's position $\vec{r}_{sat}$ can be computed by

$$q_{in} = q_\odot \left(\frac{1\ AU}{|\vec{r}_{sat} - \vec{r}_{Sun}|} \right)^2. \tag{5.7}$$

5.1.3 Albedo and Infrared Radiation Pressure (ALB, IR)

Albedo radiation is Sun light that is reflected by the Earth. Different Earth surfaces, atmosphere conditions and clouds have a huge influence on the actual reflectivity.

Earth infrared radiation is based on the fact that each body with a temperature above 0 K radiates (Stefan-Boltzmann law). Thus, temperature of the Earth surface and the atmosphere are the driver of the IR force. As for ALB, IR is dependent on the actual surface and atmosphere conditions and hence hugely time dependent.

These two radiation forces are recently also referred to as Earth Radiation Pressure (ERP) (eg. Vielberg and Kusche, 2020).

To meet the high spatial differences and fast changing character of the ALB and IR origin, the developed model is based on data from CERES (Clouds and the Earth's Radiant Energy System) (Wielicki et al., 1996; Loeb et al., 2018). The CERES project deals with the Earth radiation budget. The various CERES data products are based on measurements from several instruments on Earth observation satellites along with many other data.

Here the SYN1deg data product (Doelling et al., 2016) is used, which among others, provides Earth reflectivity or albedo and long wave flux radiation data for an epoch starting in 2000 up to now. It has a spatial resolution of $1° \times 1°$ in longitude and latitude and a time resolution from hourly to monthly. All data are top of atmosphere (TOA) values, meaning that absorption through the atmosphere is already included in the data. For the most exact results the hourly data are used (cf. Sec. 6.1.4).

Exemplary for May 1st 2006 hourly CERES SYN1deg data for reflectivity and long wave flux are shown in the Figures 5.2 and 5.3 for four times of that day. In the reflectivity plots the eclipse is distinctly visible because no data are available if no incoming light from the Sun is present. Clouds, snow and ice have the highest reflectivity, while the reflectivity of the ocean and land surface is rather small. Thus cloud coverage

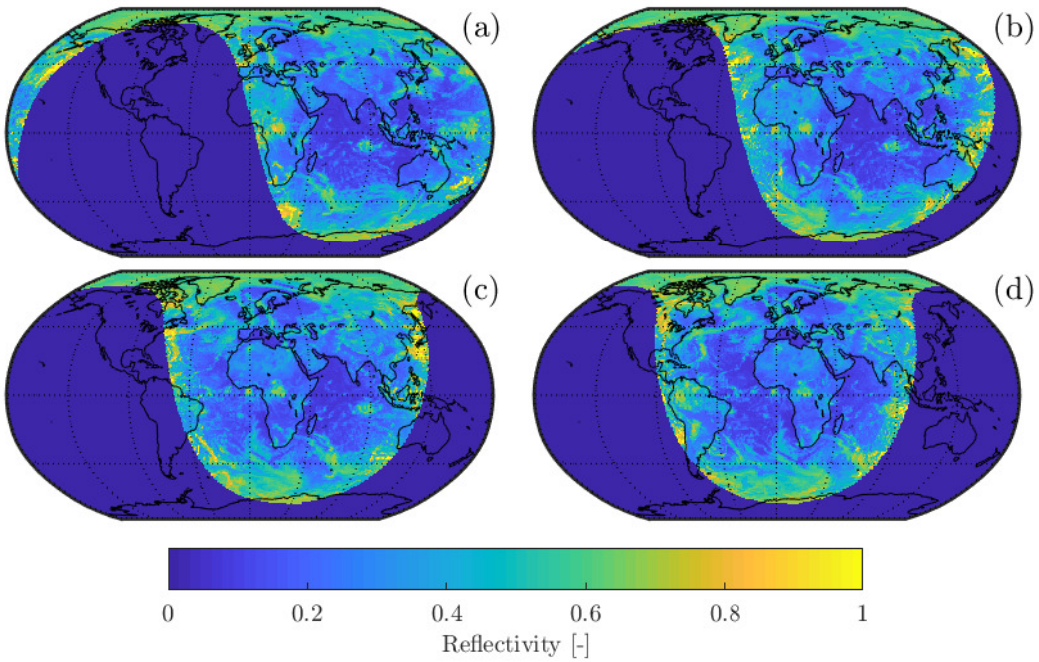

Figure 5.2: CERES SYN1deg (TOA) hourly reflectivity or albedo data from May 1st 2006 for four times a) 06:00-07:00 b) 08:00-09:00 c) 11:00-12:00 d) 14:00-15:00 (GMT).

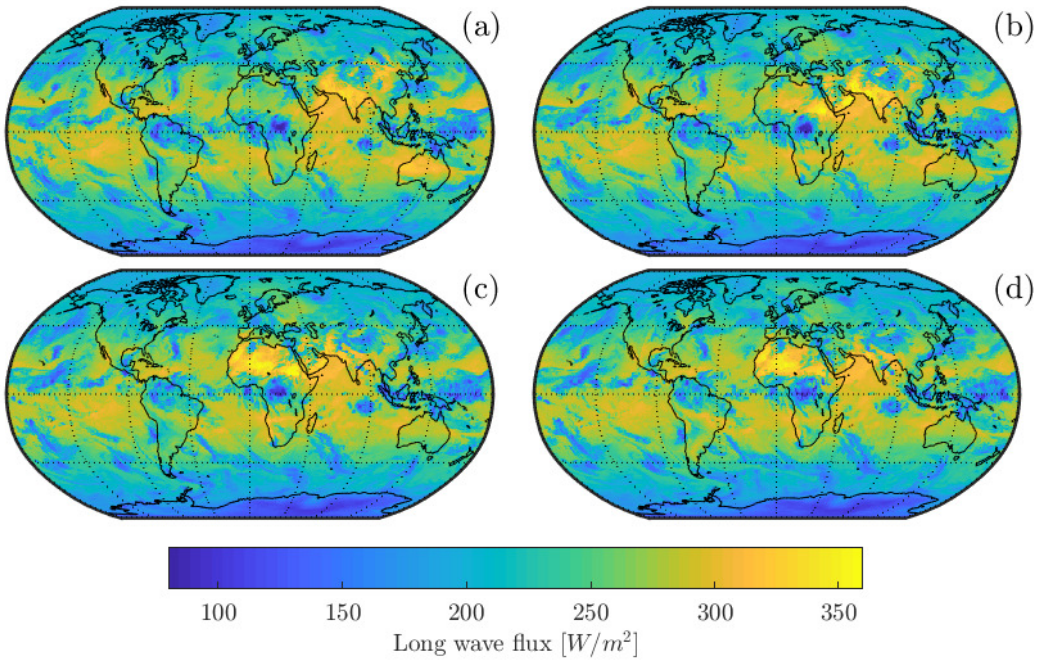

Figure 5.3: CERES SYN1deg (TOA) hourly long wave flux radiation data from May 1st 2006 for four times a) 06:00-07:00 b) 08:00-09:00 c) 11:00-12:00 d) 14:00-15:00 (GMT).

can be well distinguished. The reflectivity of snow and ice is between 0.9 and 1. Due to the fact that the shown data are TOA values, it is much lower. The loss due to absorption in the atmosphere is about 35%.

In the long wave flux data the eclipse dependency is not that prominent. Nevertheless, the hottest spot is moving with the Sun's zenith from 06:00 to 15:00 GMT from India over the Sahara region in the plots. Identified cloud formations from the refelctivity data can be recognized here again by a lower flux due to the shielding effect of the clouds and a low emission by the cold clouds itself. During the northern summer months, the South Pole is not illuminated by the Sun an thus colder than the North Pole, resulting in a lower radiation.

Unlike SRP, where the source of radiation can be assumed as a point because the Sun is so far away and has a comparably homogeneous spatial radiation, for ALB and IR radiation from all surface area of the Earth, that is in the field of view (FOV) of the satellite, has to be considered as an own radiation source. Therefore the Earth is gridded in cells with the indices ij. The resolution for that grid is inherited from the available CERES data resolution. Based on the Lambertian cosine-law, for ALB and IR a diffuse reflectance of an Earth cell into the hemisphere is assumed like in Knocke et al. (1988). This is in general a good assumption. The only study modeling ERP using different angle dependent models for several surfaces of the Earth is from Vielberg and Kusche (2020). Nevertheless, the models introduced here show a better agreement with GRACE accelerometer measurements for tests using the same methodology as in Wöske et al. (2019).

Each cell is assigned an area A_{ij}, a reflectivity ρ_{ij}, and an outgoing IR flux $q_{IR,ij}$. The forces and torques resulting from each cell in the satellites FOV are computed separately and subsequently summed up. With the radiated power $q_{in,ij}$ from cell ij reaching the satellite, the force and torque due to the radiation from each cell can be computed as for SRP with the pre-computed look-up tables because all physical processes are the same as in Equation (5.4) just with a different q_{in}. Thus the force can be written with $\vec{\Gamma}$ from Equation (5.6)

$$\vec{F}_{ALB,IR} = \sum_{ij \in FOV} \frac{q_{in,ij}}{c} \; \vec{\Gamma}(\theta_{ij}, \phi_{ij}). \tag{5.8}$$

The angles θ_{ij} and ϕ_{ij} in the satellite fixed frame (Fig. 5.1) follow from the incident direction $\vec{r}_{ij} - \vec{r}_{sat}$.

The geometrical conditions and components for the models are sketched in Figure 5.4. All measures of angles and distances are taken from the cell's geometrical center. The vectors $\vec{r}_{sat}$ and $\vec{r}_{ij}$ describe the satellite's and the ij cell's position, in the Earth fixed frame, respectively. $\Phi_{out,ij}$ is the angle under which the cell ij sees the satellite from its normal vector and $\Phi_{in,ij}$ the angle under which the Sun light hits the cell. Both angles can be determined with the definition of the vector dot product:

$$\Phi_{out,ij} = \arccos\left(\frac{\vec{r}_{ij} \cdot (\vec{r}_{ij} - \vec{r}_{sat})}{|\vec{r}_{ij}|\,|\vec{r}_{ij} - \vec{r}_{sat}|}\right), \tag{5.9}$$

$$\Phi_{in,ij} = \arccos\left(\frac{\vec{r}_{ij} \cdot \vec{r}_{Sun}}{|\vec{r}_{ij}|\,|\vec{r}_{Sun}|}\right). \tag{5.10}$$

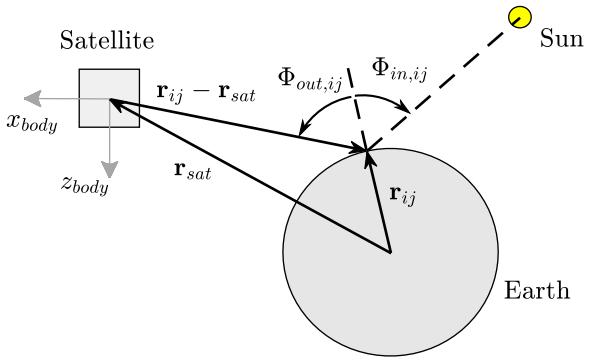

Figure 5.4: Sketch of geometrical conditions for ALB and IR model

Defining the outgoing power radiated from the cell ij by P_{ij}. Then the incoming flux at the satellite's position $q_{in,ij}$ from cell ij can be calculated by

$$q_{in,ij} = \frac{P_{ij}}{\pi \left|\vec{r}_{ij} - \vec{r}_{sat}\right|^2} \cos \Phi_{out,ij}. \tag{5.11}$$

The factor $1/\pi$ originates from the integration of the Lambertian cosine-law over the hemisphere (eg. Rievers et al., 2012), the flux decreases with the inverse square of the distance as in Equation (5.7). For ALB the power emitted by a cell P_{ij} depends on the reflectivity ρ_{ij} and the angle $\Phi_{in,ij}$ under which the Sun light hits the cell. It is calculated as

$$P_{ij,ALB} = q_{Sun,ij}\ A_{ij} \cos\left(\Phi_{in,ij}\right)\ \rho_{ij}, \tag{5.12}$$

where $q_{Sun,ij}$ is the solar flux at the position of the cell ij, or simply at the position of the Earth. It is obtained from Equation (5.7) with $\vec{r}_{sat} = \vec{r}_{Earth}$. The reflectivity ρ_{ij} is used from the CERES data.

For IR, the radiation power $P_{ij,IR}$ is directly taken from the CERES data and therefore just has to be multiplied by the cell area:

$$P_{ij,IR} = A_{ij}\ q_{CERES_{IR,ij}}. \tag{5.13}$$

As mentioned before, the satellites optical material properties are dependent on the wavelength, thus $\vec{\Gamma}(\theta, \phi)$ is usually different for ALB and IR.

5.1.4 Thermal Radiation Pressure (TRP)

TRP is the force from the satellite's radiation due to its surface temperature, according to the Stefan-Boltzmann law. Thus, for the computation of TRP the temperature of the satellite surfaces needs to be known. For the TRP model again diffuse radiation from satellite surfaces according to the Lambertian cosine law is assumed. The force is calculated for each FEM element k. With the temperature T_k of the surface element k and the emissivity ε_k, the force due to one element is

$$\vec{F}_{trp,k} = -\frac{2}{3}\frac{A_k\ \varepsilon_k\ \sigma}{c} T_k^4\ \vec{e}_{N,k}. \tag{5.14}$$

The constant σ is the Stefan-Boltzmann number. The factor 2/3 results from the integration of the cosine law over the hemisphere when considering just orthogonal

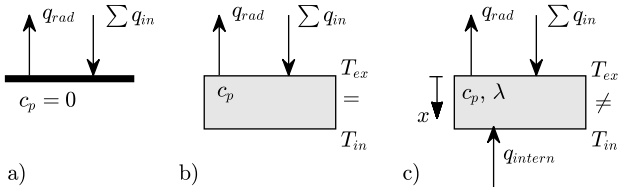

Figure 5.5: Sketch of conditions and assumptions for the three implemented temperature models: a) static, b) transient, c) transient plus heat conduction, with internal and external temperatures T_{in} and T_{ex}

components (all other directions balance out, eg. Rievers et al. (2012)). The total TRP force follows again by the summation over all elements k.

To evaluate Equation (5.14) the surface temperature T_k has to be calculated. For a temperature analysis all incoming and outgoing power needs to be determined. Incoming radiation sources are the same as for the non-gravitational forces: Sun light, albedo and Earth infrared radiation. The absorbed flux of each satellite element $q_{abs,k}$ depends on the angle of the element with respect to the incident radiation direction and the absorptivity α_k of the element. The absorbed flux due to one source can be computed from the incident radiation flux q_{in} and its direction $\vec{e}_{inc}$ as follows:

$$q_{abs,k} = \alpha_k \; f_{shadow,k} \; \vec{e}_{inc} \cdot \vec{e}_{N,k} \; q_{in} = \Lambda_k \cdot q_{in}. \tag{5.15}$$

As for SRP, all factors but q_{in} are just satellite properties and geometry. Thus the same method with pre-computed look-up tables is applied here, again. The satellite's properties are summarized in the look-up table $\Lambda(k, \theta, \phi)$:

$$q_{abs,k} = \Lambda(k, \theta, \phi) \cdot q_{in}. \tag{5.16}$$

Here the look-up table Λ is three dimensional. In contrast to the normalized force coefficients $\vec{\Gamma}(\theta, \phi)$, a value for each element is needed, and not a summed value as for the force.

The absorbed flux $q_{abs,k}$ needs to be computed for each radiation source and then summed up. For albedo and Earth infrared, radiation sources are again all surface cells on Earth in the FOV of the satellite, therefore the computation is much more intensive than for Sun light.

Additionally to the absorbed flux, an internal heat production $q_{intern,k}$ may be considered for the elements k, as well. This may be of interest if considerable heat is produced and especially if it is not equally distributed over the satellite surfaces and thus the resulting forces do not balance out.

Three different methods (or assumptions) to compute the surface temperatures T_k are implemented: a) static, b) transient, c) transient plus heat conduction. The conditions and assumptions for the three different models are sketched in Figure 5.5 and described in the following paragraphs. In all cases no conduction between elements is assumed. Each model is a simplification of a complete temperature analysis. A full transient and conductive FE analysis every simulation time step would be very slow and is not realistic for orbit propagation.

a) Static temperature model (*stat*)

The most straightforward way to compute the surface temperature is to assume instantaneous heating/ cooling and no heat conduction between and through elements. Then

the absorbed incoming radiation flux $q_{abs,k}$ is equal to the thermally radiated flux $q_{rad,k}$ and the temperature T_k can be directly calculated using Stefan-Boltzmann's law

$$T_k = \left(\frac{q_{abs,k}}{\varepsilon_k \ \sigma} \right)^{\frac{1}{4}}, \tag{5.17}$$

with the Stefan–Boltzmann constant σ.

This case can also be directly considered in the computation of the SRP, ALB and IR forces (Eq. 5.4) and included in the look-up tables. This is possible, because every incoming radiation directly results in a re-radiation depending only on the absorptiveity α_k and emissivity ε_k. This is for example commonly done by Montenbruck et al. (2015).

b) Transient temperature model (*trans*)

A more realistic model, especially for low Earth orbits with fast changing illumination conditions and eclipses, is to consider transient heating and cooling of surface walls. When again omitting heat conduction, the governing equation for the temperature is:

$$c_{p,k} \ \rho_k \ h_k \ \frac{\partial T_k}{\partial t} = q_{abs,k} - \varepsilon_k \sigma T_k^4, \tag{5.18}$$

with heat capacity $c_{p,k}$, density ρ_k, and a thermal thickness h_k of the satellite element k and the time t. Thus it is assumed that a thin surface is heated equally over its thickness. This ordinary differential equation is solved numerically for every FE during the satellite orbit propagation.

c) Transient plus heat conduction (*pde*)

An even more sophisticated model is to additionally consider a heat conduction through the satellite walls and a resulting temperature distribution over the surface thickness x_k. As in the two other models no conduction between elements is assumed. This approach leads to the following Partial Differential Equation (PDE)

$$c_{p,k} \ \rho_k \ \frac{\partial T_k}{\partial t} = \lambda_k \frac{\partial^2 T_k}{\partial x_k^2}. \tag{5.19}$$

Here, the radiated and absorbed fluxes at the outer surface $q_{abs,k} - \varepsilon_k \sigma T_{k,x=0}^4$ have to be implemented as additional boundary condition of the PDE. On the other (inner) side of the surfaces, an internal heat production $q_{intern,k}$ can be considered as boundary condition, as well. For example dissipated energy from the satellite which is usually radiated through radiator surfaces by the thermal management system of a satellite. Solving this equation inside an orbit propagation is more difficult, but may be shifted to a post processing step, especially when evaluating sampled satellite data. This is usually the case when this small differences of non-gravitational forces are of interest like for POD, GFR or density recovery applications.

5.1.5 Eclipse Model

For the radiative non-gravitational force models, an eclipse model is important. The central body, eg. the Earth, is able to shadow an orbiting satellite from the Sun. These phases are referred to as eclipses. During the eclipse, the satellite does not experience solar radiation. The different possible shadow forms are shown in Figure 5.6.

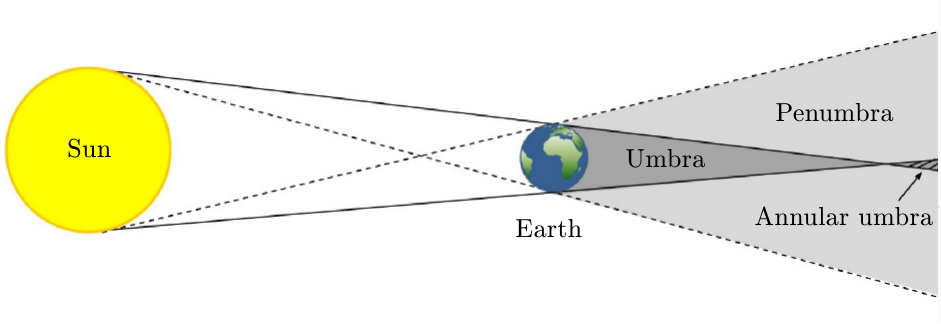

Figure 5.6: Sketch of different eclipse conditions, after Bremer (2018)

The implemented model, after Wertz (1978), p. 71 ff., considers the four different shadow forms and the transition between them. The result of the model is a scale factor between 1 and 0 scaling the incoming solar radiation q_{in} or $q_{\odot}$ based on the eclipse condition.

In this model Earth and Sun are considered as perfect spheres. Slightly more realistic models consider the oblateness of the Earth and furthermore absorption, scattering and refraction of the Sunlight in the atmosphere (Robertson, 2015). This slightly changes the values in the very short transition times between full sunlit, penumbra and umbra.

5.1.6 Atmospheric Drag

The force due to the rarefied residual atmosphere is usually the non-gravitational force affecting LEO satellites' orbits the most. The higher the orbit, the smaller the drag force, and hence SRP gets the dominating non-gravitational force. Nevertheless, compared to the radiative forces, atmospheric drag is mainly acting always in the same direction (along-track) and hence orbit changes are more sensitive to it. The interaction of the rarefied gas with very high energy in the Troposphere can not be described with continuous fluid dynamics as for instance airplanes.

Nevertheless, the general approach is quite similar to the one known from aerodynamics. The drag force is commonly modeled with a dimensionless force coefficient C_D and a quadratic dependency of the relative velocity $\vec{v}_{inc}$. The drag force $\vec{F}_D$ in the direction opposite to the incident particle flow can be written as

$$\vec{F}_D = -\frac{1}{2}\rho \; A \; C_D \; |\vec{v}_{inc}| \; \vec{v}_{inc}, \tag{5.20}$$

where A is the reference area of the satellite and ρ the local air density. The atmospheric drag model used throughout this thesis is a basic one. No lift component and cross-component orthogonal to the relative particle velocity are considered. For the GRACE satellite geometry and an attitude with an angle of attack of less than 2° this assumption is not too bad.

For the drag coefficient C_D a constant value is used. During the analysis it was determined eg. with the GRACE accelerometer data in Wöske et al. (2019) for different epochs of the GRACE mission. The resulting values between 2.1 and 2.4 are typical values used for convex-shaped LEO satellites (Montenbruck and Gill, 2005).

Nevertheless a much more complete approach is to model the drag and lift coefficients with physical models of the particle interaction, like it is especially done by Sentman (1961); Doornbos (2011); Doornbos et al. (2010) or Kato et al. (2016).

As reference area A, the projected area of the satellite FE model with respect to the incident velocity is used. This area is pre-computed and saved in a look-up table, as well. The relative velocity can be either computed with the assumption of an atmosphere that is rotating with the Earth, or by utilizing a thermospheric wind model. For the first case the velocity is

$$\vec{v}_{inc} = \vec{v}_{sat} - \omega_E \times \vec{r}_{sat}, \tag{5.21}$$

with the angular velocity of the Earth ω_E. Tests with the horizontal wind model HWM93 did not show very big differences of the force compared to the more simple approach. Thermospheric wind modeling is a complex topic on its own with many dependencies and of actual interest, also with respect to non-gravitational force modeling (eg. Visser et al., 2019; Vielberg and Kusche, 2020).

The atmospheric density is computed utilizing the JB2008 atmosphere model (Bowman et al., 2008).

5.2 Numerical Integration

Most numerical integration methods are designed to solve a system of first order Ordinary Differential Equations (ODE) of the form

$$\frac{d\vec{x}}{dt} = \dot{\vec{x}} = \vec{f}(t, \vec{x}). \tag{5.22}$$

The vector $\vec{x}$, containing all variables of the system, is commonly referred to as the state vector. The state vector may be of arbitrary dimension. The vector-valued function $\vec{f}$, the so called right-hand-side (RHS) function, may be an arbitrary function of the state variables but not of its derivatives. The order l of an ODE is defined by its highest derivative. An ODE of order l can always be reduced to a system of l first order differential equations by defining additional state variables. To obtain an explicit solution, an initial condition $\vec{x}_0$ at a specific time t_0 has to be known.

Numerical integration of ODE systems is a field of research with long history. The common Runge-Kutta (RK) method dates back to the beginning of the 20^{th} century. Thus, classical methods benefit from extensive research. For orbit propagation in space flight mechanics three classic methods are commonly used: 1. Runge-Kutta, 2. Multistep, and 3. Extrapolation methods. More recent developments also suggest symplectic (Aristoff and Poore, 2012) and implicit (Jones and Anderson, 2012) integration methods. Symplectic integration methods conserve the Hamiltonian, therefore work well with conservative forces. Although it is possible to incorporate non-conservative forces, (Mikkola, 1998) symplectic integration is not recommended when dealing with complex force models in LEOs (Jones and Anderson, 2012).

For the scope of complex time dependent force models for LEOs with coupled translational and rotational dynamics and the integration of the state transition matrix, the Adams-Bashforth-Moulton (ABM) multistep integrator (Shampine and Gordon, 1975) and two RK methods are implemented and investigated concerning their accuracy and efficiency.

5.2.1 Runge-Kutta Methods

Explicit RK methods are probably the most commonly used methods because of their simplicity and flexibility for a wide range of applications. State-of-the-art RK integrators utilize a local error control to adjust the step size automatically. Nevertheless, RK methods need much more function elevations, compared to multistep methods, which makes them less efficient if the evaluation of the force model (i.e. the RHS function) is computationally expensive.

RK schemes are explicit single-step methods. This means that the solution $\vec{x}_{n+1}$ at the time t_{n+1} can be successively determined from a previous condition $\vec{x}_n$ at time t_n. With the step size h defined as $h = t_{n+1} - t_n$. A s-stage RK scheme with s subsequent stages can be written as

$$\vec{k}_i = \vec{f}(t_n + h\,c_i,\ \vec{x}_n + h\sum_{j=1}^{s} a_{ij}\,\vec{k}_j), \qquad (i = 1, ..., s) \tag{5.23}$$

$$\vec{x}_{n+1} = \vec{x}_n + h\sum_{j=1}^{s} b_j\,\vec{k}_j. \tag{5.24}$$

The coefficients c_i, b_i and a_{ij} finally define a RK scheme. The coefficients are determined to minimize function evaluations s for a given order p. It is proven that for orders higher than four $s > p$, more precisely: $p = 5, 6$, $s \geq p + 1$, $p = 7$, $s \geq p + 2$, $p = 8$, $s \geq p + 3$ (often called Butcher barrier) Montenbruck and Gill (2005). The coefficients are typically expressed in a Butcher table

$$\begin{array}{c|c} \vec{c} & A_{s\times s} \\ \hline & \vec{b}^T \end{array}$$

Fehlberg (1968) established the so called embedded RK or Runge-Kutta-Fehlberg (RKF) methods, which use solutions of two different orders to determine a local truncation error between these two orders. A step size for the next step is determined regarding this error and a tolerance value. In the appropriate Butcher table an additional vector $\vec{b}$ is added for the calculation of the additional solution with a different order. Details are given in Kato and Wöske (2017).

Implemented Methods

Two different RK schemes are implemented and validated here. First, the popular Dormand-Prince8(7) scheme (Dormand and Prince, 1980; Prince and Dormand, 1981) (DoPri87), an 8th order scheme which needs 13 function evaluations of the RHS function and second, the Cash-Carp5(4) scheme (CK54)of 5th order with six function evaluations per step. Both methods are embedded schemes capable to compute a high order and a lower order solution for a local error estimation and subsequent step size control (the lower order is given in the brackets).

5.2.2 Multistep Methods

Multistep methods are known to be the most efficient integrators when the evaluation of the RHS function is computationally expensive, but reveal a lack of stability properties for high orders in combination with large step sizes and abruptly changes in the RHS

function. The most common and suggested methods are Adams-Bashforth-Moulton (ABM) (Shampine and Gordon, 1975) methods and the improved Störmer-Cowell (SC) method, the Gauss-Jackson (GJ) (Berry, 2004) method. SC or GJ methods directly integrate the second order differential equation of motion (cf. Eq. 2.6). The GJ integrator is often recommended as most effective multistep integration method when using fixed step sizes and non-velocity dependent forces (Montenbruck and Gill, 2005). Nevertheless, for the purpose of POD or GFR and coupled satellite translation and rotation, GJ methods lose their superiority because the corresponding ODE system is not completely of second order. Therefore the ABM multistep method is used.

The general idea of multistep methods is to gain a solution for a time point t_{n+1}, which is not only based on the last known time point t_n, but on a series of previous time points, called backpoints. This comes along with one disadvantage of these methods. To initiate this procedure, a number of previous points must be known. Thus, not only an initial condition is required, but several backpoints, depending on the methods order. This leads to the need of an initialization procedure, which is able to compute sufficient backpoints. These are usually generated by a single-step method like RK.

The principle of a multistep integrator is to interpolate the backpoints, which are the evaluations of the RHS function of previous time points, with a polynomial $\vec{p}$. The polynomial is evaluated at the desired time t_{n+1} and integrated analytically. Following Montenbruck and Gill (2005), p. 132 ff., integrating the ODE system (Eq. 5.22) from the last known time t_n to the new time t_{n+1} yields

$$\vec{x}(t_{n+1}) = \vec{x}(t_n) + \int_{t_n}^{t_{n+1}} \vec{f}(t, \vec{x}(t))\, dt \;\approx\; \vec{x}(t_n) + \int_{t_n}^{t_n+h} \vec{p}(t)\, dt, \tag{5.25}$$

where $\vec{f}(t, \vec{x}(t))$ is approximated by the polynomial $\vec{p}(t)$, which can be integrated analytically. Using Newtons formula to determine an interpolation polynomial $\vec{p}$ of order $m-1$ with m known function values $\vec{f}(t_{n-m+1}), ..., \vec{f}(t_n)$ leads to the so called Adams-Bashforth (AB) method of order m. Integrating the polynomial $\vec{p}$ to the desired next time t_{n+1}, the approximation of $\vec{f}(t_{n+1})$ is not expected to be very good because the time is outside of the known function values the polynomial has been determined with. To counteract this problem the Adams-Moulton (AM) method suggests, that the new value $\vec{f}(t_{n+1})$ is considered for the interpolation polynomial, as well. Since the polynomial depends on the desired, unknown function value $\vec{f}(t_{n+1})$, there is no explicit solution. This problem is circumvented by coupling the AB and AM method, resulting in the popular ABM approach.

The AB method provides an initial solution for $\vec{f}(t_{n+1})$ which is subsequently used in the AM scheme improving the a priori predicted value. Therefore ABM methods are also called predictor corrector methods. Various implementations are feasible. The corrector step may be repeated more often than one time, until the solution iteratively converges below a certain error threshold. This comes along with the cost of a recurrent evaluation of the RHS function for every iteration step. However, it is recommended to use just one corrector step (Montenbruck and Gill, 2005). Moreover, the order of the corrector step could be implemented to be equal to the predictor step or one order higher. With a local error estimate between predictor and corrector step, methods with adjustable step size are possible as for the RKF methods, eg. in the popular DEABM code (Shampine and Gordon, 1975), also used in MATLAB/Simulink as ode113. However, the realization is more complex due to the fact, that high order ABM methods tend to become unstable

with large step sizes. Therefore an efficient step size control needs to adjust the order and the step size simultaneously.

Implemented Method

The implemented ABM integrator resigns to use a step size control. The ABM method is implemented with one corrector step and an even order of predictor and corrector step. Thus it needs in total two evaluations of the RHS function each step. It is initialized with the DoPri87 RK method, computing the solution of the first $m-1$ steps, thus enough backpoints are available for the ABM method.

5.2.3 Validation

The beforehand introduced methods are investigated in terms of total accuracy and efficiency. By reducing the step size, even the simplest numerical integration may be quite accurate. For applications, efficiency, defined as time needed for a certain accuracy, is very important. It is here measured as total CPU time needed to integrate the test cases.

Besides the integration method, the accuracy of a solution is always limited by the used data type. The standard *double* data type is able to represent about 16 digits. Typical spatial dimensions for LEO satellites are about 10^7 to 10^8 m. Thus the total precision is definitely below 10^{-8} m. Using numerical integration, round-off and truncation errors sum up and the total precision can not be reached. This is demonstrated in this validation. Therefore the integrator is supplementary implemented with a multi-precision arithmetic, offering the possibility to use arbitrary digits for a variable. The GNU-MPFR library for C/C++ is used for that purpose (Fousse et al., 2007).

Three validation cases are defined:

- Keperian Case: The two body problem (cf. Eq. 2.15) is applied for a circular LEO orbit with an altitude of 400 km. It is propagated for about two orbits. The advantage of this scenario is that it can be solved analytically serving as true reference.
- Realistic Case 1: A static SH gravitational field model with d/o 120 is applied. A GRACE orbit with initial conditions from 2008-12-01 is propagated for about one day.
- Realistic Case 2: The previous case is extended by third body attraction of all Solar System planets and the Moon.

The advantage of the RK methods with a comparably high number of RHS function evaluations is a high step size. For a fair comparison, the resulting orbits are compared just every 100 seconds, in between the step size is automatically determined by the step size control. The mean step size is then used for comparisons.

To compare different integration methods and setups, it is helpful to define a scalar error between two solutions. Here a summed mean error E_m of the positions is defined as

$$E_m = \left|\left| \frac{1}{N} \sum_{i}^{N} \mid \vec{r}_{1,i} - \vec{r}_{2,i} \mid \right|\right|, \tag{5.26}$$

with the position vectors $\vec{r}_{1,i}$, $\vec{r}_{2,i}$ of two different solutions at the sampling point i and a total number of sampling points N.

The compared CPU times are always the total required simulation time and for ABM includes the initialization by the DoPri87 method. To avoid inconsistencies in the initial conditions for different ABM options, the local error tolerance of DoPri87 is set to high values for *double* and *mpreal*, respectively. The drawback of this is, that the initialization of the ABM method may have significant influence on the simulation CPU time, particularly for bigger step sizes.

All shown CPU times are based on computations with the same desktop PC, in particular with an Intel Core i5-4440 3,1 GHz processor.

5.2.4 Validation Against Analytic Keplerian Case

Using the analytic solution, the total error of each numerical integration can be compared using the mean error E_m.

Order of ABM Scheme

First the order of the ABM scheme is analyzed for the *mpreal* data type with 32 digits. The CPU time is plotted with the corresponding step size h over the summed mean error E_m for different orders (2, 4, 8, 12, 16, 18) in Figure 5.7. Different accuracies are obtained by varying the step size from 100 s to 0.5 s. Thus, each marker in the figure refers to one simulation.

With increasing order of the scheme, the solution reaches higher accuracies in shorter time. Pushing the order too high, while keeping the step size constant, makes the method unstable and it deviates completely. This can be observed for order 16 for step sizes $h > 5$ s, and for order 18 already for step sizes $h > 1$ s (both orders shown with dashed lines). At about $E_m = 10^{-23}$ m the maximal accuracy for all schemes is reached due to the restriction of the data type with 32 digits precision. Further reduction of the step sizes does not result in an increase of the accuracy. If using more digits, the accuracy limit is shifted to lower mean error values. In terms of efficiency and stability order 16 and 18 schemes are not superior to the order 12 scheme, using 32 digits precision for the Keplerian case.

The solutions with the biggest step sizes need more CPU time than the next one with a smaller step size (the curves for CPU time bend up mildly towards the right). This is due to the already mentioned initialization with the DoPri87 method, which is more time consuming for bigger step sizes of the ABM integrator.

The computational overhead using higher orders is very low. If the dynamic model is more complicated than for the simple Keplerian case it is completely nonrelevant. For step sizes beneath 100 s, there is no reason using lower orders than 8. Higher orders than 12 lack of stability properties, which even further increase with more complicated dynamic models. Therefore, in the following just the 8 and 12 order ABM schemes are considered.

ABM vs. RK Methods

The promising 8 and 12 order ABM schemes (ABM 8, ABM 12) are compared to the two RK schemes CK54 and DoPri87 for step sizes from 100 s to 0.1 s. In Figure 5.8 the

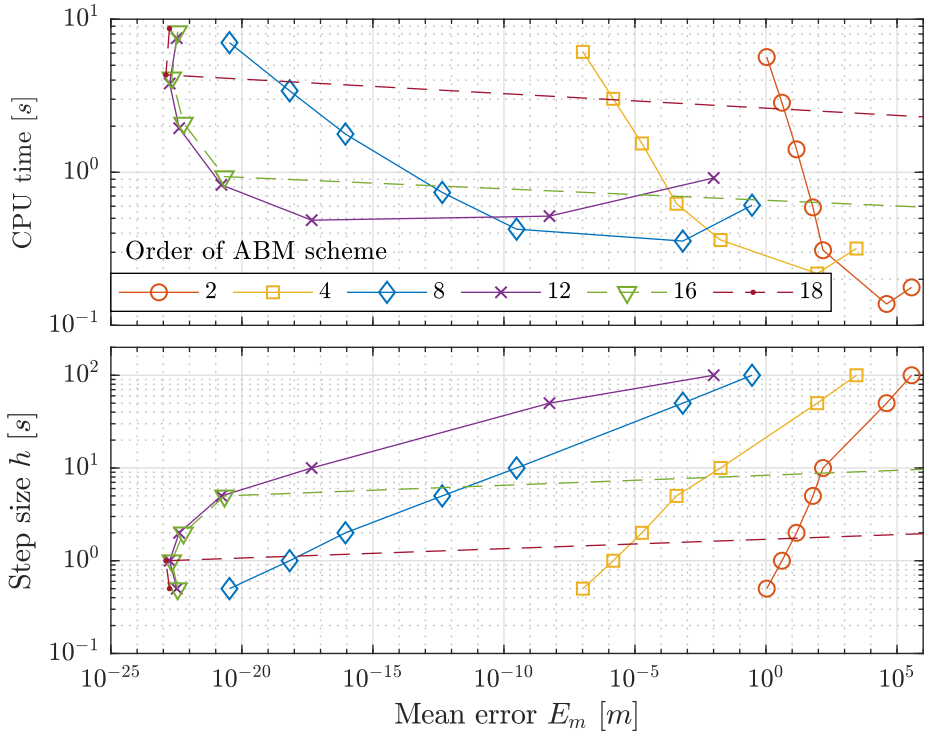

Figure 5.7: CPU time and step size h over the mean error E_m for different orders of the ABM method for the Keplerian test case, using *mpreal* data type with 32 digits. The dashed lines show that the ABM integrator is not stable with high orders with too big step sizes.

results are shown in the same way as before, again for 32 digit precision. The three high order methods can not reach a higher accuracy than about $E_m = 10^{-23}$ m, as already seen before. A further decrease of the step size slightly worsens the result, again. The ABM 12 method obviously outperforms the other methods in terms of efficiency for high accuracy.

ABM 8 is still slightly more efficient than the DoPri87 RK method. The low order CK54 RK method is not suitable for high accuracies. It is notable that for $h < 50$ ABM 12 gains higher accuracies with the same step size compared to DoPri87, taking into account that ABM schemes just use two RHS function evaluations per step compared to 13 for DoPri87. The accuracy limit is reached by ABM 12 with a step size of about $h = 2$ s and DoPri87 requires a step size of $h = 1$ s. ABM 8 requires a step size of about $h = 0.2$ s to reach the same accuracy, but is still faster than DoPri87.

For this simulation case, one has to note, that the advantage of the variable step size methods is not exhausted by the considered circular orbit. For highly elliptic orbits the DoPri87 method is well competitive, at least if RHS function evaluation is not too costly, (eg. Jones, 2012).

The same analysis is conducted for *double* data type with results shown in Figure 5.9. All four integrators reach relatively fast a precision limit which is roughly located around $E_m = 10^{-7}$ m for all integration methods. The required step size to reach this limit again strongly depends on the employed method and lies between 50 s for DoPri87 and 2 s for CK54. A further decrease of the step size, leads to an increase of the error E_m again. This is due to summation of numerical errors which increase by computing more steps. This is valid for all methods but tendentially stronger for the RK methods

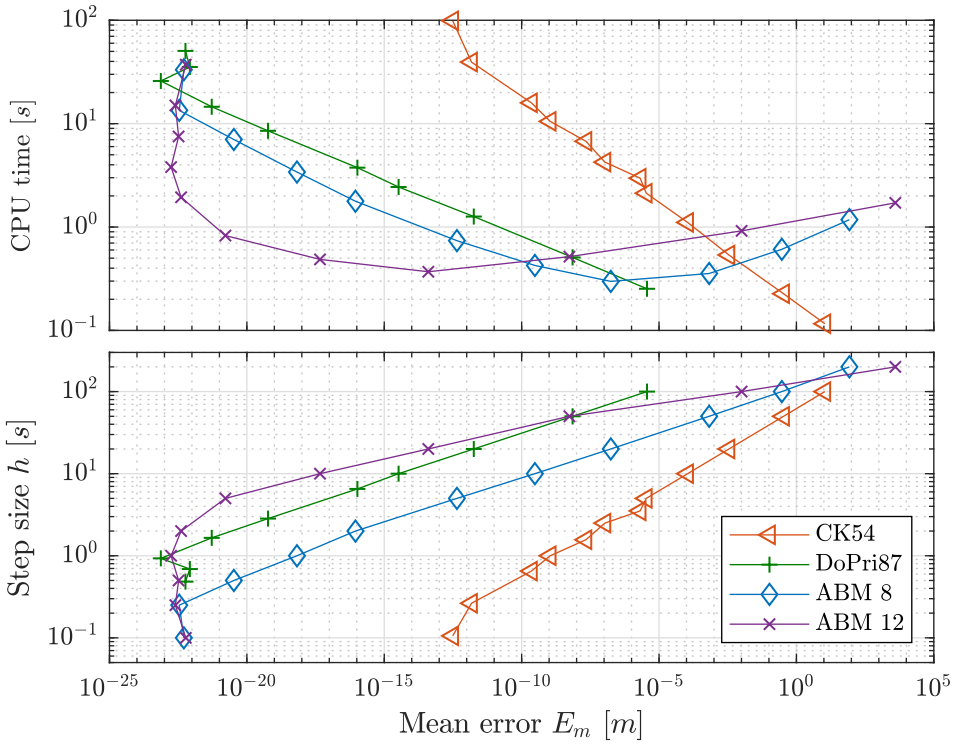

Figure 5.8: CPU time and step size h over the mean error E_m for the two ABM and RK schemes for the Keplerian test case, using *mpreal* data type with 32 digits.

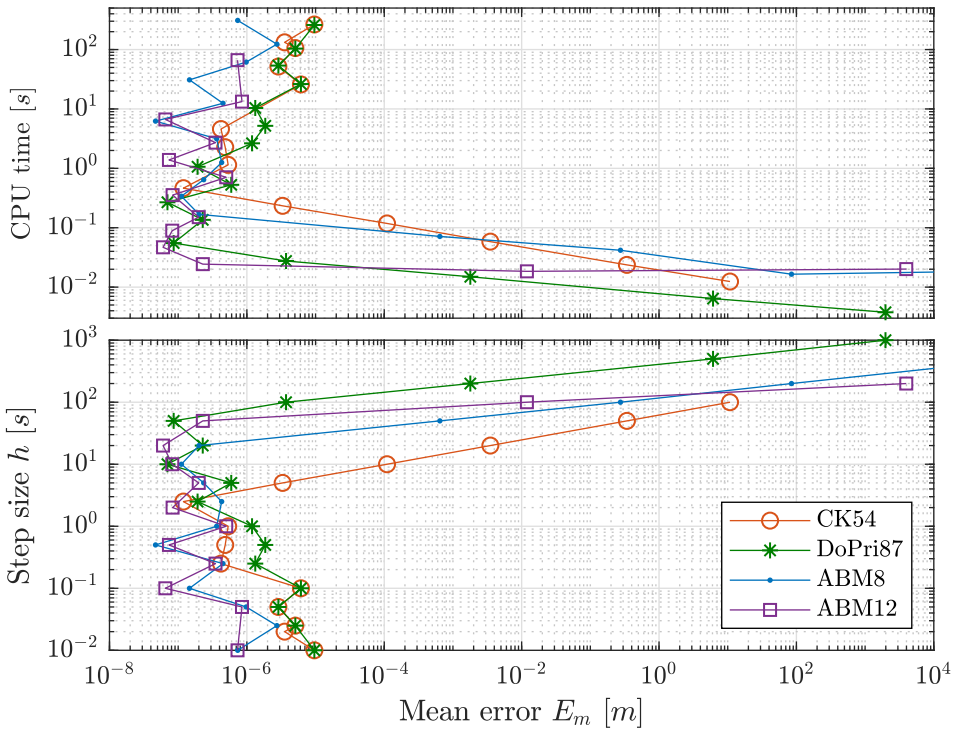

Figure 5.9: CPU time and step size h over the mean error E_m for the two ABM and RK schemes for the Keplerian test case, using standard *double* data type.

which need more RHS function evaluations per step. In the case of *mpreal* data type the summation of numerical rounding errors happens at smaller digit level, thus higher global accuracies are realizable (cf. Fig. 5.8).

5.2.5 Validation with Realistic Gravitational Model

For the realistic test cases with SH gravitational field, no exact solution exists as reference. Therefore all obtained results are compared against the solution obtained with the best integrator ABM 12, using *mpreal* with 32 digits and the smallest investigated step size of $h = 0.25\ s$. From the findings above and the knowledge that the ABM method is much more efficient if RHS function evaluation is computationally expensive, it is reasonable to define this solution as the most accurate reference. For the further investigation just the ABM 12 and DoPri87 integrators are considered.

ABM vs. RK Methods

The results for the second test case are shown in Figure 5.11 for ABM 12 and DoPri87 with *double* and *mpreal* data type with 32 digits. As for the Keplerian case, the accuracy is limited by the used data type. With both methods using *double* data type, it is not possible to exceed a summed mean error below $E_m = 2 \cdot 10^{-6}$ m. Compared to the simple Keplerian case from Figure 5.9, this limit is slightly higher. For ABM 12 the maximal accuracy is reached with a step size of about $h = 5\ s$. The limit for DoPri87 is reached with a smaller step size of $h = 1\ s$ and a larger CPU time. Further decrease of the step size leads to a drastic decrease of the accuracy for DoPri87.

For the *mpreal* data type the DoPri87 method is computationally to intensive, to produce comparable results in a reasonable time. With the ABM 12 method, the error can be further reduced, demonstrating that with enhanced data type it is possible to increase the accuracy also for realistic simulations.

In Figure 5.11 the results from the third test case, additionally including third body attraction from Solar System bodies, are shown. The basic findings from the case before stay the same. A slight decrease of the accuracy limit for both integrators using *double* can be observed. Besides more computational effort for the extended force model, and thus more potential to sum up numerical errors, this may also be a result of subtracting numbers that differ strongly in size for calculating gravitational disturbances due to Sun, Moon and planets.

As for the previous case, the accuracy limit for *double* is reached with a step size of about $h = 5\ s$ for ABM 12. The DoPri87 integrator needs a step size between $h = 1..3\ s$. Further decrease of the step size leads to oscillations, increasing the error, again, as for the Keplerian test case.

5.2.6 Conclusion

The computation with the *mpreal* data type is very slow, compared to the standard *double* data type the orbit integration is about 80 times slower. This reduces the application of such approaches mainly to general performance evaluations. For example we used it for the evaluation of general relativistic effects and comparisons with its linearized post-Newtonian description in LEOs (Philipp et al., 2018). For GFR and real

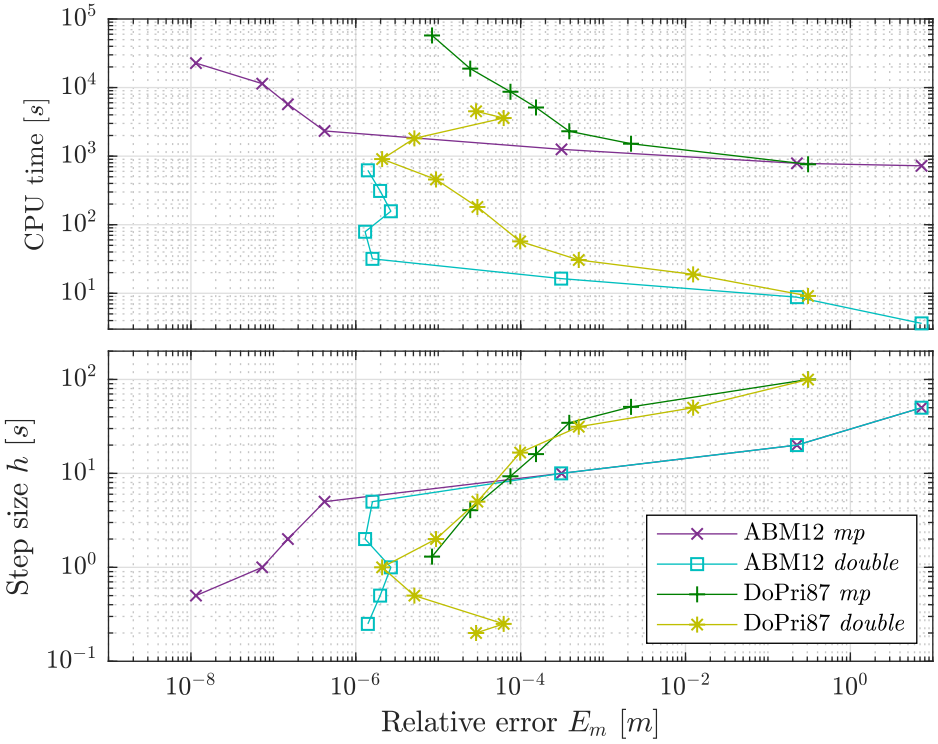

Figure 5.10: CPU time and step size h over the mean error E_m for the ABM 12 and RK DoPri87 integrators for the second test case with SH gravitational field and third body attraction, for *double* and *mpreal* data type.

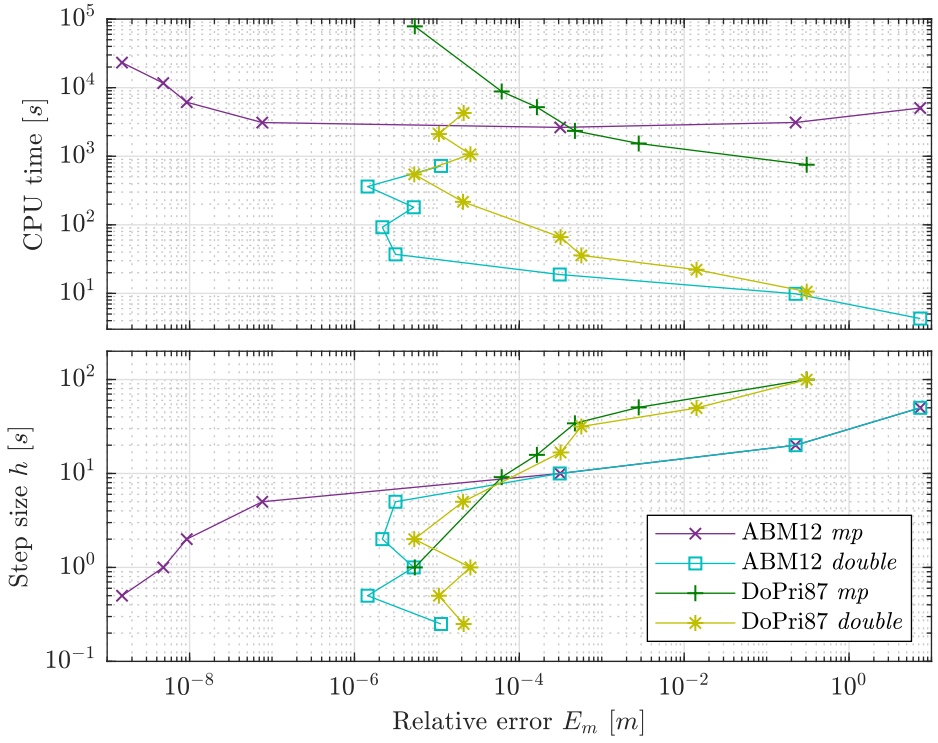

Figure 5.11: CPU time and step size h over the mean error E_m for the ABM 12 and RK DoPri87 integrators for the third test case with SH gravitational field d/o 120 and , for *double* and *mpreal* data type.

data processing this is barely an option.

All three test cases showed the superiority of the ABM integrator compared to the RK methods in terms of accuracy and efficiency, at least for the anticipated step sizes below 100 s. The not investigated effect of abrupt changes in the RHS function may be the only real drawback of the ABM integrator. For the GRACE satellites, abrupt changes may only result from residual attitude thruster effects or radiation effects during eclipse transitions, and thus are comparably small. For general AOCS simulations with thruster firings the effect might be considerable.

If the RHS function is relatively smooth, the order of the ABM scheme should not be set below 8. The computational overhead of higher orders is completely negligible, but the increase of accuracy is high. Orders higher than 12 tend to get unstable quite fast ($h > 2..5$ s) and thus are not useful. Considering the step sizes, it has been demonstrated, that too low step sizes are not just inefficient, but also decrease the accuracy. The realistic test cases showed, that for the ABM scheme the maximal accuracy is already reached with $h = 5$ s for *double* data type. Thus, again, orders above 12 have no advantage for computations with *double* data type. Especially for the RK integrators, choosing the step size too small may significantly increase the error of the integration.

5.2.7 Integrator used for all Simulations, GFR and POD

From the analysis in this section, the ABM 8 integrator was chosen as main integrator for all simulations and the propagation in POD and GFR. The step size of $h = 5$ s seems to be close to an optimum for the investigated LEOs, and is therefore used for nearly all simulations. It also coincides with the main sampling rate of the GRACE data, making it a good choice for GFR. Even though, one has to keep in mind, that the optimal step size depends on the rate of change of the RHS function.

The ABM integrator is always initialized by the DoPri87 RK method. For the dense, equidistant output of 5 s, a varying step size is not useful in terms of efficiency and especially accuracy. Therefore it is shut off for for the initialization of the multistep method.

GRACE SIMULATION 6

In this chapter the simulation of the GRACE mission is presented. This includes the application and validation of the developed non-gravitational force models (Sec. 5.1), by comparison with and the calibration of the GRACE accelerometer data. Subsequently, an attitude control scheme and simulation, including star camera, thruster and magnetic torquer models, is developed, producing similar attitude and actuator characteristics as the GRACE satellites. Furthermore, different models for the main instruments of the satellites are presented and developed, which influence on the Gravity Field Recovery (GFR) results is investigated in Chapter 8.

6.1 Non-Gravitational Force Modeling

The non-gravitational force models, introduced in Chapter 5, are utilized for the GRACE satellites. With the GRACE accelerometer data (ACC) it is possible to evaluate the models and also, at least to some extend, the ACC data itself.

Therefore, in this section, the non-gravitational force models are evaluated with the GRACE L1B data. That means that position and attitude is take from GNV and SCA data, respectively as time series for the evaluation of the models. This enables the most realistic comparison of modeled non-gravitational accelerations and measured ACC data.

After a general evaluation of the modeled forces in Section 6.1.2, in Section 6.1.6 results of the models are compared to GRACE accelerometer data. Most of this work is already published in a condensed form in Wöske et al. (2019).

The position of Sun and Earth, needed for the computation, is evaluated with the JPL DE430 ephemeris model (Folkner et al., 2014).

6.1.1 Finite Element Model (FEM)

For the computation of the non-gravitational forces according to the models introduced in Chapter 5.1, a FEM of the GRACE satellites needs to be created.

Two different models are build, tested and validated. One simple model with just six elements and one model with a slightly more accurate geometry with 3881 elements. The models are based on the dimensions given in the GRACE PSD (Bettadpur, 2012b) and on publicly available pictures of the satellites. The two implemented FEMs are shown in Figure 6.1. The GRACE satellites have a quite simple geometry. Due to their compact shape, shadowing of elements by others does not play a major role. Thus, already with the simple six face model very good results can be obtained. The large amount of elements from the detailed model is motivated by the aim to resolve the few shadowing conditions decently. For one incident direction of radiation, the illumination conditions on the satellite are shown in Figure 6.1, as well. In there, yellow indicates

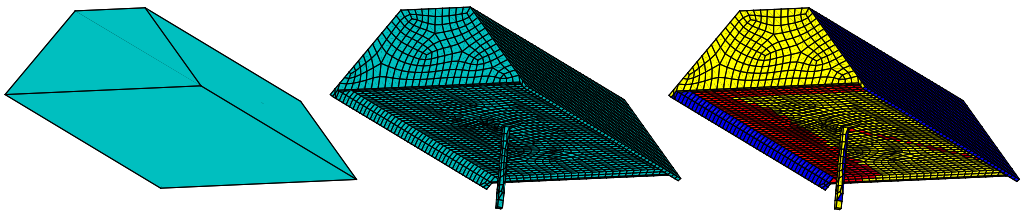

Figure 6.1: (Left, middle) Simple six face and detailed FEM. (Right) Illumination conditions of the FEM for one incident radiation direction, yellow: illuminated, blue: not illuminated, red: shadowed.

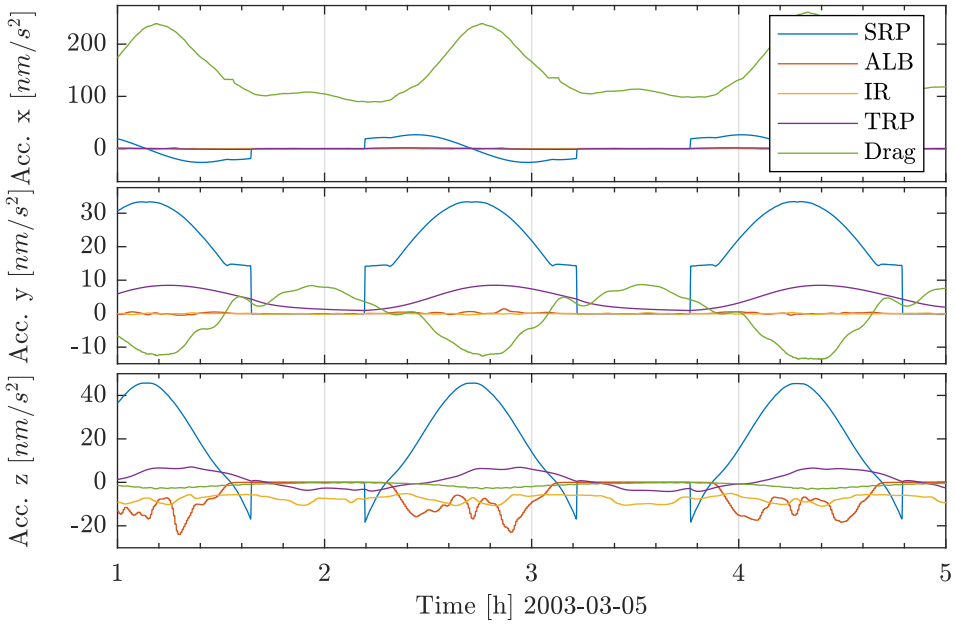

Figure 6.2: Modeled non-gravitational accelerations for GRACE A in the SRF body frame from 2003-03-05 for high solar activity and a β' angle of 37.2°.

directly illuminated areas, blue not illuminated ones and red areas that are shadowed by other elements.

All optical surface properties, needed for the models α, γ_s, γ_d and ε (cf. Sec. 5.1), for visible and infrared radiation, are also given in the GRACE PSD (Bettadpur, 2012b).

6.1.2 Modeled Non-Gravitational Forces for GRACE

The pattern of the non-gravitational forces is mainly dependent on the satellites attitude and the orientation of the orbit with respect to the Sun. A measure for the latter is the β' angle, which is defined as the smaller angle between the orbital plane and the vector pointing from Earth towards Sun.

For the GRACE satellites with a nearly constant attitude, with respect to the orbital frame, the pattern of the non-gravitational accelerations acting on the satellites is mainly determined by the β' angle. The precession of the polar GRACE orbit causes a change of the β' angle with a period of about 322 days and between about $\pm 85°$.

In the next two figures the different individual non-gravitational forces are compared for two epochs of the GRACE mission with similar β' angle. In Figure 6.2 each of the

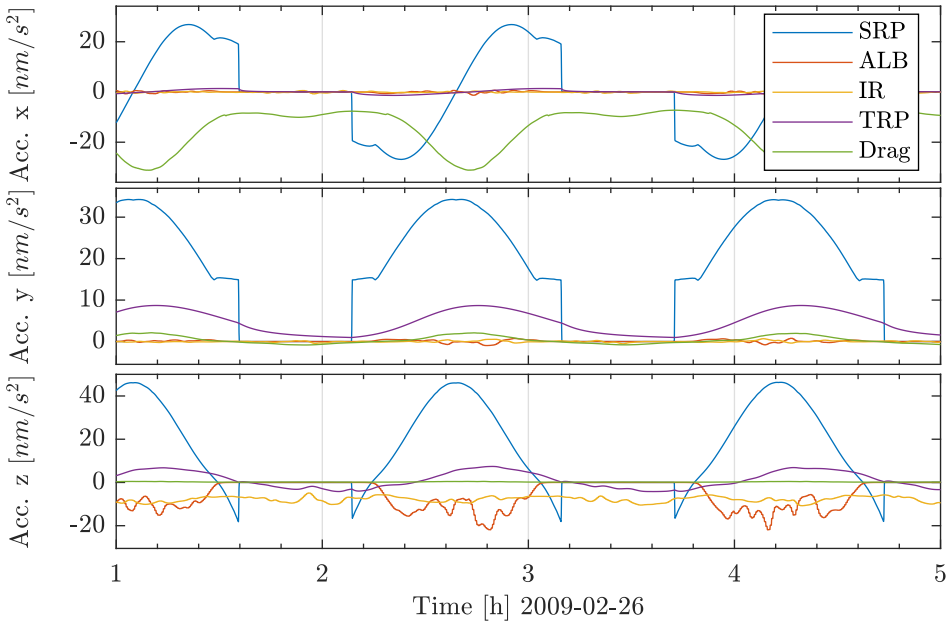

Figure 6.3: Modeled non-gravitational accelerations for GRACE A in the SRF body frame from 2009-02-26 for low solar activity and a β' angle of -35.8°.

modeled non-gravitational accelerations for the GRACE A satellite are shown for each axis in the body fixed SRF. At the date of this plot in 2003 a high solar activity is present (cf. Fig. 3.1). In Figure 6.3 the same forces are shown for a low solar activity in 2009, but for a similar β' angle (the sign is changed because a switch of the leading and following GRACE satellite was conducted meanwhile).

Particularly eye-catching is the difference of the magnitude of the drag acceleration. Even though the altitude in Figure 6.2 is slightly higher (cf. Fig. 3.1), the drag is about an order of magnitude higher. The other forces are very similar for the same β' angle. ALB and IR show a slightly different structure due to different radiation conditions over the Earth for the different epochs. For the same illumination conditions, the basically Sun related forces SRP and TRP are about the same.

Because of the close alignment of the SRF axes to the along-track, cross-track and radial directions (cf. Sec. 3.3.1), the different accelerations are mainly acting in certain directions in the SRF. The drag force, which is acting in along-track direction is basically restricted to the x-axis and the Earth related ALB and IR forces are mainly acting in radial direction, thus in satellite z-axis.

The effect of each non-gravitational acceleration on the satellite's orbit is shown in Figure 6.4. Therefore simulations with initial conditions and attitude from GRACE A from 2009-02-26, as in Figure 6.3, are conducted (low solar activity). The shown norm of the position difference is computed between a reference simulation without employing any non-gravitational force model and subsequent simulations using the respective models. Because of the big differences of the different effects, the plot is in a logarithmic scale.

The drag force has by far the biggest influence on the orbit. For the chosen epoch its magnitude is not much bigger than SRP, but it is always acting in the same direction, as well as in flight direction (along-track), which has the biggest sensitivity to orbit changes, causing the orbit to spiral down, thus the plotted position difference

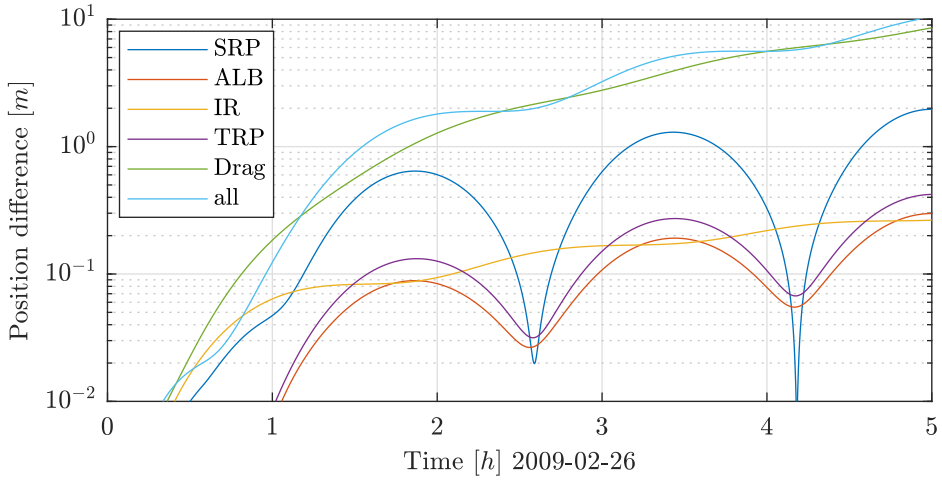

Figure 6.4: Norm of position difference between a simulation without any non-gravitational force model and with the respective force model, with initial conditions and attitude from GRACE A from 2009-02-26.

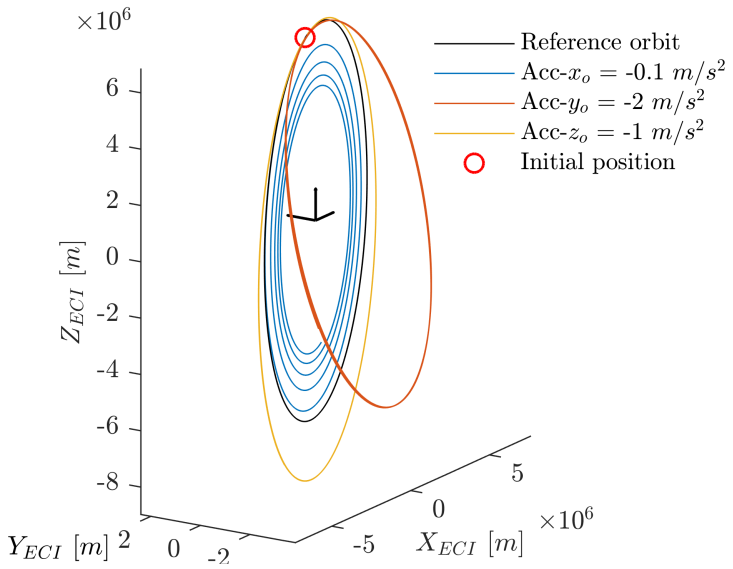

Figure 6.5: Effects on the GRACE orbit (2009-02-26, simulated for 5 h) for additional constant accelerations in the three directions of the orbital frame (nearly identical with GRACE's SRF body frame), respectively. The black reference is the orbit without additional accelerations. The applied constant accelerations are extremely huge compared to disturbing accelerations in Earth orbits, to demonstrate the effects.

is constantly increasing. In contrast to that, the effect of the SRP acceleration is very periodic. This is mainly caused by the periodic acceleration in along-track direction, rising and lowering the orbit.

The satellite's position or orbit is least sensitive to accelerations in cross-track direction. The always positive SRP component in this direction causes a constant bending of the orbit from the center of the Earth (see next plot). These effects are very tiny and also resulting in a periodic effect on the position difference. The overall positive acceleration in radial direction is affecting the satellite's orbit slightly stronger, resulting it an additional constant eccentricity, and thus having a periodic and constant effect on the position difference. ALB and IR are also mainly acting in the radial direction, but with a lower magnitude than SRP. IR is not affected so much by solar eclipses and thus showing a more constant effect on the orbit. Nevertheless, the effects are rather small. TRP is not completely isotropic and besides a superimposed periodicity with the Sun angle, it has a non zero mean acceleration (see Fig. 6.3). From the magnitude it has a similar effect as ALB.

To demonstrate the described effects of the different acceleration directions in the orbital frame more vivid, in Figure 6.5 the results from simulations with constant accelerations in each direction of the orbital frame are shown three-dimensional. The accelerations are heavily enlarged compared to anything possibly disturbing satellites in Earth orbits, to make the effects visible, qualitatively. The simulations are conducted for the same date (2009-02-26) as before and as well for 5 h. The black reference orbit is the nearly circular, polar GRACE orbit. The orbits show the change due to the applied constant accelerations, given in the plot. It demonstrates what has been basically described before.

An accelerations in along-track direction (the applied acceleration in Fig. 6.5 is one magnitude lower than for the other directions) is much stronger influencing the orbit than an acceleration in cross-track and radial direction. Furthermore, it is changing the energy of the orbit, being parallel to the orbital velocity, and hence changing its shape permanently, whereas this is not the case for the other directions, where the applied accelerations do not change the orbital energy. Thus, if the accelerations are shut-off, the orbit again changes drastically.

The constant accelerations in radial direction reduces or increase constantly the main gravitational acceleration, being mainly in that direction, too. Thus, resulting in a kind of more elliptic orbit. Described by Keplerian orbit elements, this can be expressed as a periodically increasing and decreasing eccentricity.

The acceleration in cross-track direction bends the orbit away from the Earth's center of mass. In terms of Keplerian orbit elements, this would be expressed by a periodically, phase shifted change of the ascending node and the inclination.

6.1.3 Post-Newtonian Relativistic Corrections for GRACE

The discussion of the post-Newtonian (pN) corrections for the GRACE satellites, as introduced in Section 2.3.6, is briefly inserted here for direct comparison to the non-gravitational accelerations.

For the same time as investigated for the non-gravitational accelerations in the Figures 6.3 and 6.4, the two pN accelerations *Schwarzschild* and *Lense-Thirring* are depicted in Figure 6.6 for the three satellite's SRF body axes. The third correction term *de Sitter* is tiny for GRACE's low Earth orbit, in the range of 10^{-30} m/s^2, and thus not shown in the plot.

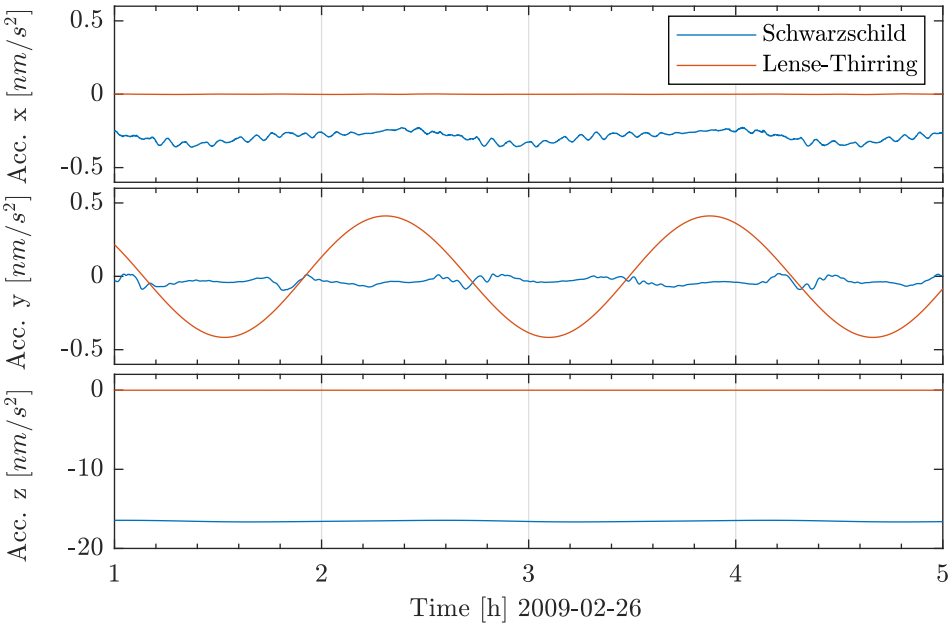

Figure 6.6: Post Newtonian correction accelerations for GRACE A in the SRF body frame from 2009-02-26.

For the circular GRACE orbit the Schwarzschild pN acceleration has a magnitude comparable to the IR acceleration. It is mainly acting constantly in the radial direction. In the other directions it is rather zero and the small deviations are mainly due to the jittering of the satellite's attitude. The magnitude of the Lense-Thirring pN acceleration is smaller and shows a distinct oscillation with the orbit frequency around zero in cross-track direction.

The influence of the two correction terms on the satellite's orbit is shown in Figure 6.7, in the same way as it has been shown for the non-gravitational accelerations in Figure 6.4. The two comparable non-gravitational accelerations IR and TRP, in terms of magnitude, are plotted again as reference. The Schwarzschild pN acceleration has a very similar effect on the orbit as the IR acceleration. This is not surprising because both are acting mainly in the same direction and having similar magnitudes. The small periodic Lense-Thirring pN acceleration has a minor effect on the orbit, which is as well oscillating.

The periodically, with orbit frequency, oscillating acceleration in cross-track direction results in a constant drift of the ascending node and the inclination, when described by Keplerian orbit elements.

For the standard GRACE POD and GFR analysis the Schwarzschild pN term has to be considered theoretically because of its magnitude. Nevertheless, the nearly constant effect is quite well absorbed by the bias estimation in the accelerometer calibration, if not considered as pN correction (cf. Sec. 7.8). The effect of the very small Lense-Thirring pN acceleration is very similar to the gravitation due to the flattening of the Earth, but on a much lower scale. The flattening is governed by the low zonal C coefficients, mainly $C_{2,0}$ and $C_{4,0}$. The accuracy of the orbit solution (GNV or KOS) is not high enough to separate the tiny Lense-Thirring effect from the classical gravitational effects. With GRACE GFR it is not possible to estimate the low zonal coefficients with a sufficient accuracy. The relative KBR measurement is much more accurate, but not very sensitive for differences on orbit frequency scale (cf. KBR range error in Fig. 6.27). Thus, the

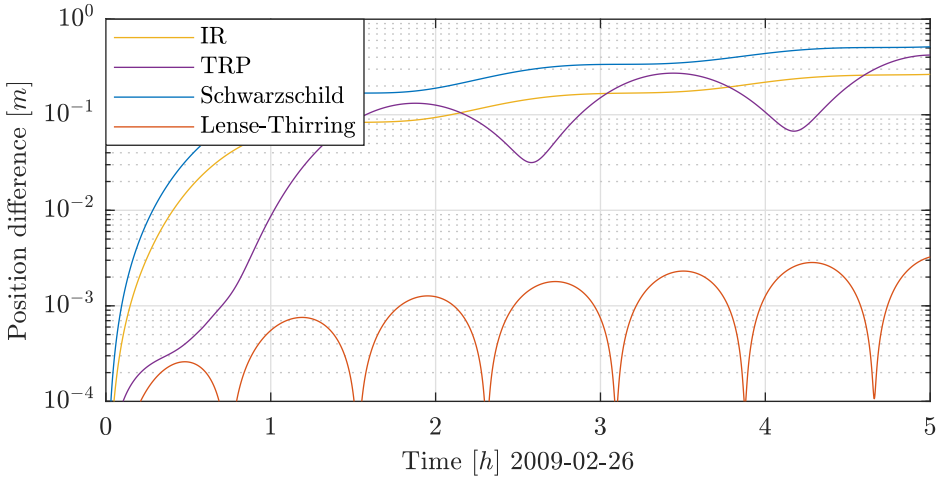

Figure 6.7: Norm of position difference between a simulation without any additional force models and with the respective post Newtonian correction acceleration and non-gravitational force model, with initial conditions and attitude from GRACE A from 2009-02-26.

effect can not be seen in the KBR measurement, as well as the KBR measurement does not contribute much to the estimation of the low degree coefficients.

Because the effect is at the edge to be detectable and having an influence, it is usually considered to not couple into the estimated gravitational fields and sensor errors.

6.1.4 ALB and IR

The main component of the ALB and IR forces is in the radial z-direction. For both accelerations the z-component is shown in Figure 6.8 (b) in the SRF for GRACE A for a six hour arc in May 1st 2006. In the same figure (a) the ground track of the satellite is shown over the 3 hourly CERES long wave flux data. The position of the satellite is marked every 15 minutes in both plots for comparison.

The most prominent structure in (b) is the eclipse cycle of the ALB acceleration. The acceleration drops to zero when the satellite is in the eclipse because no Sun light is reflected. For IR this is not the case because the driver of this acceleration is the temperature of the Earth surface and atmosphere, which is directly connected to the shown long wave flux in (a), which is not so much Sun dependent.

The ALB accelerations reaches its maxima usually over the pole because the ice and snow has a high reflectivity. Other maxima are reached when the satellite flies over large cloud systems, which have a similar reflectivity than sow and ice.

For IR the effect of clouds is the other way around. Clouds shield the long wave radiation from the surface and have a low temperature itself, thus result in low IR accelerations. The main periodic cycle of the IR acceleration are the different temperature zones on the Earth surface. Over the South Pole, which is much colder in the northern summer months, the IR acceleration reaches its lowest values. Around the equator the highest values are reached. Over the North Pole the local minima are much smaller than over the South Pole. This general characteristic is overlaid by local clouds and temperature variations and the time of passing with maxima when the Sun is in zenith (cf. also Fig. 5.3).

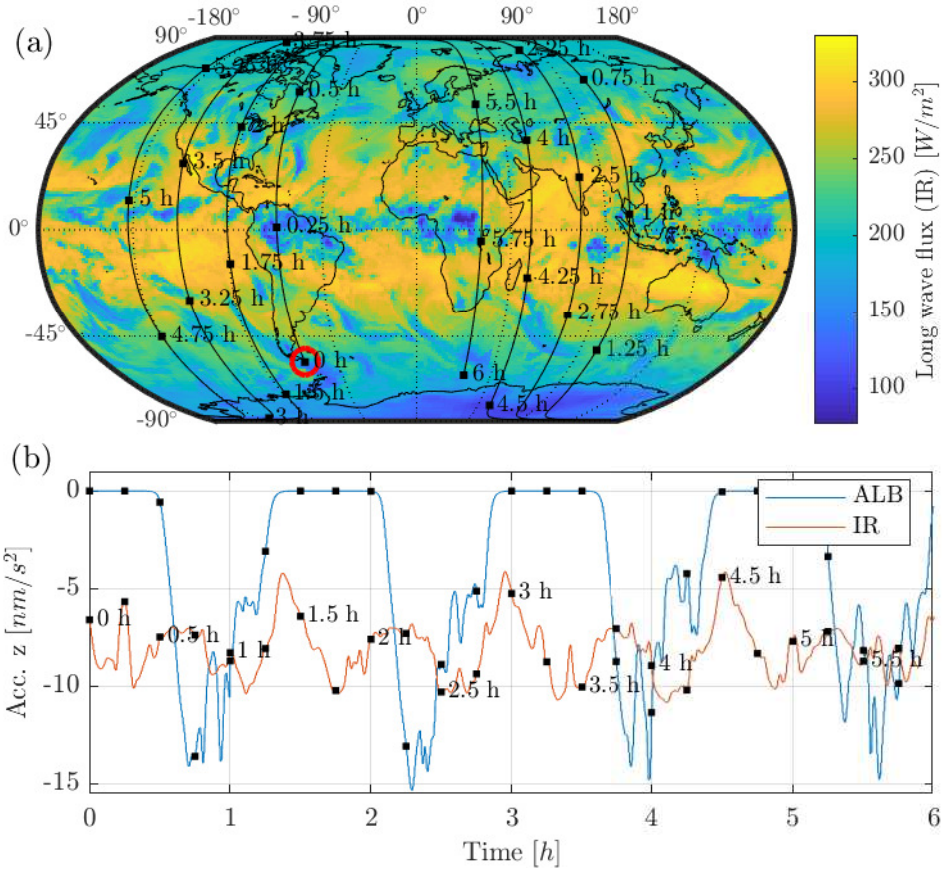

Figure 6.8: (a) CERES SYN1deg 3 hourly long wave flux radiation data from 2006-05-01 with the ground track of GRACE A for six hours (the position at every 15 minutes is marked). (b) Modeled ALB and IR accelerations (just SRF z-axis) for the same time (again, every 15 minutes are marked).

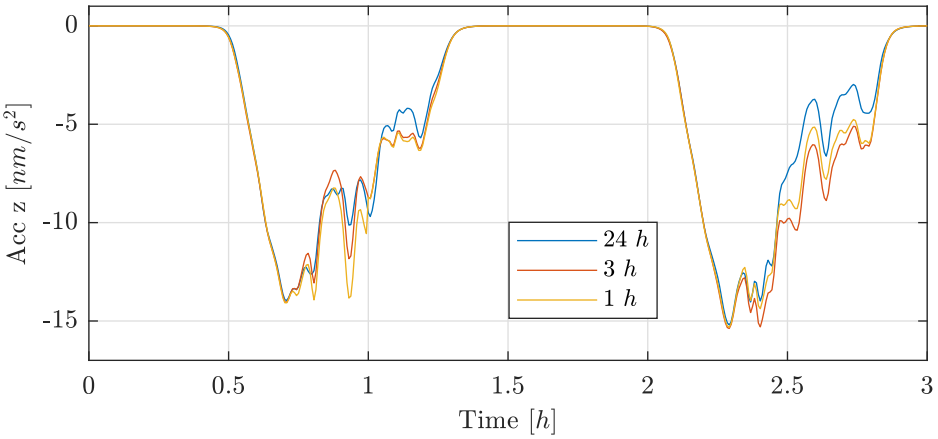

Figure 6.9: Modeled ALB acceleration (just SRF z-axis) for GRACE A from 2005-05-01 based on daily, 3-hourly and hourly CERES data.

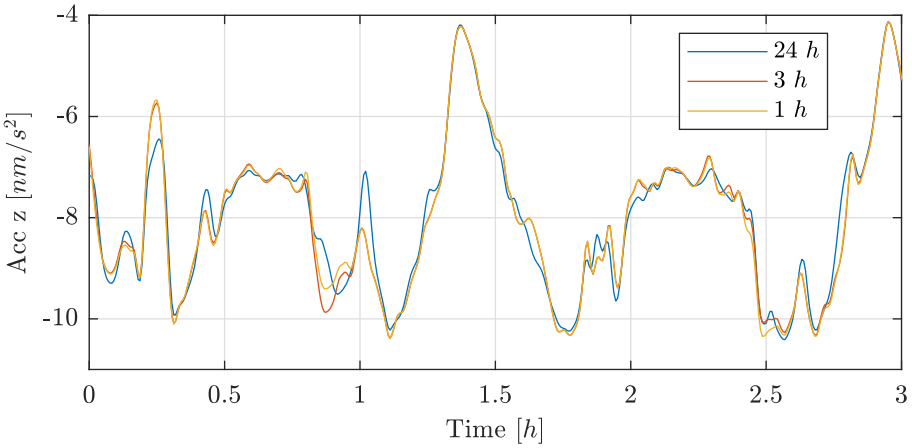

Figure 6.10: Modeled IR acceleration (just SRF z-axis) for GRACE A from 2005-05-01 based on daily, 3-hourly and hourly CERES data.

1-Hourly, 3-Hourly and Daily CERES Data

ALB and IR are modeled based on CERES SYN1deg data. The data are available in different temporal resolutions. In the following two Figures 6.9 and 6.10 the ALB and IR accelerations are computed based on CERES data with daily, 3-hourly and hourly resolution for GRACE A on May 1st 2006. Again just the body z-axis is shown, being the axis in which the forces mainly act.

The general trend, described in the section before is met with all three resolutions. Nevertheless, the finer the temporal resolution, the more details are resolved. This effect is slightly stronger for ALB than for IR.

Computationally a higher resolution does not play a role, just the amount of data is increased. This drawback is accepted to obtain the best possible results. Therefore all following modeled ALB and IR forces are based on the hourly data sets.

6.1.5 TRP

The basis for the TRP calculation is the determination of the satellites surface temperatures. Three different models were presented for that purpose in Chapter 5.1.4. For each

Table 6.1: Properties of the different layers for the temperature PDE

	c_p $[J/kgK]$	ρ $[kg/m^3]$	h $[mm]$	λ $[W/mK]$
left, right ($\mp$Y), top ($-$Z)				
Solar panel	540	2000	2.5	1.85
Insulation	1000	30	70	0.023
Honeycomb	900	45	30	0.08
front, rear ($\pm$X)				
Kapton	1095	1400	0.1	0.2
Insulation	1000	33	75	0.018
Honeycomb	900	45	30	0.08
bottom (+Z)				
Teflon-foil	1095	2000	0.1	0.2

model the incoming radiation flux is essential. Furthermore, each model needs some specific material parameters.

The second model (b) *trans* (Sec. 5.1.4) is not considered here in detail. The analysis has shown, that the third model (c) *pde* (Sec. 5.1.4) is more accurate and especially to obtain reasonable results with the *trans* model, the factor $c_p \rho h$ was tuned that results fitted well with the GRACE accelerometer data. This approach may be valid if accelerometer data are available, but a stand alone simulation approach using reasonable material properties is more general and satisfying. Nevertheless, with the tuned factor the *trans* models gives good results, as well, as shown in Wöske et al. (2019).

For the *pde* model (cf. Sec. 5.1.4) the Partial Differential Equation (PDE) (Eq. 5.19), with the independent variables time t and direction x, needs to be solved for each element k. For reasonable computation times the simple six face GRACE model is used for that purpose. For the solution of the spatial direction, a grid for x perpendicular to the surface (cf. Fig. 5.5) is defined with about 30 elements. The time step is chosen to be five seconds, as L1B data sampling. As popular in satellite manufacturing, the GRACE satellites are mainly build out of honeycomb structure plates, which are isolated towards space with an layer of insulation material and covered again with a thin surface, like a MLI-foil (Multi Layer Insulation) or solar panels.

Here three different wall types are modeled for the GRACE satellites. Each type is modeled consisting of different layers with different material properties c_p, ρ, h, and λ. The types are:

1. The three solar panel walls: top (-Z), right (+Y), left (-Y), consisting out of three layers: Solar panel, insulation and honeycomb.

2. The rear (-X) and front (+X) walls, as: Kapton layer, insulation and honeycomb.

3. The nadir bottom wall (+Z) is the heat radiation surface, modeled as a teflon foil.

For the definition of the different panels see Figure 3.3. The properties for the six satellite walls and layers and their thickness are given in Table 6.1. Most of these properties are not publicly available and are educated guesses from available manufacturing and satellite integration pictures.

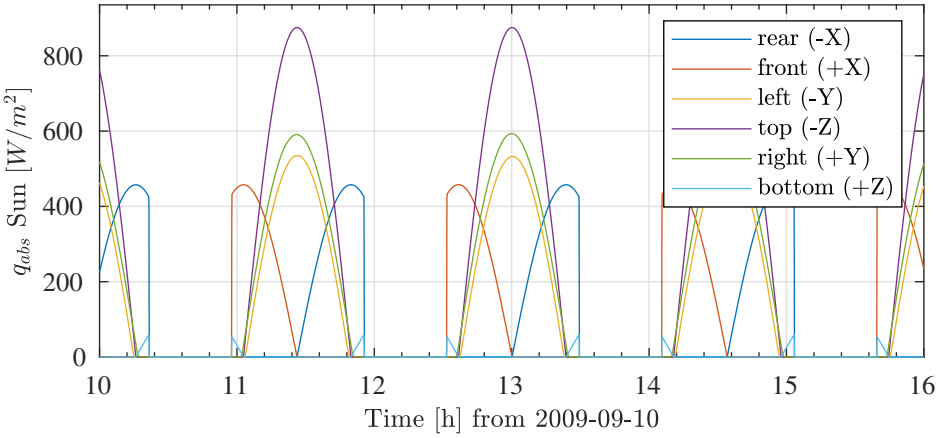

Figure 6.11: Modeled absorbed flux q_{abs} of the six GRACE surfaces from Sun radiation, GRACE A from 2009-09-10, $\beta' = 29.4°$.

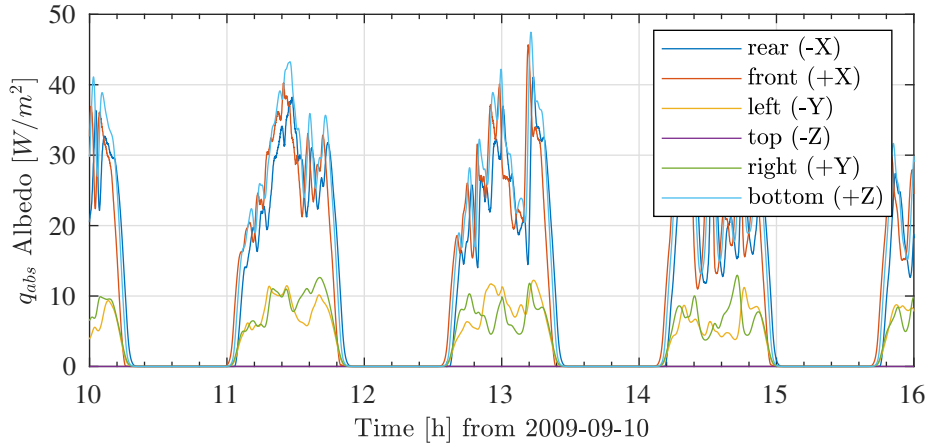

Figure 6.12: Modeled absorbed flux q_{abs} of the six GRACE surfaces from Earth albedo radiation, GRACE A from 2009-09-10, $\beta' = 29.4°$.

For the PDE the following boundary conditions are defined, see as well the sketch in Figure 5.5. Towards the outside is no heat flux, but an absorbed and radiated flux: $q_{abs,k} - \varepsilon_k \sigma T_k^4$. For the inner side it is assumed that all satellite payloads and systems produce a total power, which is transferred to the faces. Because the bottom face is the heat radiator, we assume, that 90% of the power is going through this face, the remaining 10% are distributed to the other faces. As internal power production P_{inern} = 250 W is assumed because the true value is not known. It was found that this value has just a minor effect on the resulting forces. The estimated temperatures from the previous day are used as initial condition for the temperatures, with some arbitrary initial guess for the very first day.

The modeled absorbed fluxes $q_{abs,k}$ for the three different sources Sun, Earth albedo and IR radiation are shown in the Figures 6.11, 6.12 and 6.13 for the six surfaces of the simple GRACE FEM. The fluxes are computed as described in Equations (5.15), (5.16). The date is chosen to be September 10th 2009 because of the low solar activity (cf Fig. 3.1) and thus smaller disturbing drag errors in the non-gravitational accelerations and for a medium β' angle.

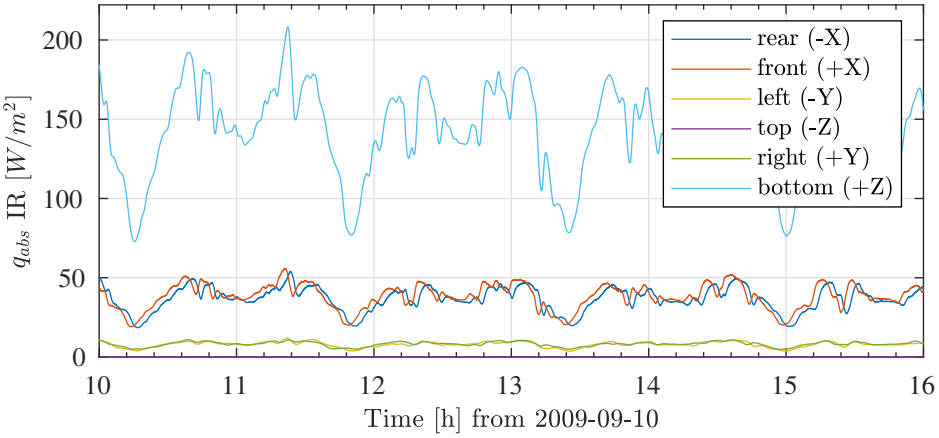

Figure 6.13: Modeled absorbed flux q_{abs} of the six GRACE surfaces from Earth IR radiation, GRACE A from 2009-09-10, $\beta' = 29.4°$.

The absorbed flux by the Sun is by far the biggest. As for albedo, it consists of the distinct drops when the satellite enters the eclipse. The bottom panel rarely is illuminated by the Sun, and if so, just under a low incident angle. The absorbed flux from albedo and IR is in a pretty similar level, but for the bottom panel. Due to the fact that this panel is used as heat radiator, it has a high emissivity and thus also a high absorptivity in that wavelength band (Eq. 5.3). Therefore the absorbed flux of IR radiation for this panel is quite high.

With the shown absorbed fluxes $q_{abs,k}$ the temperatures of the surfaces can be calculated. The results for the *stat* (a) and *pde* (c) models are shown in Figure 6.14 for the same time period and the six panels.

For the static temperature calculation, the temperature drops directly to zero when no incoming flux is present in the eclipses. The spiky fluxes from albedo and IR directly convert to the temperatures. The much more realistic *pde* model considering heat capacity, and thus the ability of storing energy, results in a smooth decay and growth of the temperature. Just the very thin Teflon-foil of the bottom panel is not capable of storing much energy, making its temperature evolution much more rough.

The resulting TRP accelerations are shown in Figure 6.15 for both temperature models and the three SRF axes. The biggest TRP acceleration is in the radial z-direction. This is because the top and bottom panel experience the highest temperature differences and hence the resulting forces are not canceling out. During eclipse the IR radiation results in an acceleration in the negative z-direction. For the times in Sunlight, the upper surface temperatures (top and right) outweigh the IR radiation on the bottom face, resulting in an acceleration in positive z-direction. Both other directions cancel out more or less for the given illumination condition or β' angle.

The TRP acceleration from the *pde* model is in general a little bit smaller and shifted compared to the *stat* model. This is reasonable because the temperature builds up more slowly due to conduction and the heating of a thick surface. As for the temperature, the TRP curve of the *pde* model is more smooth.

That the *pde* model produces the more realistic and better results is shown in the next Section 6.1.6, where the resulting accelerations are compared to the GRACE accelerometer measurements.

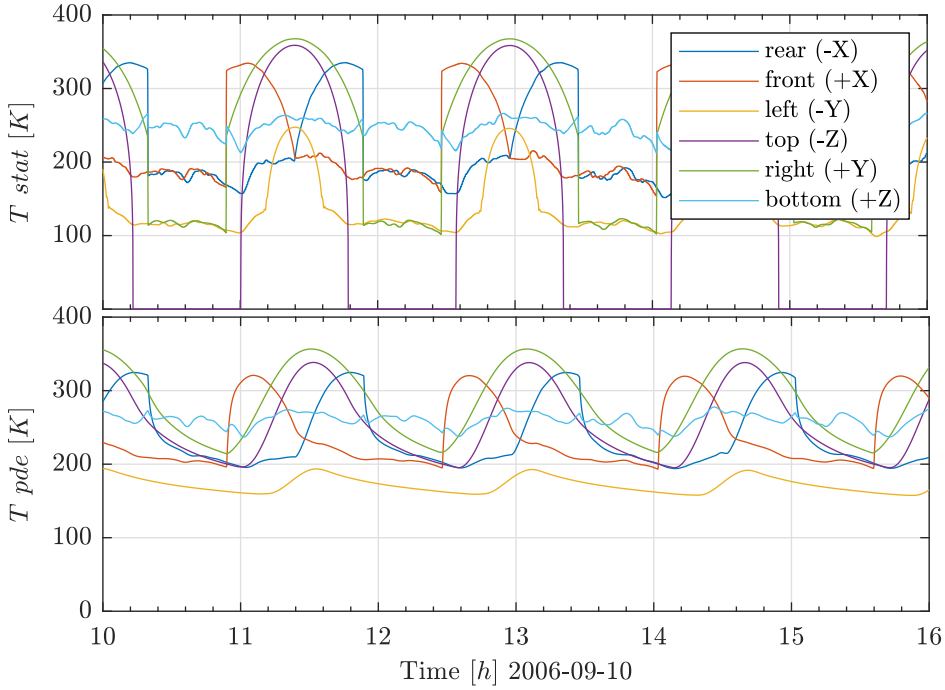

Figure 6.14: Modeled surface temperatures for the two different temperature models *stat* (a) and *pde* (c) of the six surfaces of the simple FEM. GRACE A from 2009-09-10 for a medium β' angle of 29.4° and low solar activity.

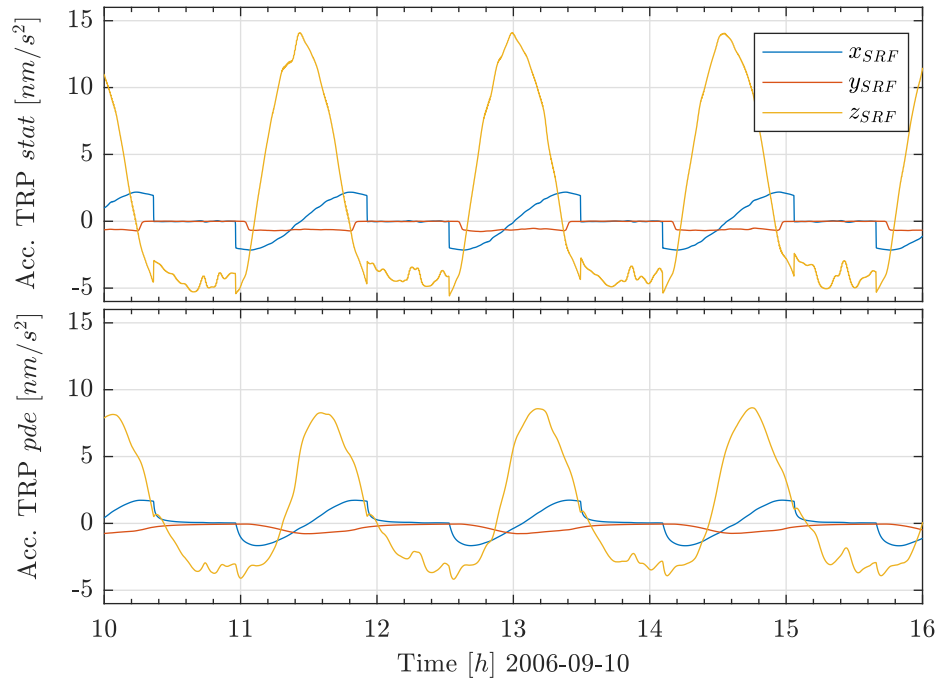

Figure 6.15: Modeled TRP acceleration with *stat* (a) and *pde* (c) temperature models, for GRACE A from 2009-09-10 for a medium β' angle of 29.4° and low solar activity.

Table 6.2: Summary of used non-gravitational force models and their main parameters and data

	Models	Parameters
SRP	GRACE FEM-detailed[a]	Solar flux at 1 AU $q_\odot = 1366\ W/m^2$
ALB	GRACE FEM-detailed[a]	CERES SYN1deg-1H (TOA) albedo[b], $q_\odot$
IR	GRACE FEM-detailed[a]	CERES SYN1deg-1H (TOA) Longwave flux[b]
TRP	GRACE FEM-6-face[a]	$stat$[c], pde[d], c_p, ρ, h, λ [e], $P_{inern} = 250\ W$
Drag	C_D, JB08[f], HWM93, GRACE FEM-detailed[a]	$C_D = 2.25$
Ephemeris	JPL DE430[g]	Sun and Earth position for all models
Satellite position and attitude		GNV, SCA L1B RL05[h]

[a] Sec. 6.1.1 and Fig. 6.1, [b] Doelling et al. (2016), [c] Sec. 5.1.4, [d] Sec. 5.1.4, [e] Sec. 6.1.5 and Tab. 6.1, [f] Bowman et al. (2008), [g] Folkner et al. (2014), [h] Case et al. (2010)

6.1.6 Comparison and Validation with GRACE Accelerometer Data

In the previous sections results of the non-gravitational force models were shown and analyzed. Nevertheless, without a reference it is not easy to evaluate the accuracy of the models quantitatively. The GRACE accelerometer data enable the direct comparison of the models with actual measurements. Besides the good GRACE accelerometer data quality, GRACE is especially suitable because of several reasons. First, additionally to the accelerometer data, high quality attitude and orbit data are available with a high sampling. Furthermore, data are available nearly continuously for 15 years. Also the geometry and optical surface properties are known and published (Bettadpur, 2012b). Last but not least, the attitude and geometry of the satellites partly allows to distinguish several non-gravitational forces through the directions they are mainly acting (cf. Sec. 3.3.1).

Anyhow, the comparison is not that simple. The accelerometer data need to be calibrated. The measured data contain a scale factor and a continuously changing bias for each axis. Accelerometer calibration is a hot topic and is of highest importance for different tasks, including POD and GFR. Different methods and approaches exist based on POD, GFR, modeling and combined methods. Nevertheless, different authors, groups and processing centers estimate different calibration parameters. Furthermore, the calibration also differs from the application of the data (Vielberg et al., 2018; Wöske et al., 2019; Calabia et al., 2015; Van Helleputte et al., 2009; Bezděk, 2010; Bettadpur, 2009; Klinger and Mayer-Gürr, 2016). This fact makes the comparison a little less quantitatively. Furthermore, the accelerometers sense all attitude thruster firings of the satellites. Du to imperfections in timing and thruster orientation, they produce a residual force additionally to the desired torque. These residual forces are visible as sharp spikes in all axes of the accelerometer data (cf. Fig. 6.16). For comparisons these random spikes have to be removed.

Here, for the comparison, the accelerometer data are calibrated with the modeled accelerations as reference. A bias vector $\vec{b}$ is estimated daily in terms of least squares. As scale factors $\vec{s}$, the constant values from the GRACE technical note TN-02 (Bettadpur, 2009) $\vec{s}_{TN}$ are used, as shown in Table 7.2. The calibration equation is given as

$$ACC_{corr} = \vec{s}\ ACC1B + \vec{b}, \tag{6.1}$$

With the corrected accelerometer measurement ACC_{corr} and the L1B accelerometer data $ACC1B$. The estimation of just a daily bias vector does not change the original data too much, i.e. they are not fitted towards the simulated reference and thus the comparison of modeled and measured data is still meaningful.

With Equation (6.1) the standard least squares equation can be set up for each axis i as

$$\min_{\alpha_i} \left|\left| \begin{bmatrix} filt(ACC1B_i) & I_{3\times1} \end{bmatrix} \alpha_i - ACC_{sim,i} \right|\right|^2, \tag{6.2}$$

with $\alpha_i = [s_i, b_i]^T$ being the vector of parameters to estimate and $I_{3\times1}$ a vector of ones. For the case of constant scale factors, s_i is replaced by the factors $s_{TN,i}$.

The function $filt$ implies, that the raw ACC L1B data are first filtered, to get rid of all spikes, caused by the attitude thruster firings (cf. Sec. 6.3.6 for a more complete discussion of the residual attitude thruster accelerations). For that purpose a moving median filter is used with order 30, 80, 45 for x-, y- and z-axis, respectively. The standard solution is obtained by

$$\alpha_i = (X_i^T X_i)^{-1} X_i^T ACC_{sim,i}, \tag{6.3}$$

using the abbreviation X_i for the matrix $\begin{bmatrix} filt(ACC1B_i) & I_{3\times1} \end{bmatrix}$. A residual for each data point can be determined as

$$\vec{r} = ACC_{corr} - ACC_{sim}. \tag{6.4}$$

From these residuals, a root mean square (rms) residual $r_{rms,i}$ for each axis i is computed as a scalar measure for one day:

$$r_{rms,i} = rms(\vec{r}_i). \tag{6.5}$$

The calibration is analyzed and validated in more detail in Wöske et al. (2019), with results over the whole GRACE mission.

All utilized non-gravitational force models, for the results shown in this Section and the whole thesis are summarized in Table 6.2, with its main parameters. If not differently stated the *pde* TRP model is used.

An example of modeled and calibrated accelerometer data is shown in Figure 6.16 for one day. The modeled data show a very good agreement with the GRACE data, especially for cross-track (y) and radial (z) directions, what is visible by direct comparison, but also from the residuals with values of $r_{rms,y} = 1.15\ nm/s^2$ and $r_{rms,z} = 1.17\ nm/s^2$. The along-track (x) direction is obviously worse with $r_{rms,x} = 10.20\ nm/s^2$. The reason is the deficiency of atmospheric drag modeling or, especially, the atmospheric density modeling. Because of the dedicated satellites attitude and its shape, the drag force is closely aligned in this direction. The sources and environmental variations for the radiation forces are better understood and measured and thus can be modeled more precisely.

In the following, the results of the two different GRACE FEMs and the *stat* and *pde* TRP models are exemplary compared in more detail to the GRACE accelerometer data.

In Figure 6.17, the modeled cross-track accelerations for the simple 6-face and detailed FEM (both shown in Fig. 6.1) are compared against calibrated ACC data. For both cases the bias is separately determined. All other used non-gravitational force models (cf. Tab. 6.2) are the same. The time for that comparison was chosen to see the influence

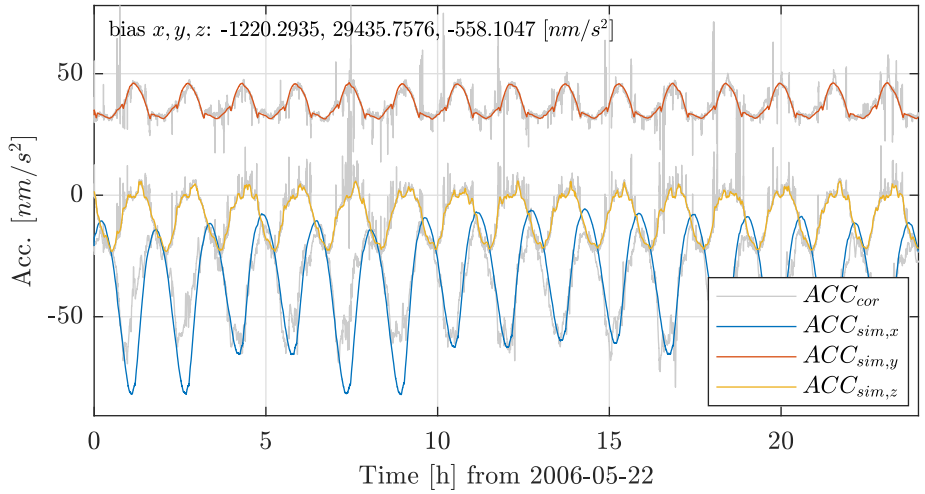

Figure 6.16: Calibrated ACC L1B data ACC_{corr} with modeled non-gravitational accelerations ACC_{sim} in SRF, from GRACE A. Bias $\vec{b}$ is estimated for one day with const. scale factors from TN-02, the estimated bias values are given in the plot. All spikes in ACC L1B data refer to attitude thruster firings.

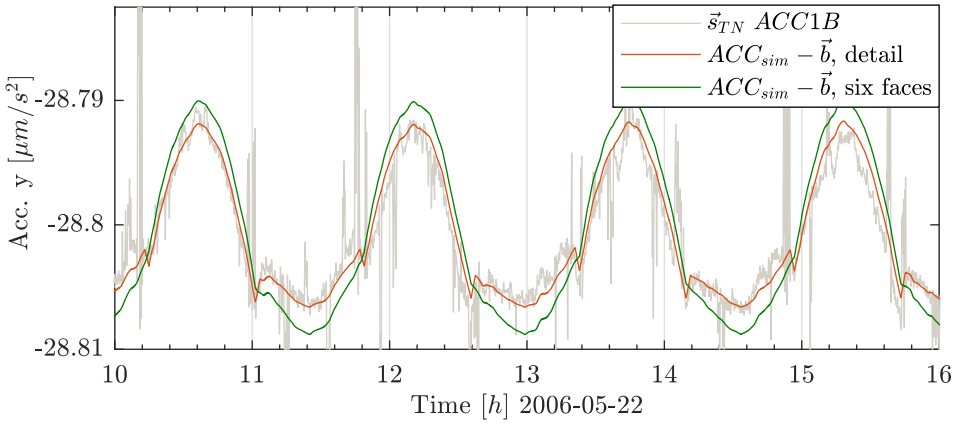

Figure 6.17: Y-component (in SRF) of modeled non-gravitational accelerations for the detailed and 6-face FEMs, both corrected with their estimated bias, respectively. All other models are kept the same. Compared to ACC L1B data for GRACE A, β' = -70.2°.

of self shadowing. Thus a β' angle not too close to 0° or ±90° is chosen (β' = -70.2°). To compare the results in one figure, the scaled ACC data $\vec{s}_{TN}ACC1B$ are plotted, which should equal the modeled accelerations minus their respective bias $\vec{b}$ (cf. Eq. 6.1). From the graph, it is clear that the detailed FEM shows better accordance with the $ACC1B$ data than the simple six face FEM. This is also obvious when comparing the residuals $r_{rms,y}$, which are 1.21 nm/s^2 and 2.56 nm/s^2 for the detailed and the 6-faces FEM, respectively. The detailed model is used for all further results in this thesis.

The static and the transient TRP models show the smallest differences for β' angles of ±90° because then no eclipses are present and the satellites are sunlit the whole time. Thus effects of heating and cooling are minimal and the differences of the *stat* and the *pde* model are very small.

In Figure 6.18 both models are compared against calibrated ACC data for a β' angle of -29.4°, hence dedicated eclipse phases are present and therefore heating and cooling

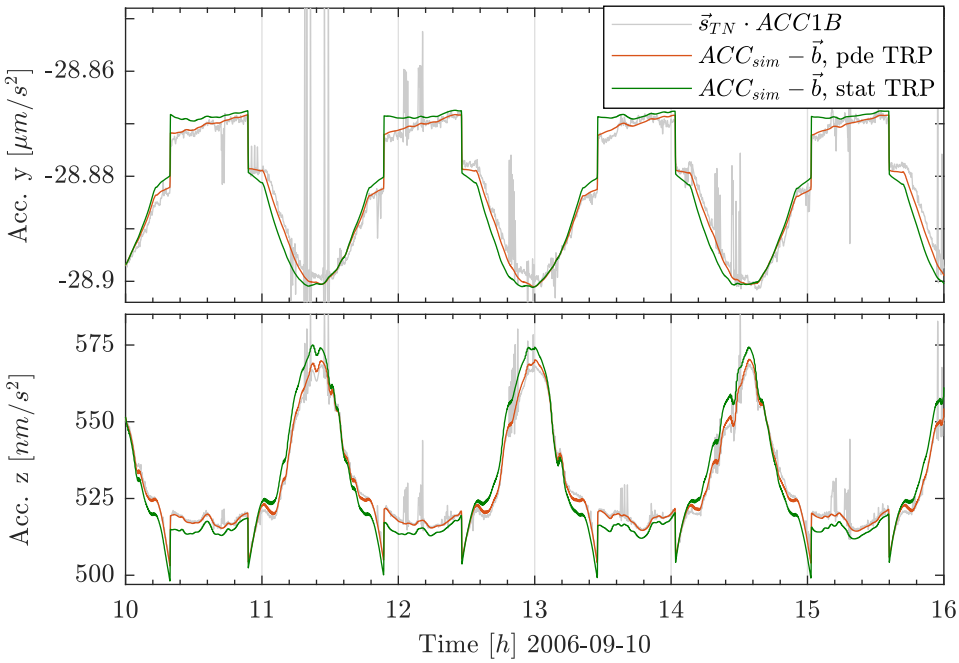

Figure 6.18: Y- and z-component (in SRF) of modeled non-gravitational accelerations with surface temperatures computed with static (*stat*) and PDE (*pde*) approach, both corrected with their estimated bias, respectively. All other models are kept the same. Compared to ACC L1B data for GRACE A, β' = -29.4°.

effects are prominent. The results are plotted as in the previous figure. The improvement of the transient TRP calculation is obvious from the comparison of the curves and again also visible in the residuals, $r_{rms,y}$ = 1.42 nm/s^2 and 2.89 nm/s^2, and $r_{rms,z}$ = 1.79 nm/s^2 and 5.11 nm/s^2 for *pde* and *stat* solution, respectively.

The computed surface temperatures, responsible for the differences, were already shown in Figure 6.14 for the *stat* and *pde* temperature models, explaining the differences.

Both figures (Fig. 6.17 and 6.18) demonstrate again the very good agreement of the precisely modeled non-gravitational accelerations with the GRACE accelerometer measurements. Even though if the bias is fitted towards the modeled accelerations, the form and trend of the curves fit pretty well.

6.2 Attitude Control

The main measurements of a GRACE-like ll-SST mission are dependent on the attitude of the satellites. The inter-satellite ranging needs an accurate pointing and the non-gravitational forces acting on the satellites are dependent on the attitude. Furthermore, accelerometer measurements are just relevant if the actual orientation is known. Thus for the modeling of a GRACE-like gravimetry mission a modeling of the attitude is important.

For the simulation of a GRACE-like mission and generation of of simulated data, here the attitude control is realized as a closed feedback control loop with models for attitude sensors and actuators. The attitude control system (ACS) for the GRACE satellites is a little more complicated than for "usual" satellites because of vibration restrictions on the satellites. Therefore, the main attitude actuators are magnetic torquers (MTQ), which work without any rotating or movable components (for details cf. Sec. 6.3.5). The

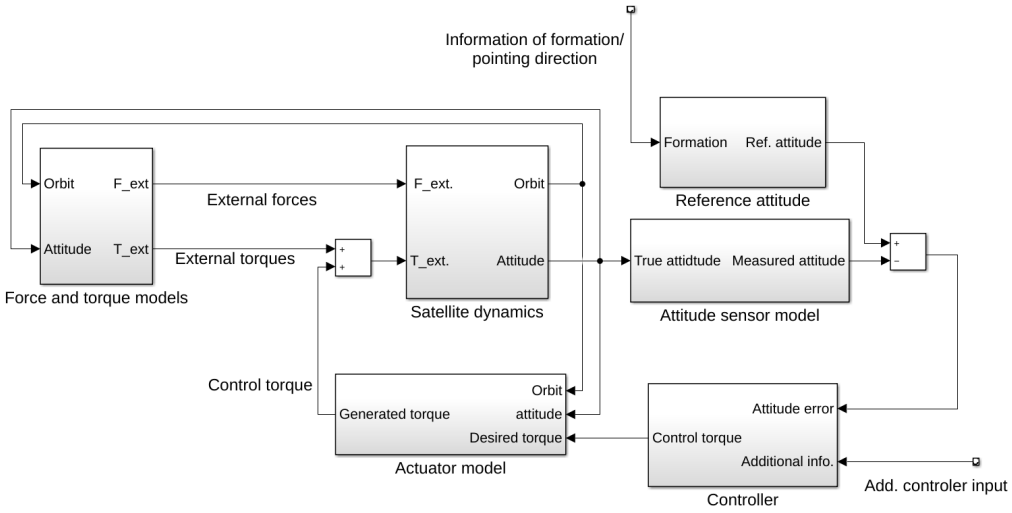

Figure 6.19: Schematic of attitude control loop.

drawback of these devices is that the generatable torque is dependent on the Earth's magnetic field, the generated torque is always perpendicular to the local magnetic field $\vec{B}$. Without a component in that direction, usually a desired torque can not be exactly generated by magnetic torquers. Therefore the attitude control is supplemented by cold gas thrusters which are activated when the actual attitude leaves predefined maximum error bands. The general control logic of the GRACE satellites is described in Herman et al. (2004). The real control algorithm is confidential and property of the satellite manufacturer and thus not publicly available.

The shown attitude controller here is the basic implementation of an investigation of different control designs and optimization strategies for a GRACE-like mission that was conducted. This controller behaves very similar to the real GRACE ones in terms of attitude evolution and errors, as well as thruster firing locations. The investigation of more optimized controllers with smaller errors and less firings (eg. for GRACE-FO or the investigation of NGGMs) would go beyond the scope here, but is published in Mashtakov et al. (2020).

The general schematic of the feedback control loop and its dependencies is shown in Figure 6.19. The control logic is explained with reference to this scheme in the following.

The satellite dynamics or the satellite states are dependent on the forces and torques acting on the satellite (cf. Sec. 2.2). In the schematic illustration the satellite states are distinguished in orbit and attitude. Here orbit is the representative for position $\vec{r}$ and velocity $\vec{v}$ and attitude comprises quaternion $\vec{q}$ and angular velocity $\vec{\omega}$. The main disturbing torque for LEO satellites is usually the Gravity Gradient Torque (GGT) (cf. Sec. 2.2.2), followed by all non-gravitational torques. As described in the sketch, forces and torques are dependent on orbit and attitude again.

The true attitude is not known. The GRACE satellites measure their attitude mainly with two star cameras, additionally gyros for the direct measurement of the angular velocity were installed, as well, but broke early in the mission. Again, the complete on-board processing of the available attitude measurements for the ACS is not known. For the simulation different approaches for the generation of an attitude solution are

investigated in terms of attitude accuracy and its influence on GFR. The different methods are described in Section 6.3.4.

From the measured attitude, the actual error to the reference attitude needs to be computed (Sec. 6.2.2). The GRACE satellites do not exchange any information directly, thus they do not know about the actual other satellite's position and attitude. Therefore the GRACE orbits are precomputed at the operation center and uploaded daily to the satellites. Hence at each time the theoretical line-of-sight direction is known on the satellites. This is used as reference attitude (Sec. 6.2.1).

From the attitude error the controller computes a control torque to reduce the error (Sec. 6.2.3 and 6.2.4). For simple feedback loop control schemes the attitude error is the only input. Usually this is complemented with additional information for example of known disturbances which then can be directly counteracted. In control theory this is referred to as feed forward control. For the implemented controller the GGT is computed with the simple model, introduced in Section 2.2.2. Additionally drag or SRP torques could be feed forward as well, but then a simple model (different to the ones used for the integration) should be be implemented. Nevertheless, drag and SRP models are much more complicated than the simple GGT model and enough real time computing resources would be needed on board the satellite (for the GRACE satellites all that is unknown). The GRACE satellites carry a magnetometer to measure the magnetic field $\vec{B}$. This is used by the controller to determine the optimally generatable torque with the actual Earths magnetic field.

The commanded control torque is then executed by the actuator. Usually the actuator has a maximum amplitude and response time or other restrictions like for the magnetic torquers. These are modeled by the actuator models. The implemented torquer and thruster models in the simulation are described in Section 6.3.5 and 6.3.6.

Subsequently the actually generated torque is feed to the dynamics calculation.

General remark to the following sections: The attitude can be represented by quaternions, rotation matrices or Euler angles. All representations have their advantages and disadvantages but are in general equivalent and interchangeable. For numeric calculations and big amount of data, usually quaternions are preferred, while Euler angles are the most descriptive and often used for visualization. Transformations can be computed by the same syntax with quaternions or matrices, as well. The quaternion algebra and its relation to rotations, as well as the conversions between the attitude representations are shown in the Appendix A.1.

6.2.1 Reference Attitude

The simulation is conducted in two steps. First the orbits of both satellites are computed together with perfect pointing, without attitude control. The resulting orbits are utilized as the "daily precomputed" orbits and used as the reference pointing for the second step, the complete simulation with attitude control for both satellites. The final orbits are slightly different to the precomputed ones because of the slightly different attitude and hence slightly different non-gravitational forces. This is like in reality where the precomputed orbits differ from the truth, as well. If the mission scenario and force models do not change, the precomputed orbit does not need to be computed for every simulation, but a saved one can be used.

The reference attitude or pointing is defined by the line of sight frame (LoS) for each satellite. It is a satellite fixed frame with its origin in the center of mass (CoM) of the

satellite. The x-axis of that frame is pointing towards the other satellite. With $\vec{r}_A$ and $\vec{r}_B$ being the position vectors of satellite A and B, respectively, it is given by

$$\vec{e}_{x,A} = \frac{\vec{r}_B - \vec{r}_A}{|\vec{r}_B - \vec{r}_A|}. \tag{6.6}$$

For an unambiguous reference pointing one more axis needs to be defined. Here the y-axis is defined to be perpendicular to $\vec{e}_{x,A}$ and the position vector $\vec{r}_A$

$$\vec{e}_{y,A} = \frac{\vec{e}_{x,A} \times \vec{r}_A}{|\vec{e}_{x,A} \times \vec{r}_A|}. \tag{6.7}$$

The third axis is perpendicular to the two other ones:

$$\vec{e}_{z,A} = \vec{e}_{x,A} \times \vec{e}_{y,A}. \tag{6.8}$$

For the other satellite B, the definition is equivalently used with $\vec{r}_B$. Assuming that the vectors $\vec{r}_A$ and $\vec{r}_B$ are given in inertial frame (ECI), the transformation matrix from inertial to LoS frame $T_{ECI2LoS}$ can be build by

$$T_{ECI2LoS,A} = T_{ref,A} = \begin{bmatrix} \vec{e}_{x,A}^T \\ \vec{e}_{y,A}^T \\ \vec{e}_{z,A}^T \end{bmatrix}. \tag{6.9}$$

With this the reference attitude is known. The control algorithm computes a control torque based on the difference between the actual attitude and the reference attitude and additionally of the difference between actual and desired angular velocity. Therefore the reference angular velocity $\vec{\omega}_{ref}$ needs to be determined, as well.

The angular velocity of a reference frame (ref) with respect to an inertial frame (i), in complete notation $\vec{\omega}_{i,ref}^{ref}$, or simply $\vec{\omega}_{ref}$, satisfies Poisson's differential equation (eg. Kabamba and Girard, 2014)

$$\dot{T}_{i2ref} = -[\vec{\omega}_{ref}]_x \, T_{i2ref}, \tag{6.10}$$

with $[\vec{\omega}_{ref}]_x$ being the skew symmetric matrix of the cross product

$$[\vec{\omega}]_x = \begin{bmatrix} 0 & -\omega_z & \omega_y \\ \omega_z & 0 & -\omega_x \\ -\omega_y & \omega_x & 0 \end{bmatrix}. \tag{6.11}$$

Rearranging equation (6.10) gives the desired reference angular velocity

$$[\vec{\omega}_{ref}]_x = \dot{T}_{i2ref} T_{i2ref}^T. \tag{6.12}$$

For the computation of the derivative of the transformation matrix $\dot{T}_{i2ref}$ the derivatives of the unit vectors (Eq. 6.9) need to be determined. Therefore the definition of the LoS frame from Equations (6.6) to (6.8) is rearranged, making it easier to determine the derivatives. The definition of the first axis $\vec{e}_{x,A}$ stays the same. The z-axis $\vec{e}_{z,A}$ is defined by

$$\vec{e}_{z,A} = -\frac{\vec{r}_A - \vec{e}_{x,A}(\vec{e}_{x,A} \cdot \vec{r}_A)}{|\vec{r}_A - \vec{e}_{x,A}(\vec{e}_{x,A} \cdot \vec{r}_A)|}, \tag{6.13}$$

where $\cdot$ denotes the scalar product. $\vec{e}_{x,A}(\vec{e}_{x,A} \cdot \vec{r}_A)$ is the orthogonal projection of $\vec{r}_A$ on the direction of $\vec{e}_{x,A}$. The second axis is then given by

$$\vec{e}_{y,A} = \vec{e}_{z,A} \times \vec{e}_{x,A}. \tag{6.14}$$

This definition is completely equivalent to the one before.

The derivative of a vector divided by its norm $\partial/\partial t(\vec{r}/|\vec{r}|)$ can be computed with the definition of the norm $|\vec{r}|^2 = (\vec{r} \cdot \vec{r})$ and the quotient rule.

$$\frac{\partial}{\partial t}\frac{\vec{r}}{|\vec{r}|} = \frac{\dot{\vec{r}} - 1/|\vec{r}|^2(\vec{r} \cdot \dot{\vec{r}})}{|\vec{r}|}. \tag{6.15}$$

With this the derivatives of the unit vectors are

$$\dot{\vec{e}}_{x,A} = \frac{\vec{v}_B - \vec{v}_A - \vec{e}_{x,A}(\vec{e}_{x,A} \cdot [\vec{v}_B - \vec{v}_A])}{|\vec{r}_B - \vec{r}_A|} \tag{6.16}$$

$$\begin{aligned} \dot{\vec{e}}_{z,A} &= \frac{\vec{h} - \vec{e}_{z,A}(\vec{e}_{z,A} \cdot \vec{h})}{|\vec{r}_A - \vec{e}_{x,A}(\vec{e}_{x,A} \cdot \vec{r}_A)|}, \qquad \text{with} \\ \vec{h} &= \vec{v}_A - \dot{\vec{e}}_{x,A}(\vec{e}_{x,A} \cdot \vec{r}_A) - \vec{e}_{x,A}[(\vec{e}_{x,A} \cdot \vec{v}_A) + (\dot{\vec{e}}_{x,A} \cdot \vec{r}_A)] \end{aligned} \tag{6.17}$$

$$\dot{\vec{e}}_{y,A} = \dot{\vec{e}}_{z,A} \times \vec{e}_{x,A} + \vec{e}_{z,A} \times \dot{\vec{e}}_{x,A}. \tag{6.18}$$

The derivative of the reference transformation matrix is then given by

$$\dot{T}_{ECI2LoS,A} = \dot{T}_{ref,A} = \begin{bmatrix} \dot{\vec{e}}_{x,A}^T \\ \dot{\vec{e}}_{y,A}^T \\ \dot{\vec{e}}_{z,A}^T \end{bmatrix}. \tag{6.19}$$

With Equation (6.12) and the matrices $T_{ref,A}$ and $\dot{T}_{ref,A}$ the reference angular velocity follows as the elements of the resulting matrix

$$\begin{aligned} \omega_{x,ref,A} &= -(\dot{T}_{ref,A}\, T_{i2ref}^T)_{2,3}, \\ \omega_{y,ref,A} &= (\dot{T}_{ref,A}\, T_{i2ref}^T)_{1,3}, \\ \omega_{z,ref,A} &= -(\dot{T}_{ref,A}\, T_{i2ref}^T)_{1,2}. \end{aligned} \tag{6.20}$$

6.2.2 Relative Attitude

With the reference attitude at hand, the attitude error, the difference between reference and actual attitude, can be computed. It is also referred to as relative attitude and relative angular velocity, respectively. The actual attitude of the satellite body frame is given as T_{i2b} or as quaternion q_{i2b} and the angular velocity in the satellite body frame with respect to the inertial frame by $\vec{\omega}_{i,b}^b$ or simply $\vec{\omega}$.

The relative attitude T_{rel} or as quaternion q_{rel} is the transformation from reference to satellite body frame. With the previous definitions it is given by

$$T_{rel,A} = T_{ref2b,A} = T_{i2b,A}\, T_{i2ref,A}^T. \tag{6.21}$$

The definition could be switched as well (from body to reference frame), being just a preference.

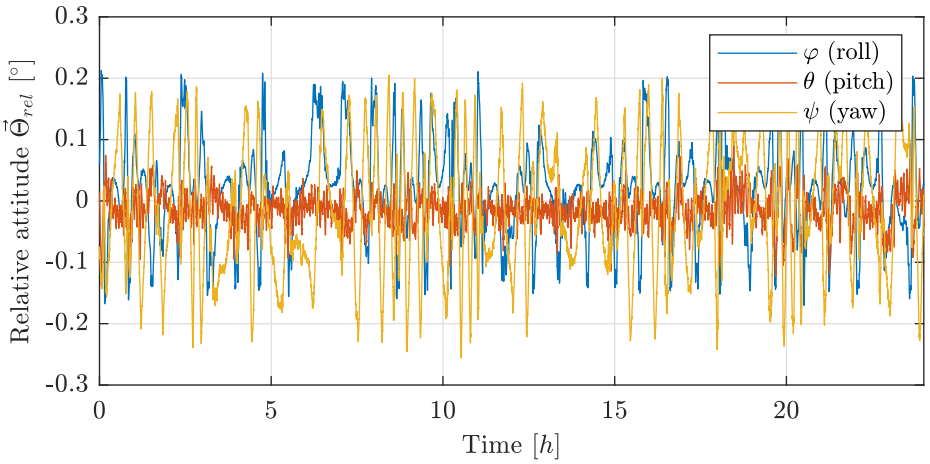

Figure 6.20: Relative attitude $\vec{\Theta}_{rel}$ of GRACE B on 2005-05-01 in Euler angle representation, computed from SCA, GNV and VKB data.

The relative angular velocity $\vec{\omega}_{rel}$ is the difference of the angular velocities in the body frame:

$$\vec{\omega}_{rel,A} = \vec{\omega}^{b}_{b,rel,A} = \vec{\omega} - T_{ref2b,A}\,\vec{\omega}_{ref}. \tag{6.22}$$

The relative attitude may be plotted best in Euler angle representation $\vec{\Theta}_{rel}$ with the three angles φ (roll), θ (pitch) and ψ (yaw). With the usual definition that roll is a rotation around the x-axis, pitch around the y-axis and yaw around the z-axis. The 12 possible rotation sequences for the computation of Euler angles are often not stated, here always x-y-z is used (for details and conversion of the attitude representations see Appendix A.1.3). Nevertheless, for the very small deviations of the attitude in the GRACE fine pointing mode, the result for all sequences is about the same.

For an arbitrary day, the relative attitude of GRACE B is shown in Figure 6.20, computed from the SCA L1B quaternion data q_{i2b} and the GNV L1B data for the reference pointing. Furthermore, the VKB data were considered, compensating for a misalignment of the K-band antenna frame from the satellite body frame, which is not of interest here and not further discussed.

The trend of the relative attitude changes slightly from day to day and over the year in terms of frequency. The allowed attitude limits of each axis are distinctly visible in the plot. Also the thruster firings are visible, creating the abrupt changes in attitude.

The attitude error of the pitch axis is the lowest and usually does not exceed the limit. This is because of the orientation of the magnetic field with respect to the pitch axis, which is always about rectangular for the polar GRACE orbit. This means that the axis is always controllable by the MTQs. For roll and yaw axis this is not the case. During the orbit both axis have times when they are about parallel to the magnetic field lines, and thus not controllable by the MTQs (for roll around the equator and for yaw over the poles).

The attitude thruster firings for the same day as in the figure before are depicted in Figure 6.21 as angular momentum. An angular momentum is calculated by the firing duration times thrust times the respective lever arm. Comparing both figures shows that the abrupt changes in attitude are always created by a firing. More exactly, usually a series of firings is conducted, visible when zooming in the plot.

The positions of each thruster firing over the Earth is shown in Figure 6.22 for each axis for the time span of five days. Here the previously mentioned shortcomings of the

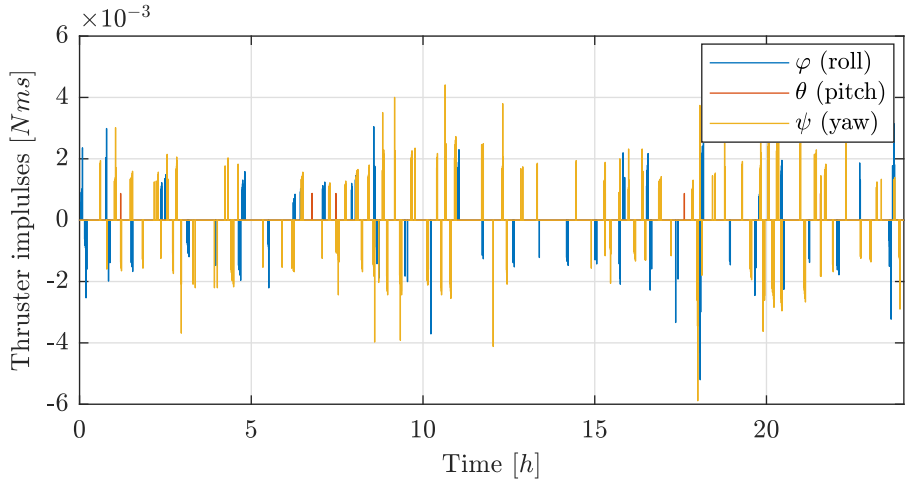

Figure 6.21: Thruster firing angular momentum (firing duration times thrust times lever arm) of GRACE B on 2005-05-01, computed from THR L1B data.

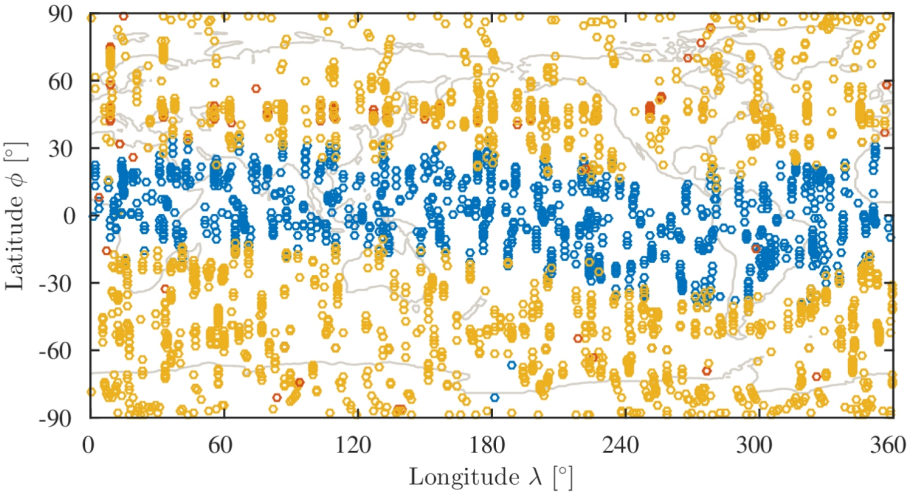

Figure 6.22: Position of firings for the three axes roll (blue), pitch (red) and yaw (yellow) for 5 days of one GRACE satellite.

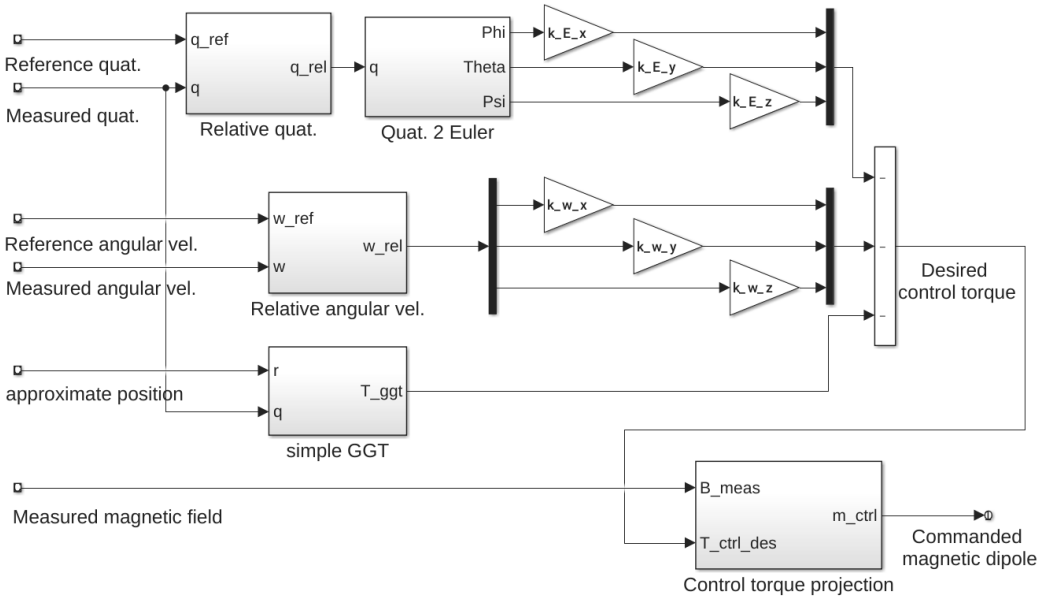

Figure 6.23: Schematic of magnetic torquer attitude control loop.

MTQ control is distinctly visible for roll and yaw axes around the equator and poles, respectively. Pitch firings are relatively rare and randomly distributed. It is also visible that a firing usually consist of a short series of firings.

6.2.3 Modeled Magnetic Torquer Attitude Controller

The magnetic torquer (MTQ) continuous controller builds the main control loop for the satellites. The thrusters are not used continuously, but just if the actual attitude leaves the predefined limits. For GRACE the limits are given as the maximal Euler angles of the relative attitude (cf. Sec. 6.2.2). The maximal Euler angles $\vec{\Theta}_{max}$ are $\pm$ 0.17°, 0.23°, 0.28°, for roll (φ), pitch (θ) and yaw axis (ψ), respectively.

As noted before, the implemented controller is a kind of a proportional-derivative (PD) controller. Meaning it uses the error of the control variable itself and its derivative to compute a correction. Here, the relative attitude in Euler angle representation $\vec{\Theta}_{rel}$ and the relative angular velocity $\vec{\omega}_{rel}$ are used. The angular velocity is not directly the derivative of the Euler angles, but closely connected to it. The Euler angles are just a different representation of the relative attitude in matrix or quaternion form and directly follow from $T_{rel,A}$ (Eq. 6.21), see the conversions in the Appendix A.1.

The error of each axis is controlled separately, ignoring the coupling of the axes from the rotational dynamics (cf. Eq. 2.7). For the very small angle errors and the nearly diagonal moment of inertia matrix I this works well (in Mashtakov et al. (2020) we considered this as well for the control torque computations).

The MTQ control scheme is depicted in Figure 6.23. The desired control torque $\vec{T}_{ctrl,des}$ is composed of three parts. The proportional, derivative and the feed forward disturbance mitigation torque.

$$\vec{T}_{ctrl,des} = -\vec{k}_{\omega}\vec{\omega}_{rel} - \vec{k}_{\Theta}\vec{\Theta}_{rel} - \vec{T}_{dist}. \tag{6.23}$$

with the control gains $\vec{k}_{\omega}$ and $\vec{k}_{\Theta}$. For all simulations just the simple computation of the GGT (Eq. 2.13) is used as known feed forward disturbance $\vec{T}_{dist}$. With the inter-satellite

Table 6.3: Attitude related parameters of the simulation

		Axis		
Parameter	Symbol	x (roll φ)	y (pitch θ)	z (yaw ψ)
max. Euler angles	$\vec{\Theta}_{max}$	$\pm$ 0.17°	0.23°	0.28°
max. MTQ dipole	m_{max}	30 m^2A	30 m^2A	30 m^2A
MTQ diff. gain	$\vec{k}_{\omega}$	3.08 $Nms/°$	10.25 $Nms/°$	9.52 $Nms/°$
MTQ prop. gain	$\vec{k}_{\Theta}$	0.0015 $Nm/°$	0.004 $Nm/°$	0.0034 $Nm/°$
nominal thrust	F_{thr}	10 mN	10 mN	10 mN
lever arm	l_{Θ}	0.3 m	1.45 m	1.45 m
THR hold time	Δt_{hold}	100 s	100 s	100 s
averaging time	$\Delta t_{d\Theta}$	200 s	1000 s	60 s
THR diff. gain	$\vec{k}_{d\Theta}$	2000 $s^2/°$	8800 $s^2/°$	3000 $s^2/°$
THR prop. gain	$\vec{k}_{\Theta}$	185 $s/°$	68 $s/°$	16 $s/°$
MoI diagonal	I	104.3 kgm^2	408 kgm^2	473.4 kgm^2

difference of about 200 km the satellites have a flight path angle of about one degree, making the GGT by far the biggest disturbance.

Usually the desired torque $\vec{T}_{ctrl,des}$ can not be generated by the MTQs. The generatable torque is limited by Earth's magnetic field $\vec{B}$. With $\vec{m}$ being the magnetic dipole generated by the MTQs, the resulting torque in the magnetic field is given by

$$\vec{T}_{MTQ} = \vec{m} \times \vec{B}. \tag{6.24}$$

With a perpendicular, or at least not parallel, composition of three MTQs each $\vec{m}$ can be generated, just limited by the properties of the MTQs and available electric power/ current. For the GRACE satellites, the three MTQs are aligned with the main SRF axes.

Therefore, a generatable torque, that is closest to the desired torque needs to be determined. From Equation (6.24) follows that a torque can just be generated which is perpendicular to $\vec{B}$. The optimal way is to determine the torque which is projected onto the plane perpendicular to $\vec{B}$. Thus the optimal dipole moment without producing unnecessary dipole moment $\vec{m}_{ctrl}$ is

$$\vec{m}_{ctrl} = \frac{1}{(\vec{B} \cdot \vec{B})} \vec{B} \times \vec{T}_{ctrl,des}. \tag{6.25}$$

The maximal generatable dipole moment $\vec{m}$ for GRACE is 30 m^2A for all three MTQ axes. In the simulation this is set as an upper limit. However, in the usual attitude mode this limit is by far not exhausted.

All relevant attitude parameters for the simulation are summarized in Table 6.3.

In the simulation the measurement of the magnetic field is assumed to have a Gaussian noise of $5 * 10^{-7}$ T. This is a very simple magnetometer model, but the influence of the magnetometer accuracy is not significant for the resulting attitude.

The magnetic field and the true generated control torque are computed with the IGRF 11 (International Geomagnetic Reference Field) model (Finlay et al., 2010).

6.2.4 Modeled Thruster Attitude Controller

The thruster attitude controller is just activated if the actual measured attitude leaves the predefined limits (cf. Tab. 6.3). It is implemented in a way that it behaves similar to the actual GRACE thruster firings (see below). Even though the control algorithm is not known, the epoch of each firing and the duration of the firings are available. Furthermore, each firing is visible in the attitude (SCA) data (cf. Fig. 6.20). The GRACE satellites have six pairs of thrusters, to generate positive and negative torques around each body axis (actually each satellite has 12 thrusters for redundancy). The thrusters have a nominal thrust of $F_{thr} = 10\ mN$ and the generated torque is controlled by the firing duration. The position of each thruster, and thus the perpendicular lever arm l_Θ for each axis, is known (Bettadpur, 2012b) and given in Table 6.3, as well.

The main characteristics of the GRACE attitude thruster controller are listed in the following:

- Thrusters of one pair always fire for the same time. Thus in the perfect case with no mounting and timing errors no force on the satellite is applied.
- After a thruster firing the thrusters are on hold for a certain time Δt_{hold} to observe the reaction of the satellite before further thruster activation.
- Just one axis is controlled at one time. If the error in more axis is out of the limit, the biggest error is counteracted first.

In the simulation these characteristics are implemented and described in the following. The control variable is the thruster pair activation time Δt_{thr}. For the GRACE satellites, the thruster activation times are between 10 ms to maximal 400 ms. For the simulation with an integration step size of 1 to 5 s this means that the applied thruster torque needs to be distributed over one step size. With the control variable Δt_{thr}, the applied torque over one step size h, exemplary for the roll-axis, is

$$T_{thr,x} = \frac{2\, F_{thr}\, l_\varphi\, \Delta t_{thr}}{h}. \tag{6.26}$$

For the comparably small external and control torques acting on the satellite, and the slow rotational motion, the blurring of the impulse over a slightly longer time in that high frequency region does not make a difference (see also 6.3.6).

The generated torque, or activation time is controlled by a PD-controller using the error of the attitude q_{rel} in Euler angle representation $\vec{\Theta}_{rel}$, and for the derivative part the mean of the numerical derivative of Θ_{rel} from the previous $\Delta t_{d\Theta}$ seconds is used. Because the controller is not continuous, the mean value is more appropriate. Hence the thruster activation time is given by

$$\Delta t_{thr} = -\vec{k}_{d\Theta}\, \frac{1}{\Delta t_{d\Theta}} \int_{t-\Delta t_{d\Theta}}^{t} \dot{\vec{\Theta}}_{rel}\ dt - \vec{k}_\Theta \vec{\Theta}_{rel}. \tag{6.27}$$

The gains and parameters for the thruster control are tuned by trial and error with the main goal to achieve a similar characteristic as for GRACE. We show a more effective way of determining the thruster control gains for an improved thruster controller in Mashtakov et al. (2020). All gains and parameters are given in Table 6.3, as well.

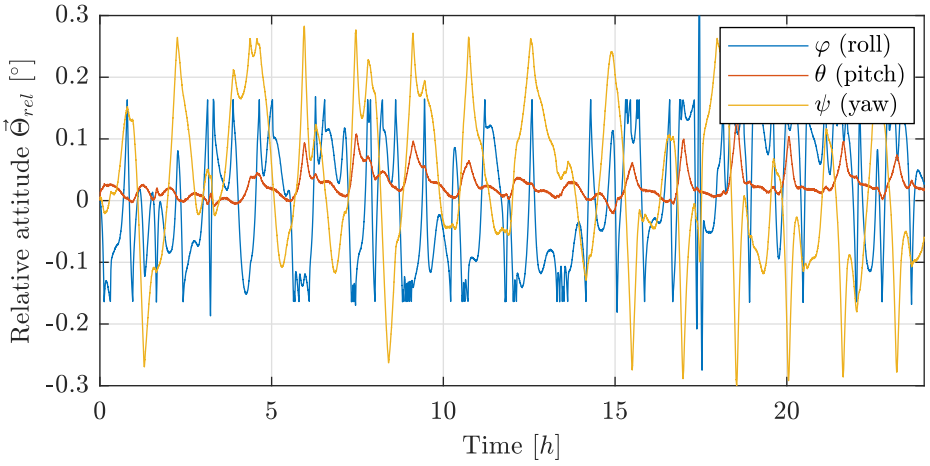

Figure 6.24: Relative attitude $\vec{\Theta}_{rel}$ of one simulated satellite in Euler angle representation.

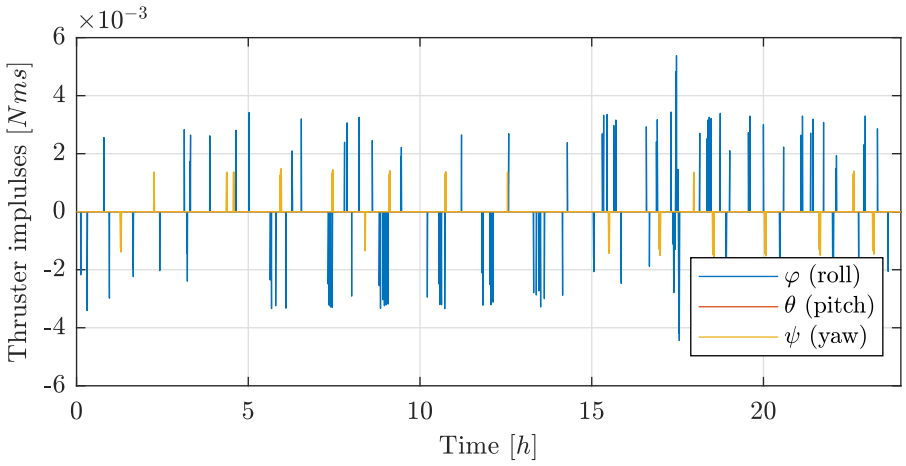

Figure 6.25: Thruster firing angular momentum (firing duration times thrust times lever arm) of one simulated satellite.

6.2.5 Attitude Simulation Results

The relative attitude $\vec{\Theta}_{rel}$ for a simulation with the implemented controller is shown in Figure 6.24 for one day. The corresponding thruster firings represented as angular momentum are shown in Figure 6.25 for the three axes. For the simulation the attitude sensor model with the Kalman filter (3.) was used, as described in Section 6.3.4.

Firings for the pitch axis θ are rare because the axis is usually controllable by the MQTs and not exceeding the limits. For roll and yaw axes this is different and regular firings are required to keep the attitude in the desired limits. Compared to the exemplary day of GRACE attitude data, shown in Figures 6.20 and 6.21, the number of firings is slightly lower. On the GRACE satellites usually more firings are successively conducted in a row, rather than using one stronger impulse. This is also distinct when comparing the positions of the firings over the Earth surface in Figures 6.26 and 6.22 for the simulated and GRACE data, respectively. Nevertheless, the positions of the firings show in general the same pattern. Also the trend of the resulting attitude data is similar enough for the purpose of generating simulated GRACE-like data for GFR.

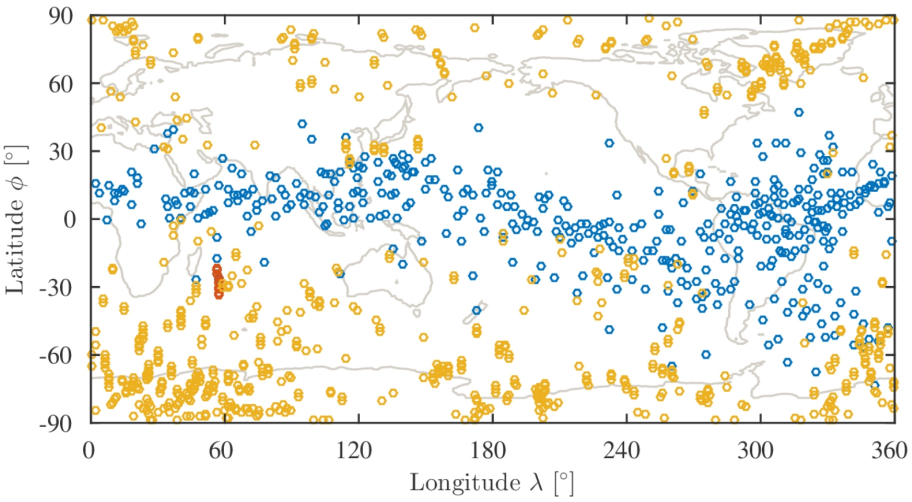

Figure 6.26: Position of firings for the three axes roll (blue), pitch (red) and yaw (yellow) for 10 days of one simulated satellite.

6.3 Instrument (Noise) Models

For the analysis in Chapter 8 simulated measurement data are generated for all major instruments of a satellite gravimetry mission. Different noise models for these instruments are investigated. The approach here is to add specific noise to the "true" values obtained from the simulations. The real noise behavior of the different instruments is usually not exactly known, but their general characteristics are. In the following the used models for the major instruments and its parameters and variations are introduced and some results are displayed.

Usually noise characteristics of instruments or sensors are described and given in terms of Amplitude Spectral Densities (ASD) or Power Spectral Densities (PSD). This representation is frequently used throughout this thesis, also for the analysis of GFR results. Therefore the ASD and PSD are briefly introduced and discussed in the Appendix A.2, as well as its computation used for all plots in this thesis.

6.3.1 Inter Satellite Ranging (KBR)

The principle measurement quantity of the KBR system is the range. Range-rate and range-acceleration follow from the range by differentiation. The theoretical noise sources of the KBR inter-satellite ranging device are investigated in detail by Kim (2000).

The main sources are the oscillator noise and the system noise. The GRACE satellites use ultra stable oscillators (USO) which were already flight tested with a classified noise behavior from another missions. Its characteristic is a slope proportional to $1/f^2$ for low frequencies in the ASD.

The system noise arises from the receiver subsystem and is dependent on the separation of the satellites. It can be modeled as white noise with about 1 $\mu m/\sqrt{Hz}$ in the ASD for a separation of about 220 km.

Additionally, a minor noise source exists, which is a relation between the satellites pointing accuracy and KBR accuracy. This is not considered and analyzed in this thesis.

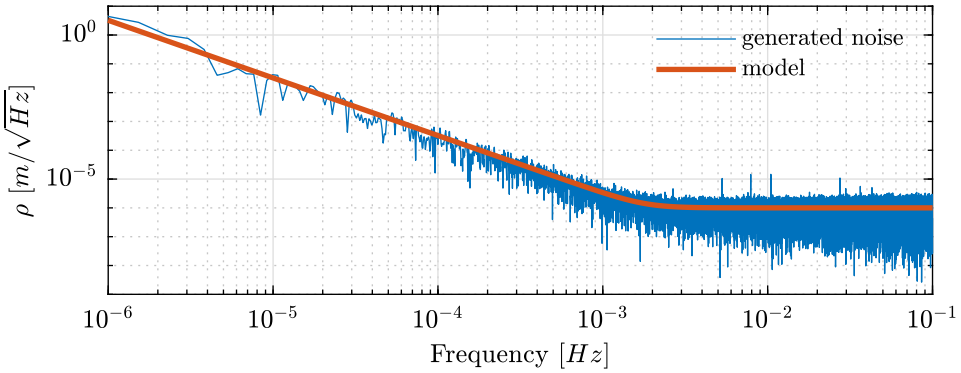

Figure 6.27: ASD of the KBR noise model and of the generated noise time series.

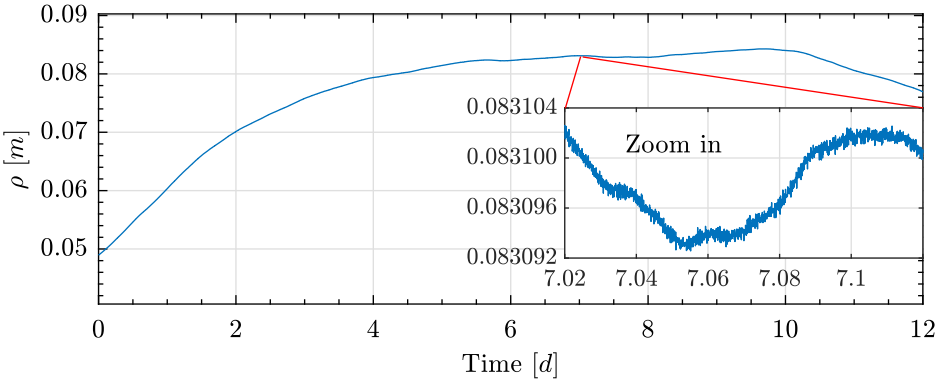

Figure 6.28: Time series of the generated KBR range noise.

The combined noise model is given as ASD function with the unit $[m/\sqrt{Hz}]$ as

$$d_{KBR}(f) = 10^{-6}\sqrt{1+\left(\frac{0.0018Hz}{f}\right)^4}. \tag{6.28}$$

The model is shown in Figure 6.27 in terms of ASD together with generated noise for 30 days. The high frequency noise level of this model is varied for the sensitivity studies in Chapter 8.4. Therefore the pre-factor 10^{-6} in Equation (6.28) is varied, shifting the whole model upwards. The pre-factor, referred to as $\sigma_{hf,KBR}$, is investigated in the range of 1e-5 to 5e-7 m. The value of $\sigma_{hf,KBR}$ = 1e-6 m is used as default.

For the generation of noise time series from ASD models, the LISA Technology Package Data Analysis (LTPDA) toolbox (https://www.elisascience.org/ltpda/) for MATLAB is used. The function *noisegen1D* uses Franklin's random noise generator method (Franklin, 1965) for noise generation with a given spectral density. The noise is generated with a sampling frequency of 0.2 Hz and a minimal frequency of $3.8 * 10^{-7}$ Hz (30 days).

The generated noise time series from the ASD model is depicted in Figure 6.28. The low frequency variation is distinctly visible, just the zoom-in reveals the high frequency noise content.

For GFR usually the range-rate is used, which is obtained by derivation. Mathematically this means a multiplication by $2\pi f$ in the frequency domain. The noise time series is obtained by numerical derivation of the range, as it is done in the real GRACE processing. The resulting range-rate noise model and the derivated noise are shown as ASD in Figure 6.29 and the noise time series in Figure 6.30.

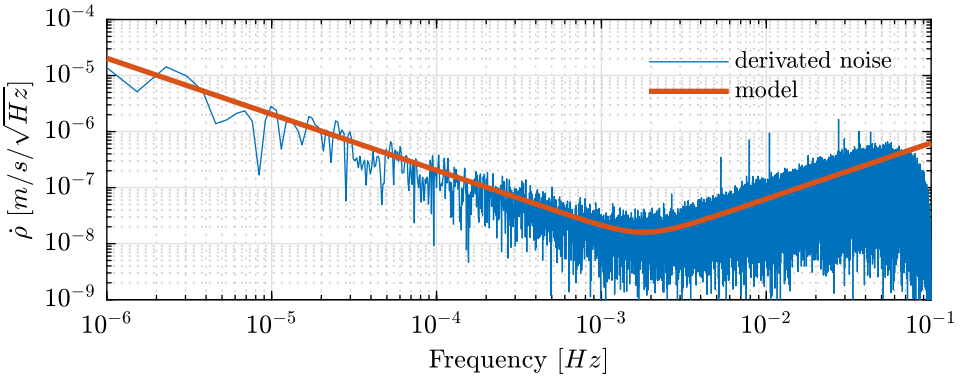

Figure 6.29: ASD of the KBR range-rate noise model and of the derivated noise time series.

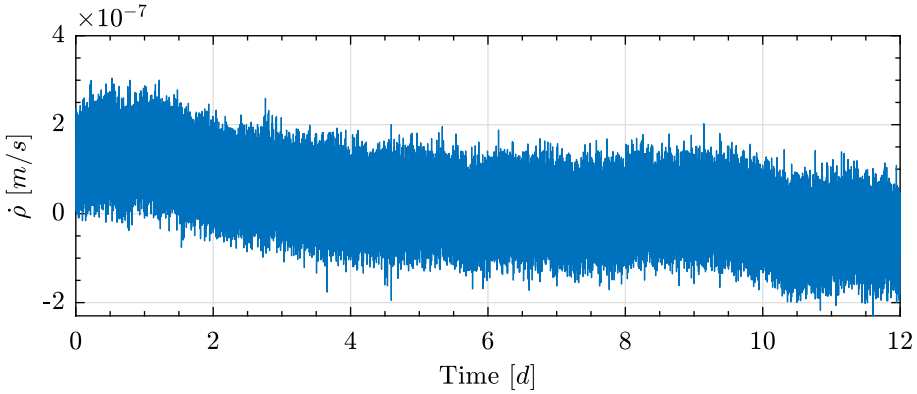

Figure 6.30: Time series of the derivated KBR range-rate noise.

On the left hand side of the spectrum, the low frequency noise is attenuated by the derivation, the high bias and drift are vanishing in the time series, which is one reason that rather range-rate is used for GFR instead of the range. On the right hand side, the high frequency noise is amplified.

6.3.2 Accelerometer (ACC)

Besides the inter-satellite ranging, the accelerometers are the other crucial instrument of a ll-SST gravimetry mission. It allows to distinguish a change of range or range-rate due to a gravitational or a non-gravitational disturbing source. Hence, the noise of the instrument has a major influence on the achievable gravity field accuracy.

The real noise of the GRACE on-board accelerometers is unknown. From the ACC data it is not completely possible to distinguish signal and noise effects. The same holds for the residuals and deviations from POD and GFR estimations: The noise of all sensors (KBR, ACC, SCA, GNV) and errors of the estimation process are combined and the distinction what relates to which source is not completely possible, as well. From the general physical function of the device an assumption of the noise level and its spectrum can be drawn. Nevertheless, the CHAMP, GRACE and GOCE missions showed, that the real devices on the satellites did not fully agree with the predictions and some not completely understood effects occurred. Furthermore, the space environment and interactions of the device with the satellite are hard to predict and also not totally measured on the actual satellites. Thus different models for the noise of the GRACE accelerometers exist.

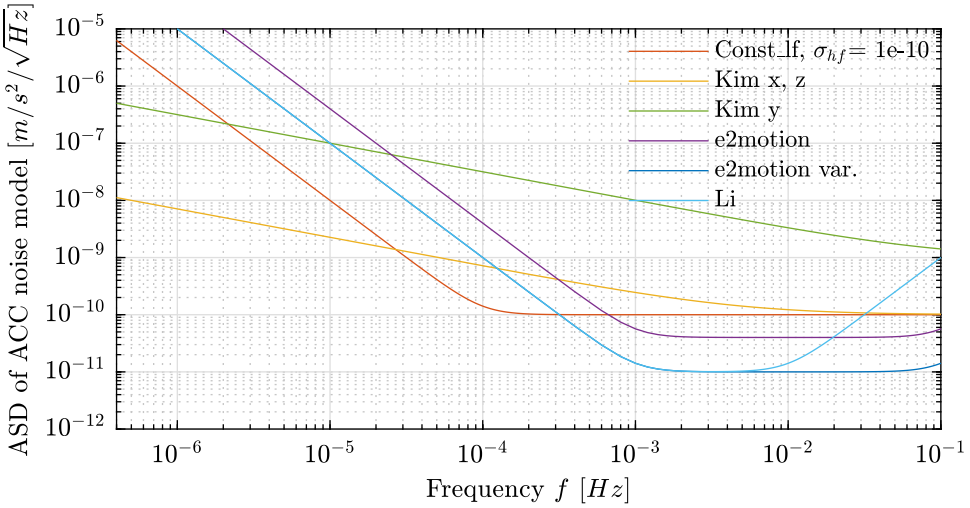

Figure 6.31: ASD of the different ACC noise models

In this thesis some prominent models are used to determine their influence on the resulting gravity field solutions and especially the influence of the main parameters of these models. Subsequently, the results are compared to the ones of real GRACE data (cf. Ch. 8.5).

From the literature the following models are used: The model from Kim (2000), which is frequently used for NGGM studies and for instance by Darbeheshti et al. (2017). It technically consists of two models, because for the accelerometer y-axis a different model is used than for x- and z-axis. Here the model is referred to as Kim y and Kim x,z.

A more recent, frequently used model is based on the e2motion NGGM project (Gruber et al., 2014). It is used here in two variations, referred to as e2motion and e2motion var. It is also used by eg. Li et al. (2017) with another slight variation, here referred to as Li. Furthermore, this is also used by eg. Daras and Pail (2017) and Hauk and Pail (2019) with clipped amplitudes in the very low frequencies, probably reasonable for already calibrated ACC data (not shown and used here).

Based on models from the literature and GRACE ACC data analysis, a further model is developed for which the high frequency noise level is varied. It is referred to as Const_lf. Furthermore, a model with simply white noise, with variance σ_w, is used in the evaluation for comparison.

The literature models are shown in terms of their ASD in Figure 6.31 and the Const_lf model in Figure 6.32 for different values of the parameter σ_{hf} which determines the high frequency noise level.

The Kim model shows a small slope of the low frequencies, starting earlier than for the other models. The amplitude of the low frequency noise is much to low compared to the real GRACE data. The later models have a steeper slope and have higher low frequency noise. The Kim model shows a very big difference between y- and x-,z-axis. In the real GRACE data this is definitely not that prominent.

The e2motion model has an increase of the noise at the very right end of the spectrum. The e2motion var. model is just shifted slightly down. The Li model agrees with the e2motion var. model besides the rise of the high frequency noise.

For the Const_lf model just the high frequency noise level is varied, but the low frequency part stays the same, hence the name. The slope of the low frequency starts

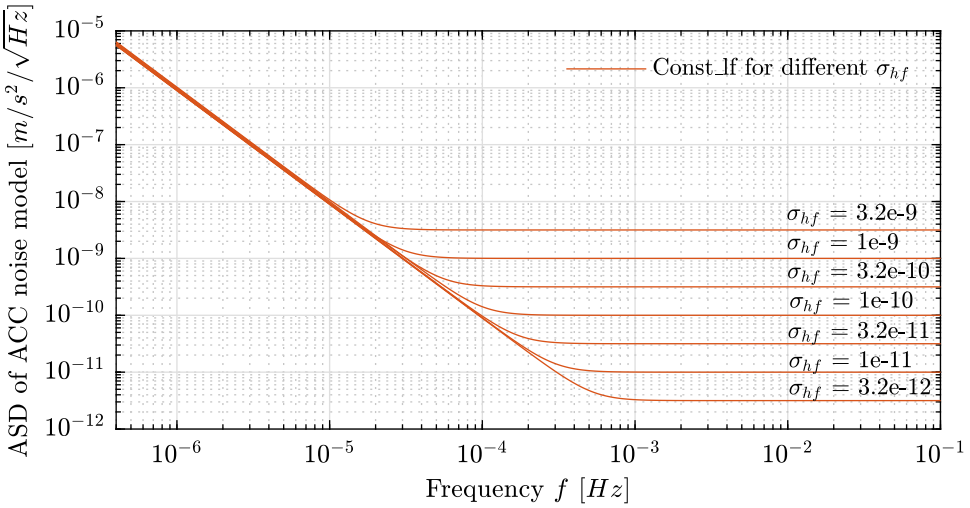

Figure 6.32: ASD of the Const_lf ACC noise model for different values of the σ_{hf} parameter.

slightly later than for the other models. The high frequency noise of the GRACE L1B data (which are filtered) is below 1e-10 $m/s^2/\sqrt{Hz}$. Even though the raw ACC data may have another high frequency characteristic, the down-sampled and filtered (cf. Sec. 3.3) L1B data should be the basis for models, because these data are used for POD and GFR processing.

The equations for all models are given in the following as ASD functions with the unit $[m/s^2/\sqrt{Hz}]$.

$$\text{Kim x,z: } d_{ACC}(f) = 10^{-10}\sqrt{1+\frac{0.005Hz}{f}} \tag{6.29}$$

$$\text{Kim y: } d_{ACC}(f) = 10^{-9}\sqrt{1+\frac{0.1Hz}{f}} \tag{6.30}$$

$$\text{e2motion: } d_{ACC}(f) = 4*10^{-11}\sqrt{1+\left(\frac{0.001Hz}{f}\right)^4+\left(\frac{f}{0.1Hz}\right)^4} \tag{6.31}$$

$$\text{e2motion var.: } d_{ACC}(f) = 10^{-11}\sqrt{1+\left(\frac{0.001Hz}{f}\right)^4+\left(\frac{f}{0.1Hz}\right)^4} \tag{6.32}$$

$$\text{Li: } d_{ACC}(f) = 10^{-11}\sqrt{1+\left(\frac{0.001Hz}{f}\right)^4+\left(\frac{f}{0.01Hz}\right)^4} \tag{6.33}$$

$$\text{Const lf: } d_{ACC}(f) = \sigma_{hf}\sqrt{1+\left(\frac{f_k}{f}\right)^4} \tag{6.34}$$

For the Const_lf model the frequency f_k where the slope starts is chosen according to σ_{hf} to result in the same low frequency noise characteristic.

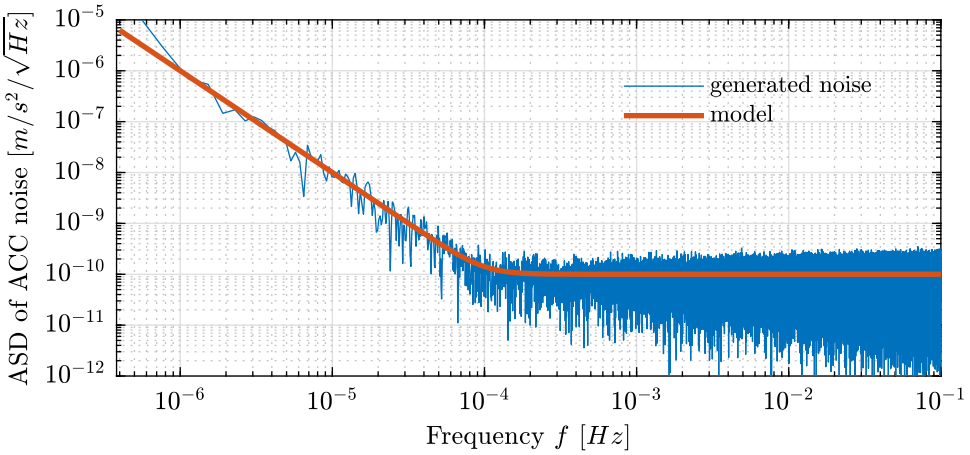

Figure 6.33: ASD of generated noise from the Const_lf model with σ_{hf} = 1e-10 for one axis.

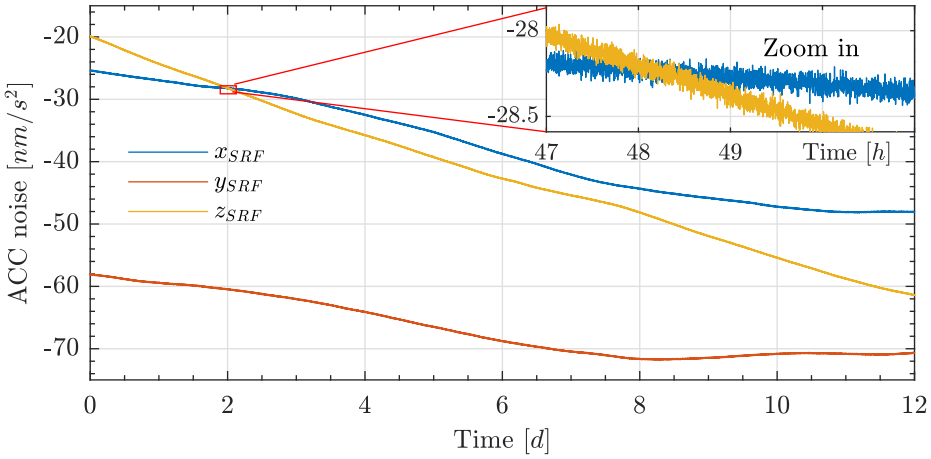

Figure 6.34: Time series of generated noise from the Const_lf model with σ_{hf} = 1e-10 for the three accelerometer axis for one satellite.

Again, noise time series are generated with the LTPDA toolbox for 30 days. For each accelerometer axis and each satellite different realizations of the same noise model are generated. In Figure 6.33 the ASDs of generated noise and of the model are exemplary shown for the Const_lf model with σ_{hf} = 1e-10. The time series of that noise is plotted in Figure 6.34 for a time span of 12 days and for all three accelerometer axis. The low frequency noise is obviously visible. The high frequency noise is depicted in the zoom-in.

6.3.3 Orbit Solution (GNV and KOS)

An orbit solution of the satellites, so mainly 3d-position data, may be obtained by dynamic (GNV) or kinematic (KOS) orbit determination (cf. Sec. 3.2.3 and 4.1). The results of both techniques are very similar and for the simulation of GRACE-like observation data no difference is made between them, here.

In the literature the noise characteristic of the orbit data is usually modeled as white noise for all three axes (eg. Darbeheshti et al., 2017). In reality this is not necessarily the case. Even though, at least the kinematic solution should not contain correlated noise, usually some small periodic errors are still contained in the solutions (eg. Weinbach and

Table 6.4: Star camera model parameters in each star camera frame

		Axis		
Parameter	Unit	boresight φ (roll)	θ (pitch)	ψ (yaw)
White noise σ	*arcsec*	40	5	5
optional misalignment SC1	*arcsec*	37	-15	84
optional misalignment SC2	*arcsec*	-71	58	-18

Schön, 2013; Zehentner and Mayer-Gürr, 2016). This is also visible in the GRACE GFR position residuals and deviations from GNV and KOS data (eg. Fig. 7.35 and 7.43).

Nevertheless, as in other studies, here white noise is used. As an estimate for the error of GRACE orbit solutions a standard deviation of $\sigma = 2\ cm$ is realistic. At some times it might be even smaller. This is used here as basis. In Section 8.6 the influence of lower and higher noise levels is investigated.

The dynamic GNV solution provides velocity data in addition. For GRACE GFR processing these are just needed as initial condition for each arc. They are not independent measurements with respect to the position and thus not used as observations for GFR. Since the initial conditions are estimated in the GFR process, their error is of very minor importance. A white noise with standard deviation of $\sigma = 0.08\ mm/s$ is applied here for all cases.

6.3.4 Star Cameras and Attitude Solution (SCA)

The star cameras are an important sensor on board the GRACE satellites and in general for satellite gravimetry missions. The satellite's attitude is determined mainly from the star cameras. It is crucial to relate the accelerometer measurements to a reference frame. Thus, the star camera measurement is directly influencing the quality of the accelerometer data for POD and GFR.

Star cameras are the most precise attitude sensor available. The accuracy is mainly determined by two factors. First, the resolution of the camera and hence the accuracy with which the position of a star can be determined, and second, by the digital processing. In a first step the positions of stars in pictures are determined by image processing techniques and subsequently feed to an attitude determination algorithm.

Besides the technical limitation of each device, all star cameras have in common, that rotations around the cameras boresight have a much worse accuracy because the stars do not move so much in the camera frame compared to rotations around the other axes.

For the GRACE star cameras, errors are given in Kim (2000) as withe Gaussian noise with σ_φ for the boresight direction of 240 μrad and σ_θ and σ_ψ for the other two axes of 30 μrad. Harvey (2016) concludes that the boresight error is about one order of magnitude bigger than in the other directions.

Futhermore, the measurement is biased because of mounting errors and exhibits a drift mainly due to temperature variations (Harvey, 2016). These errors can be eliminated or at least reduced by calibration of the star cameras and by producing an optimal attitude solution, which is partly done in the L1B data processing. Therefore these effects may not be considered in a realistic star camera model for L1B data. Nevertheless, the influence of a constant misalignment is investigated here.

The used star camera noise model is $\sigma_\varphi = 40\ arcsec \approx 194\ \mu rad$ and $\sigma_\theta = \sigma_\psi = 5\ arcsec \approx 24\ \mu rad$ for each star camera in its respective star camera frame. An algorithm

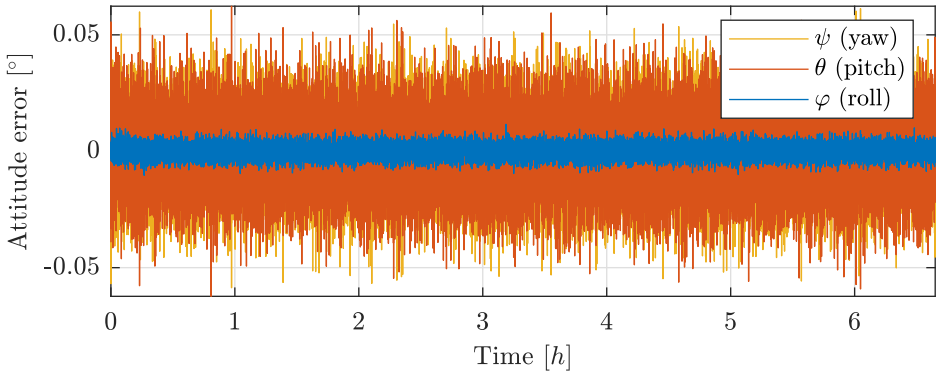

Figure 6.35: Attitude sensing error of the simulation using just one star camera (condition 1.)

for the combination of multiple star camera measurements is given in the GRACE L1B data processing document (Wu et al., 2006). It is a weighted combination, considering the sensitivity of the different axes. This algorithm is used to combine the measurement of both star cameras to a final attitude solution, giving a quaternion from inertial to the satellite's body frame q_{i2b}. The mounting of the star cameras in the satellite body frame is assumed to be known and inherited from the GRACE satellites. For the investigation of a star camera misalignment the star camera frames of each camera are rotated by [37 -15 84] *arcsec* and [-71 58 -18] *arcsec* from the assumed orientation, respectively.

For an optimal attitude and angular velocity determination from the star camera measurements, a Kalman filter is designed. As known attitude disturbances the applied control torques and the simple model of the GGT are considered for the Kalman filter. As observations the two star camera measurements are used. Optionally a rate measurement from a gyro could be added as observation for the Kalman filter, as well. The output is the estimated attitude quaternion $\vec{q}_{i2b}$ and the angular velocity $\vec{\omega}_b$. Furthermore, the standard deviation of the noise of each star camera axis is assumed to be known. The complete implementation of the Kalman filter is described in detail in Mashtakov et al. (2020) and not performed here. The star camera model parameters are summarized in Table 6.4.

In Section 8.7 different combination of star camera errors are investigated with respect on the resulting gravity fields. Also the influence of the advanced attitude processing using the Kalman filter is considered.

In the following, the attitude error with the described star camera models is shown for different processing methods. Attitude error is defined as the processed star camera measurement minus the true attitude (not to confuse with the relative attitude $\vec{\Theta}_{rel}$). The following four conditions are investigated:

1. Just one star camera measurement is used.
2. Both star cameras are used and the measurements are combined with the mentioned algorithm.
3. Both star camera measurements are used as input to the Kalman filter.
4. Both star cameras contain a misalignment, their measurements are combined.

When using just one star camera (Fig. 6.35), the error of the different satellite axes is dependent on the mounting of the camera. For the GRACE camera mounting, a

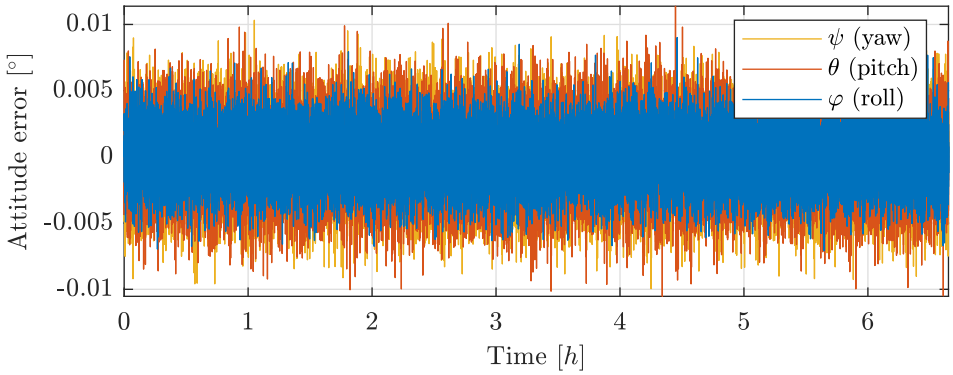

Figure 6.36: Attitude sensing error of the simulation using two star cameras with combination algorithm (condition 2.)

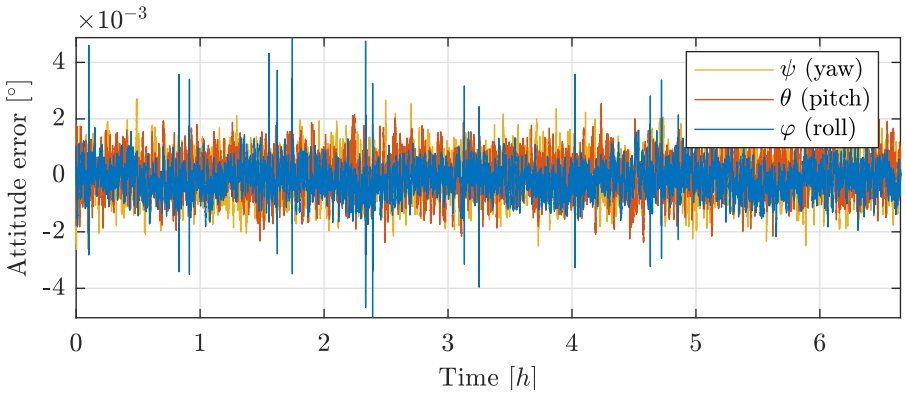

Figure 6.37: Attitude sensing error of the simulation using two star cameras with Kalman filter (condition 3.)

rotation around the cameras boresight is a combination of a pitch and yaw rotation of the satellite. Thus pith and yaw axes show bigger errors. The satellite's roll rotation is parallel to a sensitive camera axis, hence the roll error is smaller.

With an additional star camera (condition 2.), that is mounted differently, both measurements can be combined, considering the sensitivity of each axis. The result is depicted in Figure 6.36. It shows a nearly equal error level for all three axes, which is below the error level of one single sensitive camera axis. The roll axis is still a little bit more precise, being a sensitive axis in both camera frames.

Additionally considering the attitude dynamics with the Kalman filter (condition 3.), increases the precision again by a factor of about five (Fig. 6.37). This is a huge improvement and maybe a possibility to increase the accuracy of the GRACE SCA L1B solution. This would require the knowledge of the attitude control torques which are theoretically known and recorded, but I can not assess its accuracy.

If the star cameras are misaligned (Fig. 6.38), the error shows a constant offset. The random noise in each axis is reduced, nearly as much as for condition 2. with the combination of two star cameras.

The influence of these different star camera data processing approaches, and hence the star camera error, on the GFR results is investigated in Chapter 8.7.

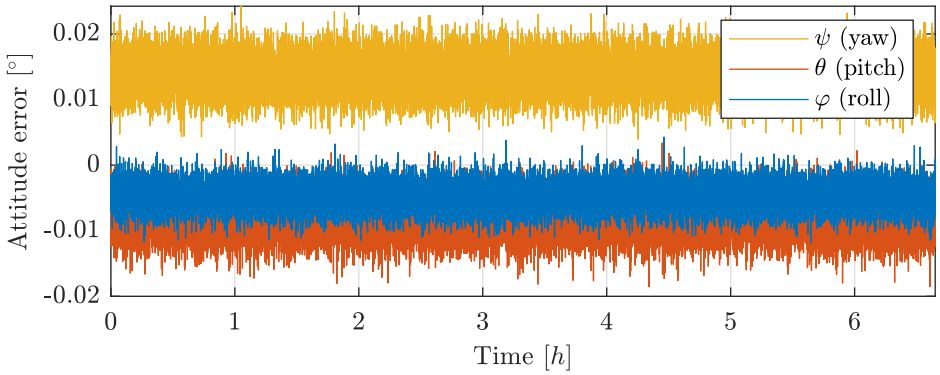

Figure 6.38: Attitude sensing error of the simulation using two misaligned star cameras with combination algorithm (condition 4.)

6.3.5 Magnetic Torquer

The main magnetic torquer (MTQ) model is that a torque only can be produced perpendicular to Earth's magnetic field $\vec{B}$. It is determined by the already mentioned equation with $\vec{m}$ being the magnetic dipole moment generated by the MTQs

$$\vec{T}_{MTQ} = \vec{m} \times \vec{B}. \tag{6.35}$$

The magnetic field is computed with the IGRF 11 (International Geomagnetic Reference Field) model (Finlay et al., 2010).

Furthermore, just the maximal generatable dipole moment is limited. No other models like delays are used. The magnetic dipole $\vec{m}$ of the torquers builds up pretty fast after switching on the current. Thus modeling a delay effect would require a much smaller simulation step size and has no significant influence, especially not on the GFR.

6.3.6 Attitude Thrusters

For the thrusters no real model is used. Du to the fact that the thruster activation time is far below the integration step size, a detailed modeling of effects like response delay and building up the nominal thrust is not necessary. Errors of misaligned thrusters and slightly different firing times of thrusters of one pair are not influencing the attitude dynamics much for realistic error assumptions.

Much more interesting is the response of the accelerometers to these effects and how these errors affect the GFR. Thus for the closed loop GFR simulation the "thruster model" is actually and additional accelerometer model.

In the GRACE L1B ACC data each thruster firing is distinctly visible by spikes in the signal (eg. Fig. 6.16), proving that the thrusters do not work perfectly. A thruster firing to produce a torque around a certain axis results in a disturbance of all three accelerometer axes. Meyer et al. (2012) investigated this effects in a stochastic manner, giving mean values and standard deviations of the disturbances of the firing around one axis onto the three accelerometer axes. In the same way the disturbance of a thruster firing on the accelerometer is modeled here. The vlalues from Meyer et al. (2012) are completed and adjusted to achieve comparable effects as in real GRACE ACC data.

With $\vec{\Delta t}_{thr}$ being the vector of the firing time in each direction φ, θ, ψ (only one direction at a time) and the coupling matrix C_f and the standard deviation of the

coupling $C_{\sigma,f}$, the acceleration on the three body axes due to the firing ACC_{thr} is modeled by

$$ACC_{thr} = (C_f \vec{\Delta t}_{thr} + (C_{\sigma,f}.\vec{n}_n)\ \vec{\Delta t}_{thr}) F_{thr}/m_{sat}. \tag{6.36}$$

$\vec{n}_n$ is a normally distributed random number and (.) meaning the element-wise multiplication of each matrix row with the concerning element of the vector. Thus $(C_{\sigma,f}.\vec{n}_n)$ is a matrix of white noise with the dedicated standard deviation. In the simulation for satellite A and B the coupling factors $C_{f,A}$ and $C_{f,B}$ and their standard deviations $C_{\sigma,f,A}$ and $C_{\sigma,f,B}$ are assumed to be

$$C_{f,A} = \begin{bmatrix} 0.0945 & 0.1085 & 0.0945 \\ 0.042 & 0.0805 & 0.14 \\ 0.4025 & 0.1925 & 0.455 \end{bmatrix}$$

$$C_{f,B} = \begin{bmatrix} -0.119 & 0.063 & -0.1505 \\ 0.0035 & -0.1855 & -0.133 \\ 0.2625 & -0.4725 & -0.455 \end{bmatrix}$$

$$C_{\sigma,f,A} = \begin{bmatrix} 0.015 & 0.04 & 0.03 \\ 0.01 & 0.045 & 0.03 \\ 0.005 & 0.025 & 0.015 \end{bmatrix}$$

$$C_{\sigma,f,B} = \begin{bmatrix} 0.01 & 0.025 & 0.03 \\ 0.01 & 0.035 & 0.025 \\ 0.005 & 0.01 & 0.015 \end{bmatrix}.$$

The disturbing accelerations ACC_{thr} are added as accelerations in the satellite dynamics integration, acting for the length of one integration step size. Thus the modeling approach is dependent on the integration step size because it is modeled as acceleration and not as an finite impulse. Nevertheless, the used integration step size is always 5 seconds and thus the effects is constant.

Additionally, an error in the sensing of the thruster induced peaks by the accelerometer can be modeled. Therefore, a normal distributed error is added onto the thruster peaks in all axes. The previous equation is extended by the error factor $\sigma_{acc,thr}$:

$$ACC_{thr} = (C_f \vec{\Delta t}_{thr} + (C_{\sigma,f}.\vec{n}_n)\ \vec{\Delta t}_{thr}) F_{thr}/m_{sat}(1 + \vec{n}_n\ \sigma_{acc,thr}). \tag{6.37}$$

The vector $\vec{n}_n$ consists again of normally distributed random numbers. This additional error is just added to the modeled ACC data, but not feed to the dynamics integration.

The influence of this error is investigated for standard deviations of $\sigma_{acc,thr} = 0.005$, 0,01 and 0.02 in Chapter 8.8. If a sensing error of very short and sharp impulses is realistic for the GRACE accelerometers is hard to assess. First, the general influence of such an error is investigated and subsequently it may be related to the real data processing.

The modeled accelerometer signal with the added thruster disturbances is shown in Figure 6.39. The disturbing accelerations are added to the non-gravitational forces at the times of the firings for the length of one integration step size (5 s), giving the sharp spikes. This is looking different than the GRACE ACC L1B data because during

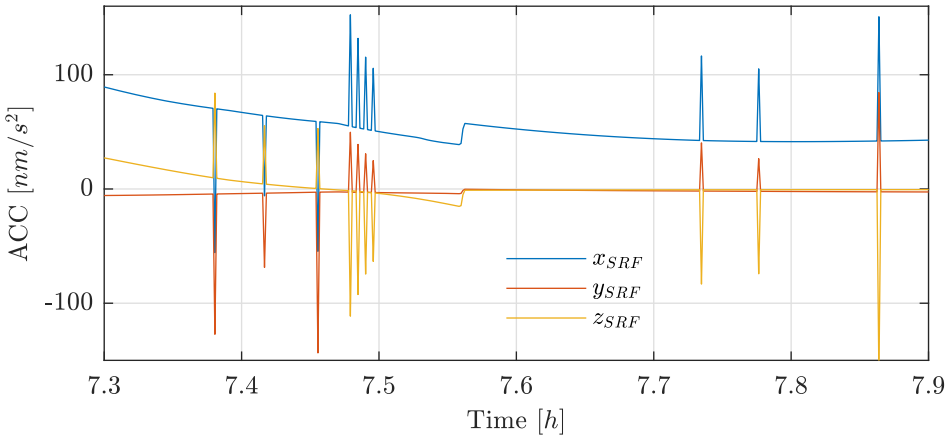

Figure 6.39: Modeled accelerometer signal with disturbances due to imperfect thruster firings.

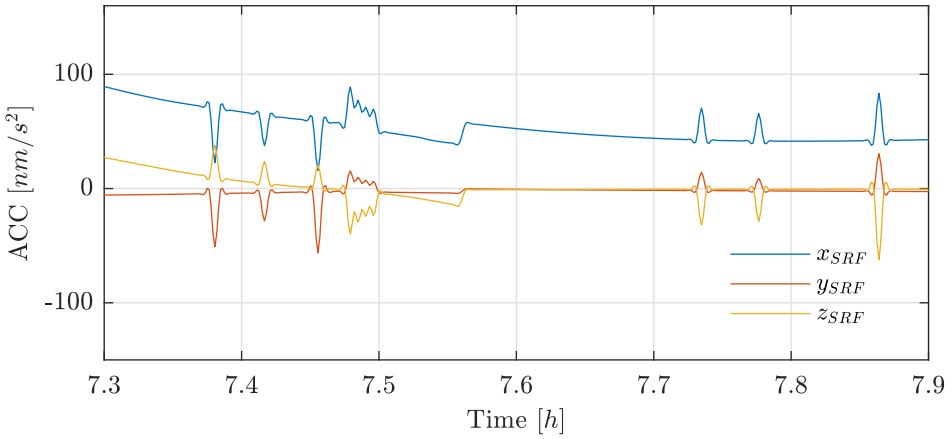

Figure 6.40: Filtered modeled accelerometer signal with disturbances due to imperfect thruster firings (the same filter as for GRACE L1B data processing is used).

the processing of the raw accelerometer data to the published, and usually used L1B data, the measurements are filtered and down sampled. A digital CRN filter (N-th order self-Convolution of Rectangular time-domain window function) is applied for that purpose, described in Wu et al. (2006). Due to this filter, the sharp pulses in the ACC data are decreased and broadened. The filtered modeled accelerometer signal, using the same filter, is shown in Figure 6.40, for the same time as shown before in Figure 6.39. The filtered peaks are blurred into positive and negative time direction and show a typical "overshooting" at both ends.

For comparison real GRACE ACC L1B data (bias corrected) are shown in Figure 6.41 for an arbitrary epoch. The disturbances due to the thruster firings look very similar to the filtered modeled signal from the previous figure. It exhibits the same "overshooting" characteristic and width of the peaks.

The influence of the filter compared to the true, measured ACC data is negligible for the GFR, as analyzed in Chapter 8.8. The total impulses are kept the same by the filtering, it is just blurred over a slightly longer time. On these time scales this has no influence on the GFR.

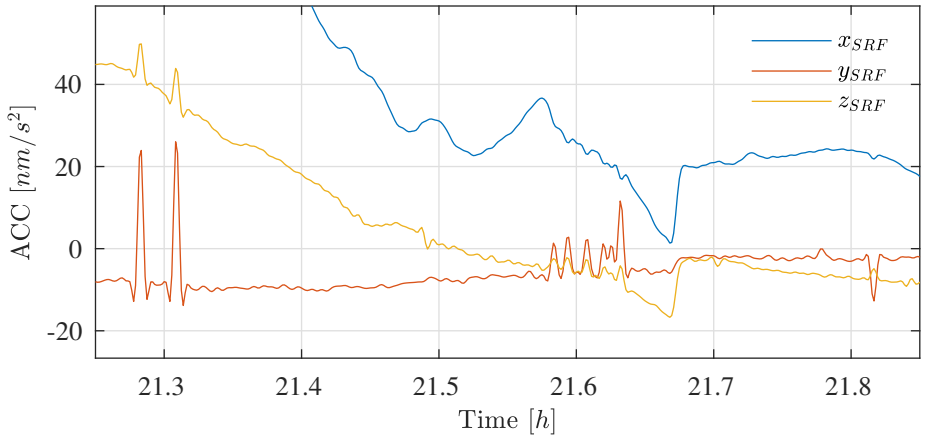

Figure 6.41: GRACE ACC L1B data (bias corrected) showing thruster disturbances.

GRAVITY FIELD RECOVERY RESULTS FROM GRACE

7

In this chapter the Gravity Field Recovery (GFR) from real GRACE data is analyzed. The GFR tool, as described in detail in Chapter 4 is validated with respect to all main parameter choices, options and sensitivities, extensively. GRACE results are shown here from the year 2006, exemplarily. The environmental conditions for that year are not especially smooth, but also not too rough (eg. Fig. 3.1). The data quality has settled compared to the first years and is more or less average.

For testing and evaluating the influence of different estimation parameters, like weighting, arc length or accelerometer calibration, different months are investigated in the following. Because the data quality and environmental conditions are not constant, the quality of the gravity field solutions differs from month to month. The influence of different options in the GFR processing differs over the months, as well. Therefore, usually results for different months are investigated and shown.

The results and plots shown in this chapter are also used for the comparison with the simulation studies in the next Chapter 8. Through this, the GFR simulation loop is validated but also different influences and relations between sensor noise characteristics and options in the processing of the real GRACE data will be revealed.

In this thesis usually a gravitational field with degree and order (d/o) 60 is estimated. In this region Earth's hydrological signal is detectable by GRACE. Some processing centers also estimate gravity fields up to d/o 96, but the additional information is small compared to the computational effort. Due to restrictions on the used computation cluster, d/o 60 is used as default here. Usually the shown GFR solution consider data from one month, especially when comparing results to monthly solutions from other processing centers, like CSR and TU Graz. In some cases, for parameter analysis, a gravity field is just computed for 12 days to reduce computation time. Of cause this has an effect on the quality of the solution, and the results are not directly comparable to the monthly solutions with data of about 30 days.

Gravity field solutions can be compared and assessed in different ways. The two most important ones used here are: First, the degree amplitude, degree difference or degree variance plots (cf. Sec. 2.3.3). They give a condensed insight of the estimated parameters and the sensitivity over the degree. To assess small differences between solutions or the hydrological signal, the difference with respect to a reference gravitational field is usually plotted. A static, mean gravitational field is used for that purpose. In this thesis the GGM05s model (Ries et al., 2016) is always utilized for that (cf. Sec. 2.3.2). Also the formal error (Sec. 4.3.12) can be plotted as degree variance to asses the accuracy of the solution over the degrees.

Second, the solution can be assessed in the spatial domain. The equivalent water height (EWH) or the geoid height are commonly plotted quantities (cf. Sec. 2.3.2 and 2.3.2). Again a reference or a mean field is useful to assess small differences and the time varying gravitational signal. Unphysical signals can be detected quite well in

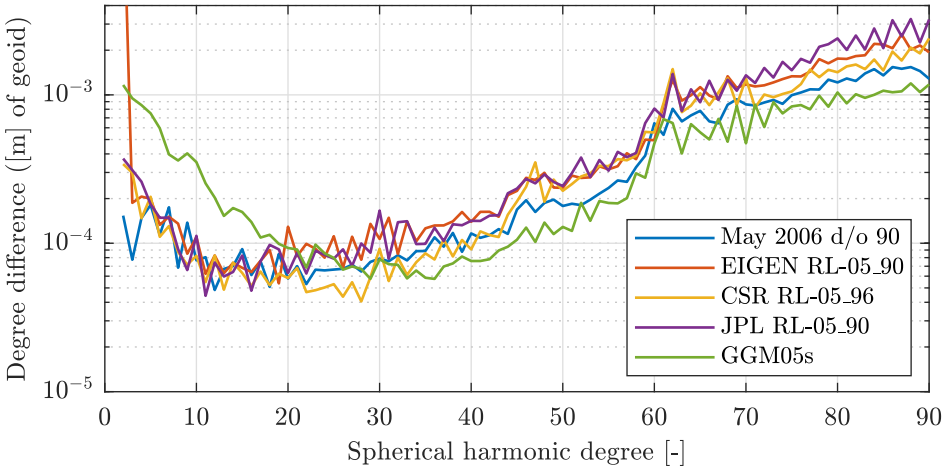

Figure 7.1: Degree difference with respect to ITSG2018 May 2006 solution from estimated May solution, the official solutions from GFZ, CSR and JPL and the mean GGM05s model. For the estimated solution the weighting of $\sigma_g = 0.02$, $\sigma_k =$ 1e-8 and bias plus drift parametrization with 3h arc length is used.

spatial difference plots. Especially over the oceans the expected signal in most regions is extremely small, hence a smooth signal over the oceans and a low striping are general indices of a good solution. For all spatial plots shown in the following a 465 km Gaussian smoothing filter is applied, as discussed in Section 2.3.4.

Compared to the results from the simulations studies in the next Chapter 8, here no true solution exists to asses errors and to compare the results to. Nevertheless, the renown mean GGM05s model is generally used as reference, here. Being a mean model based on about 10 years of data it is well suited to assess differences between various solutions. To evaluate the differences of the monthly solutions and the mean GGM05s model, they are compared in terms of degree difference in Figure 7.1. As reference the monthly ITSG2018 solution from TU Graz (Kvas et al., 2019), which are renowned for its quality, is used. Shown are an estimated monthly solution of May 2006 up to d/o 90, and the three respective official solutions from GFZ, CSR and JPL and the GGM05s model. The big difference of the EIGEN solution from GFZ in the very first degree is due to a different used reference radius R and the used tide-free system, while all other models are given in the zero-tide system (cf. Sec. 2.3.2). All three monthly solutions show some differences over the whole spectrum. Compared to the mean GGM05s model it is distinct, that bigger differences are in the lower degrees up to about d/o 20. This is where the most hydrological signals are detectable with GRACE data, and thus the monthly solutions show the biggest differences to the mean gravitational model. For the higher degrees, where the noise in the coefficients is increasing, the monthly solutions are much closer to the mean model. For d/o higher 30, the monthly ITSG solution is closer to the mean GGM05s model than all other monthly solutions. Thus, especially for the higher degrees the differences are small, and the mean model might be used as a reasonable general reference.

All additional models, referred to as background models, used for the GFR processing are listed in Table 7.1. The different modeled effects were mainly introduced in Chapter 2. The listed effects are usually considered by all processing centers for GRACE GFR solutions. However, the explicitly employed models for the different effects may differ.

Table 7.1: Used Background models for GFR

Perturbation	Model	Remark
Earth static gravity field	GGM05c[a]	d/o 180
Third body	JPL DE430 ephemeris[b]	Sun, Moon, Jupiter
Dealiasing	AOD1B RL05[c]	d/o 180
Atmospheric tides	N1 Biancale & Bode[d]	d/o 8 (S1 and S2)
Solid Earth tides	IERS 2010[e]	d/o 4
Ocean tides	EOT11a[f]	d/o 120
Pole tides	IERS 2010[e]	c_{21}, s_{21}
Ocean pole tides	IERS 2010[e], Desai2002[g]	d/o 180
Relativistic corrections	IERS 2010[e]	-
Earth rotation	IERS 2010[e]	IERS EOP 14C04_2000A
Non-gravitational forces	ACCL1B RL05[h]	-

[a] Ries et al. (2016), [b] Folkner et al. (2014), [c] Dobslaw et al. (2013), [d] Biancale and Bode (2006), [e] Petit and Luzum (2010), [f] Savcenko et al. (2012), [g] Desai (2002), [h] Case et al. (2010)

In the following the influence on the solution of different parameters and options in the GFR processing is investigated. To analyze the influence of one parameter, all other parameters are kept constant. In all following sections and plots, all not explicitly given parameters are constant for that investigation, making results shown in one plot consistent.

7.1 Weighting

The weighting of observations is one of the most important parameters in GFR processing. This is particularly the case for GRACE, where two very different observations are used. The influence of different weighting combinations of the 3d-position (GNV or KOS) and range-rate (KBR) observations is investigated. The standard deviations of GNV and KBR data are referred to as σ_g and σ_k, respectively. As weighting the inverse of the variances $1/\sigma^2$ are used, as discussed in Section 4.3.5. The automatic weighting via VCE is discussed in the next Section 7.1.1.

In Figure 7.2 six different weighting combinations are depicted for a monthly solution of May 2006. The weighting of the range-rate observations is varied while the weighting of the position observations is kept constant. In general just the relative difference of the weighting factors is decisive (cf. 4.3.5). The plot shows the degree differences with respect to the GGM05s mean model in terms of geoid height. Additionally the solution from CSR (CSR_05_96, Bettadpur (2012a)) is plotted for comparison.

With increasing weighting of the KBR observations (meaning lower σ_k values) the solutions get better and for σ_k = 1e-8 the result is the best. Nevertheless, the results for σ_k between 1e-7 and 5e-9 are not much worse. Further increasing the KBR weighting

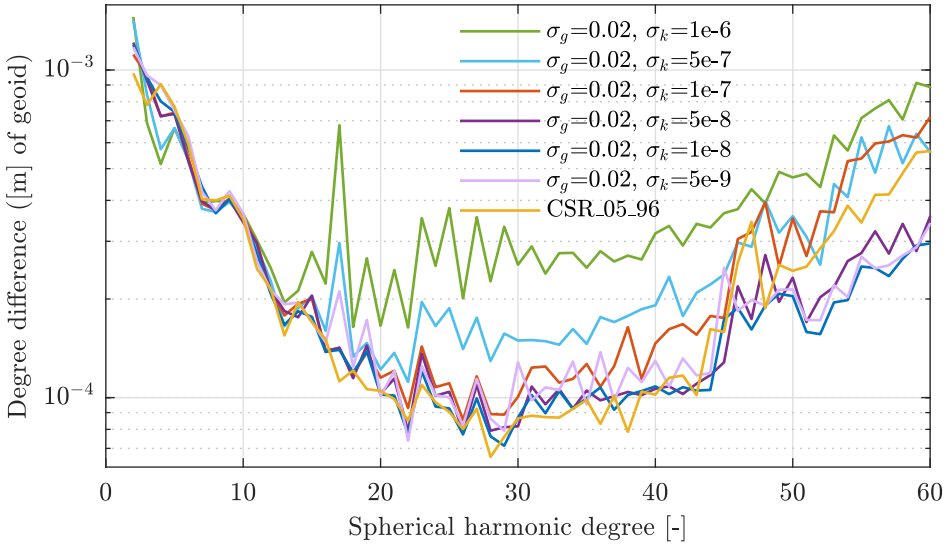

Figure 7.2: Degree difference of May 2006 solution with respect to GGM05s for different weighting combinations of GNV and KBR observations with standard deviations σ_g and σ_k, respectively.

results in a slightly worse quality (σ_k = 5e-9).The result for σ_k = 1e-9 is already three orders of magnitudes worse and does not fit in the plot.

Until around d/o 12 the solution is not changing much for the different weighting combinations. The first d/o are not that sensitive to the range-rate observations and rely heavily on the GNV observations, thus the KBR weighting is not that decisive for the solution in this area. The higher d/o which rely much more on KBR observations are getting worse with a decreasing ratio of σ_g/σ_k.

The results look surprisingly different for different months. The same investigation is shown for April 2006, which is a month with smooth KBR data, like May (cf. Fig. 7.25) and for November 2006, with lots of outliers in the KBR data. In the Figures 7.3 and 7.4 the degree differences of the estimated gravity fields are shown for different weighting combinations, again.

It is obvious, that the quality of the results differs for the different months. The influence of the weighting is different for different months, as well. While for May 2006 the result is in very good agreement with the CSR solution and the weighting combinations with σ_k = 1e-7 to σ_k = 5e-9 give nearly similar results, the conditions are quite different for the other two months. The overall sensitivity is lower in both cases than for May. The differences to the CSR solution are much bigger. Furthermore, for April and November some of the weighting combinations show big oscillations of the gravity field coefficients and make the solutions unacceptable. Nevertheless, the solutions with σ_k =1e-8 are clearly better and may be used for hydrology analysis. The reason why the May solution is better is not completely understood, yet.

The higher number of outliers in the KBR data in November and thus the amount of discarded data seems not to have a big influence when comparing it to the April solution.

The solutions for May and April 2006 are shown in the spatial domain in terms of EWH in the Figures 7.5 and 7.6. For comparison the CSR and ITSG solutions are shown for both months in the plots, as well. Again, all plots are with respect to the GGM05s mean model.

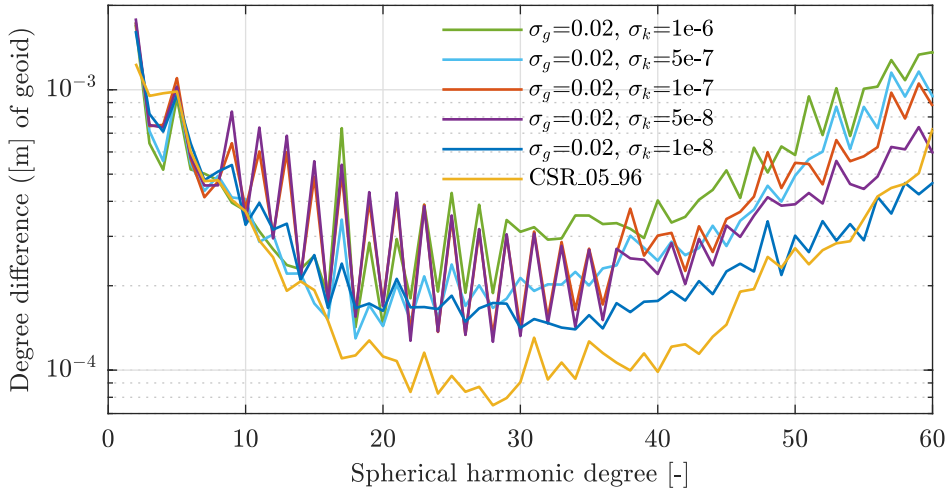

Figure 7.3: Degree difference of April 2006 solution with respect to GGM05s for different weighting combinations of GNV and KBR observations with standard deviations σ_g and σ_k, respectively.

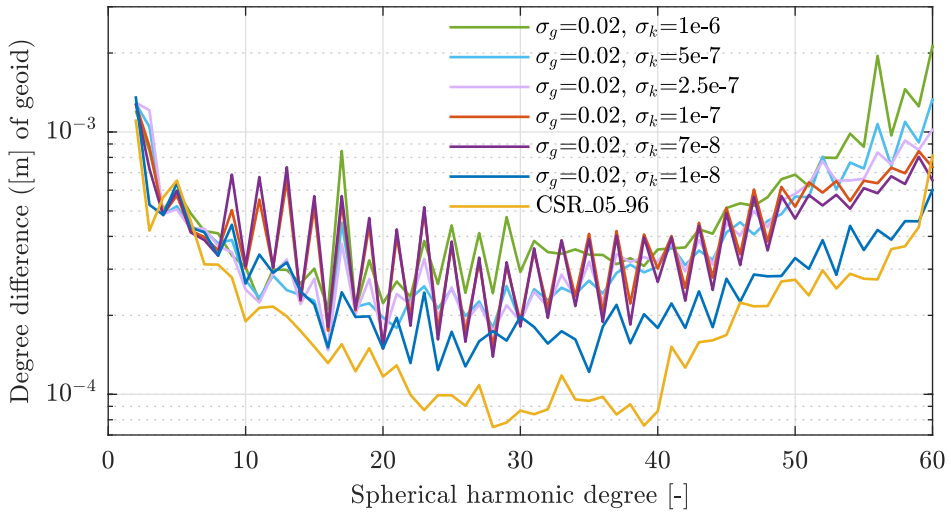

Figure 7.4: Degree difference of November 2006 solution with respect to GGM05s for different weighting combinations of GNV and KBR observations with standard deviations σ_g and σ_k, respectively.

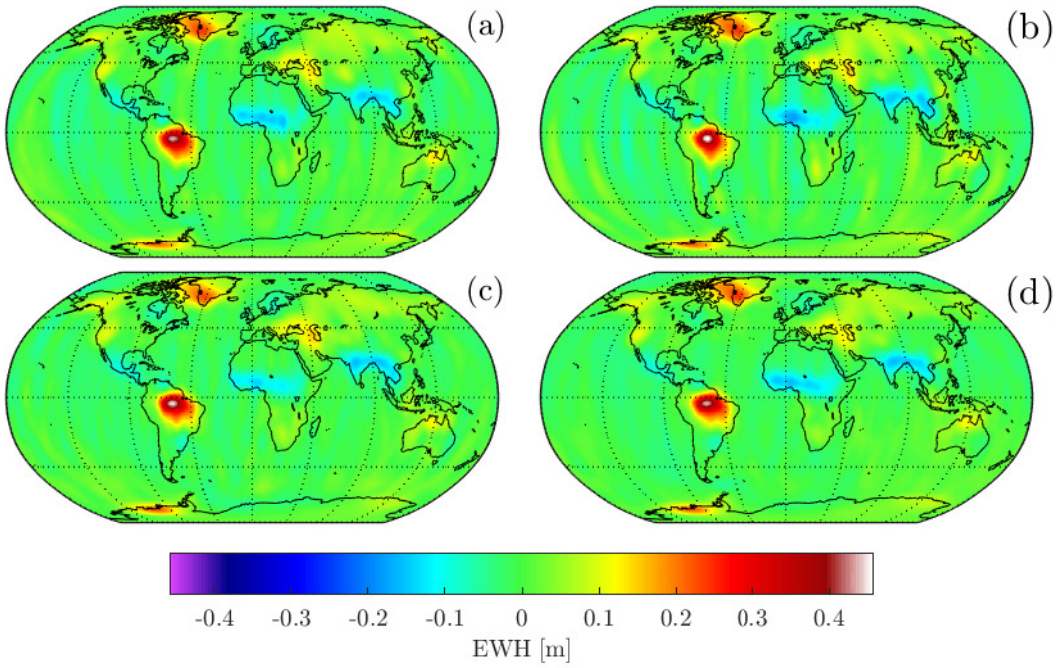

Figure 7.5: Spatial plot of EWH for May 2006 solution with respect to GGM05s, for (a) 3h bias plus drift solution (as used in all previous deg. diff. plots), (b) 2h bias plus drift solution, (c) CSR solution (RL05), (d) TU Graz solution (ITSG2018). Gaussian filter with 465 km radius applied.

In both Figures the first two plots (a) and (b) are obtained with a different parametrization and are used a little in advance here since Section 7.2 deals with the influence of the parametrization, explicitly.

The solution for May (Fig. 7.5) shows a very low striping, and the signal over the oceans is smooth. It is in good comparison with the solutions from CSR (c) and TU Graz (d). The annual hydrological signal over the continents and the signals in Greenland and Antarctica are clearly visible and good comparison marks with the other solutions. It is also visible, that the two reference solutions from CSR and TU Graz show slight differences among each other.

In contrast to May, the solution for April 2006 (Fig. 7.6) has a more distinct striping for both parametrizations (a) and (b). Also the hydrological signal shows bigger differences to the CSR and the TU Graz solutions. The bigger differences were already visible in the degree difference plots (Fig. 7.2 and 7.3).

When for May the parametrization in (a) give slightly better results, for April the results of the parametrization shown in (b) are better. This is a typical finding that for the smoother months slightly bigger arc length give better results. This topic is elaborated in more detail in Section 7.2.

7.1.1 Variance Component Estimation (VCE)

The solution with VCE does not work well for the GRACE processing. The weighting of the the GNV observations is estimated too good in comparison to the KBR observations by the VCE algorithm. In Figure 7.7 the degree difference using VCE is shown for the 12 days solution from the first half of May 2006. The estimated standard deviations from VCE are about σ_g = 2.59e-3 and σ_k = 7.46e-7. For comparison the solution with

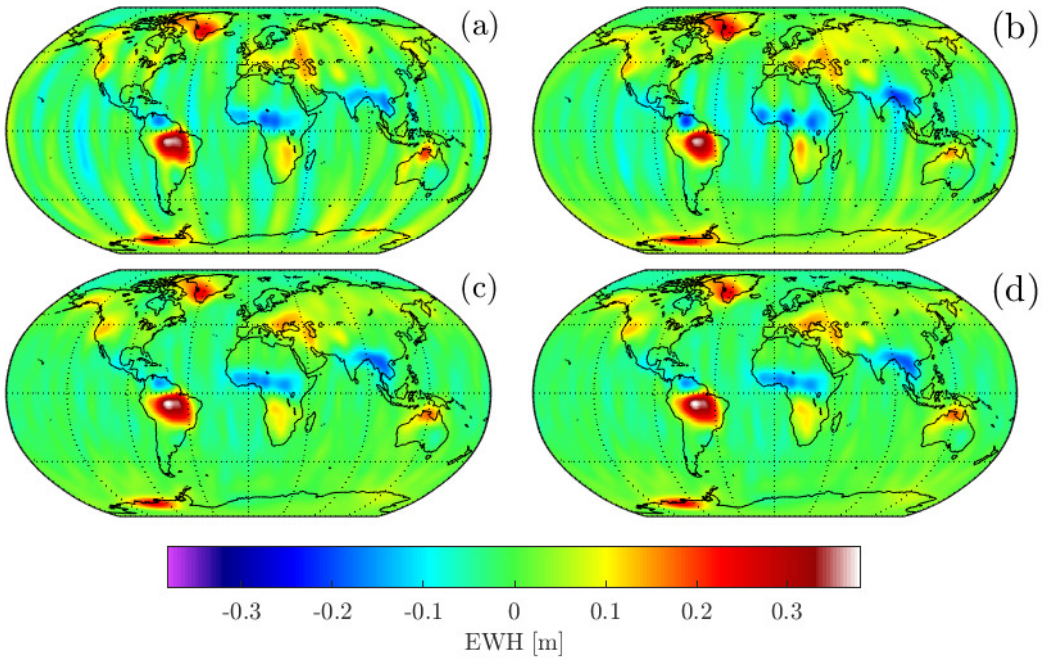

Figure 7.6: Spatial plot of EWH for April 2006 solution with respect to GGM05s, for (a) 3h bias plus drift solution (as used in all previous deg. diff. plots), (b) 2h bias plus drift solution, (c) CSR solution (RL05), (d) TU Graz solution (ITSG2018). Gaussian filter with 465 km radius applied.

constant weighting of $\sigma_g = 0.02$, $\sigma_k =$ 1e-8, which is giving the best results, is plotted as well. Another solution with constant weighting, but using the finally estimated standard deviations from the VCE approach is shown. It performs like the VCE solution, verifying the algorithm in general.

After about d/o 12 the sensitivity of the VCE solutions gets quite bad. This was seen before eg. in Figure 7.2, when the ratio of σ_g/σ_k is small.

The problem that the GNV observations are weighted too high is also encountered in the official solution from CSR. Their, not further specified, automatic weighting approach is capped to a minimal standard deviation of the GNV observations $\sigma_g = 0.02$ m to avoid a too high ratio of σ_g/σ_k, as described in (McCullough, 2017, Ch. 4).

7.2 Parametrization

Besides the weighting, the parametrization has the biggest influence on the GFR processing. Parametrization is referred to the definition of all estimation parameters $\hat{\vec{x}}$. Besides the SH coefficients up to the desired d/o and the initial satellite states position and velocity of each arc, especially all additional parameters $\vec{p}$ (Eq. 4.73) are of interest. Common parameters for GRACE were already introduced in Section 4.3.14. These were mainly calibration parameters of the accelerometers.

Each group or processing center (and even their different releases) estimate different sets of parameters. The parameter vector can include much more parameters, like KBR calibration, antenna offsets, pointing or attitude parameters. This is one reason why the results from different groups are slightly different, as well.

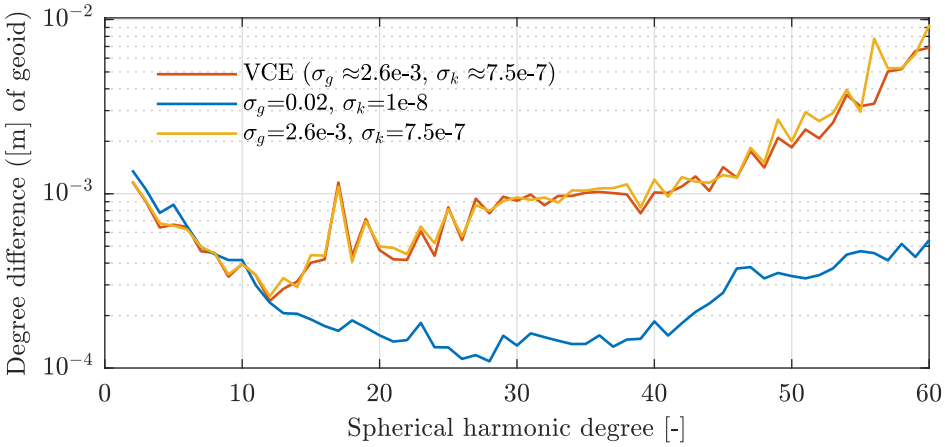

Figure 7.7: Degree difference from first half of May 2006, 12 days solution with respect to GGM05s for different weighting approaches.

Table 7.2: Constant scale factors $\vec{s}_{TN}$ from GRACE TN-02 (Bettadpur, 2009)

	GRACE A	GRACE B
x	0.9595	0.9465
y	0.9797	0.9842
z	0.9485	0.9303

Here only the local accelerometer calibration parameters and the arc length are regarded, which are the most important parameters. The arc length is indirectly a parameter as well, because the amount of local parameters and the initial states $\hat{\vec{x}}_k$ that are estimated depend on the arc length.

As introduced in Section 4.3.14 for each accelerometer a constant bias $\vec{b}$, a linear drift $\vec{d}$ and a scale factor $\vec{s}$ for each accelerometer axis are investigated here. The calibration equation was given in Equation (4.76) as

$$\vec{\ddot{r}}_{acc,b} = \vec{s} * ACC + \vec{b} + \vec{d} * t. \tag{7.1}$$

Tests with a quadratic or cubic drift were not promising and are not shown here.

The estimation of the scale factor is troublesome and could not be achieved satisfactorily. The scale factor $\vec{s}$ and the bias $\vec{b}$ are strongly coupled. Considering that the integration is, up to some extend, averaging the acceleration, the same calibration can be achieved by either one of the parameters. The convergence of the scale factor $\vec{s}$ is very slow compared to bias or drift and even does not seem to really converge at all, at least not in a reasonable amount of iterations (<15 to 20). Thus the constant values for the scale factors $\vec{s}_{TN}$ were used, advertised in the GRACE technical note TN-02 (Bettadpur, 2009) and are shown in Table 7.2. Probably an estimation in two steps, first just bias and subsequently scale could be more expedient. Nevertheless, the scale factor has a major influence and should be selected with care (cf. Sec. 7.8).

The accelerometer calibration parameters and the arc length are dependent on each other (the time t directly appears in the calibration equation Eq. 7.1) and thus are investigated together. All results shown in this section are obtained with the weighting combination of $\sigma_g = 0.02$, $\sigma_k =$ 1e-8, unless otherwise explicitly stated.

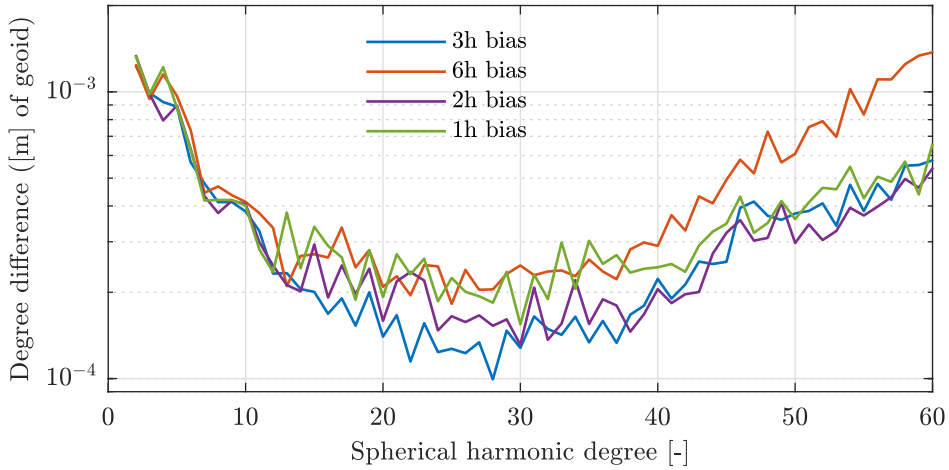

Figure 7.8: Degree difference from first half of May 2006, 12 days solution with respect to GGM05s for different arc lengths with bias $\vec{b}$ estimated for each accelerometer.

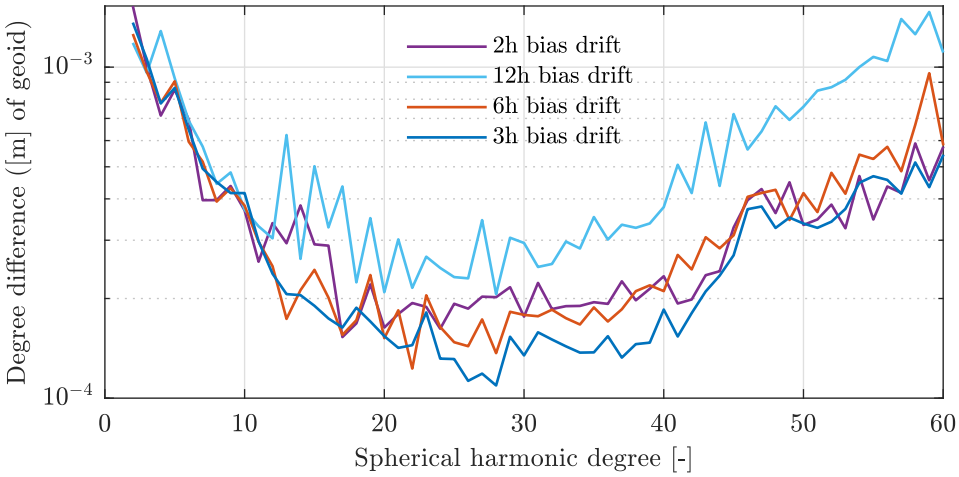

Figure 7.9: Degree difference from first half of May 2006, 12 days solution with respect to GGM05s for different arc lengths with bias $\vec{b}$ and drift $\vec{d}$ estimated for each accelerometer.

In the following plots the degree differences with respect to GGM05s for different combinations of the arc length and the estimated accelerometer calibration parameters is shown. The arc length was varied between 1h and 24h. Each accelerometer is calibrated using just a bias parameter or bias plus drift together.

In the Figures 7.8 and 7.9 the results for a 12 day solution of May are shown for the case of bias and bias plus drift, respectively. Arc lengths longer than 6h for bias or 12h for bias plus drift are so poor that they are not included in the figures. For arc lengths lower than 2h the same holds, as well. With a decreasing arc length the results are getting better until about an arc length of 3h. The 2h solution is again a bit worse for both cases. Including a drift parameter allows to use a little longer arc lengths. For both cases, the best results are obtained with a 3h arc length and are of the same quality. Thus just from this case it is hard to judge if the additional drift parameter is beneficial.

But again, the results for other months are different. The month May is rather an exception with a comparably smooth solution. For November 2006 the results are shown

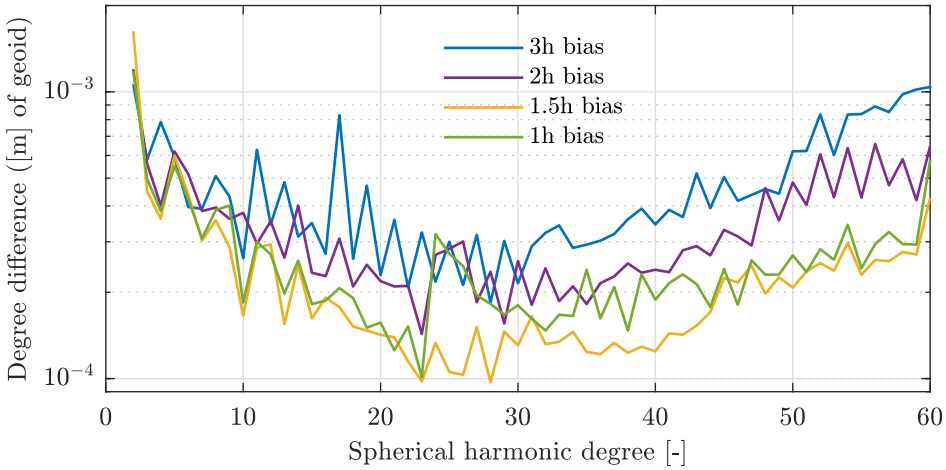

Figure 7.10: Degree difference of November 2006 solution with respect to GGM05s for different arc lengths with bias $\vec{b}$ estimated for each accelerometer.

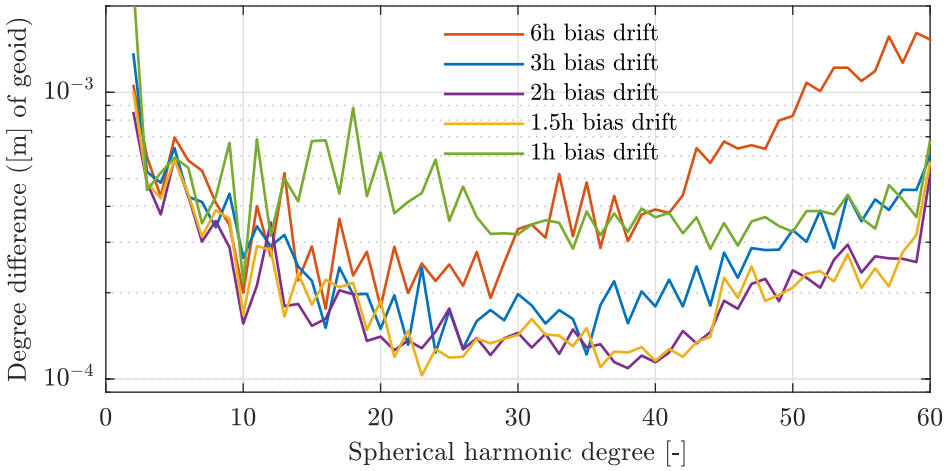

Figure 7.11: Degree difference of November 2006 solutions with respect to GGM05s for different arc lengths with bias $\vec{b}$ and drift $\vec{d}$ estimated for each accelerometer.

in Figure 7.10 for bias and in Figure 7.11 for bias plus drift for different arc lengths, respectively.

Compared to May, the arc length needs to be smaller to obtain acceptable results for both cases. For November, solutions with arc lengths bigger than 3h for bias and 6h for bias plus drift are quite bad and not shown. As for May, the solution with an additional drift parameter tolerates slightly longer arcs. The border towards the other directions is shifted downwards, as well. The solutions with 1.5h arcs are among the best, where for May it was not worth to plot. The quality of the 1h solution is distinctly worse for both cases.

The solutions for bias with 1.5h arc length and bias plus drift with 1.5h and 2h arc length are very close and in the degree difference plots it is not possible to judge which gives the best result. Therefore, the most promising results are plotted in the spatial domain in terms of EWH in Figure 7.12, with respect to the GGM05s model.

This plot reveals the differences of the solutions more clearly. The 2h bias solution (a) shows the most distinct striping, and is not competitive. The striping in the other solutions is much lower, and may be best for the 2h bias plus drift solution (c). The

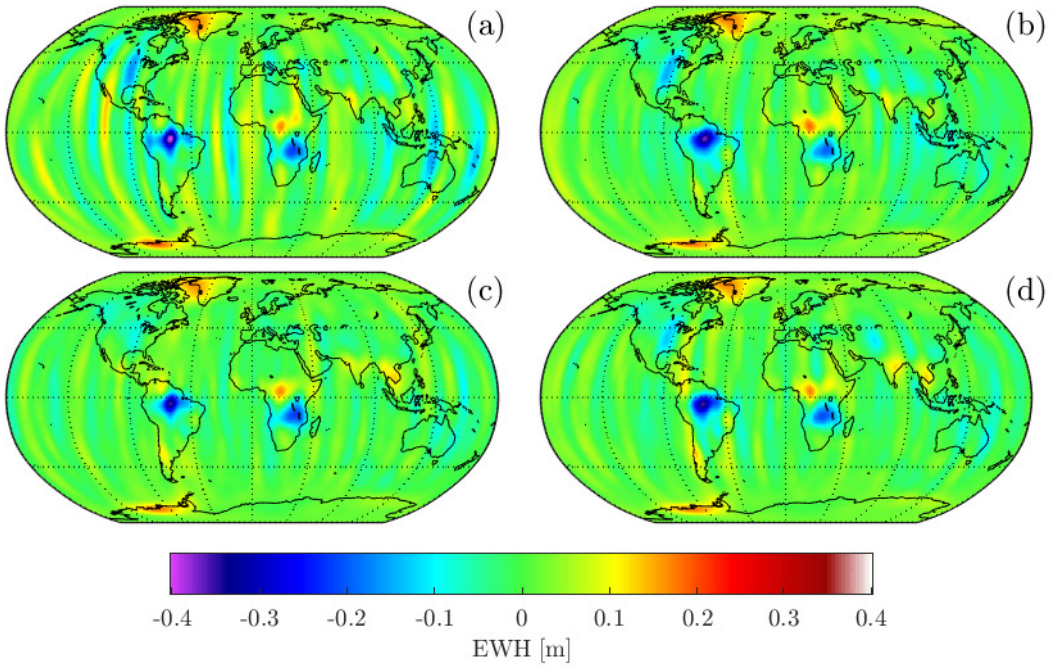

Figure 7.12: Spatial plot of EWH for November 2006 solution with respect to GGM05s for different parametetrizations (a) 2h bias (b) 1.5h bias (c) 2h bias drift (d) 1.5h bias drift. Gaussian filter with 465 *km* radius applied.

hydrological signal for the bias solutions is slightly higher than for the bias plus drift solutions. The main patterns (Amazon, central Africa and south east Asia) are slightly different for all solutions. Comparisons with the solutions from CSR and TU Graz show the best accordance with the 2h bias plus drift solution (c).

Because the results for May and November are contradictory to nail down the best parametrization, the results for another month are shown. While May is the month with the highest quality and November about average, the results for February, with the lowest quality are shown in Figure 7.13 as degree difference. The estimation of the additional drift parameter is definitely advantageous, thus just the bias plus drift solutions is depicted. The situation is very similar to the November solutions. The 1.5h and 2h solutions are very close and the 3h solution slightly worse. The 1h solution is distinctly worse, as well. The four solutions are plotted in the spatial domain in Figure 7.14 as EWH with respect to GGM05s.

As already seen in the degree difference plot, the 1h (a) and 3h (b) solutions are not good and show a very strong striping. The shorter arc length in (c) and (d) reduce the striping, but compared to the other months it is still much more pronounced. The striping for the 1.5h (d) solution may be slightly better, but the hydrology signal of the 2h solution may be closer to the references from CSR and TU Graz, even though it is hard to assess with the distinct striping and the used filter.

Concluding the investigation, also considering results not shown here for other months, the 2h bias plus drift parametrization gives the best results in total. For months with higher data quality (like May), the slightly longer arc length of 3h is a little advantageous. For the whole year 2006 the monthly results in terms of EWH with respect to GGM05s

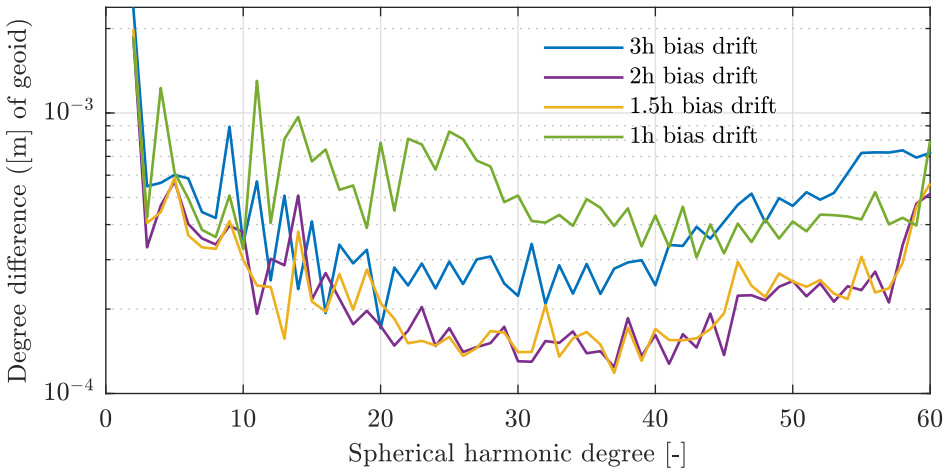

Figure 7.13: Degree difference of February 2006 solutions with respect to GGM05s for different arc lengths with bias $\vec{b}$ and drift $\vec{d}$ estimated for each accelerometer.

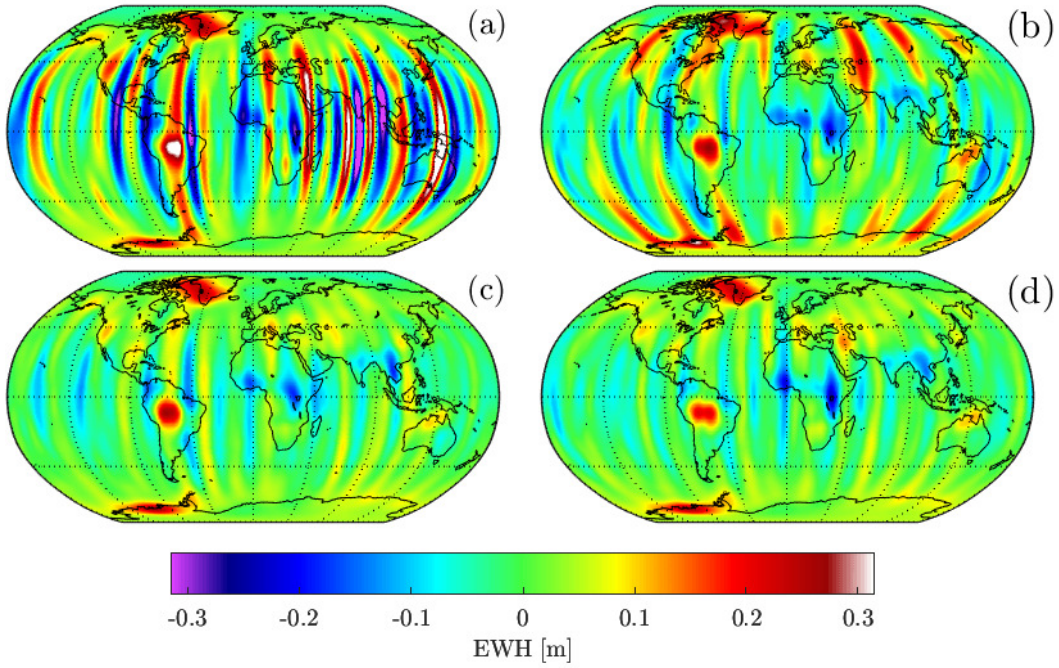

Figure 7.14: Spatial plot of EWH for February 2006 solution with respect to GGM05s for different parametetrizations (a) 1h bias drift (b) 3h bias drift (c) 2h bias drift (d) 1.5h bias drift. Gaussian filter with 465 km radius applied.

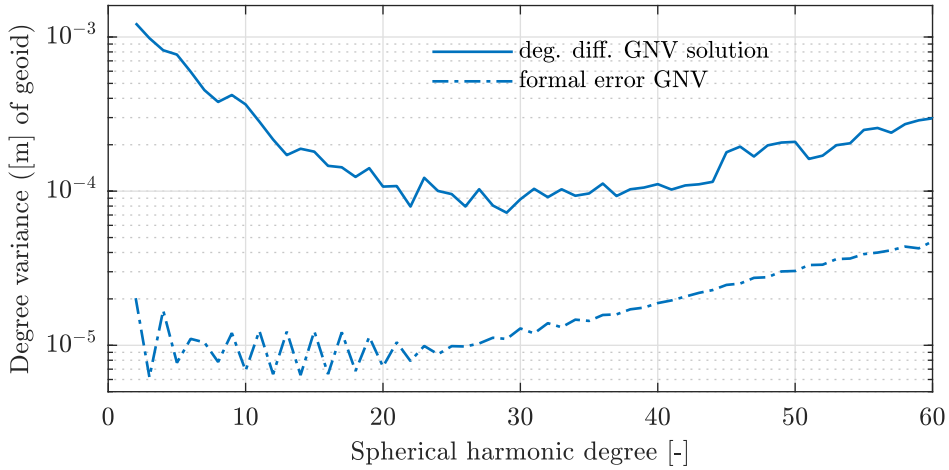

Figure 7.15: Degree variance of May 2006 solution and degree difference (deg. diff.) with respect to GGM05s.

are shown in Section 7.6 for 3h bias drift parametrization in Figure 7.45 and 2h bias drift parametrization in Figure 7.46.

7.3 Formal Error

The formal error (cf. Sec. 4.3.6, 4.3.12) can be plotted as degree variance to assess the accuracy of the solution over the degrees, as well (Sec. 2.3.3). The significance or the reliability of the formal error estimates for the GRACE results seems to be low. The reason is most probably the lack of a detailed modeling of the variance-covariance matrix $C_{\epsilon\epsilon}$ of the observation data (Sec. 4.3.6). This is investigated in the following.

7.3.1 Formal Error of Global Gravity Field Parameters

In the following formal error estimates of the monthly solutions of May and November are presented exemplarily. The formal errors are computed according to Section 4.3.12.

From the sections before it is clear that the quality of the May solution is the best, and November around average. In Figure 7.15 the formal error is shown as degree variance for the May 2006 solution. For comparison the degree difference of the solution with respect to GGM05s is plotted, as well.

The general error level is about one order of magnitude below the degree difference with respect to GGM05s, which seems too optimistic. The trend for increasing formal error with increasing degree is reasonable and as expected. For the very first degrees the formal error is increasing as well, what is in agreement with the general consideration, that for these degrees the GRACE data may be supplemented by data of higher flying satellites (eg. LAGEOS).

In Figure 7.16 the results of the November 2006 solution are depicted for the solutions using GNV and KOS data. Both solutions are very similar, the degree differences are nearly the same. Nevertheless, the formal error of the KOS solution is higher. The general trend looks the same as for May. But relatively, the error level of the May solution (Fig. 7.15) is slightly lower than the error level of the November solution, which is reasonable from the results presented in this chapter. This is also visible in the

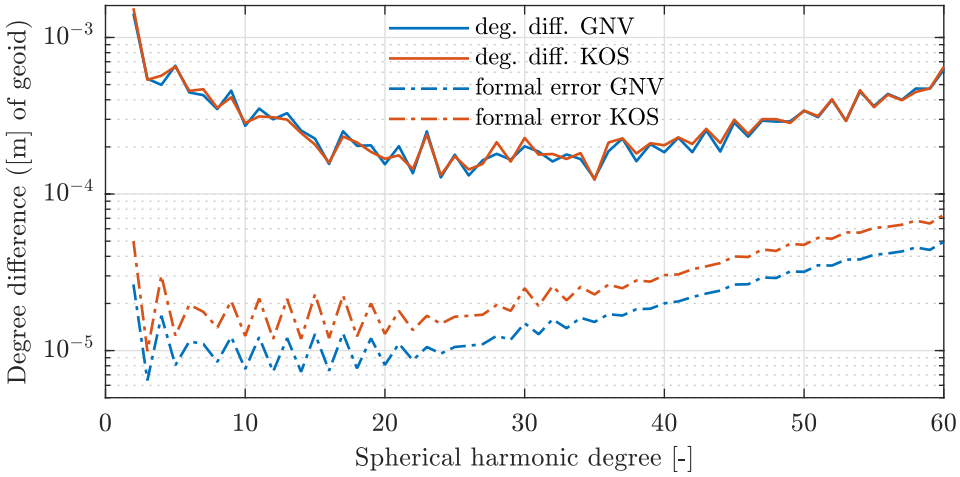

Figure 7.16: Degree variance (formal errors) of November 2006 solution using GNV or KOS observation data and degree difference (deg. diff.) with respect to GGM05s for both solutions.

overall variances $\hat{\sigma}_{ges}$ (Eq. 4.69), which are $\hat{\sigma}_{ges,May,GNV} = 7.24$ and $\hat{\sigma}_{ges,Nov,GNV} = 8.30$, $\hat{\sigma}_{ges,Nov,KOS} = 10.36$.

It can be concluded, that the general trend seems to be reasonable and in accordance with the in the previous sections, but the overall error level is too optimistic. This may be reasoned in the lack of a covariance modeling of the observation data.

7.3.2 Formal Error Weighting

The impact of different weighting options, as discussed in Section 7.1, on the formal error is discussed in the following. Results are shown for 12 day solutions from the first half of May 2006 for different weighting factors of the KBR range-rate measurement σ_k, while the GNV weight is constant σ_g=0.02 for all cases (as discussed in Sec. 7.1 and shown in Fig. 7.2). A 3h arc length and bias plus drift calibration is utilized. The formal errors are shown as degree variances in Figure 7.17 together with the respective degree differences with respect to the GGM05s model.

The weighting is affecting the formal error differently over the degree of the SH coefficients. The overall standard deviations $\hat{\sigma}_{ges}$ for the three cases are: $\hat{\sigma}_{ges,1e-8} = 8.50$, $\hat{\sigma}_{ges,1e-7} = 0.95$ and $\hat{\sigma}_{ges,5e-7} = 0.32$. Thus the overall standard deviations are completely contradictory to the results and conclusions obtained before (eg. Fig. 7.2).

A higher KBR weighting reduces the formal error of the higher degrees. But this is just true up to a certain limit. The formal error of the σ_k=1e-8 solution is the same as for the σ_k=1e-7 solution for degrees higher 30. For the lower degrees the solutions with a relatively higher GNV weighting (σ_k=5e-7 and σ_k=1e-7) give smaller formal errors and reduce the oscillation. Theoretically this is reasonable because the KBR measurement is more sensitive to the higher degrees and the absolute position to the lower degrees. Nevertheless, the obtained results show that the KBR weighting with σ_k=1e-8 definitely gives the best overall gravity field results.

7.3.3 Formal Error Parametrization

The formal error estimates of the monthly solutions from November 2006 for different arc length are presented here, as already investigated in Section 7.2 and Figure 7.11. In

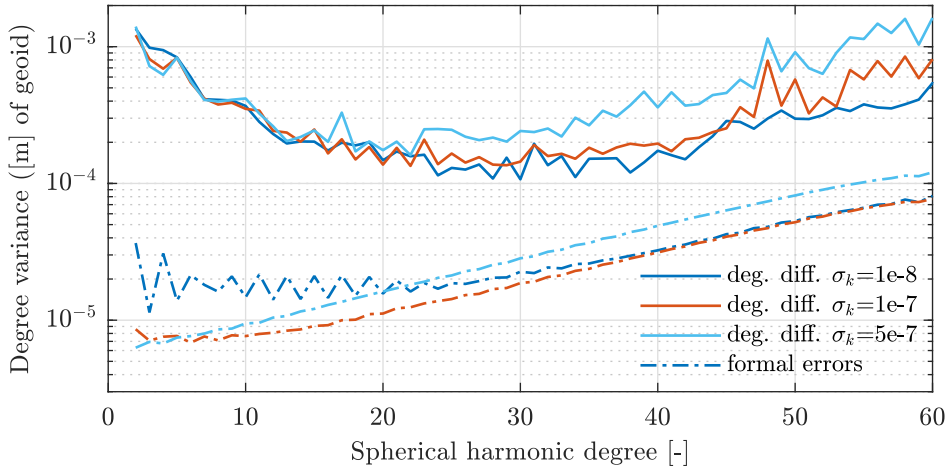

Figure 7.17: Degree variance (formal errors) of 12 day solutions from May 2006 for different weighting factors of the KBR range-rate measurement σ_k, GNV weighting σ_g=0.02 for all cases. And degree difference (deg. diff.) with respect to GGM05s for each solution (3h arc length with bias plus drift parametrization).

Figure 7.18 the formal errors for three solutions with bias plus drift parametrizartion and arc lengths of 6h, 3h and 2h are shown. Additionally the degree difference of each solution with respect to GGM05s is plotted.

For the longest arc length (6h), the formal error is the lowest, and continuously increasing with shorter arc length. This is completely contrary to the results from the previous sections, where the 2h solution was definitely performing best.

The overall standard deviations $\hat{\sigma}_{ges}$ show this trend as well, which are: $\hat{\sigma}_{ges,6h} = 8.76$, $\hat{\sigma}_{ges,3h} = 8.50$ and $\hat{\sigma}_{ges,2h} = 6.99$.

Summarizing, it can be said that for the parametrization and arc length the formal error is not a reasonable indicator and may be misleading.

7.3.4 Formal Error of Local Parameters

The formal error of the local parameters can be computed, as well (cf. Sec. 4.3.12). The formal errors of the single local parameters are computed for each arc and shown in the following for GRACE A. For the computation of the overall standard deviation $\hat{\sigma}_{ges}$ the GNV residuals of both satellites are considered. Because the estimation of the local parameters is coupled by the KBR observations, where the residuals are used for both satellites, this is reasonable. The overall standard deviation is shown for each arc in Figure 7.19.

The trend agrees closely with the converged Root Mean Square (RMS) KBR deviation shown in Figure 7.32. After convergence (cf. Sec. 7.5) residuals and deviation are interchangeable. Hence this is reasonable because, compared to the GNV observations, the KBR observations are much higher weighted in the computation of $\hat{\sigma}_{ges}$ and thus dominating.

In Figure 7.20 the formal error of the initial position is shown for the three inertial axes for each arc. It shows a distinct oscillation in each axis with a period of about six arcs or 18 hours. The general estimated error level in the range of 0.2 to 0.4 mm seems not too far from reality. The error level of the radial z_{ECI} axis is obviously a little higher than the others, which is also known from POD (eg. Weinbach and Schön, 2013).

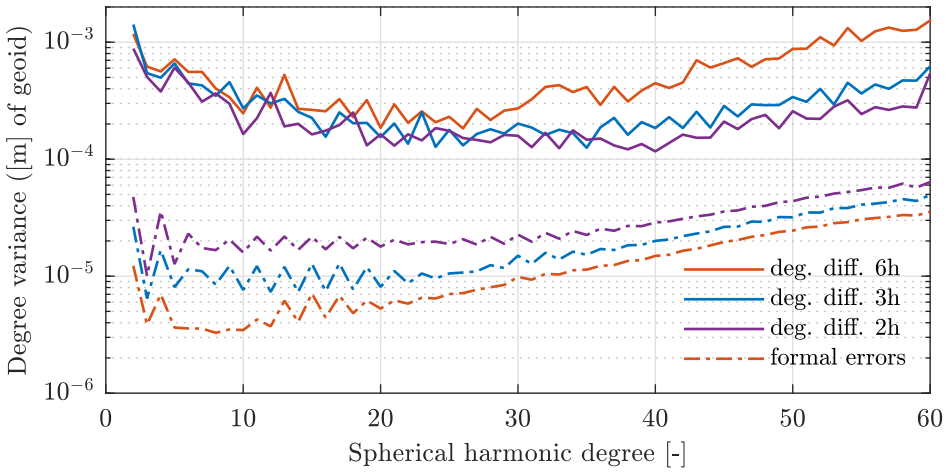

Figure 7.18: Degree variance (formal errors) of November 2006 solution for different arc lengths using bias plus drift parametrization and degree difference (deg. diff.) with respect to GGM05s for each solution.

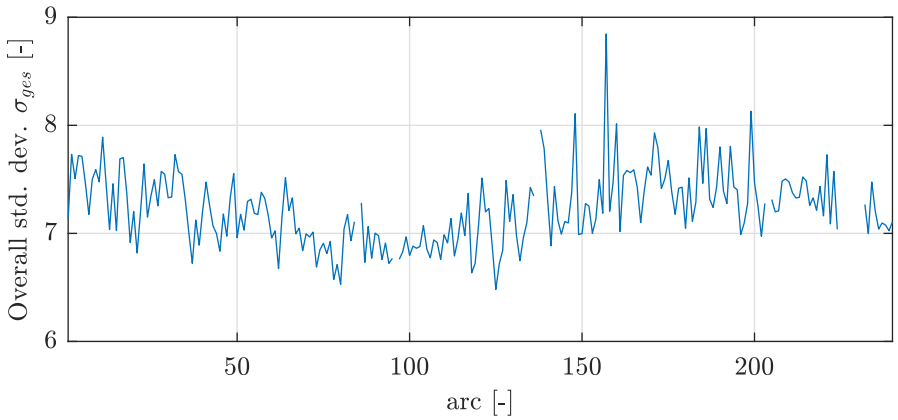

Figure 7.19: Overall standard deviation $\hat{\sigma}_{ges}$ for each arc of November 2006 solution.

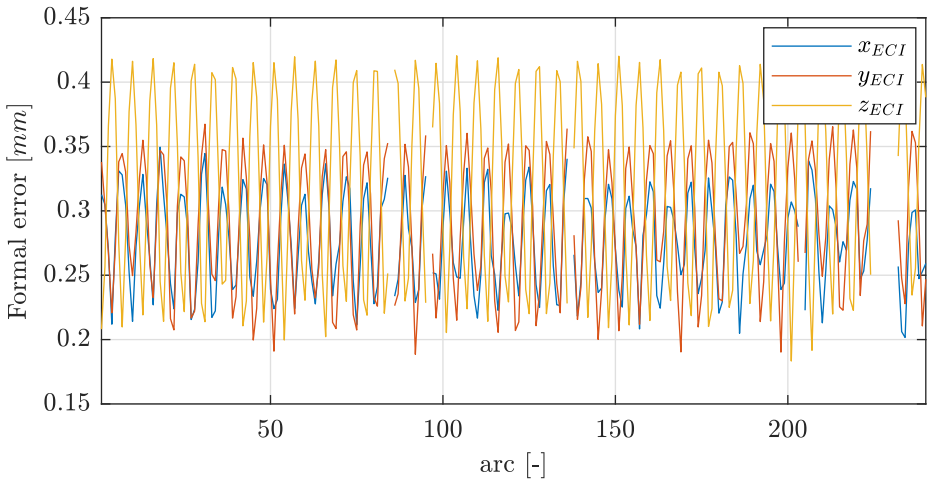

Figure 7.20: Formal errors of November 2006 solution for the local parameters initial position for each arc and GRACE A.

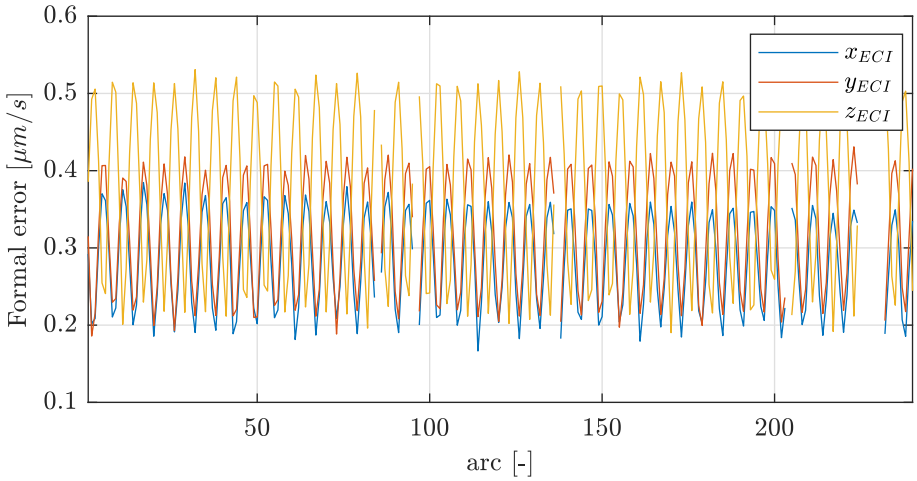

Figure 7.21: Formal errors of November 2006 solution for the local parameters initial velocity for each arc and GRACE A.

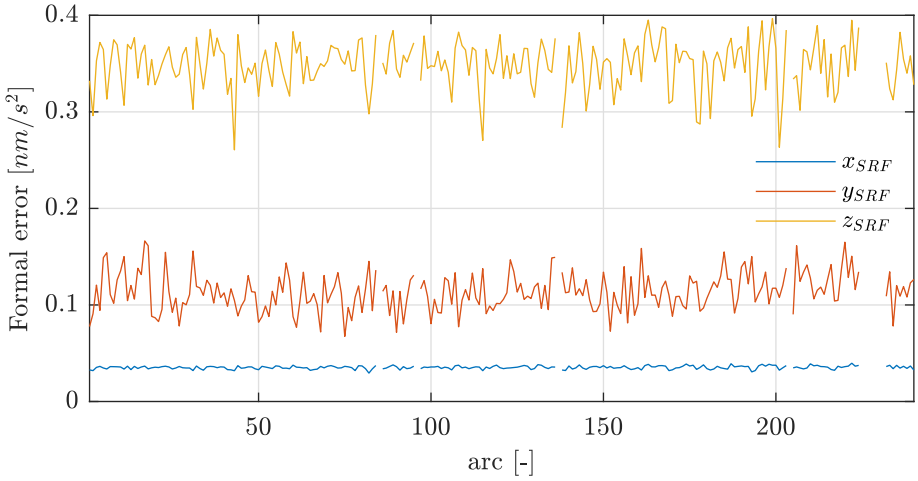

Figure 7.22: Formal errors of November 2006 solution for the local bias parameter $\vec{b}$ from the accelerometer calibration for each arc and GRACE A.

The initial velocity is shown in Figure 7.21. It is very similar to the initial position in terms of trend and oscillation. The formal errors for GRACE B are very similar to the GRACE A results and thus not shown here.

The formal errors of the local accelerometer calibration parameters are presented here for the monthly solution of November 2006, as well. The solution with 3h bias plus drift parametrization is depicted, as in Section 7.7.2 where the estimated calibration parameters are analyzed, (eg. Fig. 7.52).

In Figure 7.22 the formal error of the bias parameter is plotted for each arc and SRF-axis. The next Figure 7.23 shows the formal error of the drift parameter.

First, compared to the analysis in Section 7.7.2, the error level of both is at least about the factor 10 too low. Nevertheless, relatively the error levels for the different axes are reasonable. Also the variability over the arcs, which is much stronger for y- and z-axis, is in agreement with the analysis in Section 7.7.2. This holds as well for the higher error level of the drift compared to the bias.

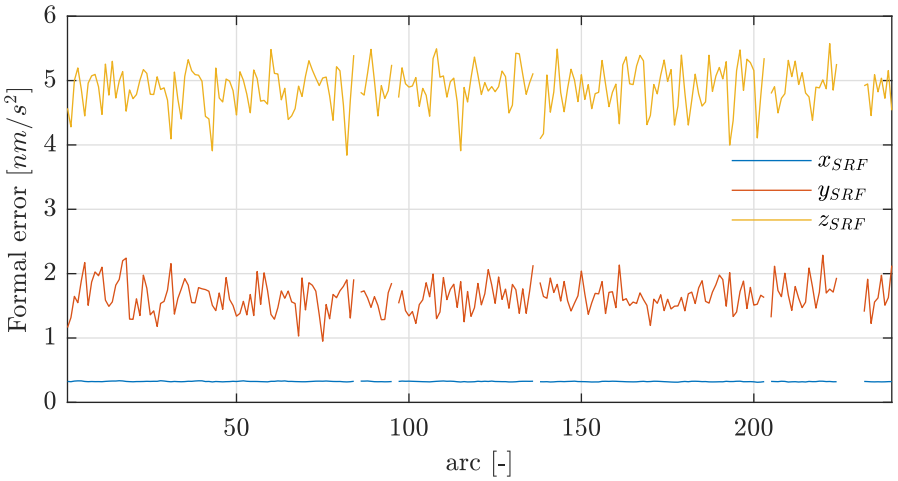

Figure 7.23: Formal errors of November 2006 solution for the local drift parameter $\vec{d}$ from the accelerometer calibration for each arc and GRACE A.

7.4 Discarding KBR Data from POD Pre-Processing

The L1B KBR data contain data gaps, as all the other L1B data. The length of the gaps varies from some seconds to a whole day. For the GFR processing times where no measurement data are available, are simply ignored when accumulating the normal equations in the batch algorithm.

Unfortunately, this may not be sufficient to determine reasonable gravitational field solutions. After a gap in the KBR data the instrument does not necessarily continue the time series, but "recalibrates" and continues with a different phase (see also Sec. 3.4.1). This very small effect in the range-rate, in the area of around 1 to 15 $\mu m/s$, has a strong effect on the GFR solution. Furthermore, after these jumps it might happen that the measurement accuracy is worsen up to an order of magnitude for some time.

These small effects are not directly visible in the KBR measurement data, which vary with a much higher amplitude, in the range of some m/s, due to the slightly different orbits of both GRACE satellites. The effects are also not visible in the post-fit deviations or residuals of the GFR, because they are affecting and deteriorating the gravitational field and hence the residuals too strong to detect these irregularities. Nevertheless, it is visible in the POD deviations or residuals, if POD is executed for both satellites simultaneously including KBR ranging as observation.

To demonstrate this phenomenon Figure 7.24 shows the KBR deviation from POD for June 15, 2006 for two arcs (113 and 114). The arc length is three hours and POD is conducted with VCE. The first arc is normal, it has no missing data and the post-fit deviation is in the range of 1 $\mu m/s$. The second arc has several data gaps and especially after the first gap, the time series is not continued and shows a jump.

In Figure 7.25 the KBR deviation is evaluated over the complete year 2006. Therefore for each arc the RMS value of the deviation is plotted. The situation for the month June is depicted in the zoom-in in more detail. The plot of the estimated standard deviation σ_k from the VCE estimation gives nearly the exact same curve.

For June it is visible that there are two peaks over several arcs with unusually high deviations. After the jump in arc 114 from June 15 (Fig. 7.24) for about ten more arcs the deviation stays high even though just in arc 118 another jump occurs.

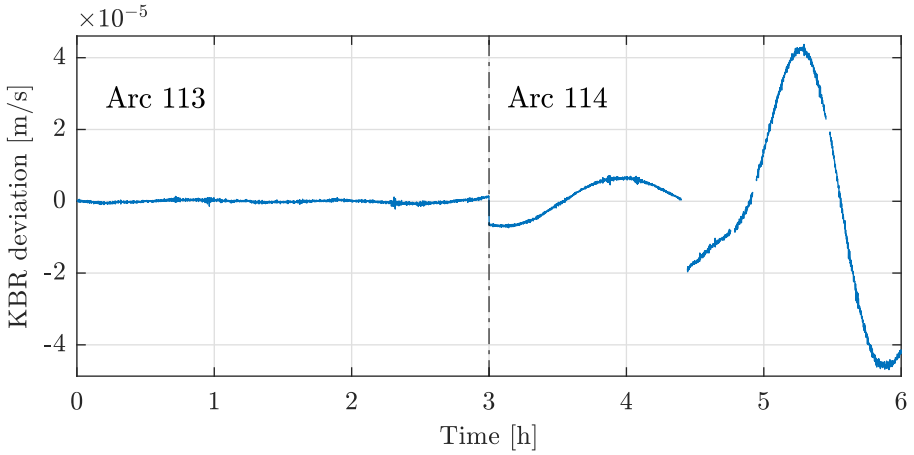

Figure 7.24: KBR post-fit range-rate deviation of POD from June 15, 2006 for two arcs (3h arc length, POD with VCE).

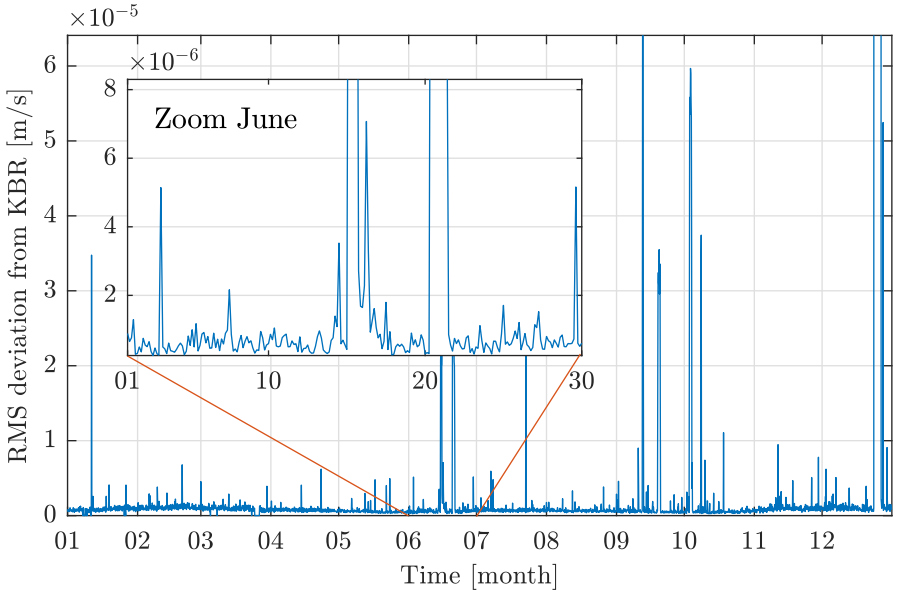

Figure 7.25: Arc wise RMS of KBR range-rate deviation of POD from the whole year 2006 and zoom-in for the month June (3h arc length, POD with VCE).

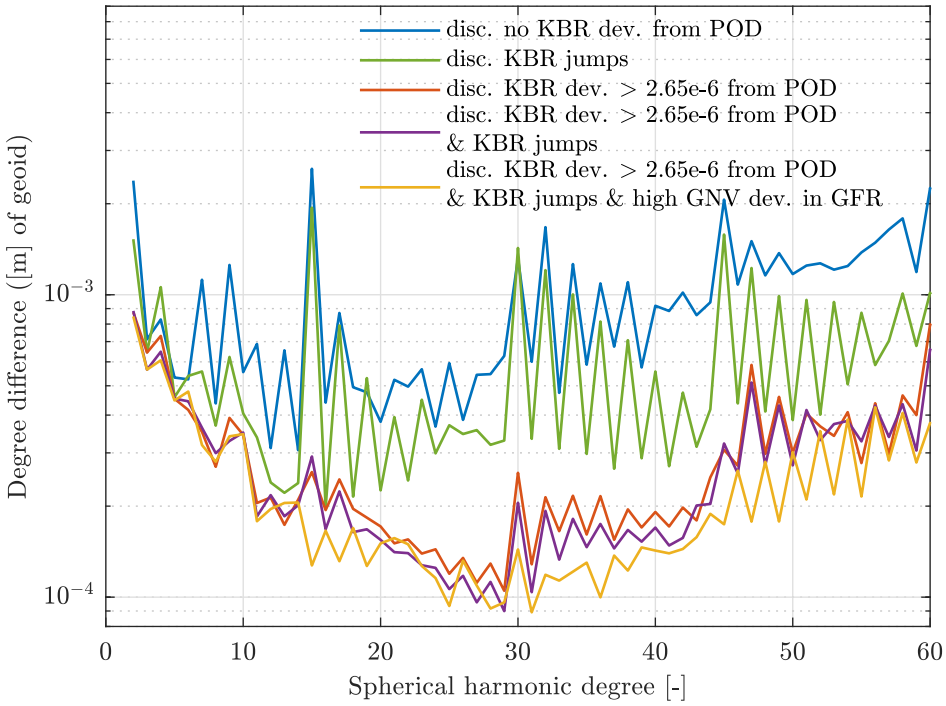

Figure 7.26: Degree difference of June 2006 solution with respect to GGM05s for different criteria of discarding arcs.

Over the year 2006 further very prominent peaks in the deviation occur in January, August, September, October and December, and some smaller ones in nearly all months. Its effects on the gravity field solutions are investigated in the following.

7.4.1 Influence of POD-Outlier Elimination Strategies on GFR

The effects of the different influences are investigated by discarding respective arcs in the GFR processing. For different months the results are again quite different. In Figure 7.26 results are shown in terms of degree differences for the monthly solutions of June 2006 considering different discarding criteria. The first curve (blue) shows the solution without considering KBR anomalies or KBR range-rate deviations (dev.) by POD. It is quite bad with low sensitivity and big oscillations and definitely no hydrology signal may be resolved with it. By discarding (disc.) all arcs where jumps occur in the KBR data after data gaps, the solution increases a little bit (green curve), but is still bad. Discarding arcs where the RMS value of the range-rate deviations from POD is higher than 2.65 $\mu m/s$ the quality of the solution increases dramatically (red curve). This criterion does not necessarily cover all jumps in the KBR data, but in most times it does. Nevertheless, two small jumps are not detected with this criterion in June. Discarding these as well (purple curve) again increases the solution slightly. After discarding arcs with high POD range-rate deviations, the GFR KBR deviations are quite smooth over the arcs. In a few cases this is not true for the GNV deviations, which may have a few peaks. Discarding these arcs as well and repeating the GFR, results in the even better yellow curve in Figure 7.26. The smoother curve between degree 30 to 40 has a distinct positive effect on the striping pattern in the spatial domain.

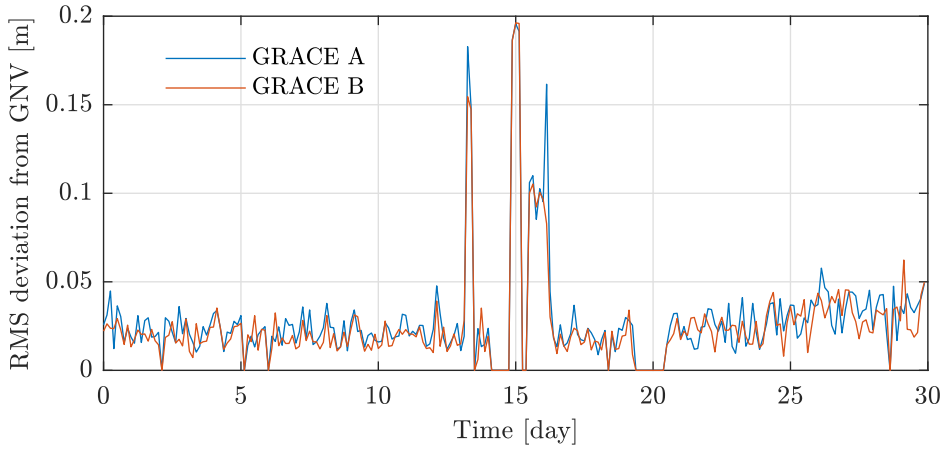

Figure 7.27: RMS of GNV deviation of all three axes of GFR from June 2006 for both GRACE satellites.

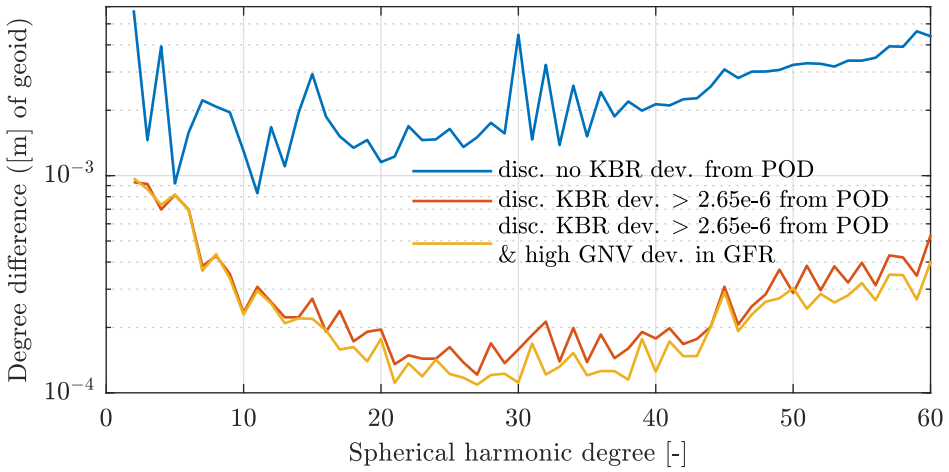

Figure 7.28: Degree difference of September 2006 solution with respect to GGM05s for different criteria of discarding arcs.

The GNV deviation for June 2006 from GFR is shown in Figure 7.27, demonstrating the unusual peaks. These deviations are not visible in the POD, but happen much less than the KBR anomalies and have less influence on the resulting gravity field.

The effect on the GFR solution from discarding arcs by the POD RMS range-rate deviation is not the same for each month. Figure 7.28 depicts the results for September 2006. The solution without considering the POD pre-processing is even worse than it is for June. For months with more smooth KBR deviations like eg. May 2006 (cf. Fig. 7.25) the effects on the GFR solutions are nearly not visible. The degree differences for the May 2006 solutions are shown in Figure 7.29 for different discarding criteria. Just two arcs are discarded in May due to high KBR deviations which is a comparably small amount. Nevertheless, just the amount is not a criterion, one arc with bad KBR data may destroy the solution of the whole month.

The value 2.65 $\mu m/s$ for discarding arcs by the POD RMS range-rate deviations is chosen more or less arbitrarily to catch the prominent peaks. Figure 7.29 illustrates that choosing smaller values, to catch smaller peaks, as well, has barely an effect on the GFR solution.

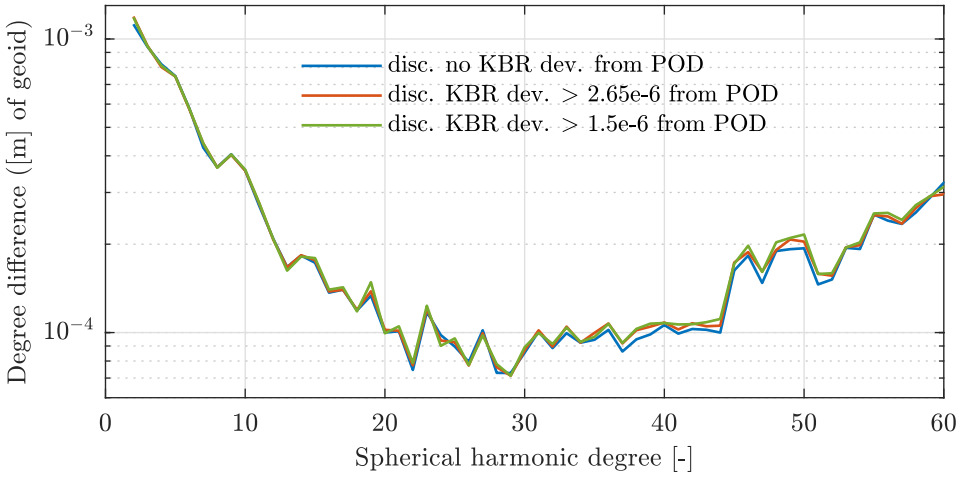

Figure 7.29: Degree difference of May 2006 solution with respect to GGM05s for different criteria of discarding arcs.

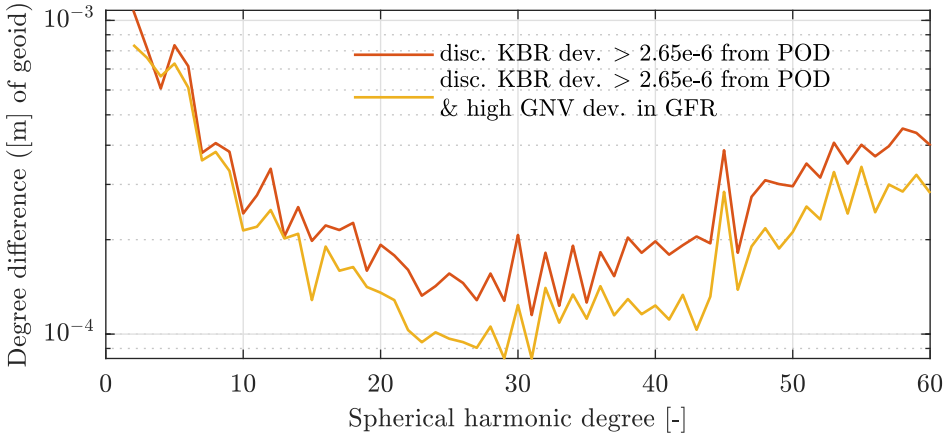

Figure 7.30: Degree difference of October 2006 solution with respect to GGM05s for different criteria of discarding arcs.

As mentioned above, the effect of discarding arcs from GNV residuals in GFR is not that big, but as well not the same for different months. In some months like January or July it has no influence on the solution, for June and September (Fig. 7.26 and 7.28) a small improvement is obvious. Nevertheless, the peaks in the GNV deviations for all months look similar. For October the improvement is quite big and shown in Figure 7.30. Even though just arcs with bad GNV observations are discarded, the gravity field solution improves over the whole spectrum, also in the higher degrees.

The results shown here conclude that an arc dependent weighting, for example using VCE, of KBR and GNV observations in the GFR process would be definitely reasonable.

7.5 Residuals and Deviations

The post-fit residuals or deviations (cf. Sec. 4.3.4 and Eq. 4.51) of the GFR processing are a further way to assess the quality and characteristics of the solutions. Furthermore, it gives information about the data quality and how it evolves over the time. Here the deviations are shown being the true difference of the model and the measured quantities,

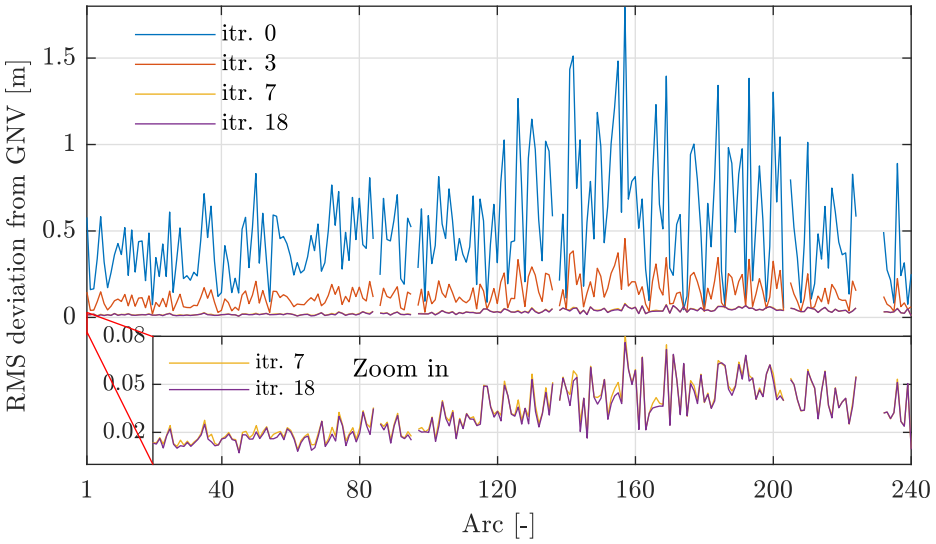

Figure 7.31: Arc wise RMS of GNV position deviations from GFR for different iterations for a monthly solution of November 2006 (3h arc length, discarded arcs from POD). The zoom-in shows the final iterations in detail.

whereas the residuals are the difference of the linearized model and the measurement. The computation of the residuals make it necessary to save all design matrices H (cf. Sec. 4.3.4), which might be a problem depending on the available hardware. The drawback of this is that the deviations need much more iterations to converge, as shown in this section. Nevertheless, with a sufficient amount of iterations residuals and deviations become similar (cf. the comparison in Sec. 8.1, Fig. 8.5 and 8.6). Hence, the residuals can be used for analysis instead of the deviations, which usually converge nearly instantaneously.

Figure 7.31 shows the evolution of the arc wise Root Mean Square (RMS) of the GNV position deviation from a monthly solution from November 2006. For each 3h arc an RMS value of the deviation over all three axes is plotted. The solution was iterated 18 times. After about seven iterations the GNV deviations do not change any more. In the deviations is an oscillation or trend over the month: At the beginning of the month the deviations are smaller, then increase and decrease again. This trend does not vanish with further iterations and the converged deviations show the same trend as the initial ones, just on a lower level. This means that the data itself is of different quality over the month.

For the KBR deviation the situation is a little different. The deviations are shown in Figure 7.32 in the same way and for the same time epoch as before. The KBR deviations need about 15 iterations to converge, hence much longer than the GNV deviations. After the first iterations they also show a trend, which vanishes after convergence. This is the usual case for all months after eliminating explicit KBR data errors. Du to the highly nonlinear dependency and the very accurate range-rate measurement, it takes more iterations until the linearized model has converged.

In the Figures 7.33 and 7.34 the same plots are shown for the month May, which is the month with the best quality of the gravitational field solution (cf. eg. Fig. 7.5 and 7.6). Compared to November, the RMS GNV deviations do not show a trend after convergence and are constantly between 1 and 2 *cm* over the month. As for November, the deviations are converged after about seven iterations. Most other months, where the gravitational field solutions are slightly worse than for May, show a trend in the

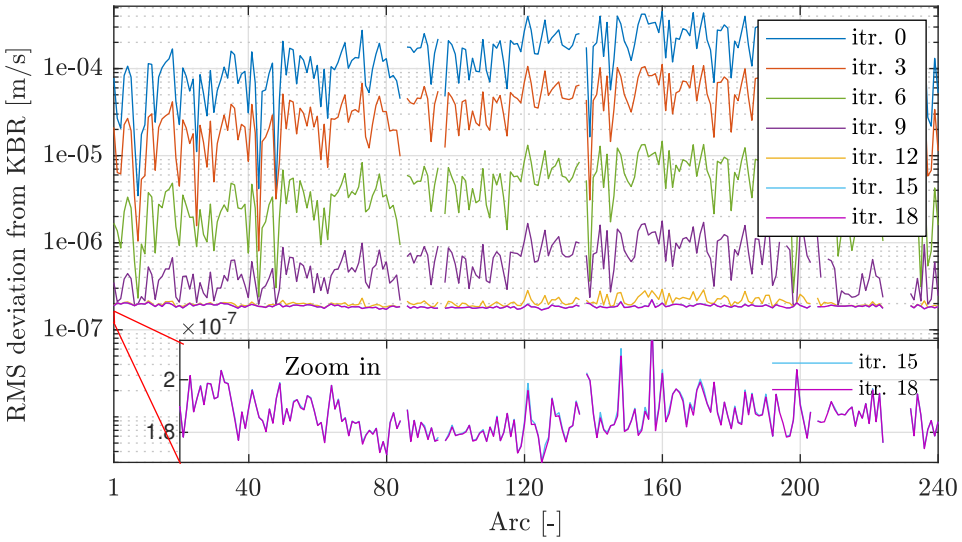

Figure 7.32: Arc wise RMS of KBR range-rate deviations from GRACE A for different iterations of monthly GFR solution of November 2006 (3h arc length, discarded arcs from POD). The zoom-in shows the final iterations in detail.

GNV deviations for the 3h arc lengths solutions. With the shorter arc length this trend vanishes a little, as also observed for the accelerometer calibration (cf. Fig. 7.53).

The KBR deviations are converged after 13 iterations, thus a little faster than for November, but initially start at a more equal level. After convergence, the deviations are surprisingly slightly higher than for November. This may highlight the importance of good position data (GNV) for the overall GFR solution.

For one exemplary arc (70) the deviation is plotted over time in Figure 7.35 for all three axes, for GRACE A. The GNV deviations show barely any high frequency noise (cf. also the ASD, Fig. 7.37), but a longer wavelength signal is distinctly visible. This is the case for all arcs. The signal is an error or an unmodeled effect acting on the satellites. It is not an error or difference in the processing of the GNV data by dynamic POD, because the same trend is visible in the deviations of the kinematic orbit data (KOS), as well, cf. Figure 7.43 and Section 7.5.1.

The zoom-in reveals a periodic relict in the GNV data with a frequency of $1/30\ Hz$. It is just affecting the x_{SRF} and y_{SRF} axes. Most probably it arises from a model or parameter that is updated every 30 seconds in the processing of the GNV data from the GNSS observations in the L1B processing.

In the Figures 7.36 and 7.37 the Amplitude Spectral Density (ASD) of the GNV position deviation from arc 70 is shown for the first and 18th iteration, respectively (the ASD and its computation, that is used throughout the thesis, is briefly discussed in the Appendix A.2). The high frequency part after the first and last iteration looks the same. The periodic relict with $1/30\ Hz$ and multiples of that are clearly visible as spikes. The z_{SRF} axis has a notable lower high frequency noise level, which also tends do decrease with higher frequencies. The low frequency part shows higher amplitudes, for the first iterations, which successively decrease, as expected.

In Figure 7.38 the ASD from the KBR range-rate deviations is shown for the first and 18th iterations for the same arc. The low frequency amplitudes drop over several magnitudes over the iterations, because the main gravity signal is decoded in that spectrum of the data. The high frequency part ($> 0.01\ Hz$) contains mainly noise and

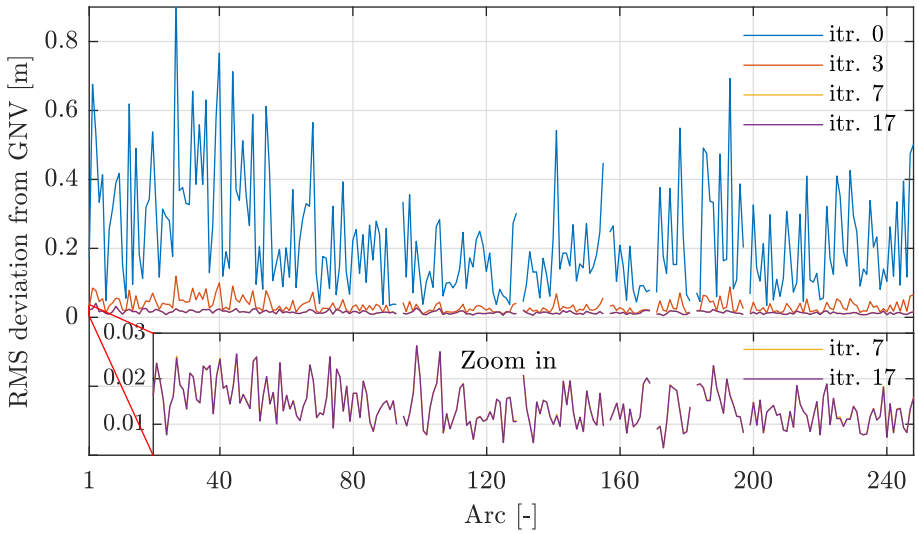

Figure 7.33: Arc wise RMS of GNV position deviations from GRACE A for different iterations of monthly GFR solution of May 2006 (3h arc length, discarded arcs from POD). The zoom-in shows the final iterations in detail.

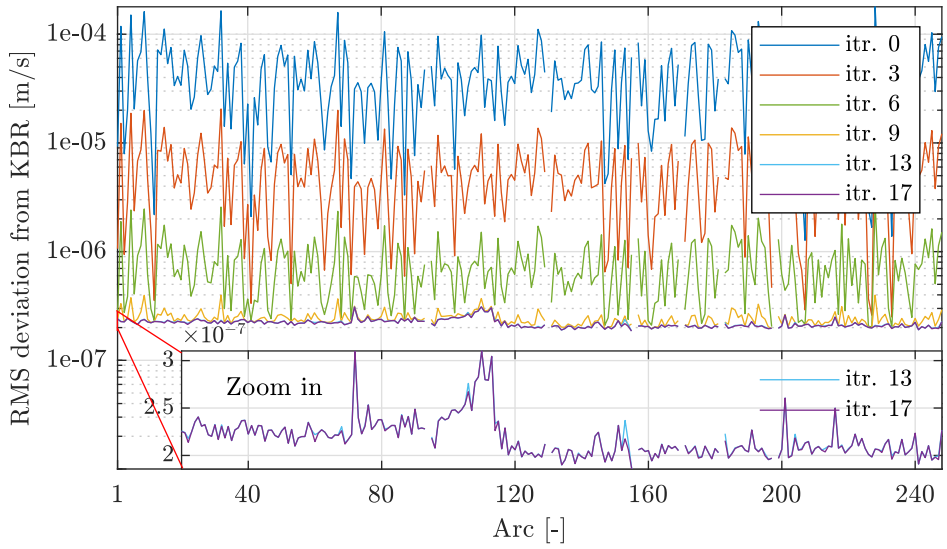

Figure 7.34: Arc wise RMS of KBR range-rate deviations from GRACE A for different iterations of monthly GFR solution of May 2006 (3h arc length, discarded arcs from POD). The zoom-in shows the final iterations in detail.

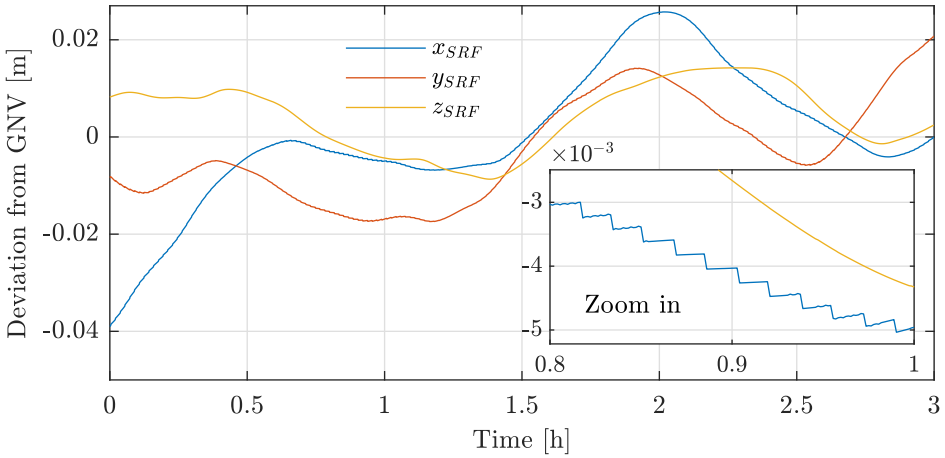

Figure 7.35: GNV position deviation of GFR after 18th iteration from November 2006 for each axis, arc 70, GRACE A.

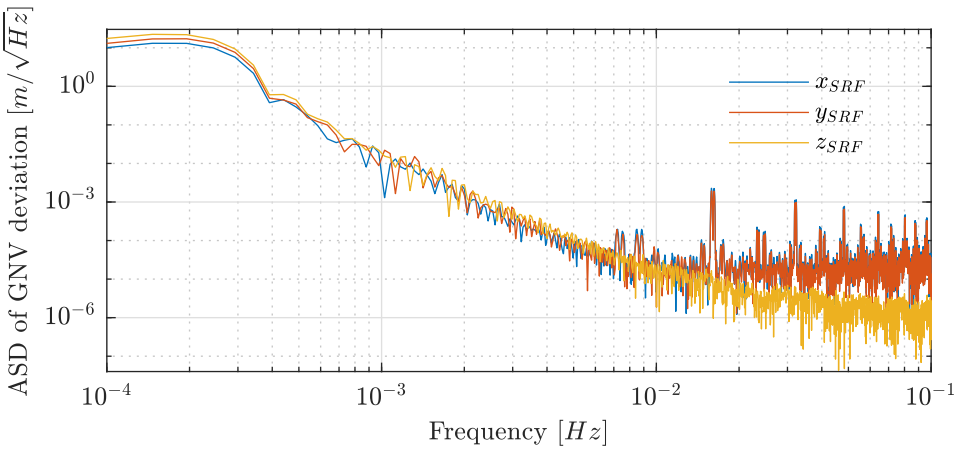

Figure 7.36: ASD from GNV position deviation of GFR after first iteration from November 2006 for each axis, arc 70, GRACE A.

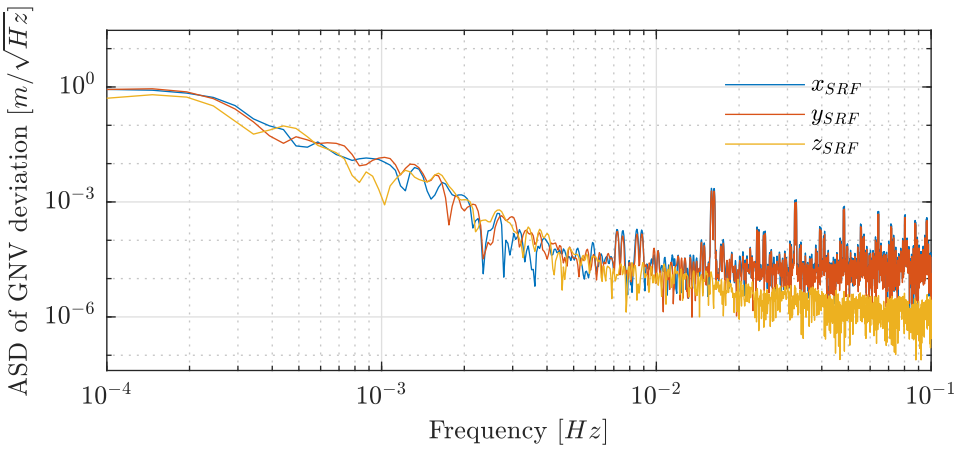

Figure 7.37: ASD from GNV position deviation of GFR after 18 iterations from November 2006 for each axis, arc 70, GRACE A.

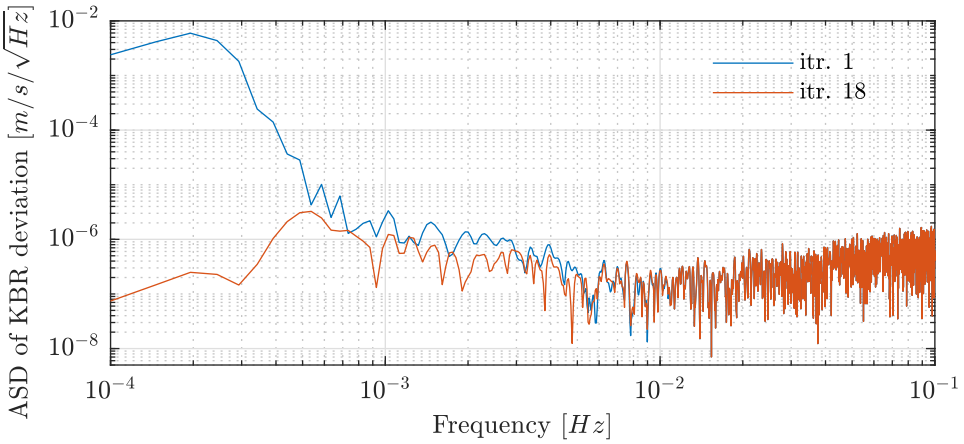

Figure 7.38: ASD from KBR range-rate deviation of GFR after the first and 18th iteration from November 2006, arc 70, GRACE A.

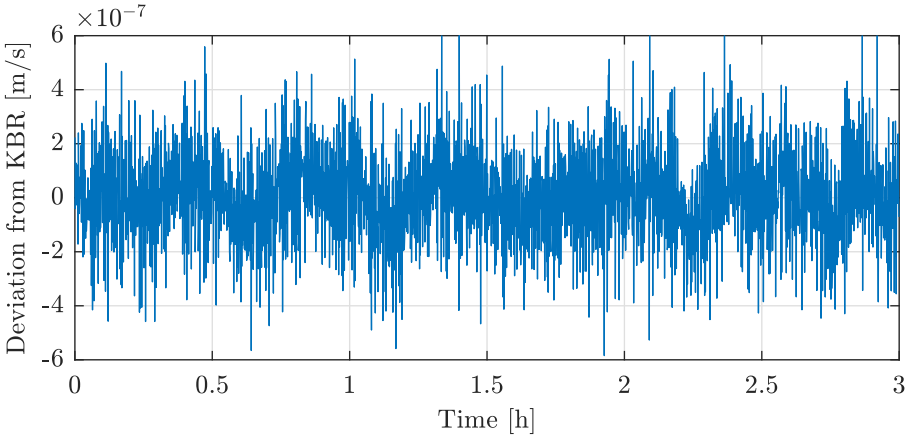

Figure 7.39: KBR range-rate deviation of GFR from November 2006 after 18th iteration, arc 70, GRACE A.

does not change over the iterations. It shows the typical linear increase caused by the derivation of the range when deriving range-rate observations in the L1B processing.

The range-rate deviations for that arc are shown in Figure 7.39 as time series from the 18th iteration. As seen before in the ASD, also in the time domain a colored noise characteristic of the KBR instrument is visible.

In contrast to the analysis of GNV and KBR deviations, the resulting gravity field converges much faster. After about four iterations the solution does not change much, anymore. For selected iterations the degree difference of the November solution with respect to GGM05s is shown in Figure 7.40.

7.5.1 Using Kinematic Orbits

Solutions computed using kinematic orbit data (Kinematic Orbit Solution, KOS) instead of the dynamic GNV data (cf. Sec. 3.3) do not differ much from each other in all aspects.

In Figure 7.41 the degree difference for the monthly solutions using GNV and KOS data (additional to KBR range-rate data) for November and May 2006 are compared. All other parameters are the same. It is obvious, that the quality is very similar over

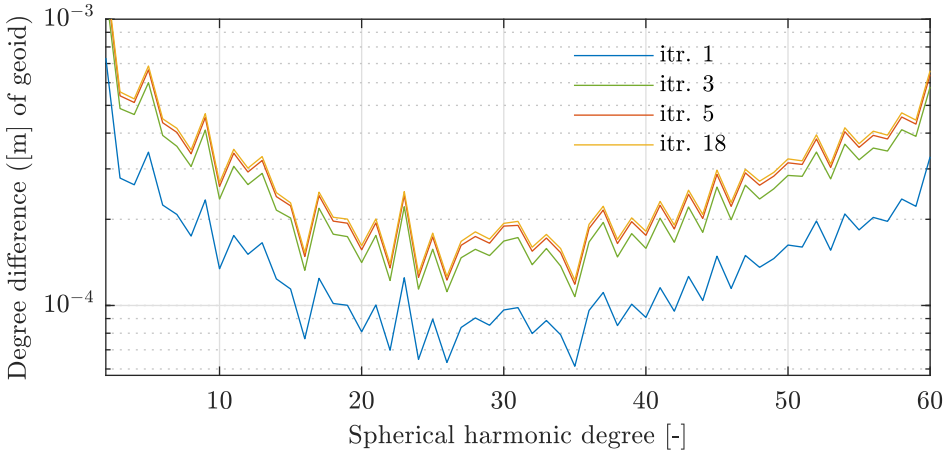

Figure 7.40: Degree difference of different iterations with respect to the initial gravity field from monthly solution of November 2006 (3h arc length).

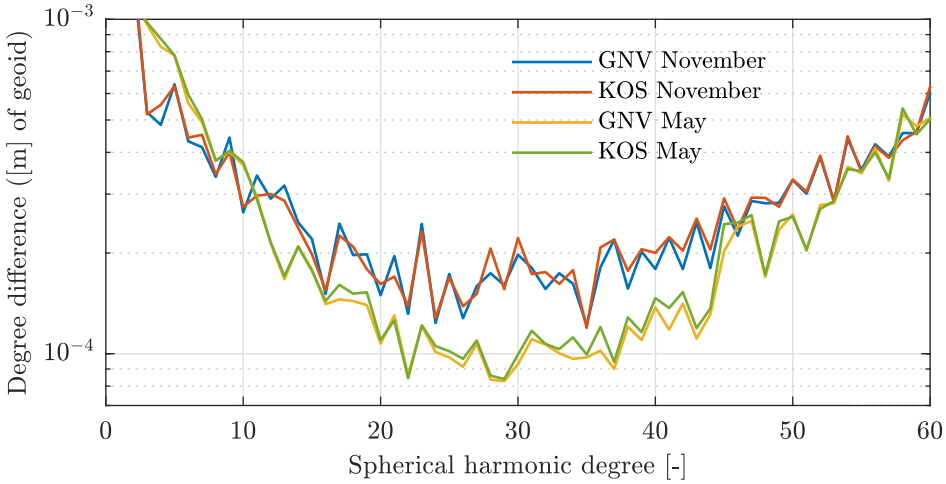

Figure 7.41: Degree difference of November and May solution using GNV and KOS data (additional to KBR data) with respect to GGM05s.

the whole range of the spectrum and for both months. This is also the case for all other investigated epochs.

The RMS deviation over one month (November) is shown in Figure 7.42 for selected iterations. The same plot has been shown before for the GNV data (Fig. 7.31). As before, the deviations are converged after about seven iterations. The general level of the deviations is slightly higher, here. Nevertheless, the same trend over the month is visible in the KOS deviations. This is reasonable because GNV and KOS data are determined with the same GNSS observations. The trend is also the same for GRACE A and B, thus one can conclude that the quality of the GNSS measurement changes over the months and year.

The deviation of the KOS data for one arc is shown in Figure 7.43 (cf. Fig. 7.35 for the GNV deviation). While the general trend (the arc wise RMS) is more or less the same, for KOS and GNV position data, the actual deviation is a little different. The KOS deviation has a much stronger high frequency noise, which is due to the kinematic generation of KOS data from the raw GNSS observations. Nevertheless, the already observed longer wavelength trend is very similar for most of the time, as already

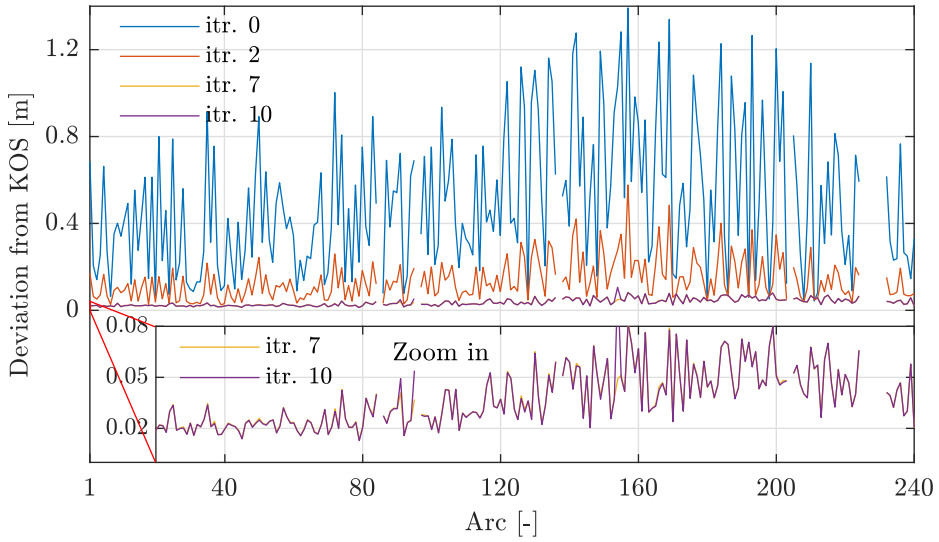

Figure 7.42: Arc wise RMS of KOS position deviations from GRACE A for different iterations of monthly GFR solution of November 2006 (3h arc length, discarded arcs from POD). The zoom-in shows the final iterations in detail.

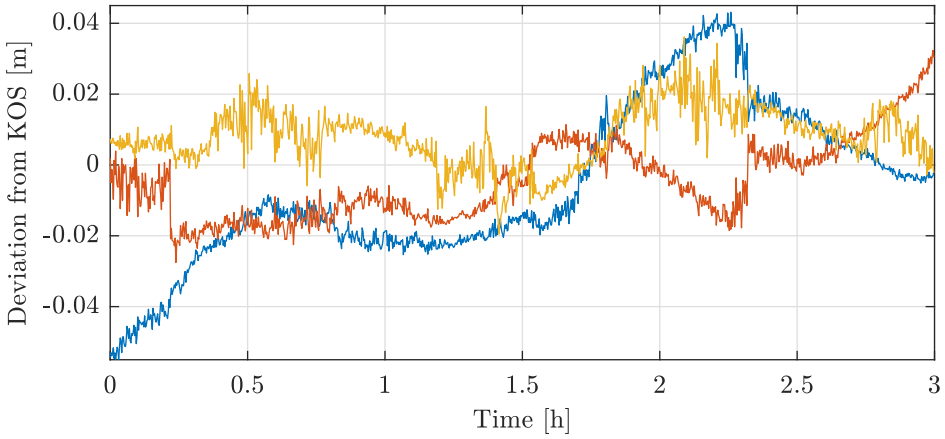

Figure 7.43: KOS position deviation of GFR from November 2006 for each axis, arc 70, GRACE A.

mentioned before. That means that the uncaptured or unmodeled signal in the GNV deviations can not be pinned on the generation of the GNV data by a POD technique with different and unknown models.

The ASD of the KOS deviation for this arc is shown in Figure 7.44. The high frequency noise is about white with a standard deviation of $\approx$1 *cm*. In general the KOS data show some spikes and irregularities due to their heritage from the raw GNSS data.

The solution using KOS data is more "physical" or "clean", because compared to the GNV data, no additional gravitational (and other) models are used in its processing. Nevertheless, KOS data are not directly published from the GRACE mission but need to be computed from the raw data or used from different sources like eg. from TU Graz (cf. Sec. 3.3). Because it is based on kinematic orbit determination, KOS data exhibit gaps just like KBR, ACC and SCA data and thus more than GNV data. Furthermore, its sampling rate is 1/10 Hz compared to the 1/5 Hz of the other data. Hence more

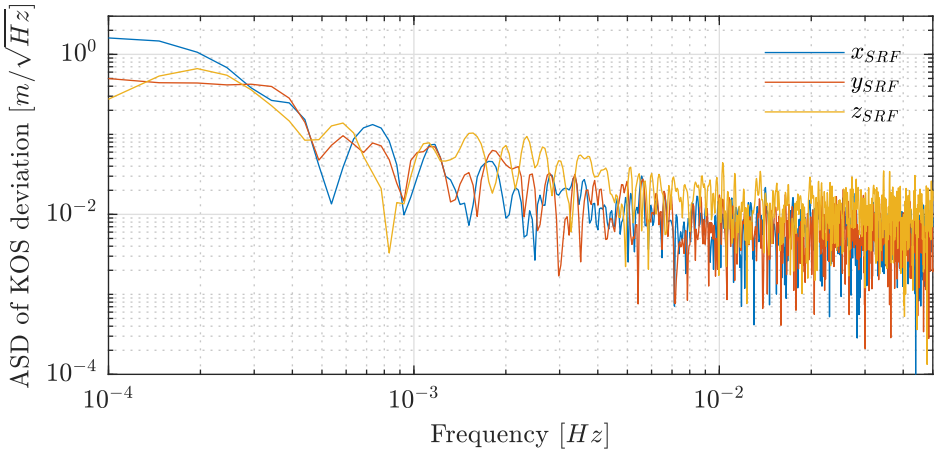

Figure 7.44: ASD from KOS position deviation of GFR from November 2006 for each axis, arc 70, GRACE A.

pre-processing is needed to use KOS data instead of GNV data. Because the results are very similar, as default the GNV data are used in this thesis, nevertheless.

7.6 Estimated Annual Gravitational Fields from the Year 2006

From the analysis conducted in the previous sections, the optimal parameter choices and options for the GFR from GRACE data have been determined. Even though the optimal choices are slightly dependent on the the epoch, settings that work quite well in general have been identified.

The advertised pre-processing of the L1B data, especially the POD pre-processing for KBR data (Sec. 7.4 and 3.4) has proven to be indispensable for most months.

For the GFR processing the weighting (Sec. 7.1) of the GNV 3d-position and KBR range-rate observations and the parametrization (Sec. 7.2) are of highest importance to obtain reasonable results. The weighting combination of $\sigma_g = 0.02$ and $\sigma_k =$ 1e-8, has proven to be the best. The results for parametrizartion are more unambiguous. Nevertheless, the bias plus drift accelerometer calibration with an arc length of 2h to 3h performed best.

In the following two Figures 7.45 and 7.46 the twelve monthly solutions for the year 2006 are shown spatially for the bias plus drift calibration for 3h and 2h arc length, respectively, in terms of EWH with respect to the mean GGM05s gravitational field model. In Figure 7.47 the difference between both is shown in the same way.

For the majority of the months the shorter arc length of 2h is definitely superior and reduces the prominent striping error pattern. For some months, like May and October, the 3h solution gives slightly better results.

In general the typical north-south striping is still visible in most solutions. The striping and the overall quality of the solutions is very different for nearly each month. Especially the February solution exhibits a very prominent striping. Due to a higher filter radius of the applied Gaussian filter (cf. Sec. 2.3.4) this might be reduced, but of cause also smoothing or blurring the signal content. The best solution is obtained in May, where the results are comparable with the official solution (cf. Fig. 7.5). Nevertheless, in all solutions the typical annual hydrological cycle and the prominent trends at the poles, as

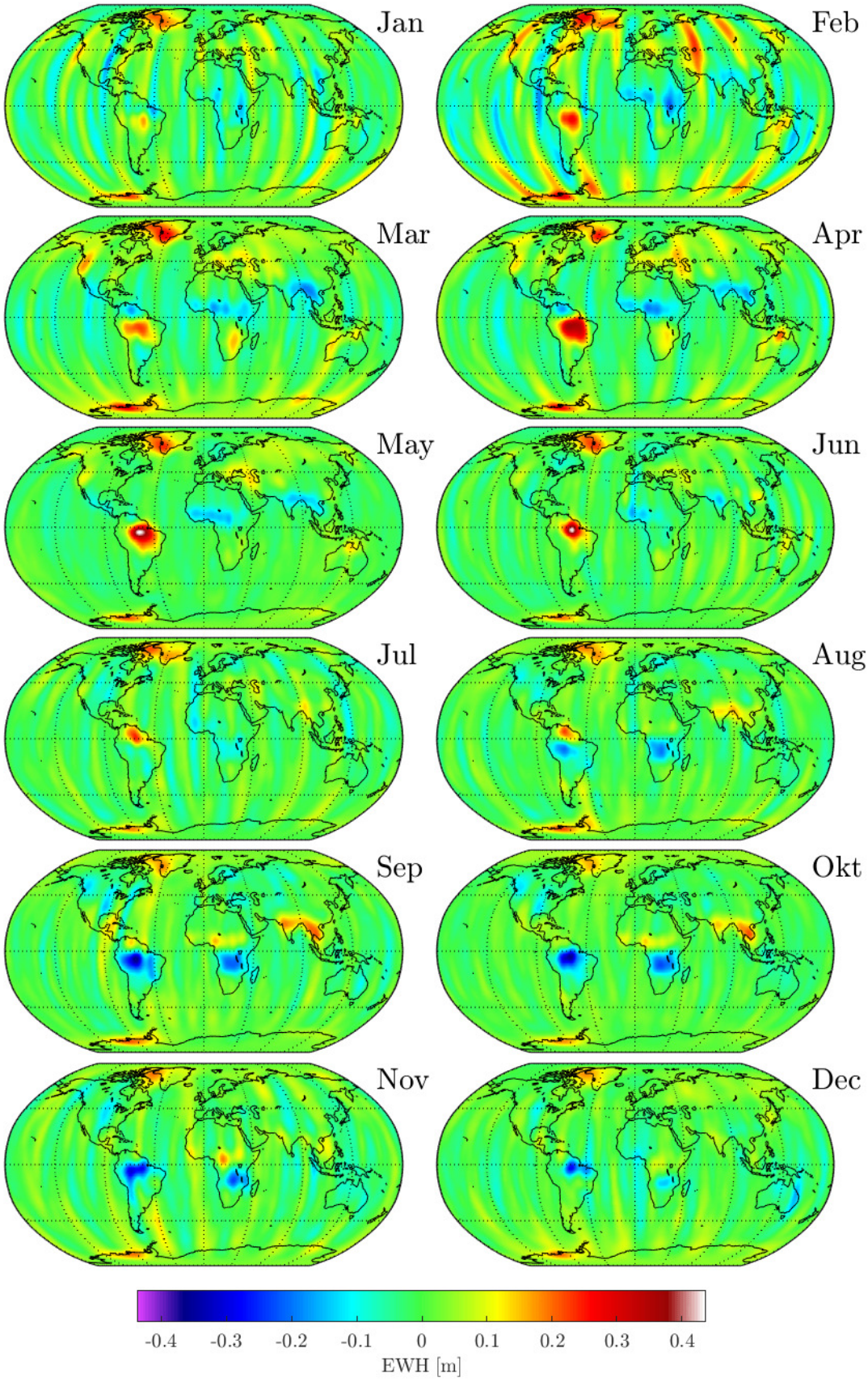

Figure 7.45: Monthly solutions of 2006, EWH with respect to GGM05s. For 3h arc length, bias plus drift ACC calibration. Gaussian filter with 465 km radius applied.

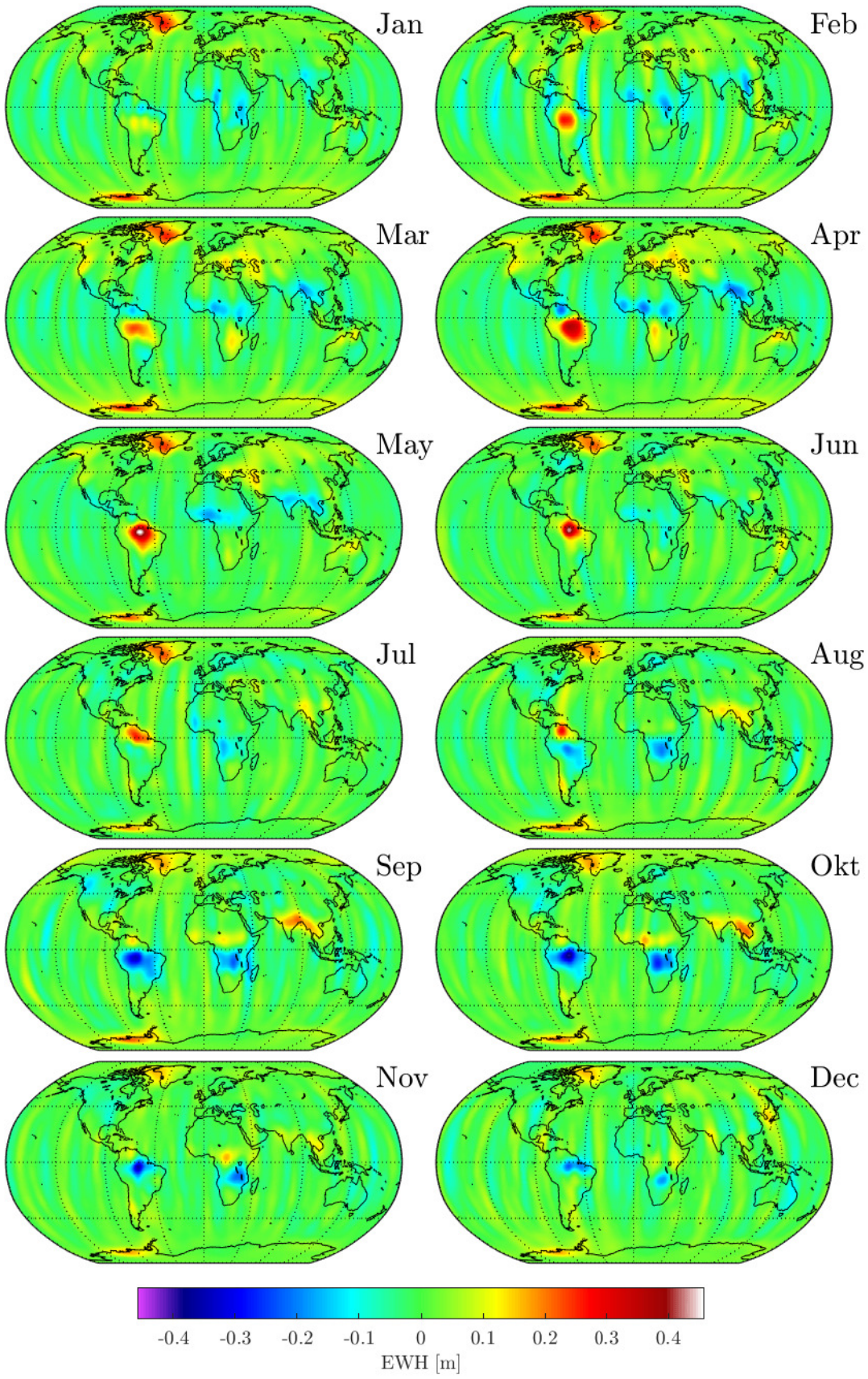

Figure 7.46: Monthly solutions of 2006, EWH with respect to GGM05s. For 2h arc length, bias plus drift ACC calibration. Gaussian filter with 465 km radius applied.

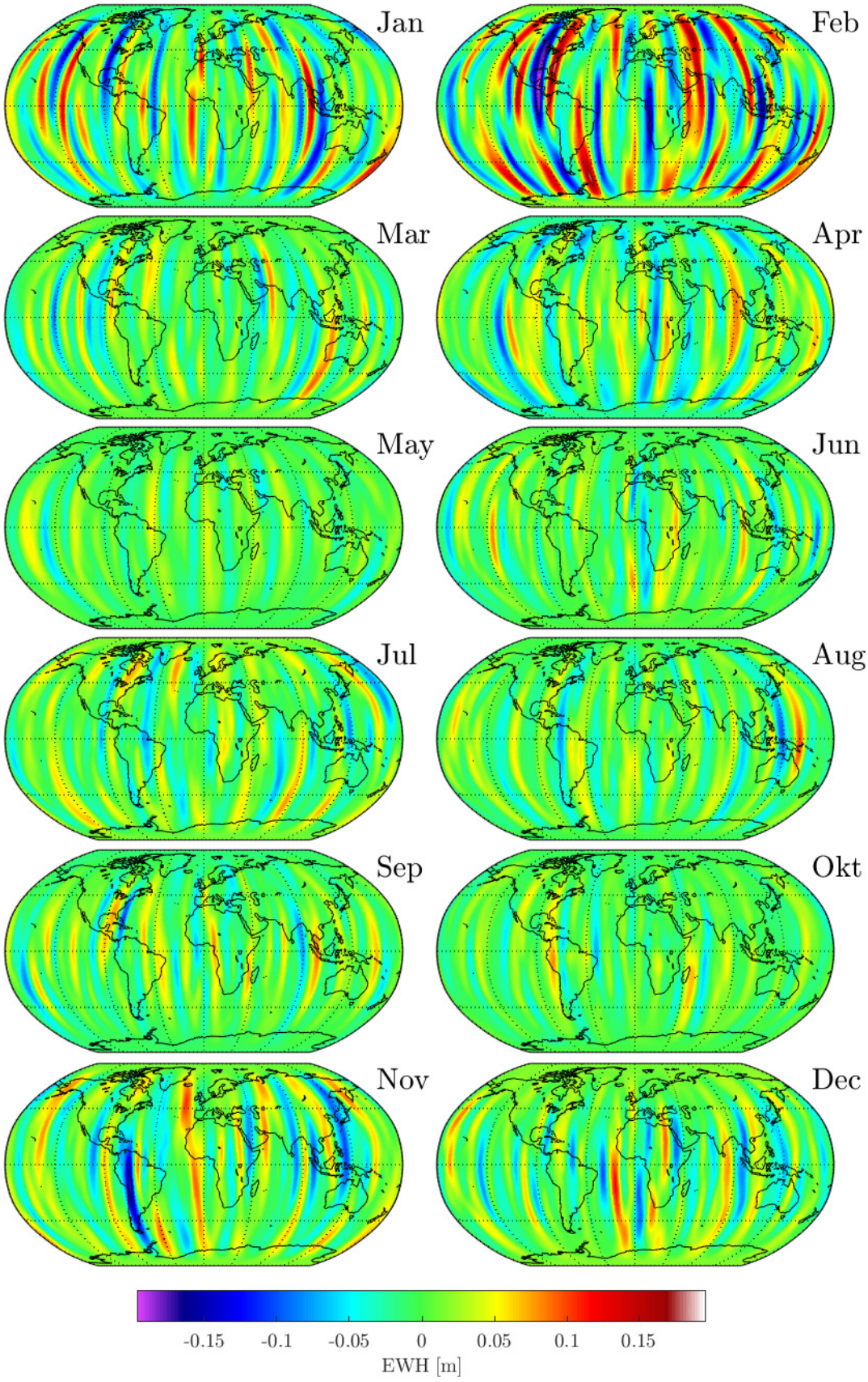

Figure 7.47: Difference of monthly solutions with 2h and 3h arc length of 2006, in terms of EWH, bias plus drift ACC calibration. Gaussian filter with 465 *km* radius applied.

described in detail in the Introduction (Ch. 1.1) and Section 2.3.2, are directly visible in the plots.

The differences between the 3h and 2h solutions are explicitly shown in Figure 7.47. In the differences just the prominent striping pattern is visible. A typical hydrology signal or pattern is not recognisable between the different arc lengths solutions. Nevertheless, the differences are rather big, so that small differences in the signal are not detectable in these plots. Especially for the first and last months of the year the striping amplitude is high, which is also directly visible by comparing the two solutions plotted with respect to the mean GGM05s model in the Figures 7.45 7.46. It has to be concluded, that the 3h arc length is not optimal for most of the months.

7.7 Accelerometer Calibration

It has been demonstrated (eg. Sec. 7.2) that the accelerometer calibration is a crucial point for GFR. In this section the estimated accelerometer calibration, defined by the parameters bias $\hat{\vec{b}}$ and drift $\hat{\vec{d}}$, is shown and investigated for the different GFR processing options and epochs.

7.7.1 Influence of Weighting on Accelerometer Calibration

The weighting of GNV position measurements and KBR range-rate measurements has a big influence on the GFR solutions, as demonstrated in Section 7.1. For the different weighting combinations the estimated accelerometer calibration parameters differ considerably.

For different weighting combinations from GFR of May 2006 with 3h arc length and bias plus drift parametrization (cf. Fig. 7.2), the estimated accelerometer calibration parameters are shown in Figure 7.48, for GRACE A. The results for GRACE B are similar in trend and structure and thus not shown here. The parameters, estimated for each arc, are plotted over the time for the whole month. For better presentation in one plot, the calibration for each of the three SRF-axes is shifted by the values given in the figure. The mean value over the month is indicated by the dotted lines. As in Section 7.1, the weighting factor for the GNV position observations σ_g is 0.02 for all cases and σ_k is varied: (a) σ_k=1e-6 (b) σ_k=1e-7 (c) σ_k=1e-8 (d) σ_k=5e-9.

The calibration exhibits a distinct variation around the mean. For all four weighting combinations, the general structure is the same. The x-axis has the lowest variation, and the z-axis the biggest. The difference of the variation around the mean is high. Its minimal value is around 3 nm/s^2 in x-axis, but reaches up to 300 nm/s^2 in z-axis. This high variation with big jumps between arcs and steep drifts of the calibration is definitely not a physically description of the accelerometer processes, and the real non-gravitational accelerations acting on the satellites, at least on short time scales (cf. Sec. 6.1.6). In contrast to that, the mean values are rather constant over time and for the four different cases with differences of maximal 10 nm/s^2.

The magnitude of the variation is distinctly increasing with lower KBR weighting σ_k. Nevertheless, the GFR solutions for the lower σ_k weighting factors (a), (b) are distinctly worse than the higher ones (c), as shown in Section 7.1 or the Figures 7.2 and 7.4. Thus the nonphysical calibration results in a better overall solution.

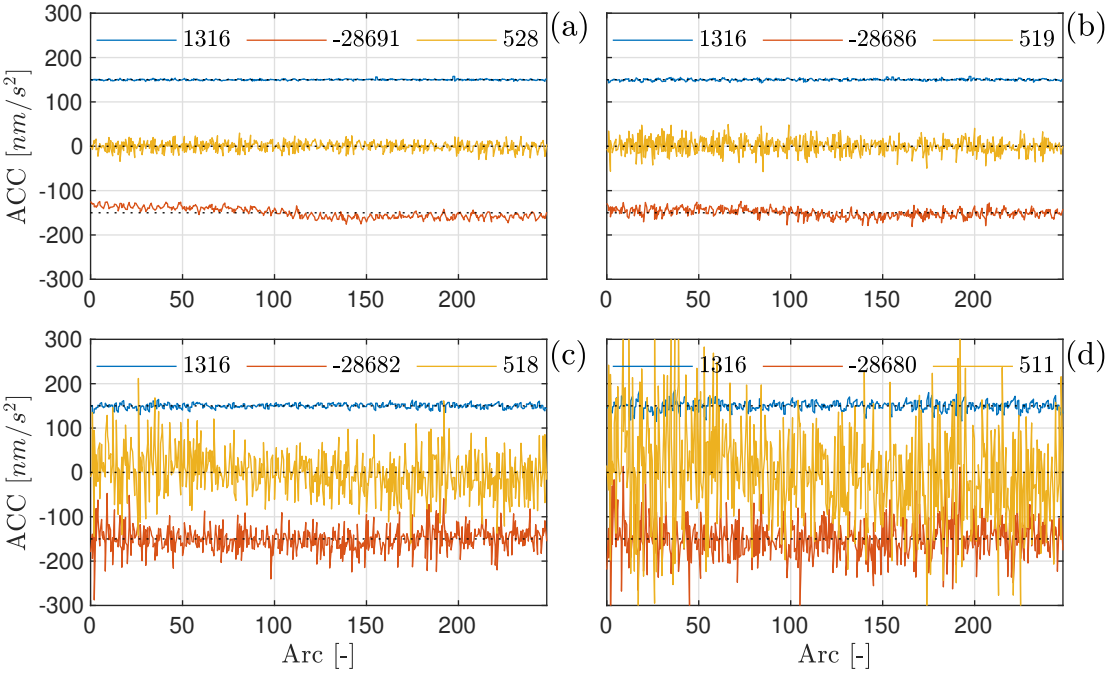

Figure 7.48: Estimated accelerometer calibration from GFR solutions of May 2006 with 3h arc length and bias plus drift parametrization, for GRACE A for different weighting factors of the KBR range-rate measurement σ_k: (a) σ_k=1e-6 (b) σ_k=1e-7 (c) σ_k=1e-8 (d) σ_k=5e-9. GNV data are always weighted with σ_g=0.02. The calibration of all three SRF axes (x: blue, y: red, z: yellow) is shifted for better visibility in one figure by the values given in each plot in nm/s^2. The mean values are depicted as black dotted line.

The variation of the calibration is illustrated qualitatively in Figure 7.49, where the standard deviation of the calibration is plotted over six different weighting factors for σ_k.

7.7.2 Influence of Parametrization on Accelerometer Calibration

Besides the weighting, the calibration of the accelerometer data has a major influence on the resulting gravitational field solutions, as shown before in Section 7.2. Hence it is worse to have a closer look on the estimated calibration parameters for different parametrizations.

Results are shown for monthly solutions from November 2006 for different arc length and just bias or bias plus drift parametrization, as investigated in Section 7.2 and Figures 7.10 and 7.11 (with the standard weighting of σ_g=0.02, σ_k=1e-8).

For just bias parametrization the estimated accelerometer calibration parameters are shown in Figure 7.50, for GRACE A, in the same way as in the previous subsection. The results are obtained for arc length of: (a) 3h (b) 2h (c) 1.5h (d) 1h.

The data quality over the month November varies stronger as for May, thus, in the plots (a) and (b) a variability over the month is visible. It follows the same trend as the post-fit GNV deviations, shown in Section 7.5 and Figure 7.35. With decreasing arc length this trend is neutralized (c), (d) and the variability is reduced. For the shortest arc length of 1h, it is again increasing slightly. Even though, for the best overall

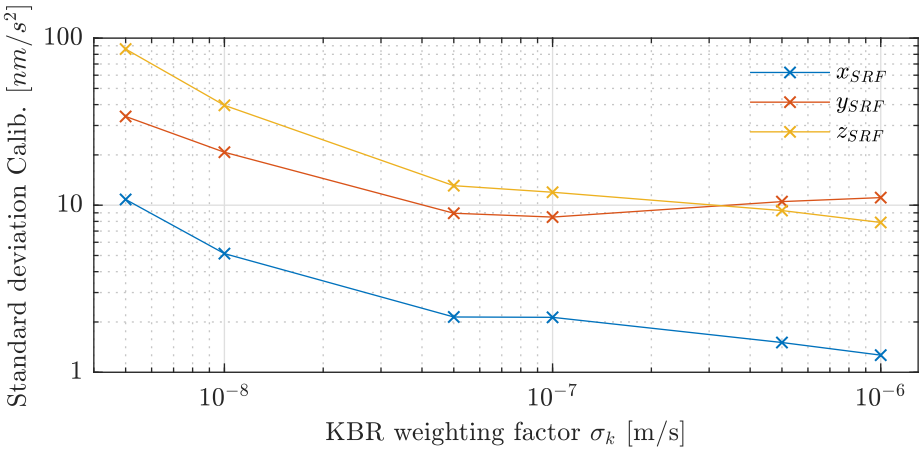

Figure 7.49: Standard deviation of estimated ACC calibration plotted over the different weighting factors of the KBR range-rate measurement σ_k, showing the variability of the ACC calibration parameters. From GFR of May 2006 solutions with 3h arc length and bias plus drift parametrization, for GRACE A.

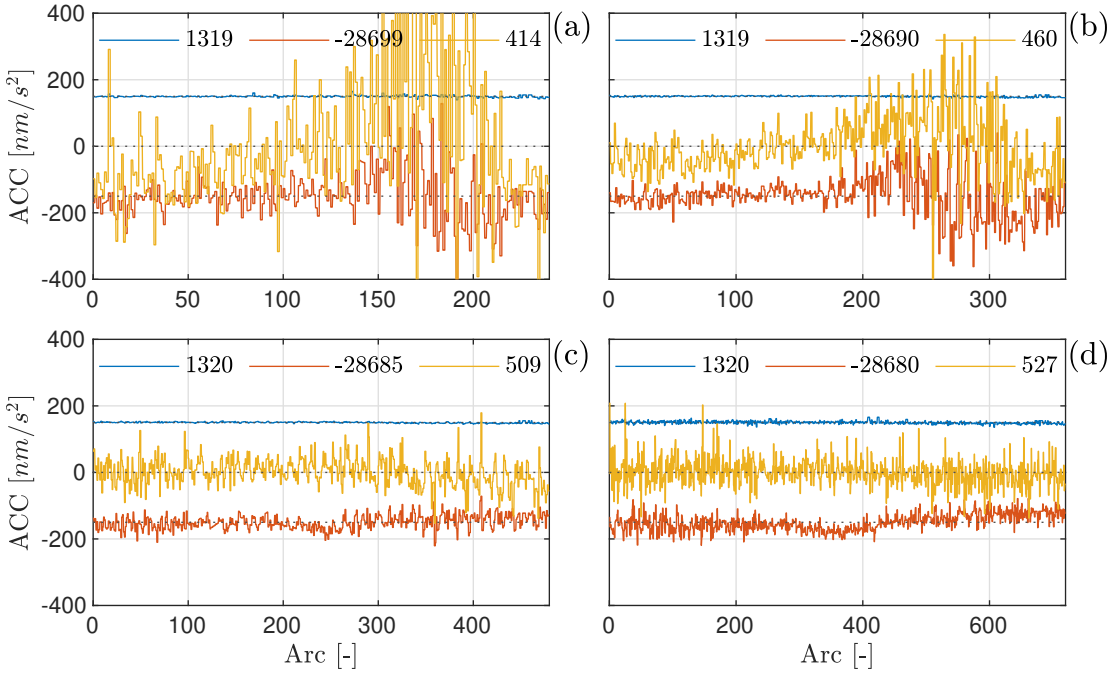

Figure 7.50: Estimated accelerometer calibration from GFR solutions of November 2006 with just bias parametrization, for GRACE A for different arc lengths: (a) 3h (b) 2h (c) 1.5h (d) 1h. The calibration of all three SRF axes (x: blue, y: red, z: yellow) is shifted for better visibility in one figure by the values given in each plot in nm/s^2. The mean values are depicted as black dotted line.

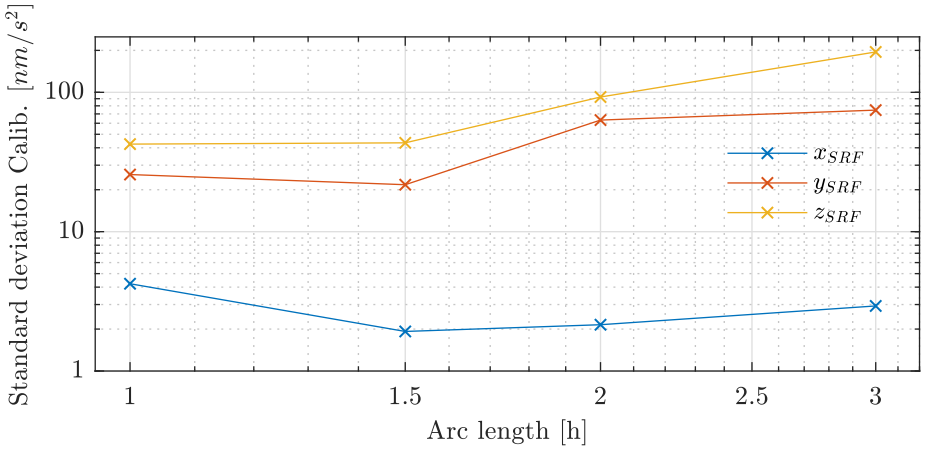

Figure 7.51: Standard deviation of estimated ACC calibration plotted over different arc lengths, showing the variability of the ACC calibration parameters. From GFR of November 2006 solutions with just bias parametrization, for GRACE A.

gravitational field solution with 1.5h arc length (c) the short term variation around the mean of the calibration up to 100 nm/s^2 is still non-physical.

The mean of the calibration changes for different arc length especially for y- and z-axis, where a definite trend is visible (both increasing with shorter arc length).

The standard deviation of these calibrations is depicted in Figure 7.51. It shows the increasing variability with bigger arc length qualitatively for each SRF-axis.

For the parametrization with bias plus drift, which is giving the best overall gravity field solution (cf. Sec. 7.2), the estimated calibration is shown in Figure 7.52 for the same arc lengths as before: (a) 3h (b) 2h (c) 1.5h (d) 1h.

When for the 3h arc length a trend is observable, for the 2h solution it is already vanished. Compared to the just bias parametrization 7.50 this is accomplished with a slightly longer arc length. Compared to the just bias parametrization the mean values of y- and z-axis show the same trend but with lower difference.

Again, the standard deviation over the arc length is plotted in Figure 7.53. The variation around the mean is higher than for the just bias parametrization case for all arc length. But still the even more non-physical calibration gives the better overall gravity field results.

7.7.3 Estimated Accelerometer Calibration Comparison

For the whole year 2006 the accelerometer calibration for the GFR solutions with 3h arc length and bias plus drift parametrization is shown in Figure 7.54 for each SRF-axis for GRACE A and in Figure 7.55 for GRACE B. In both figures a median filtered time series of the calibration is plotted, as well. The filter order is set to 50 hours. Notice the different scales for the three axes, the x-axis calibration is still much smoother than z-axis.

It is obvious that the high variation of the estimated calibration, as also seen before for November in Figure 7.52, persists over the whole year, for all months. Especially the estimated drift parameters make the results very unrealistic. The median filtered calibration exhibits some trends and gives a good mean value to compare it to the non-gravitational force model based calibration (Sec. 6.1.6 and Wöske et al. (2019)) and

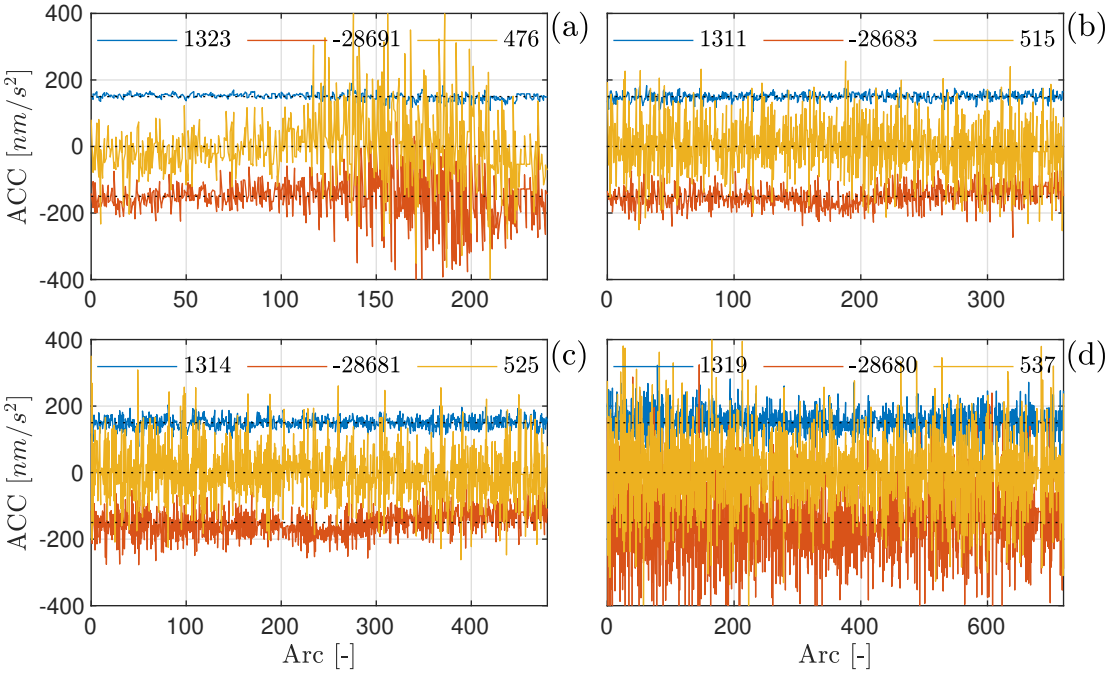

Figure 7.52: Estimated accelerometer calibration from GFR solutions of November 2006 with bias plus drift parametrization, for GRACE A for different arc lengths: (a) 3h (b) 2h (c) 1.5h (d) 1h. The calibration of all three SRF-axes (x: blue, y: red, z: yellow) is shifted for better visibility in one figure by the values given in each plot in nm/s^2. The mean values are depicted as black dotted line.

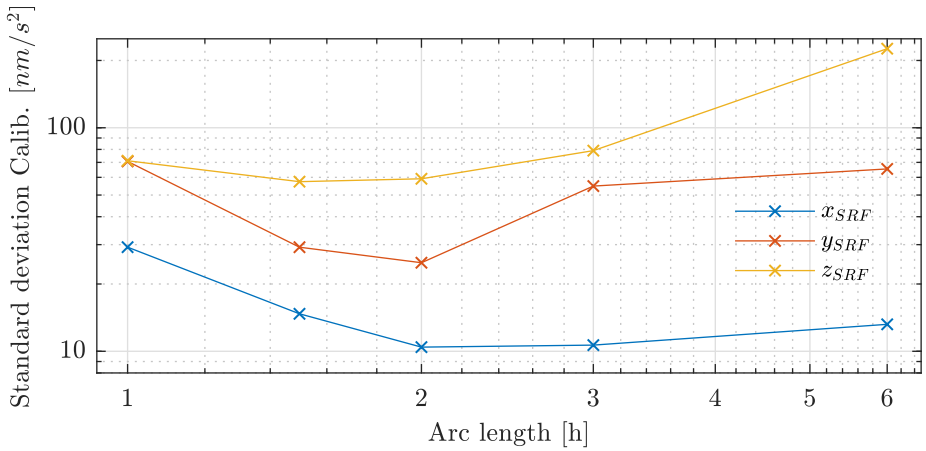

Figure 7.53: Standard deviation of estimated ACC calibration plotted over different arc lengths, showing the variability of the ACC calibration parameters. From GFR of November 2006 solutions with bias plus drift parametrization, for GRACE A.

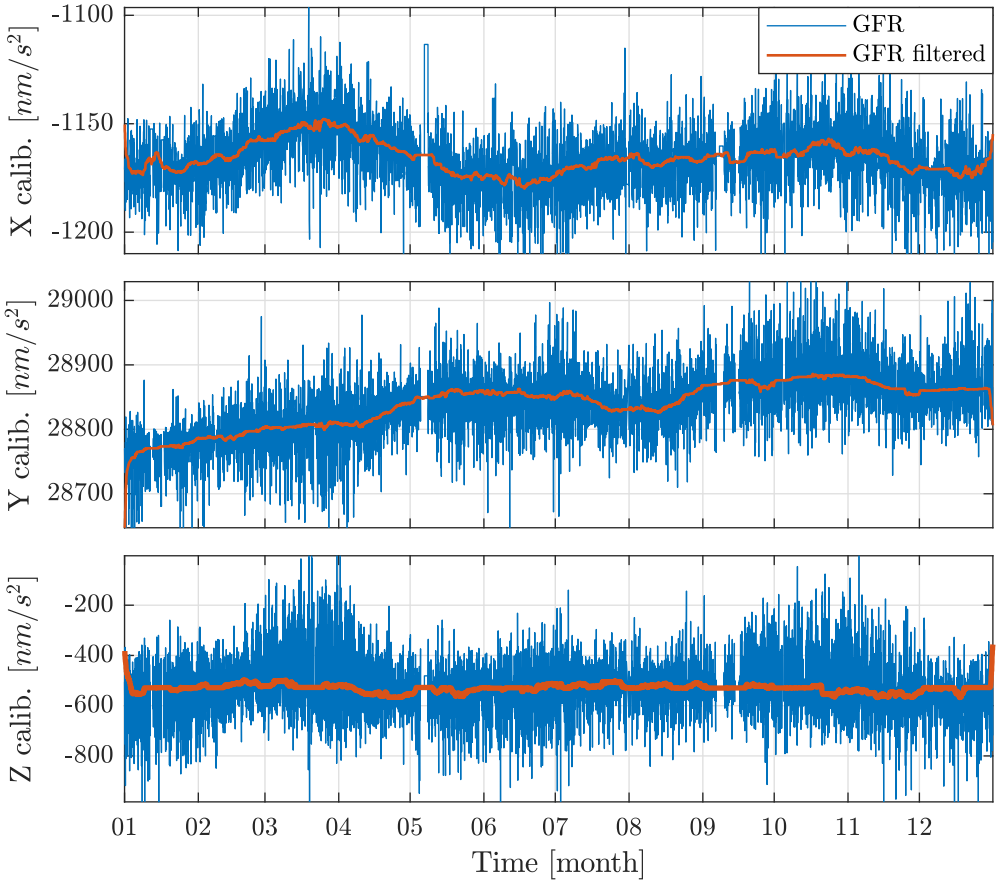

Figure 7.54: Estimated accelerometer calibration for the year 2006 for the three ACC *SRF*-axes, for GRACE A. Shown are the results from GFR with 3h arc length and bias plus drift parametrization, and the median filtered time series with a filter order of 50 hours.

the calibration from POD, as used for the data pre-preocessing (Sec. 7.4).

The dynamic POD for the GRACE data pre-processing is conducted with the same parametrization as used for GFR. The only difference is the used VCE weighting, which works very good for POD, but has in general not that big influence like for GFR. This is because the orbit and the accelerometer calibration are much more sensitive to the 3d-position observation than to the relative range-rate observation. Thus, the relatively lower weighting of the KBR observations from VCE is not significant for the results. The POD is conducted for both satellites simultaneously, being connected by the KBR observation.

In Figure 7.56 the accelerometer calibration from the POD for GRACE A for 2006 is shown. It is plotted in the same way as before for the GFR calibration, including a median filtered calibration with the same order of 50 hours.

The variation of the calibration is distinctly lower for all three axes. It is biggest for z-axis and lowest for x-axis, as for GFR. Nevertheless, the trend of POD and GFR calibration is noticeable different. It is depicted in the next two Figures 7.57 and 7.58 for GRACE A and B, respectively. Additionally, the non-gravitational force model based calibration is plotted.

The trends of the POD and GFR based calibration are distinctly different for all three axes and for both satellites. The model based calibration is not very reliable for the

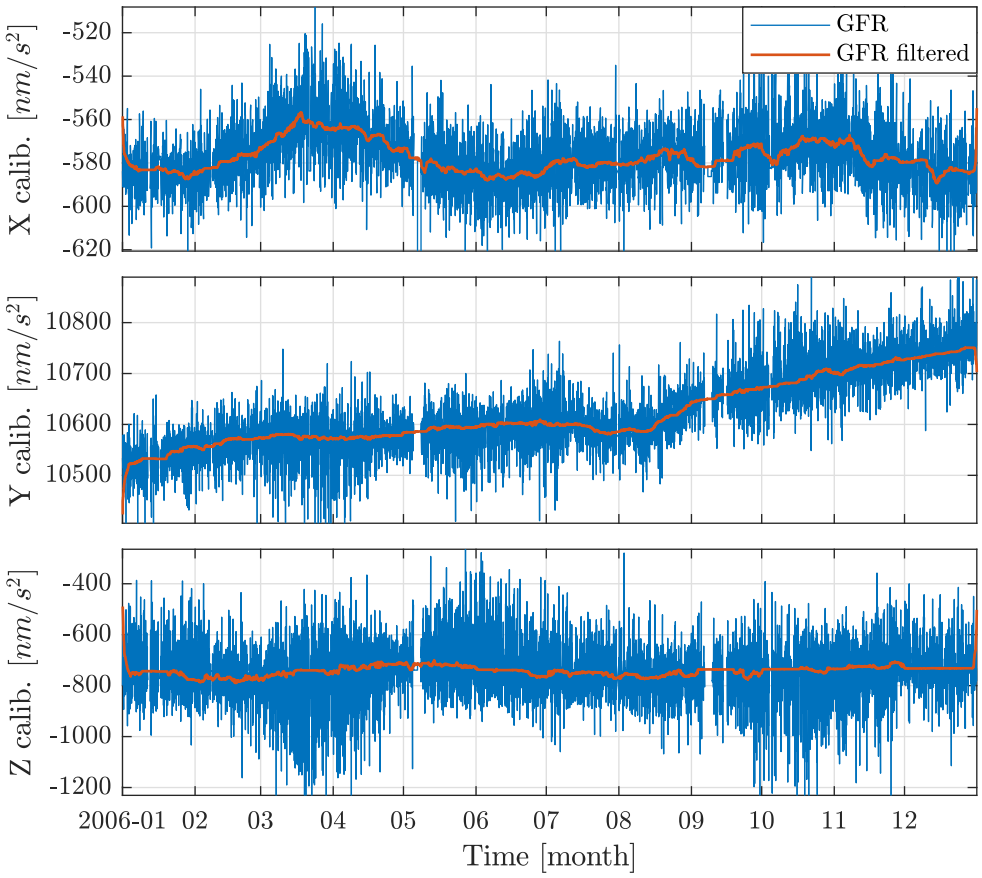

Figure 7.55: Estimated accelerometer calibration for the year 2006 for the three ACC *SRF*-axes, for GRACE B. Shown are the results from GFR with 3h arc length and bias plus drift parametrization, and the median filtered time series with a filter order of 50 hours.

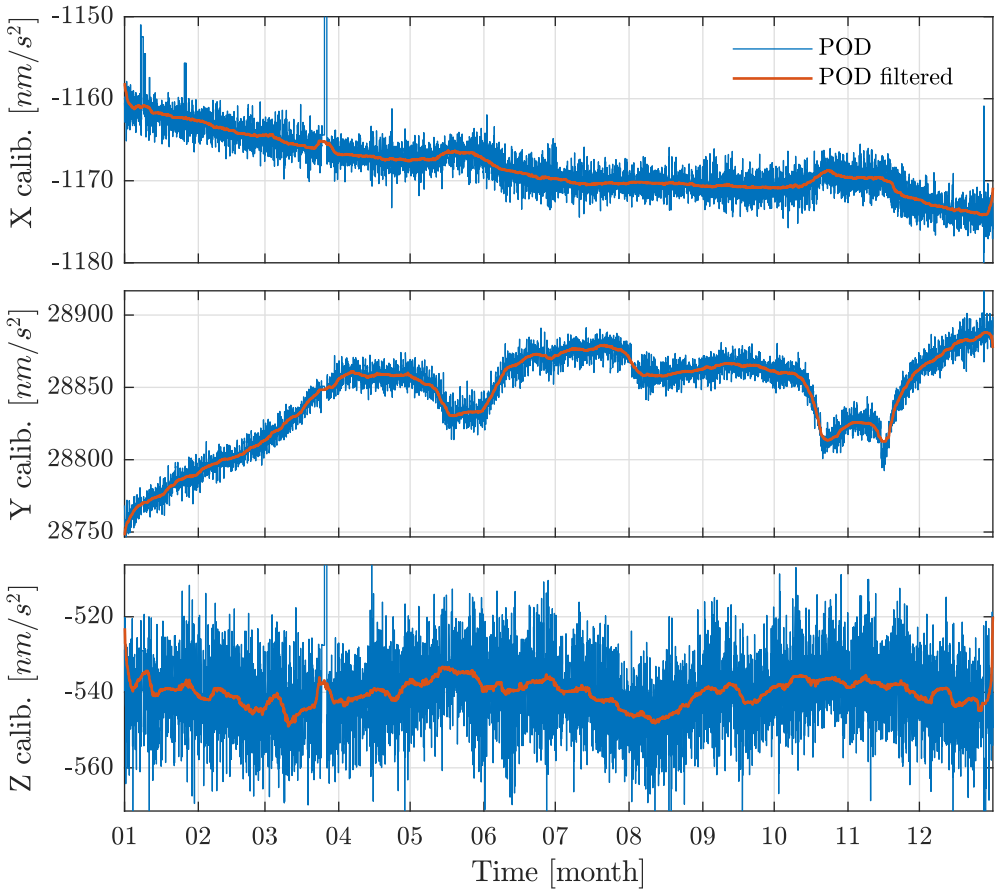

Figure 7.56: Estimated accelerometer calibration for the year 2006 for the three ACC *SRF*-axes, for GRACE A. Shown are the results from POD with 3h arc length and bias plus drift parametrization, and the median filtered time series with a filter order of 50 hours.

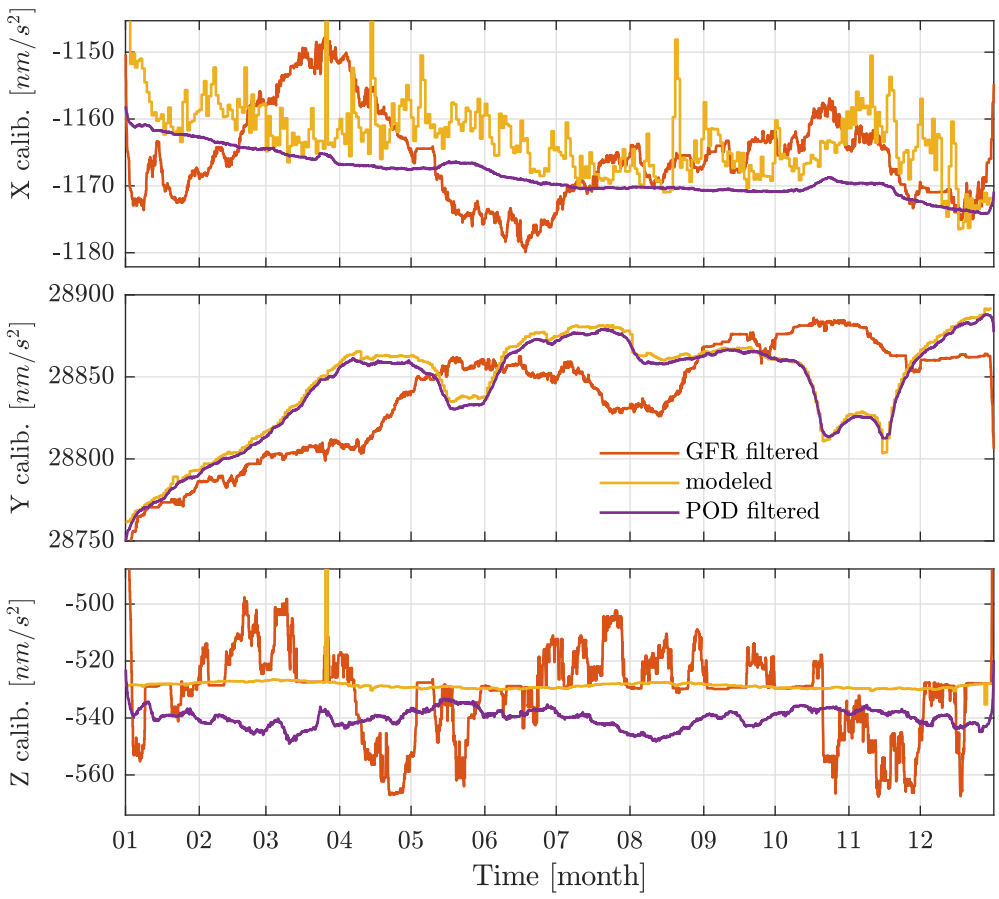

Figure 7.57: Estimated accelerometer calibration for the year 2006 for the three ACC SRF-axes, for GRACE A. For filtered GFR calibration, filtered POD calibration and the non-gravitational force model based calibration (Sec. 6.1.6). With 3h arc length and bias plus drift parametrization, median filter with 50 hour order.

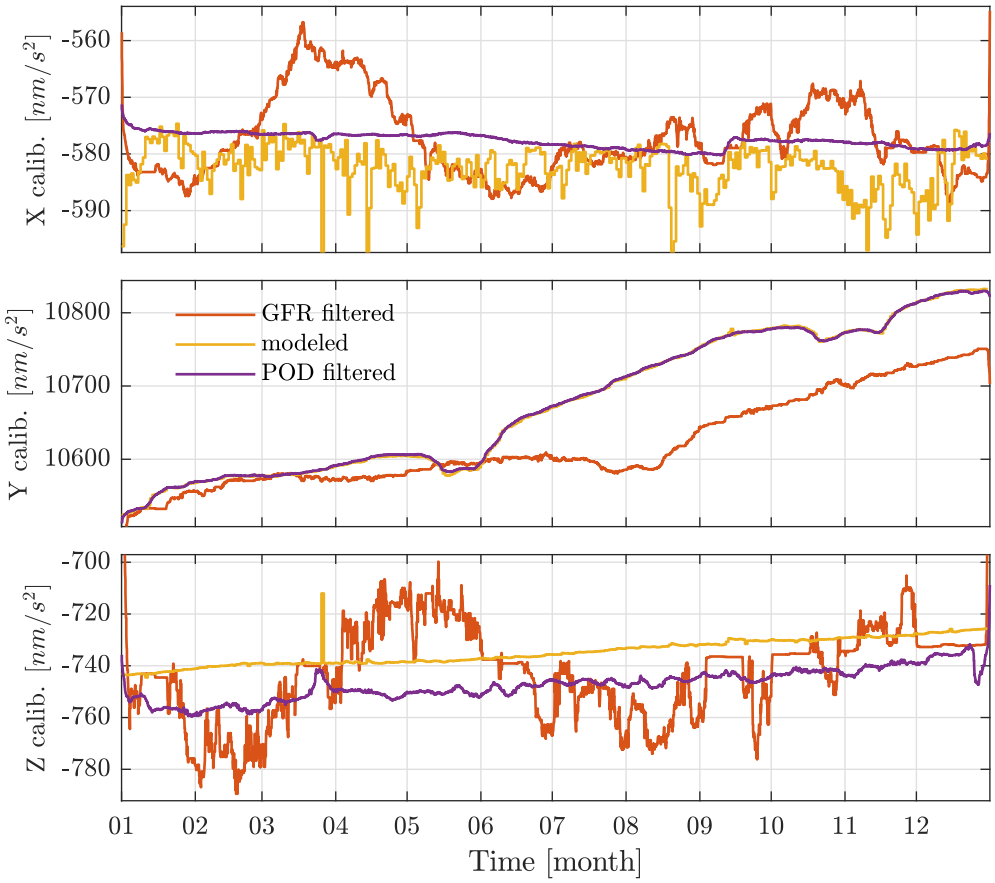

Figure 7.58: Estimated accelerometer calibration for the year 2006 for the three ACC SRF-axes, for GRACE B. For filtered GFR calibration, filtered POD calibration and the non-gravitational force model based calibration (Sec. 6.1.6). With 3h arc length and bias plus drift parametrization, median filter with 50 hour order.

x-axis, as the atmospheric drag model is quite uncertain (cf. Sec. 5.1.6). Nevertheless, the general trend agrees. For the y-axis it coincides very well with the POD calibration. In the z-axis an offset is prominent. That offset has been observed before in Wöske et al. (2019) for the comparison with an other POD and GFR based calibration, and is still not resolved. The GFR calibration may follow the general trend, as well, but with big oscillations and variations.

It can be concluded, that considerably big variations of the non-gravitational accelerations at the time scales of some hours are not really affecting the GFR process when the mean acceleration over a little longer time scale is not too far from the truth. Otherwise the very reasonable GFR results can not be explained with these definitely unphysical accelerometer calibration. This is further investigated in the simulation study with different applied accelerometer noise models in Section 8.5.

7.8 Influence of Models on GFR Results

The influence of some further processing options and background models is shown in the following. All solutions are obtained for the first half of May 2006 with data of 12 days. Furthermore, the standard weighting of $\sigma_g = 0.02$ and $\sigma_k =$ 1e-8 is used with bias plus drift parametrization with 3h arc length. The different used background models are listed in detail in Table 7.1.

The influence of the following options is investigated, where subsequently the options from all previous tests are engaged, as well.

1. No static gravity background model (just d/o 60 as estimated), Low d/o tide models: Solid Earth tides d/o 4, ocean tides d/o 12, pole tides d/o 12, constant accelerometer scale factors set to one ($\vec{s} = \vec{1}$), 12 days solution.
2. Static gravity (GGM05c) d/o 120
3. High d/o background models: Static gravity (GGM05c) d/o 180, ocean tides d/o 120, pole tides d/o 180
4. AOD dealiasing d/o 180
5. The constant accelerometer scale factor is set to the values advertised in TN-02, as shown in Table 7.2
6. Atmospheric tide model (ATM) d/o 8 included
7. Monthly solution with 31 days of data

The results are shown as degree difference in Figure 7.59 with respect to GGM05s. With the estimation up to d/o 60 and no higher static background gravity field (1.), the result is surprisingly bad. With the high weighting of the accurate KBR measurement, the static gravity field needs to be modeled much more precisely. Using a background gravity field up to d/o 120 (2.) drastically increases the quality of the solution.

Increasing the d/o of the static gravity field further, as well as the d/o of the ocean and pole tide models (3.) has just a minor effect. Nevertheless, a small increase of the quality can be seen.

Adding the AOD dealiasing model has a slightly bigger positive effect on the solution (4.).

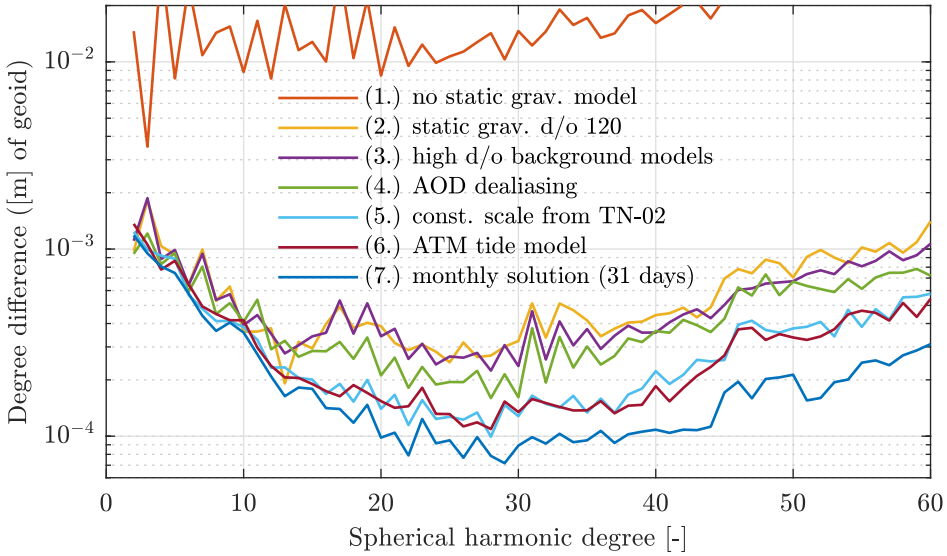

Figure 7.59: Degree difference of solutions from May 2006 from 12 days (but the last) with respect to GGM05s, for different options of the used background models. All options apply to the next case, subsequently. The options of the seven cases are enumerated in detail in this Section 7.8.

A bigger influence can be observed by changing the constant scale factor (5.). Even though, the change from $\vec{s} = \vec{1}$ to $\vec{s} = \vec{s}_{TN}$ is maximal less than 0.07 for one axis, it has a remarkable positive effect on the solution. A good estimate of the scale factor, or a stable estimation approach within the GFR processing would maybe further increase the solutions.

The atmospheric tide model has a very slight influence on the solution (6.). It may smoothen the solution a little. But for this small differences a significant statement of the effect would need to consider more than one investigated month.

Considering more data for the solution (7.) has of cause a positive effect. The monthly solution from 31 days is definitely more sensitive than the 12 days solution.

Additionally, the effect of considering or neglecting the relativistic post-Newtonian (pN) corrections, in terms of additional accelerations in the background models, on the resulting gravitational fields is depicted. As pN corrections the Schwazschild and Lense-Thirring terms are considered, as discussed in the Sections 2.3.6 and 6.1.3.

The following cases are regarded and results are shown in a further plot in Figure 7.60, again with respect to the GGM05s model. The last solution (7.) from the previous figure is also plotted as reference.

8. All options like (6.) but no relativistic post-Newtonian corrections

9. All options like (6.) with relativistic post-Newtonian corrections

The pN corrections have just a small, but positive, effect on the overall result. A more pronounced effect is visible when comparing the estimated accelerometer calibrations of both cases. Their difference is shown in Figure 7.61 for GRACE B over the 12 days for the three accelerometer axes. The mean values of the difference for each axis are given in the plot, as well. It is obvious, that the lack of the relativistic correction is mainly compensated by the z-component of the accelerometer calibration. The mean value of

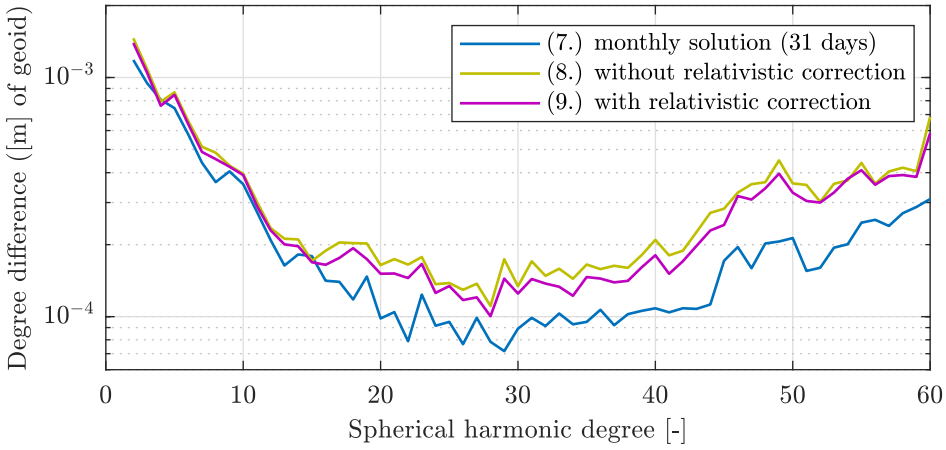

Figure 7.60: Degree difference of solutions from May 2006 from 12 days (but the first) with respect to GGM05s, showing the effect of post-Newtonian relativistic corrections on the GFR processing.

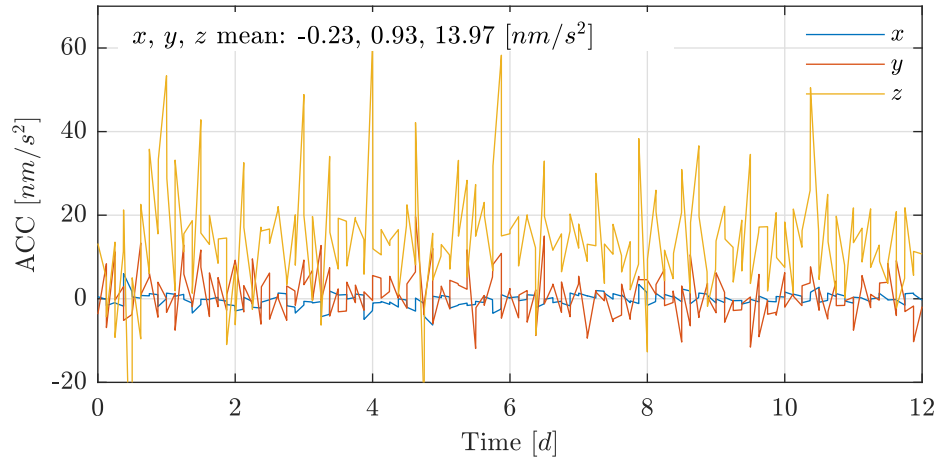

Figure 7.61: Difference of accelerometer calibration between 12 day GFR estimations from May 2006 with and without relativistic post Newtonian corrections as background model, bias plus drift, 3h arc length. The mean difference is given in the plot for each axis.

the difference between both calibrations is distinctly shifted (13.97 and 10.80 nm/s^2 for GRACE B and A, respectively). The mean difference in the other axes is much smaller. For the nearly circular orbit of the GRACE satellites, the Schwarzschild pN correction is nearly constant and mainly acting in the radial or nadir direction (cf. Fig. 6.6), and thus can be absorbed relatively well by the accelerometer calibration.

7.9 GFR with Modeled Non-Gravitational Accelerations

The modeled non-gravitational accelerations from Chapter 6.1 are used instead of the accelerometer data to produce a monthly solution. All other GRACE data processing stays the same. For this approach an a-priori known error is the missing of the attitude thruster impulses in the accelerometer data. Even though the time and duration of the firings is known, the residual force on the satellite is not completely systematic but a lot influenced by random errors, as described in Section 6.3.6 and investigated by (Meyer et al., 2012). With a lot of effort, these effects could be extracted and re-modeled to

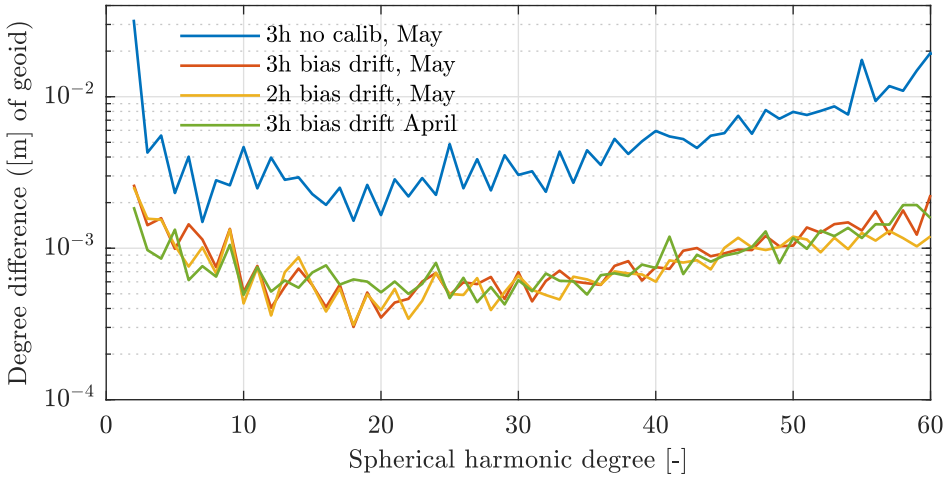

Figure 7.62: Degree difference of monthly solutions with modeled non-gravitational accelerations instead of accelerometer data from May and April 2006 with different parametrizations, with respect to GGM05s.

some extent from the known thruster data, which is not done here. Nevertheless, for the processing of the broken accelerometer on one of the GRACE-FO satellites this is done to overcome the problems (eg. Bandikova et al., 2019).

In Figure 7.62 monthly solutions with modeled non-gravitational accelerations for May and April 2006 are shown in terms of degree differences with respect to GGM05s. Different parametrizations are investigated. Using no accelerometer calibration gives the worst result (blue). The used 2h and 3h bias plus drift calibration increases the quality of the solution distinctly. The arc length does not have a major influence. The solutions for May and April are generally of the same quality. Speaking about quality, compared to the results with the original GRACE accelerometer data, this solutions are about an order of magnitude worse, see eg. Figures 7.2 and 7.3.

From the evaluation of the non-gravitational models in Section 6.1.6 it is clear that the atmospheric drag exhibits the biggest differences to the accelerometer measurements. Therefore this study is conducted again but including the estimation of the drag coefficient c_D in the drag model as additional parameter in the GFR scheme for both satellites.

In the A matrix (cf. Sec. 4.3.14) the partial of the acceleration with respect to the drag coefficient $\partial\vec{\ddot{r}}/\partial C_D$ follows from the definition of the atmospheric drag (Eq. 5.20)

$$\frac{\partial\vec{\ddot{r}}}{\partial C_D} = -\frac{1}{2}\rho\ A\ |\vec{v}_{inc}|\ \vec{v}_{inc}. \tag{7.2}$$

The atmospheric density ρ needs to be drawn from a model. When using sampled drag data $\vec{a}_{drag}$ computed with a nominal drag coefficient $c_{D,nom}$ the partial is simply

$$\frac{\partial\vec{\ddot{r}}}{\partial C_D} = \frac{1}{C_{D,nom}}\vec{a}_{drag,i}. \tag{7.3}$$

The index i indicates the inertial frame. For the estimation C_D is added as local parameter for both satellites and estimated for each arc.

The results of this strategy for the monthly gravity field solution of May 2006 is shown in Figure 7.63. It is conducted with and without additional bias plus drift calibration. For comparison the according two results from the previous figure are shown as reference.

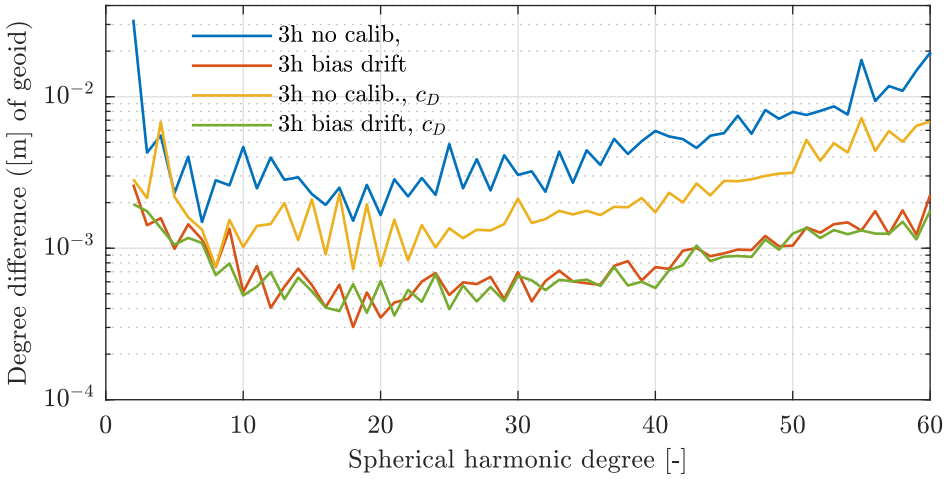

Figure 7.63: Degree difference of monthly solutions with modeled non-gravitational accelerations instead of accelerometer data from May 2006 with additional estimation of the drag coefficient C_D, with respect to GGM05s. As reference the two results from the previous figure are shown again.

For the case with no additional accelerometer calibration the result is slightly improved with the additional estimation of the drag coefficient (yellow). If bias and drift are estimated, as well, the additional drag coefficient does not improve the result further (green). The estimated values for the drag coefficient are not physically interpretative values. They vary between minus and plus four, and are pretty much the same for both satellites.

The investigation with modeled thruster firings and its coupling into the accelerometer data in Chapter 8.8 shows a big sensitivity of the GFR solution to errors of the attitude thruster firings in the accelerometer data. Thus, this might be a major error limiting the quality of the shown solutions here, where in the modeled non-gravitational accelerations this is not considered. Furthermore, the modeled drag acceleration (eg. Fig. 6.16) shows distinct differences in the very sensitive short timescales to the ACC data. The analysis in Section 8.5.2 also shows a high sensitivity of this kind of accelerometer errors especially for the x-axis and a little less also for the z-axis. Thus both errors may accumulate to the obtained sensitivity of the GFR solutions.

GRAVITY FIELD RECOVERY RESULTS FROM SIMULATION

8

Gravity Field Recovery (GFR) with simulated data offers the possibility to study the effect of each sensor characteristic and noise level, environment models and the processing itself. Compared to the real data processing, each effect can be switched on or off and the sensor models and noise levels are known and can be set arbitrarily. Furthermore, the true gravity field and all observations are known and thus the absolute error of each solution can be determined and compared.

The conducted simulations and subsequent GFR solutions are based on the GRACE mission setup in this thesis. The sensor models are based on the GRACE instruments. Its noise characteristics are varied around the assumed GRACE precision, as described in Chapter 6 and especially Section 6.3. As mentioned in the previous chapters, the simulation approach allows exceptional investigations of the mission design and GFR methodology on its own, but furthermore, the comparison with the GRACE data also gives insights to the real data.

Therefore, the results in this Chapter are investigated independently and subsequently compared to the results obtained with the real GRACE data from the previous Chapter 7.

The general scheme of the closed loop simulation of a GFR mission is shown in Figure 8.1. It consists of four main steps.The first step is the mission or scenario definition, where all force models, the dynamics and relevant models of the satellite system like attitude control, shape and initial conditions of the satellites are set. This is followed by the simulation, meaning the numeric integration of the dynamic models to generate the true satellite states and the true observations, eg. inter satellite range or range-rate in the GRACE case. From the true observations real observations are simulated with noise models of the instruments and sensors. This might happen either subsequent to the simulation if no further model is depending on this observation, or during the simulation if another model is dependent on that observation, like for example the attitude control, which is dependent on the star camera attitude sensor. These simulated observation data are then equivalently used as real data from a satellite mission in the third step, the processing. The processing is conducted with specified options and parameters. The final step is the analysis and comparison of the results with the initial i.e. true input parameters and observations. From this analysis conclusions on the initially imposed scenario definition, processing options and employed models can be drawn.

The whole loop does not always need to be executed completely, a simulated mission may be processed with different options, thus the generated observation data do not change and hence do not need to be computed again, or a change in several sensor noise models does not necessarily require to simulate the true satellite states again, but just adding different noise models to the true data.

In this chapter first the general characteristics of the solutions are investigated (Sec. 8.1). Subsequently, as for real GRACE data, the influence of weighting (Sec. 8.2) and

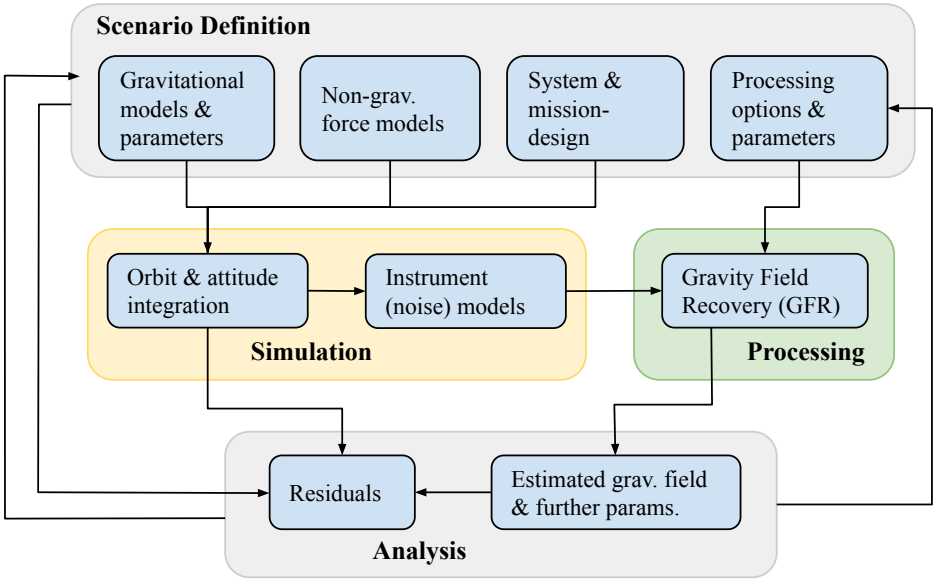

Figure 8.1: Scheme of the closed loop GFR simulation. With the main steps of mission or scenario definition, generation of simulated satellite and observation data and the subsequent GFR processing. The final step is the comparison of the results with the initial i.e. true input parameters and observations.

parametrization (Sec. 8.3) is investigated. The influence of the major measurement devices KBR (Sec. 8.4), ACC (Sec. 8.5), GNV (Sec. 8.6) and SCA (Sec. 8.7) with characteristic noise models and parameters is investigated in the following sections. Finally, the influence of the attitude thruster firings is depicted in Section 8.8.

For the simulation initial conditions of the GRACE satellites from May 1st 2005 are used. And all shown results are based on data from 12 days.

For the investigation of the before mentioned aspects, usually a default model setup is used. Based on the introduction of all different instrument models in Section 6.3, the 2 cm GNV noise model, the KBR model with $\sigma_{hf,KBR}$=1e-6 m and the Const_lf ACC model with σ_{hf}=1e-10 m/s^2 is used. The SCA solution with two combined star cameras is utilized, but having a very small influence. The other SCA and thruster models are just used for their respective investigation, usually having a minor influence. Furthermore, the bias plus drift parametrization is used with 2h and 6h arc length as default. For the analysis of the sensor models, generally just one model is varied and the default setup is used for the other sensors. Different setups are explicitly stated.

8.1 General Characteristics of the Solutions

In this Section the general characteristics, like residuals and deviations of the measurements in time and frequency domain, convergence over the iterations and the formal error are investigated. For the results in this section the bias plus drift parametrization with an arc length of 3h or 6h is utilized.

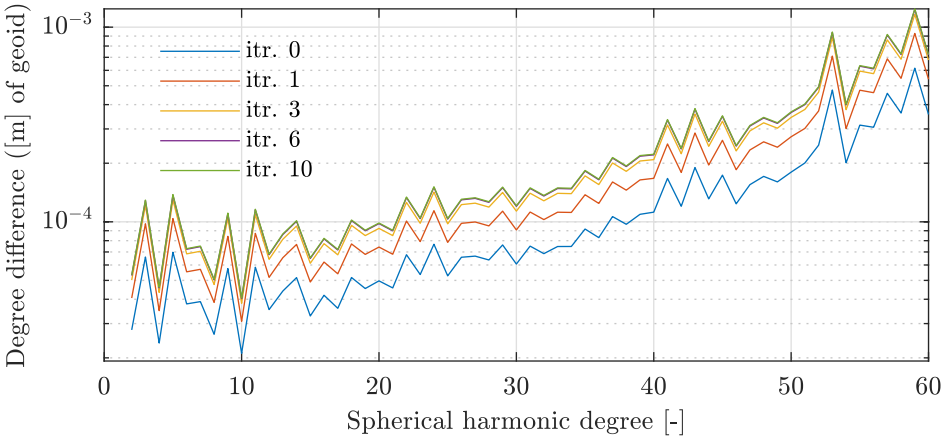

Figure 8.2: Degree difference of 12 days solution for different iterations with respect to the true gravity field.

8.1.1 Convergence

First the convergence of the gravity field solution is investigated. In Figure 8.2 the degree difference with respect to the true gravity field (GGM05s) for different iterations is shown.

As for the GRACE data processing, the initial guess is very close to the truth and the convergence is achieved after the third iteration. This is very similar to the GRACE case (cf. Fig. 7.40).

A short remark on the initial conditions: The influence of the initial conditions of all parameters (local and global) is the same: Bad initial conditions just slow down the convergence. With a sufficient amount of iterations the result is the same (assuming the approach does not diverge with too bad initial conditions). Thus the initial conditions do not have an effect on the final solution. Mathematically this is clear and nice to see that this turns out to be the case for the implemented GFR processing, as well.

8.1.2 Error Pattern in the Spatial Domain

One of the big problems of the GRACE type mission is the striping of the monthly solutions, especially visible in relative plots of the gravitational fields in the spatial domain, for instance in terms of EWH. As demonstrated in Section 2.3.4 and eg. Figure 2.8 or Figure 7.46 for the GRACE data from one year.

In the simulation approach one of the drivers for the striping is eliminated. No error in the tidal models used for the GFR is implemented in the simulation loop. Thus the aliasing due to a slight mismodeling of the fast changing tidal effects, mainly in the ocean tide model, is not present. Therefore, the remaining striping is caused by the main measurement direction of the GRACE concept, which is only in north-south direction.

In Figure 8.3 the EWH with respect to the true gravity field GGM05s for an unfiltered and filtered solution is shown, with bias plus drift parametrization and 3h arc length with VCE weighting. The unfiltered solution has an error amplitude of about ± 20 cm and the filtered one in the mm range. Compared to the results for the GRACE solution of May 2006 in Figure 2.8, with an unfiltered amplitude of ± 1.5 m, this is considerably lower. Nevertheless, a direct comparison of the plots is not reasonable. It has to be considered, that for the GRACE solution not an error is plotted, but the difference with respect to a mean field. Thus for the GRACE solution mainly the hydrological signal is

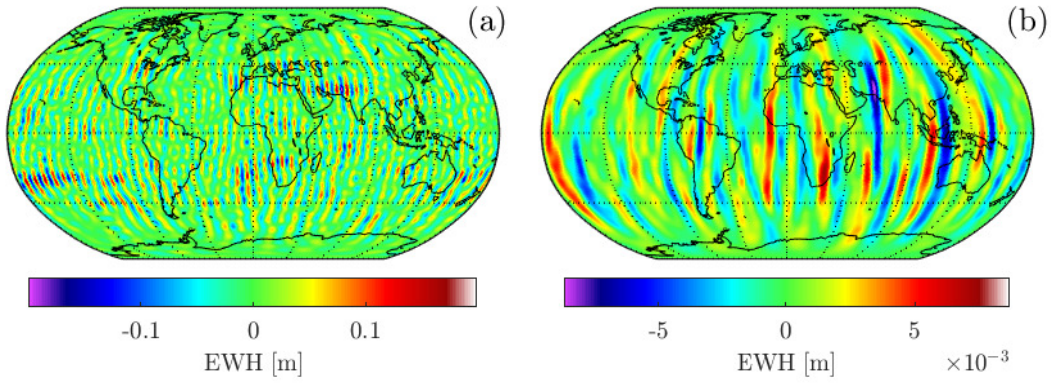

Figure 8.3: Spatial plot of EWH with respect to the true gravitational field GGM05s from estimated gravitational field for (a) no filter and (b) Gaussian filter with r = 465 km. Bias plus drift parametrization, 3h arc length and VCE weighting.

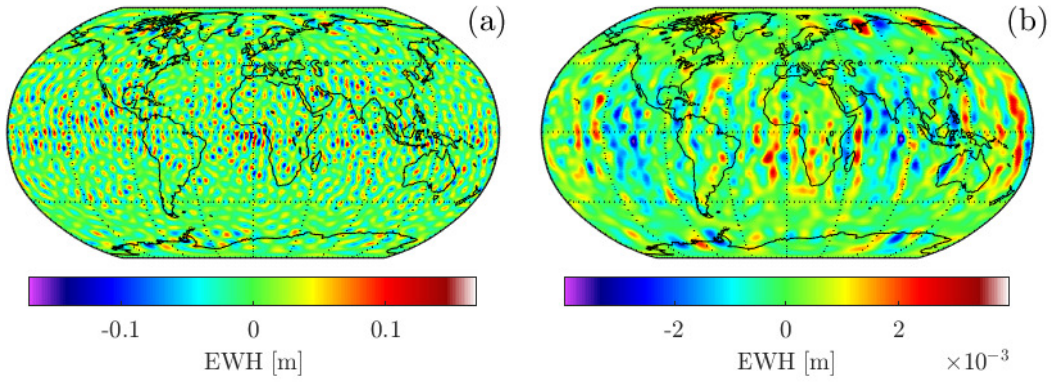

Figure 8.4: Spatial plot of EWH with respect to the true gravitational field GGM05s for a Bender concept with two GRACE-like pairs, one polar and one with 63° inclination, from 6 days of data, for (a) no filter and (b) Gaussian filter with r = 465 km. Bias plus drift parametrization, 3h arc length.

visible, additionally to an unknown error.

The striping errors can be distinctly reduced by an advanced measurement concept or geometry. For example the prominent Bender constellation, which is one favored candidate for a GRACE-FO successor mission. It utilizes two GRACE-like satellite pairs, one in polar orbit and one in an inclined orbit. The results of that concept, simulated with the same instrument models, amount of observation data (hence 6 days) and in general the same processing, is shown in Figure 8.4, in comparison to Figure 8.3 for the GRACE-like mission.

The errors are not just reduced in magnitude but much more important, the north-south striping is heavily reduced. Thus, the benefit of adding another range-rate measurement in a further direction does not just improve the result by adding more observation data but by more isotropic observations, which is also reflected in the result.

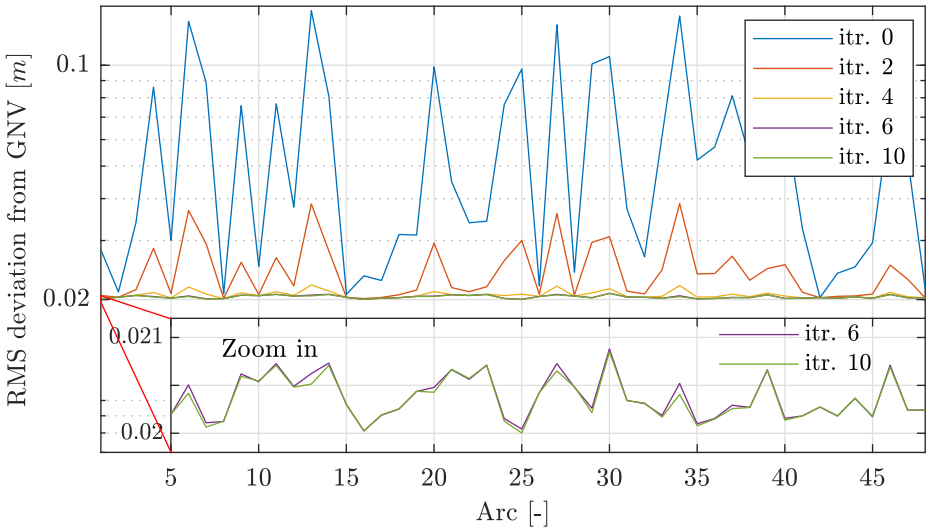

Figure 8.5: Arc wise RMS of GNV position deviations from GFR for different iterations for 12 days solution (6h arc length). The zoom-in shows the final iterations in detail.

8.1.3 Residuals and Deviations

In Figure 8.5 the evolution of the arc wise RMS of the GNV deviations over the iterations is depicted. After about six iterations the deviation does not change anymore and the big initial differences between the arcs are vanished. The convergence is very similar to the GRACE data processing (cf. Fig. 7.31). The white noise with the standard deviation $\sigma = 2\ cm$, applied as GNV model, is nearly recovered exactly in the converged deviations. Just a very small variation over the arcs exists. The GNV deviations of the GRACE data change over the course of the month and year. At times it is in the same area of about 2 cm, but also reaches values of about 5 cm (eg. for November, Fig. 7.31). For the very good month May (Fig. 7.33) the converged deviations vary around 1 to 2 cm.

The results for the arc wise RMS of the KBR range-rate deviations are shown in Figure 8.6 in the same way. The convergence takes longer than for the GNV deviations. This is the same as for the GRACE data (cf. Fig. 7.32 and 7.34). The resulting arc wise RMS values are in the same range and also show a variance over the arcs due to the applied KBR noise model. Nevertheless, for the real GRACE data again a superimposed accuracy variation over the month and year is visible. A slightly more realistic model could include a very low frequency time dependency of the simulated GNV and KBR accuracy.

Compared to the deviations, the residuals converge much faster. The arc wise RMS of the KBR range-rate residuals are shown in Figure 8.7 for different iterations. More or less after the first iteration the residuals do not change anymore and look the same as the deviations after the 10th iteration (cf. Fig. 8.6). If the residuals or deviations should be computed and analyzed, one should keep in mind the big difference in convergence speed.

The GNV position deviation of one arc is shown in Figure 8.8. It demonstrates that the deviations are close to white noise and show just a very low longer wavelength content, as visible in the Amplitude Spectral Density (ASD) of the deviations for that arc in Figure 8.9 (the ASD and its computation, used throughout the thesis, is briefly discussed in the Appendix A.2).

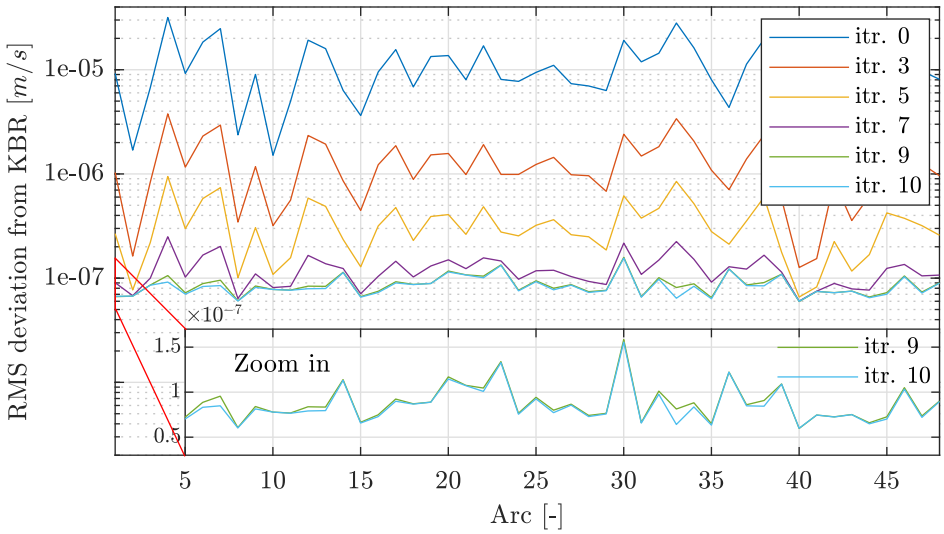

Figure 8.6: Arc wise RMS of KBR range-rate deviations from GFR for different iterations for 12 days solution (6h arc length). The zoom-in shows the final iterations in detail.

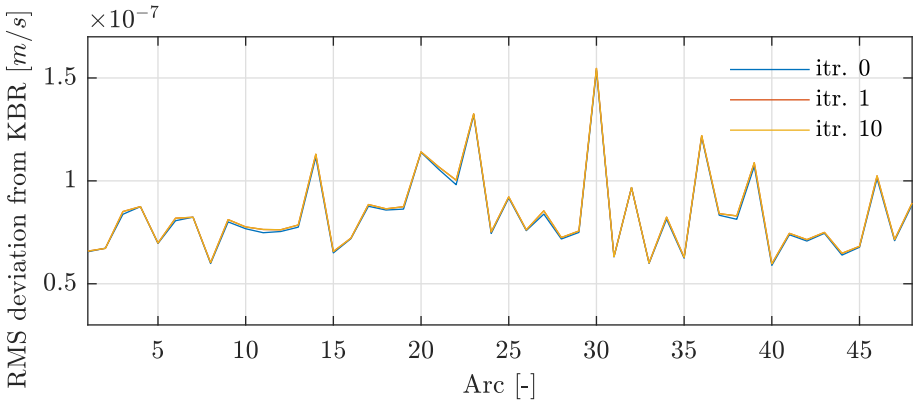

Figure 8.7: Arc wise RMS of KBR range-rate residuals from GFR for different iterations for 12 days solution (6h arc length).

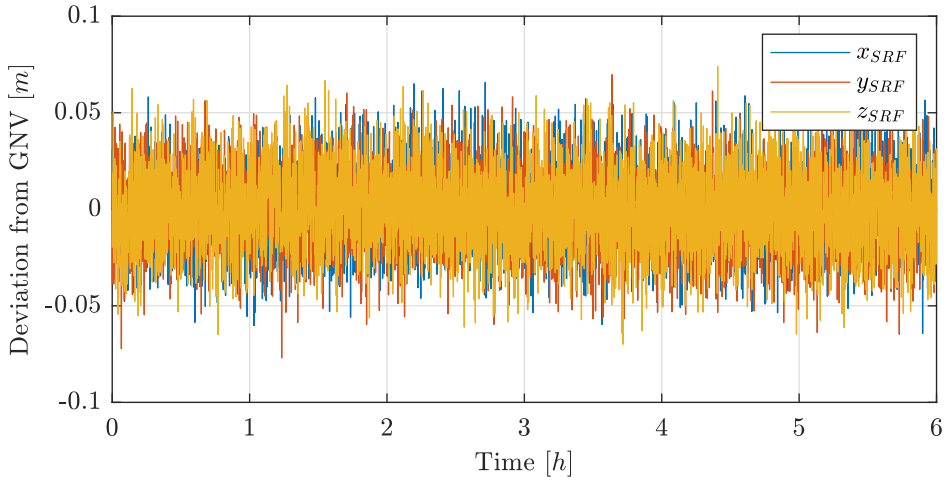

Figure 8.8: GNV position deviation of GFR after 10th iteration for each axis, arc 26, GRACE A.

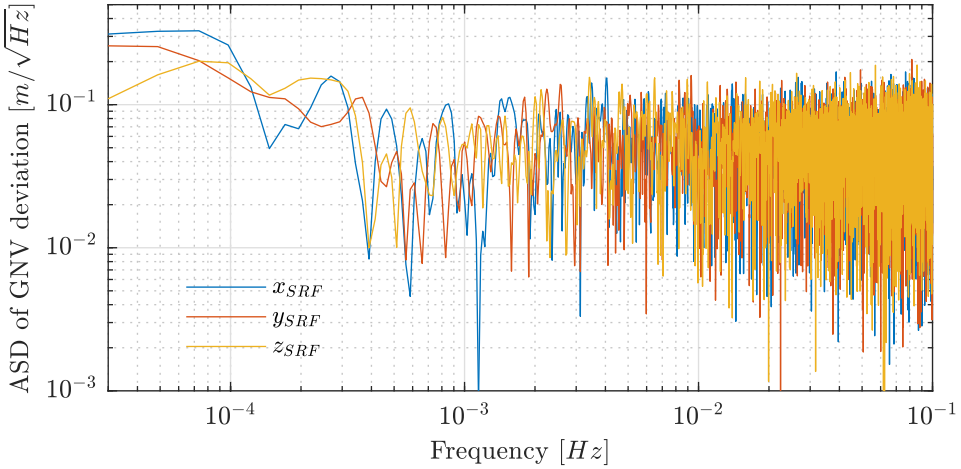

Figure 8.9: ASD from GNV position deviation of GFR for each axis after 10th iteration, arc 26, GRACE A.

Compared to the results from GRACE for GNV deviations (Fig. 7.35) and KOS deviations (Fig. 7.43), which showed a distinct long wavelength signal, this is different. Unfortunately it is not possible to pin the error in the real GRACE position deviations to a clear source. Most probably it is a not modeled or miss-modeled gravitational effect. In the modeled data this is not visible because the time dependent gravitational models are the same in the simulation and the GFR.

The KBR deviations are shown for the same arc in Figure 8.10. A clear time dependency of the deviations is visible, which is due to the colored KBR and ACC noise models (Sec. 6.3.1 and 6.3.2). The ASD of the deviation is shown in Figure 8.11. The curve in the ASD is a result of the utilized KBR noise model and the ACC noise model. The high frequencies are determined by the KBR noise and the lower ones by the ACC noise. Hence the ASD does not directly show the curve of the introduced KBR noise (Fig. 6.29). The exact influence of KBR and ACC noise models on the gravity field solution and the deviations is investigated in detail in the next two sections.

Compared to the results from GRACE in Figure 7.39, the general trend looks the same, but the noise level is a little lower here. The analysis for different KBR noise

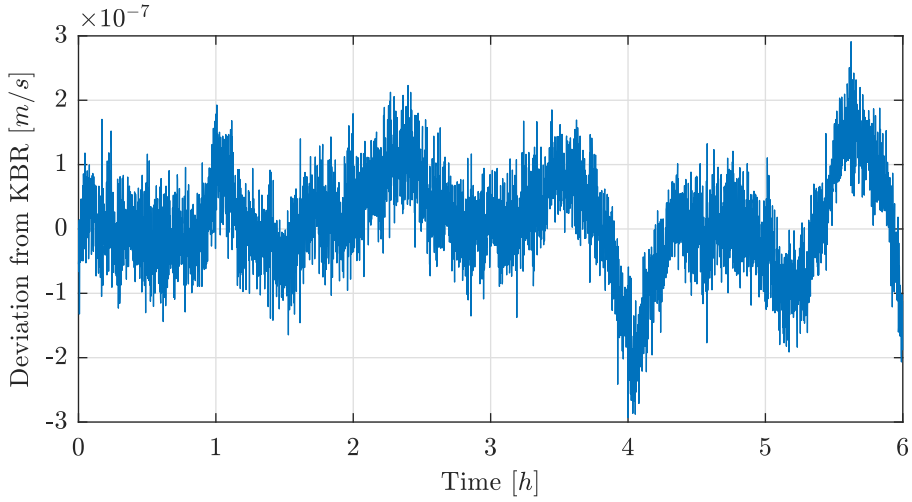

Figure 8.10: KBR range-rate deviation of GFR after 10th iteration, arc 26.

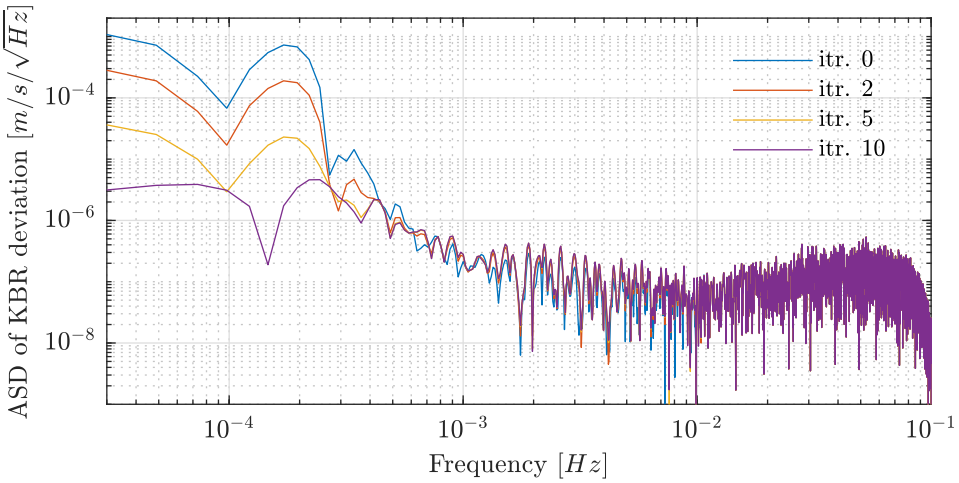

Figure 8.11: ASD from KBR range-rate deviation of GFR for different iterations, arc 26.

levels in Section 8.4 also suggests that the KBR noise model with $\sigma_{hf,KBR}$ = 1e-6 is a little too optimistic.

8.1.4 Formal Error

In the previous chapter (Sec. 7.3) the formal error has been investigated for the real GRACE data. Without knowledge of the true error, just an approximate assessment could be done. Nevertheless, in general the formal error was found to be too optimistic. In the simulation case, the formal error can be compared directly with the true error, and an estimation on its significance can be made.

For two different ACC noise models (Const_lf with σ_{hf} = 1e-10 and σ_{hf} = 3.2e-9 m/s^2) the formal errors of the simulation results are shown in Figure 8.12 and 8.13 for 6h and 2h arc lengths, respectively. The concerning overall standard deviations $\hat{\sigma}_{ges}$ (Eq. 4.69) are: $\hat{\sigma}_{ges,1e-10,6h} = 1.0004$, $\hat{\sigma}_{ges,1e-10,2h} = 1.0012$, $\hat{\sigma}_{ges,3.2e-9,6h} = 1.0004$ and $\hat{\sigma}_{ges,3.2e-9,2h} = 1.0012$.

The overall standard deviations $\hat{\sigma}_{ges}$ are about the same for all four cases and nearly exactly the same for the different noise models and arc length, respectively. This is

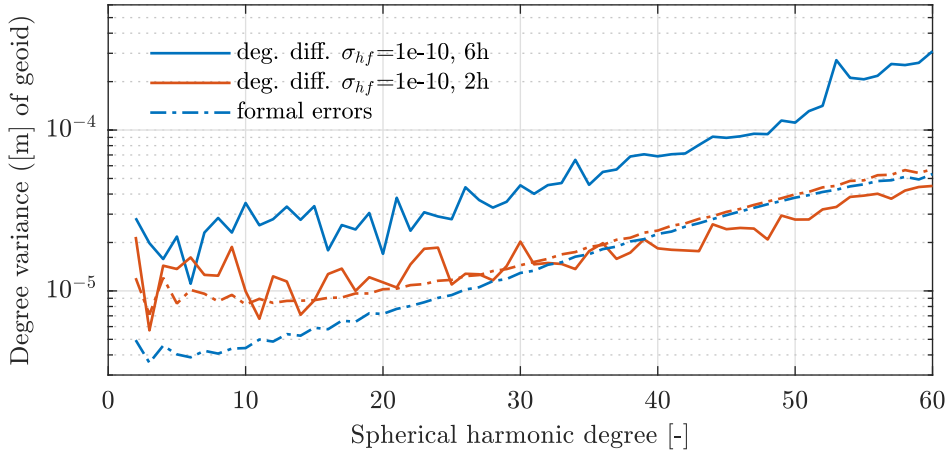

Figure 8.12: Degree variance (formal errors) of solutions with Const_lf ACC noise model with σ_{hf} = 1e-10 m/s^2 for different arc lengths (6h and 2h) and degree difference (deg. diff.) with respect to the true gravity field for each solutions.

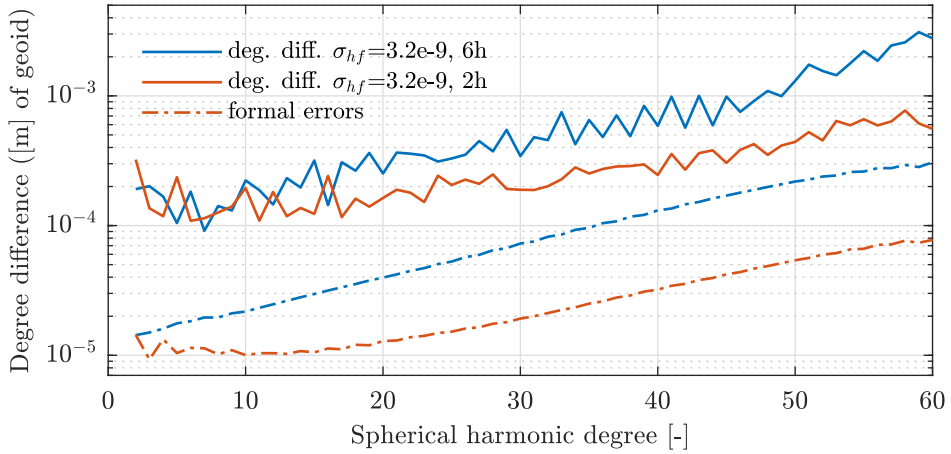

Figure 8.13: Degree variance (formal errors) of solutions with Const_lf ACC noise model with σ_{hf} = 3.2e-9 m/s^2 for different arc lengths (6h and 2h) and degree difference (deg. diff.) with respect to the true gravity field for each solutions.

because the GNV part is dominant here and the same for all cases and the difference of KBR residuals is small, too.

For both 6h solutions, the formal error is about an order of magnitude lower than the true error, for the lower ACC noise model (σ_{hf} = 1e-10) it is a little bit less. This confirms the supposed results from the real GRACE data where the formal error seemed to be too small. As for the GRACE data (Fig. 7.18), the arc length has a big influence on the formal errors. But here, the trend for the two ACC models is completely different. For the lower noise (σ_{hf} = 1e-10) the formal error slightly increases with smaller arc length, while it strongly decreases for the higher noise model (σ_{hf} = 3.2e-9) and is far off the true error. The trend for the first case is the same as observed for real GRACE data. Nevertheless this does not correspond to the true error, which decreases with smaller arc length.

Even though, for the more realistic noise model with σ_{hf} = 1e-10 m/s^2 and the best arc length of 2h, the formal error and true error are very close, the contrary trends for

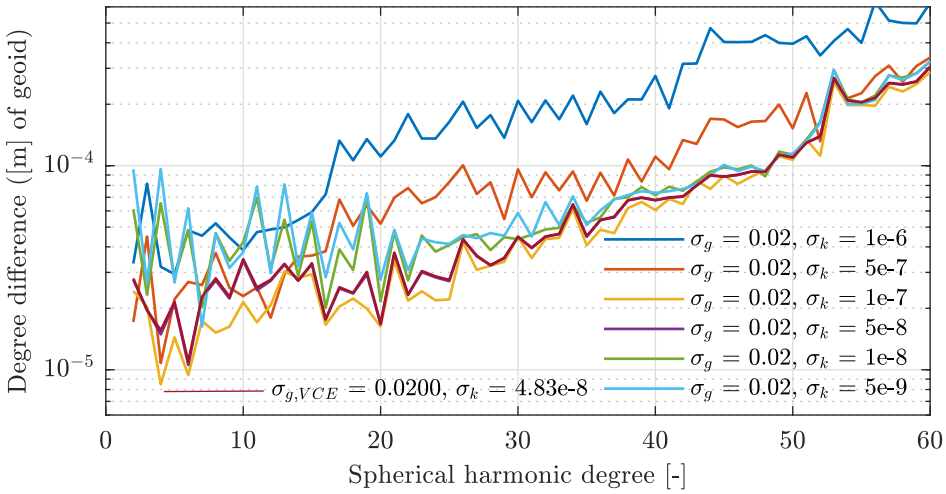

Figure 8.14: Degree difference with respect to the true gravity field for different weighting combinations of GNV and KBR observations with standard deviation σ_g and σ_k, respectively.

different arc length and noise model make the formal error analysis not significant and informative.

8.2 Weighting

As for the real GRACE data, the weighting of the different observations has a big influence on the solutions. It is investigated for different weighting combinations of GNV and KBR observations in the following. The standard deviations of GNV and KBR data are σ_g and σ_k, respectively. As weighting the inverse of the variances $1/\sigma^2$ are used, as discussed in Section 4.3.5 and 4.3.9.

In Figure 8.14 the results from solutions with six different weighting combinations are depicted for a 12 days solution. They are shown as degree differences with respect to the true gravity field. As for the real GRACE data processing (Sec. 7.1), σ_k is varied, while $\sigma_g = 0.02$ is kept constant. Additionally the result from the VCE solution is plotted. For all cases the the KBR noise model with $\sigma_{hf,KBR}$ = 1e-6 m and the ACC noise model Const_lf with σ_{hf} = 1e-10 m/s^2 is used (cf. Sec. 6.3.2).

For the higher degrees (d/o $\geq$ 20) with an increasing weighting of the KBR observations (meaning lower σ_k values) the solutions get better until around σ_k = 1e-7. Higher weighting of the KBR observations does not further increase the accuracy, but does no worsen it either. For the lower degrees a high KBR weighting has a distinct negative effect on the accuracy.

Comparing this to the GRACE data processing (Fig. 7.2 to 7.4) it is slightly different. First, from the degree difference plots the sensitivity in the low degrees looks much better, here. But it has to be regarded, that here the results are compared against the true solution and in the GRACE case to a mean GFR solution (cf. introduction of Chapter 7 and Fig. 7.1). Nevertheless, the sensitivity in the very low degrees is slightly better, the curve is not increasing again for the first degrees (eg. Fig. 7.1). This is most probably related to not considered background model errors from ocean and atmospheric tides.

For the comparison to the GRACE results it has to be distinguished for the very smooth months like May and the more average or rougher months like November. The

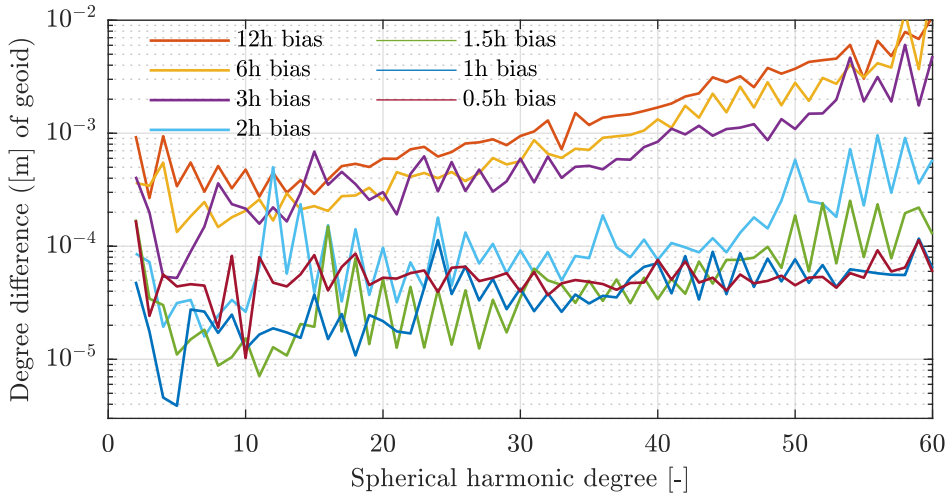

Figure 8.15: Degree difference with respect to the true gravity field for different arc length with bias $\vec{b}$ estimated for each accelerometer.

simulation solution is more similar to the May solution. The very low and very high KBR weighting does not result in oscillations and such low accuracies as for the GRACE November solution (Fig. 7.4). This is an indicator, that the varying GNV data quality over the month in November (Sec. 7.5), which is not the case for May and the simulation, might be the reason for the worse solution of November compared to May. The negative effect of the high KBR weighting for the lower degrees seems not to have that big effect on the solutions, but can not be assessed in that detail for the GRACE solutions, having no true reference.

For the case of the simulated data, the VCE approach works exceptionally well. The automatically determined weighting of KBR and GNV observations from VCE results in a good solution over all degrees. The standard deviation of the Gaussian white noise of the GNV data is estimated with at least 3 digits accuracy. The solutions with VCE weighting usually gives the best result. This is verified in more or less all investigated cases and will be again emphasized at appropriate places.

8.3 Parametrization

Besides the weighting, the parametrization, meaning arc length and additionally estimated parameters, plays an important role for the GFR results. As for the real GRACE data, just for the accelerometer calibration additional parameters are estimated. Again just bias and bias plus drift calibration is investigated with different arc length between 24h and 1h, respectively.

As in the previous section, in this investigation the KBR noise model with $\sigma_{hf,KBR}$ = 1e-6 m and the ACC noise model Const_lf with σ_{hf} = 1e-10 m/s^2 is used (cf. Sec. 6.3.2).

The GFR results are shown in terms of degree differences with respect to the true gravity field in Figure 8.15 for bias parametrization and in Figure 8.16 for bias plus drift parametrization.

The results are pretty similar to the ones for the real GRACE data in Section 7.2. The bias plus drift parametrization works with longer arc lengths and gives in general better results. With shorter arc length the quality of the solutions increases. For 2h and

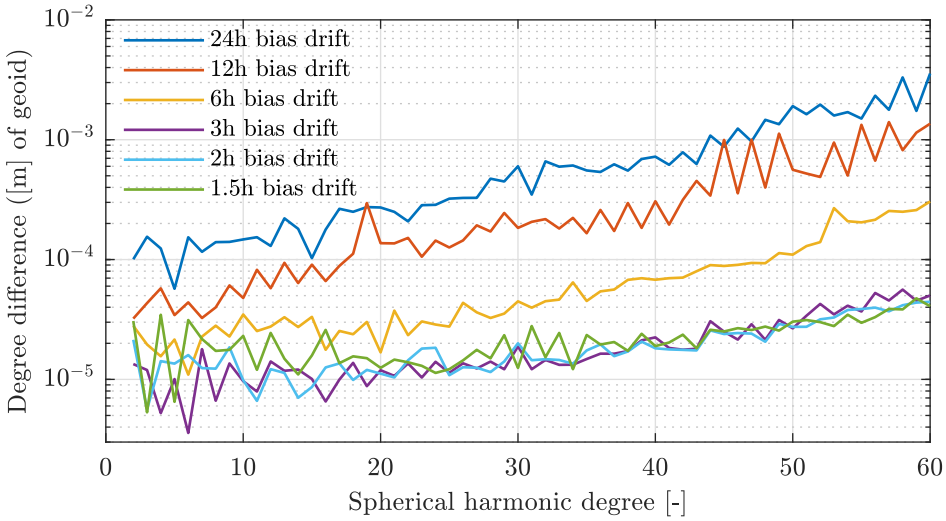

Figure 8.16: Degree difference with respect to the true gravity field for different arc length with bias $\vec{b}$ and drift $\vec{d}$ estimated for each accelerometer.

3h arc lengths the best solutions are obtained, the 1.5h solution is already a bit worse again. The results with just bias parametrization show a distinct separation up to 3h arc length and smaller ones. Up to 3h the results are comparably bad, with lower arc lengths they are increasing, and the best solution is obtained with 1h. However, the oscillation between the degrees is big and the results are worse than for bias plus drift parametrization with respectively small arc lengths.

The four best or most promising parametrizations of different arc lengths with bias and bias plus drift are also shown in spatial domain in Figure 8.17 in terms of EWH with respect to the true gravitational model. The smoother curves of the bias plus drift parametrizations in the degree difference plots is distinctly visible in the spatial plots, as well. The bias plus drift solutions (c) and (d) show a distinctly lower striping. The bias parametrization with 1h arc length (b) turns out to be slightly better than the 1,5h arc length (b). The 2h and 3h arc lengths for bias plus drift parametrization are closer together, but the 3h (c) solution shows a slightly lower striping.

Thus for all following investigations the bias plus drift parametrization is used, as also for the GRACE data processing.

The small differences of the 2h and 3h arc lengths solutions were also found for the GRACE GFR processing. There, for the months with better data quality, like May, the 3h arc lengths is slightly advantageous, as here. And hence is in good accordance. In general, the accordance of the parametrization results with the GRACE data processing is an indicator that the used ACC noise model, especially in the lower frequencies, is not too far from the real one.

The ASD of the KBR range-rate deviation with bias plus drift parametrization is shown in Figure 8.18 for all arc lengths for an arbitrary arc, number 10. The high frequency part is determined by the KRB range-rate noise (cf. Sec. 6.3.1, Fig. 6.29). The lower frequencies are dependent on the accelerometer noise, hence the parametrization and arc length. The best solution in terms of the gravity field with 3h arc length (eg. Fig. 8.16, 8.17) also results in the lowest deviation amplitudes. The long arc lengths solutions have a high deviation in the low and mid frequencies because less parameters are estimated and hence the deviations can not be adjusted as good as for the smaller arc

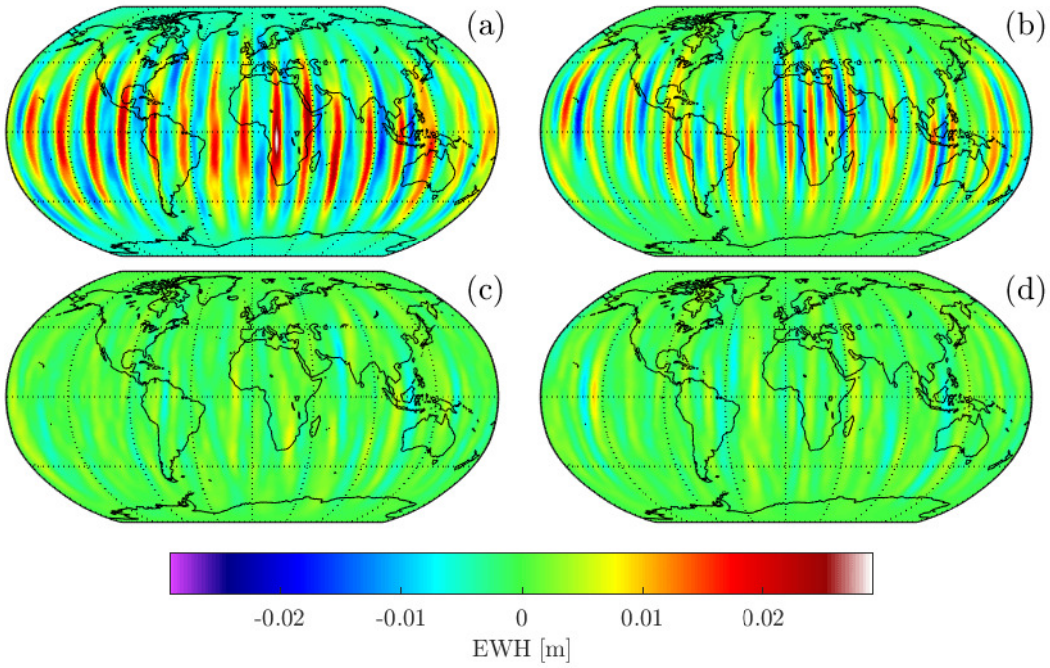

Figure 8.17: EWH $[m]$ with respect to the true gravitational field GGM05s from estimated gravitational field for different parametrizations (a) 1.5h bias, (b) 1h bias, (c) 3h bias plus drift, (d) 2h bias plus drift. Gaussian filter with 465 km radius applied.

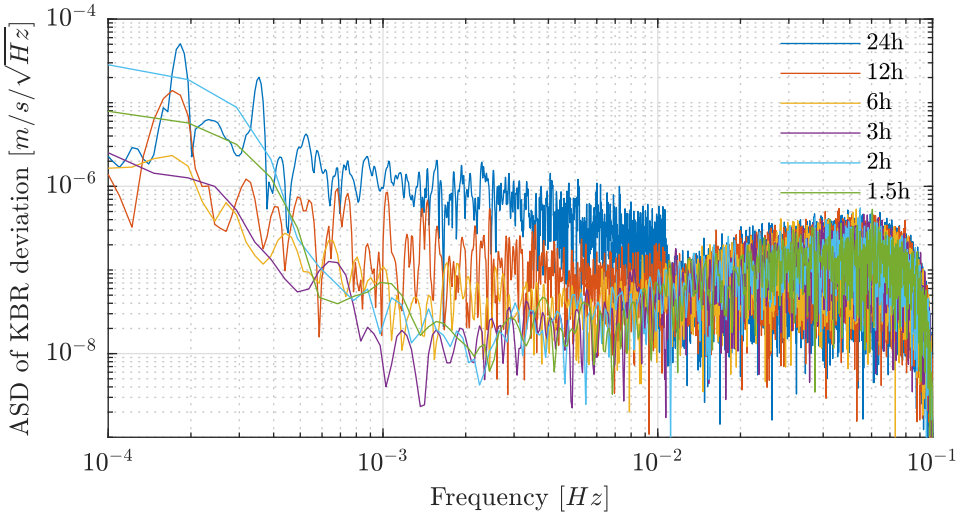

Figure 8.18: ASD of KBR range-rate deviation for different arc length with bias plus drift parametrization. With Const_lf ACC noise model $\sigma_{hf,ACC}$ = 1e-10 m/s^2, arc 10 and 26.

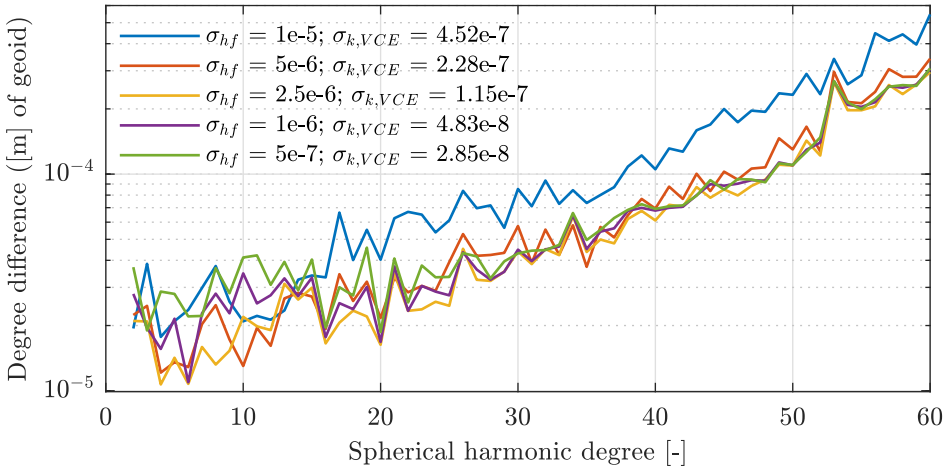

Figure 8.19: Degree difference for different KBR noise levels σ_{hf} with respect to the true gravity field. For 6h arc length and Const_lf ACC model with $\sigma_{hf,ACC}$ = 1e-10 m/s^2. The estimated KBR weighting factors and variances $\sigma_{k,VCE}$ for each solution are given in the plot.

lengths. Too small arc lengths show again higher deviations in the very low frequencies. This is because of a worse accelerometer calibration for smaller arc length due to fewer data. Nevertheless, the higher deviation in this frequency band seems not to affect the GFR solutions too much, the 2h and 1.5h solutions are still better than the 6h solution with a much lower deviation in this band. This is further demonstrated for the accelerometer noise investigation in Section 8.5.

8.4 KBR Noise

The inter-satellite ranging is the key feature of a GRACE-like ll-SST mission. The impact of the measurement accuracy on the resulting gravitational field solutions is investigated in the following.

The high frequency noise level $\sigma_{hf,KBR}$ from the KBR range noise model (cf. Sec. 6.3.1) is varied between 1e-5 to 5e-7 m. The used range-rate observable follows by derivation of the range and thus the higher frequencies are amplified while the low frequency signals are attenuated.

The influence on the estimated gravity field solutions is shown in Figure 8.19 in terms of degree difference with respect to the true gravitational field. The Const_lf ACC model with $\sigma_{hf,ACC}$ = 1e-10 m/s^2 is used with 6h arc length. The estimated weighting factors i.e. variances from the VCE algorithm are given in the plot, as well.

The solutions with KBR noise levels with σ_{hf} smaller than 1e-5 are more or less of the same quality. With $\sigma_{hf} \geq$ 5e-6 the solutions are not limited by the KBR noise level, but the ACC noise. Thus a further reduction of the noise does not increase the overall GFR solution. The solution with the lowest noise level (5e-7) is a little worse in in the low degrees, but slightly smoother in the higher degrees. This is a result of the estimated KBR weighting factors $\sigma_{k,VCE}$. With lower KBR noise level the KBR observations are weighted stronger and the quality of the low degree is worsen slightly. The decrease of the estimated variances $\sigma_{k,VCE}$ with lower noise level σ_{hf} is obviously visible.

From the results of the previous section, it is clear, that the results with 6h arc length are not giving the best solution (eg. Fig. 8.16). Therefore the KBR noise variation is conducted again with an arc length of 2h, shown in Figure 8.20. The result is com-

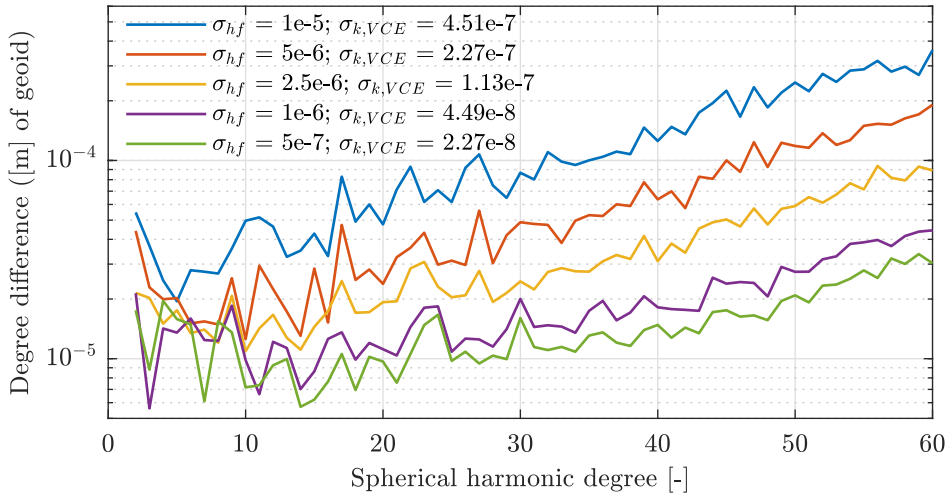

Figure 8.20: Degree difference for different KBR noise levels σ_{hf} with respect to the true gravity field. For 2h arc length and Const_lf ACC model with $\sigma_{hf,ACC}$ = 1e-10 m/s^2. The estimated KBR weighting factors and variances $\sigma_{k,VCE}$ for each solution are given in the plot.

pletely different, each decrease of the KBR noise level is giving a better gravity field solution. Just for the lowest noise level, the improvement is getting smaller and the ACC noise is starting to limit the solution. The statement from the 6h case, that the solutions are limited by the ACC noise, has to be modified slightly, in the sense that the combination of accelerometer noise and the applied accelerometer calibration was limiting the solutions.

For the five cases the ASD of the KBR deviations is shown in Figure 8.21 for the 6h arc length solutions and in Figure 8.22 for the 2h arc length solutions, for one specific arc, respectively. The typical linear slope of the high frequencies is distinct for both solutions. For the 2h case, the bend in the ASD occurs at lower frequencies, corresponding better with the modeled KBR noise (cf. Fig. 6.29). For the 6h arc length this is superimposed by the residual ACC noise of the calibration, which is worse for the 6h arc length. As expected, with increasing $\sigma_{hf,KBR}$ the high frequency part of the deviation is shifted upwards. The high frequency noise level $\sigma_{hf,KBR}$ has just a small effect on the lower frequencies of the deviation. For the shorter arc length of 2h it is slightly higher because of the characteristics of the calibration (cf. Sec. 8.3). Furthermore, with the lower KBR noise level $\sigma_{hf,KBR}$ and hence a stronger weighting of the range-rate observation, the low frequencies of the deviations are attenuated due to a worse accelerometer calibration in that frequency spectrum.

8.5 ACC Noise

The accelerometer noise is the other important factor mainly determining the quality of the gravity field solutions. The different noise models and its characteristic parameters, introduced in Chapter 6.3.2 and the Figures 6.31 and 6.32, are investigated in the following regarding their effect on the gravitational field solutions and range-rate deviations. The names of the different ACC noise models are used, as they were introduced in Chapter 6.3.2.

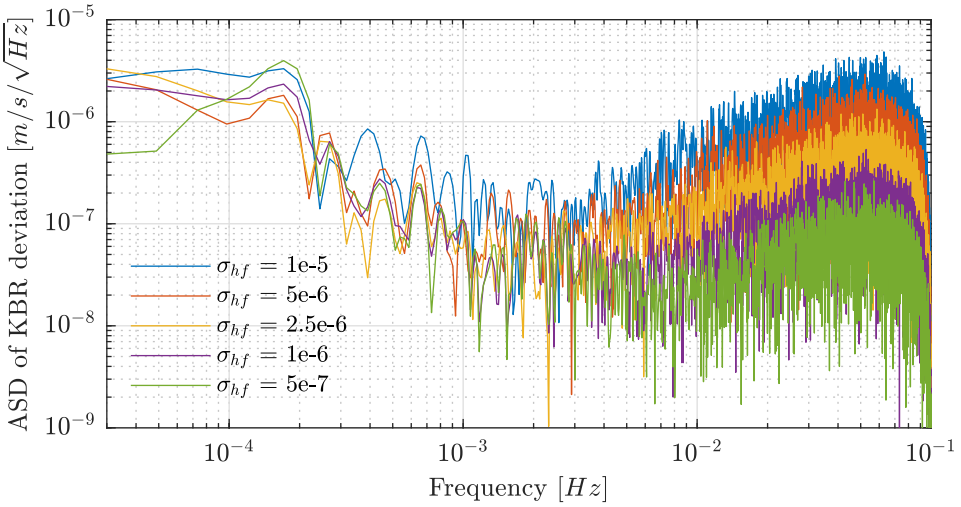

Figure 8.21: ASD of range-rate deviation for different KBR noise levels σ_{hf}. For 6h arc length, with ACC noise level $\sigma_{hf,ACC}$ = 1e-10 m/s^2, arc 26.

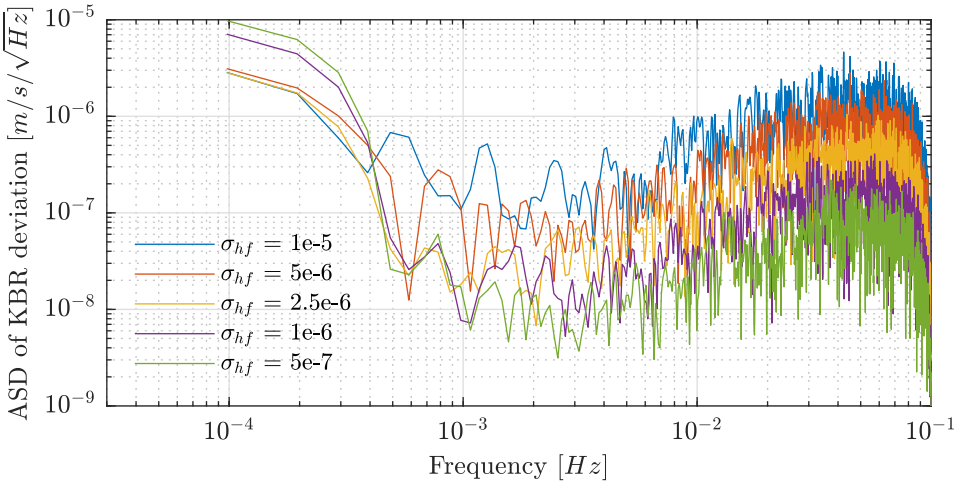

Figure 8.22: ASD of range-rate deviation for different KBR noise levels σ_{hf}. For 2h arc length, with ACC noise level $\sigma_{hf,ACC}$ = 1e-10 m/s^2, arc 84.

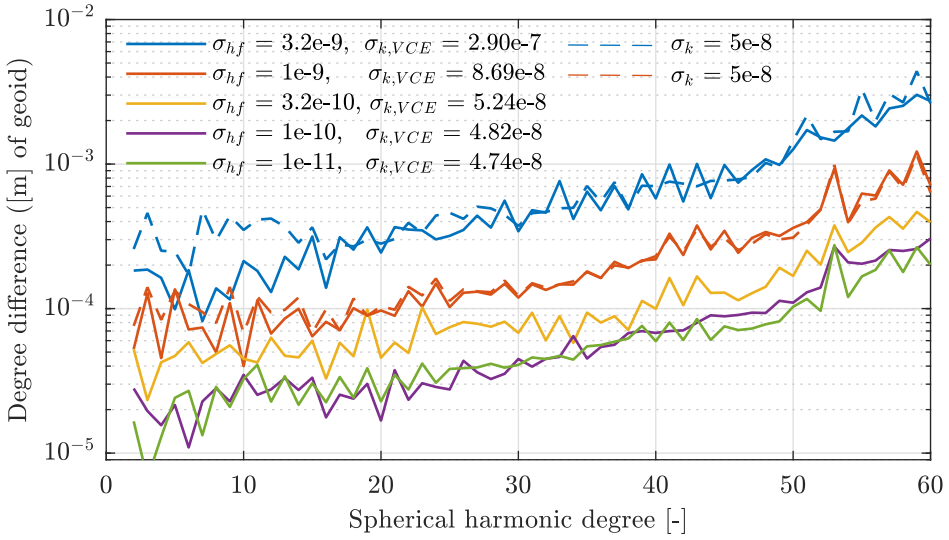

Figure 8.23: Degree difference for Const_lf ACC noise model for different σ_{hf} with respect to the true gravity field for 6h arc length. KBR noise level $\sigma_{hf,KBR}$ = 1e-6 m. The estimated KBR weighting factors and standard deviations $\sigma_{k,VCE}$ for each solution are given in the plot. The dotted lines show results without using VCE but the constant weighting factors for two cases.

For all following results presented in this section the KBR noise level of $\sigma_{hf,KBR}$ = 1e-6 m is used. Furthermore, bias plus drift parametrization and the VCE weighting is utilized. An interesting influence of the arc length for different ACC models was found, thus results with 6h and 2h arc length are shown here, as well.

8.5.1 Const_lf Noise Model

We begin the analysis with the Const_lf ACC noise model, for which the high frequency noise σ_{hf} is varied, as for the KBR noise in the section before. This ACC model utilizes the the same ASD noise characteristic for all three accelerometer axes.

Results in terms of degree differences are shown in Figure 8.25 with respect to the true gravitational field for 6h arc length. Again, the estimated weighting factors i.e. variances from the VCE algorithm are given in the plot, as well. Additionally, the dotted lines show the solutions for two cases without using the VCE approach, but with the given constant weighting.

The high frequency ACC noise level σ_{hf} has nearly a constant influence over all d/o. With decreasing σ_{hf}, the solutions are improving until about σ_{hf} = 1e-10. A further reduction does not have an influence anymore. The solutions are limited by the other noise sources.

A very interesting fact can be seen in the estimated weighting factors or standard deviations. Even though the KBR noise level is constant for all cases, the estimated standard deviation $\sigma_{k,VCE}$ of the KBR observations are decreasing with decreasing ACC noise level σ_{hf}. The high frequency ACC noise also influences the standard deviation of the KBR range-rate measurement. This is because the accelerometer measurement is not treated as an observable in the GFR approach, but the noise or the error in the used non-gravitational accelerations strongly influences the inter-satellite range and its derivatives on these scales. Therefore, the KBR weighting and its standard deviation σ_k is a combined measure of the ACC and KBR noise level.

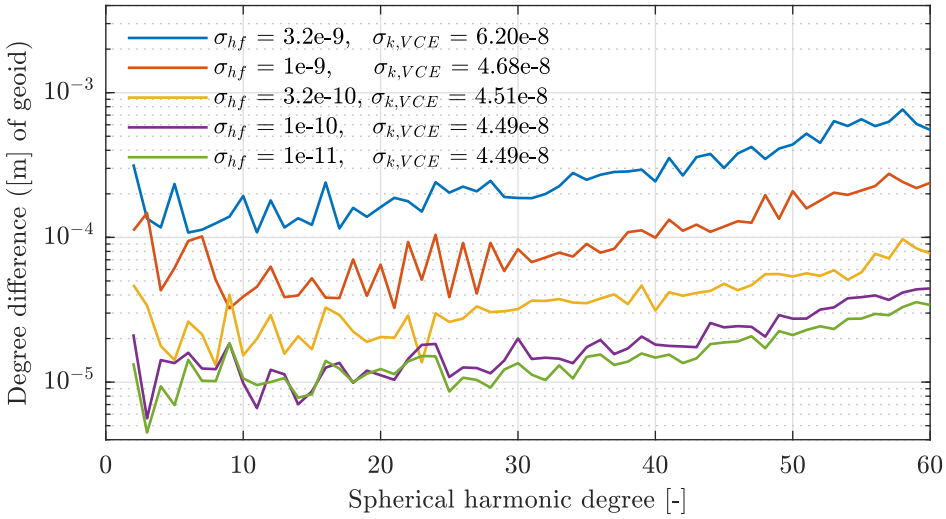

Figure 8.24: Degree difference for Const_lf ACC noise model for different σ_{hf} with respect to the true gravity field for 2h arc length. KBR noise level $\sigma_{hf,KBR}$ = 1e-6 m. The estimated KBR weighting factors and standard deviations $\sigma_{k,VCE}$ for each solution are given in the plot.

Using a high weighting of the KBR observations σ_k with higher ACC noise levels results in a worse solution, shown for the two highest noise levels by the dotted lines. It is important to mention that the solutions using the automatic VCE weighting give the best results. Solutions are not better because of the higher weighting of the KBR observations. This will be taken up again and demonstrated in some of the following figures.

The results for of the same investigation with 2h arc length are shown in Figure 8.24 with the same ACC models. Compared to the 6h arc length results from Figure 8.23, each solution is distinctly improved. This result is not particularly unexpected as the parametrization analysis in Section 8.3 and Figure 8.16 revealed that the solutions with 2h and 3h arc length are giving the best solutions. The improvement is slightly bigger for the higher degrees and the lower ACC noise levels σ_{hf}. Nevertheless, as for the solutions with 6h arc length, for lower noise levels than σ_{hf} = 1e-10, the quality of the solutions is not increasing anymore.

In the following the effect of the low frequency noise in the accelerometer signal and the estimation of the accelerometer calibration via bias and drift to counteract it, is investigated. In Figure 8.25 the degree difference for three cases with no ACC noise are shown. As reference, the result for σ_{hf} = 1e-11 m/s^2 from the previous figure is shown as well (green), all with 6h arc length.

In the first test case (blue) no ACC noise is considered and no accelerometer calibration is estimated, thus the perfect non-gravitational accelerations are used. The result is about one order of magnitude better than the reference solution (green). Lets remember, that the reference solution with σ_{hf} = 1e-11 m/s^2 could not be enhanced by further decreasing of the high frequency noise σ_{hf}. This result shows, that not the KBR noise is the limiting factor for the reference solution, but the low frequency ACC noise.

Very surprising is the result of the next test case (red), with again no ACC noise but the estimation of bias and drift parameters. It has about the same accuracy than the solution without calibration, and tendentially even better. Considering that the bias plus drift calibration is far from the truth (see Fig. 8.26), this means that not the error of the bias and drift calibration is the reason for the order of magnitude difference between

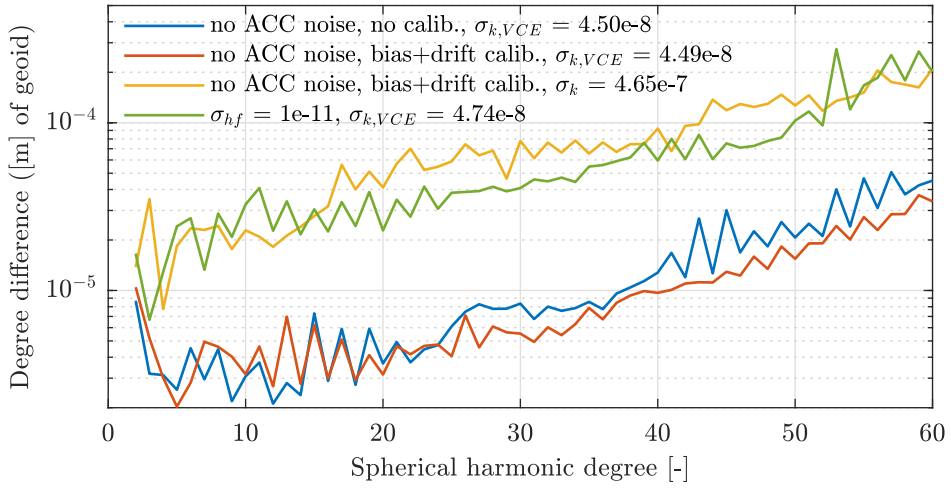

Figure 8.25: Degree difference with respect to the true gravity field for different ACC noise levels and accelerometer calibrations for 6h arc length. KBR noise level $\sigma_{hf,KBR}$ = 1e-6 m. The estimated KBR weighting factors and standard deviations $\sigma_{k,VCE}$ for each solution are given in the plot.

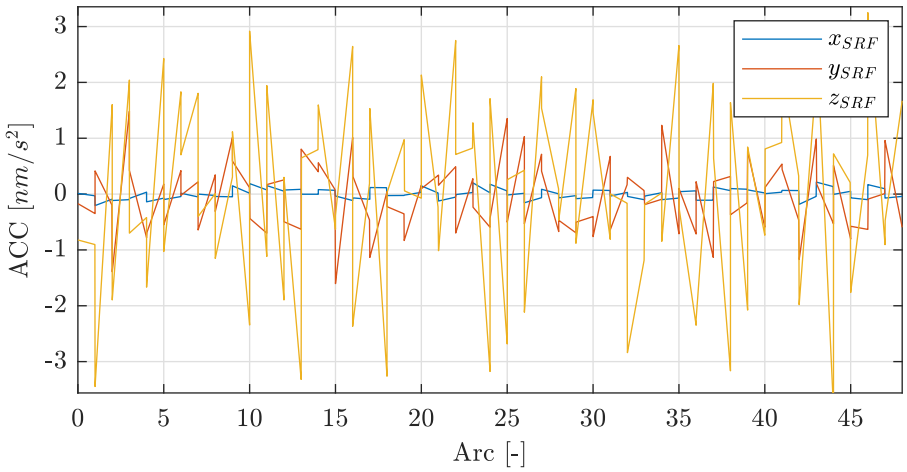

Figure 8.26: Estimated accelerometer calibration for GRACE A with 6h arc length and bias plus drift parametrization. No accelerometer noise and KBR noise level $\sigma_{hf,KBR}$ = 1e-6 m.

the results with and without ACC noise. The estimated accelerometer calibration for this case (red) is shown in Figure 8.26 for one satellite. Because no ACC noise is used, the estimated calibration would be perfectly always zero for all axes. It is obvious that this is not the case. The estimated calibration is just "oscillating" around zero. The variance of the oscillation is just slightly lower than for the case with using the Const_lf ACC noise model, see Figure 8.40 (b).

This allows the following two conclusions: 1. The rather big error of the calibration is in a frequency band that is not affecting the gravity field solution. This has been observed before, for the processing of GRACE data, where better solutions were obtained with very unrealistic estimated accelerometer calibration parameters (eg. Fig. 7.49). And consequentially, 2. The difference of the two solutions (red and green) must result from the mid frequency accelerometer noise.

The case not yet discussed in Figure 8.25 (yellow), is obtained without ACC noise, but bias plus drift calibration, as for the second case (red), but with a manual weighting

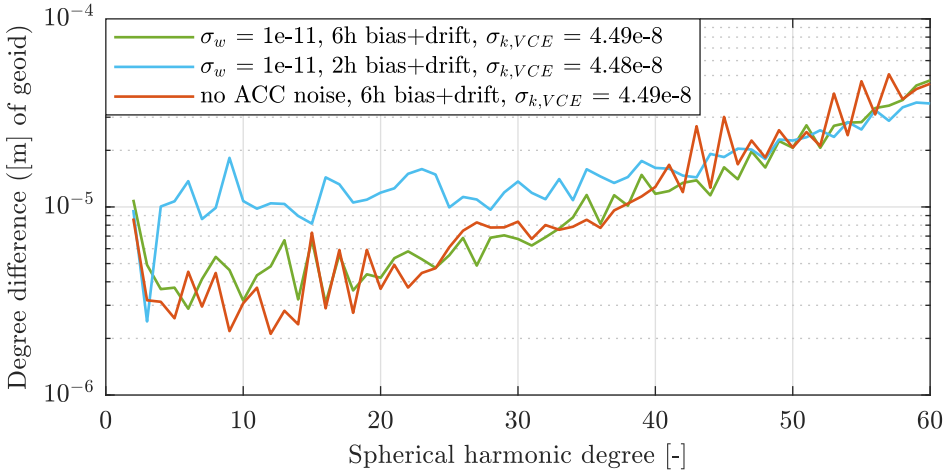

Figure 8.27: Degree difference with respect to the true gravity field for solutions with a completely white ACC noise model with σ_w and the solution without ACC noise model from before as reference. KBR noise level $\sigma_{hf,KBR}$ = 1e-6 m. The estimated KBR weighting factors and standard deviations $\sigma_{k,VCE}$ for each solution are given in the plot.

of $\sigma_g = 0.02$ and σ_k = 4.65e-7. This difference in the weighting results in an order of magnitude worse solution. It is a further example, that the automatic VCE weighting works quite well and the optimal weighting of the KRB range-rate observations is distinctly dependent on the ACC noise, too.

The fact that fact that the mid frequency noise seems to have a rather strong influence is further investigated with the use of an ACC noise model employing just white noise with $\sigma_w = 1e-11$. The results are shown in Figure 8.27 in terms of degree differences for the arc lengths of 2h and 6h, as used before. Additionally, the solution without any ACC noise from Figure 8.25 is plotted as reference (red). Especially with the 6h arc length the solution is as good as the reference with no ACC noise. Thus the conclusions from before, that the mid frequency ACC noise is limiting the solutions is confirmed. The effect that the result for the shorter arc length of 2h is slightly worse is revisited in the following paragraph.

The surprising results without ACC noise are further investigated for different arc lengths in Figure 8.28. The figure shows the degree difference of solutions with no ACC noise but bias plus drift estimation for arc lengths between 12h and 1.5h.

It is obvious, that the shorter arc lengths, below 6h, have a negative effect on the results. Especially the lower degrees are affected more strongly. The 12h and 6h solutions still agree with the solution without calibration (Fig. 8.25), for shorter arc length the results are degrading. The weighting for all solutions is about the same, $\sigma_{k,VCE}$ = 4.89e-8. As observed before, the error of the accelerometer calibration is increasing with shorter arc length. The estimated calibration for the 2h arc length solution is shown in Figure 8.29. Because no ACC noise is applied, the calibration is directly the error, as well. Compared to the 6h calibration from Figure 8.26, the amplitude is increased and of cause the frequency, too due to the shorter arc length. Thus, without and with very low ACC noise, a longer arc length is beneficial. The statement from before that the error of the calibration is not affecting the solution needs to be regarded with respect to the arc length, as well. Too short arc length are slightly affecting the solution negatively, especially the lower degrees up to about d/o 40. It is not completely unambiguous

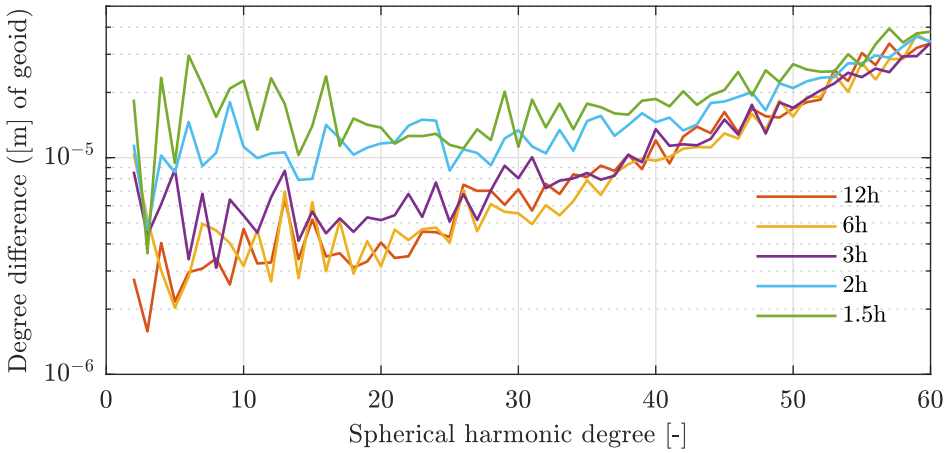

Figure 8.28: Degree difference with respect to the true gravity field with no ACC noise model for different arc length. KBR noise level $\sigma_{hf,KBR}$ = 1e-6 m.

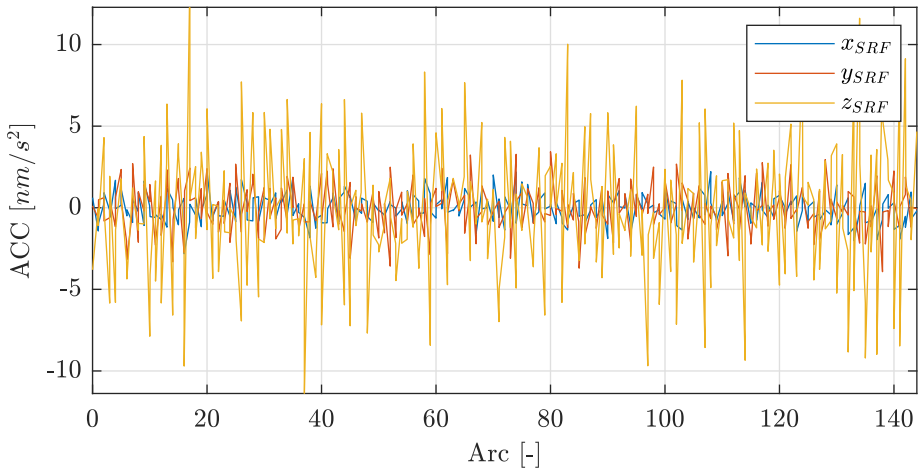

Figure 8.29: Estimated accelerometer calibration for GRACE A with 2h arc length and bias plus drift parametrization. No ACC noise and KBR noise level $\sigma_{hf,KBR}$ = 1e-6 m.

if either the higher frequency of the calibration error or the increasing amplitude is decisive, because both condition each other.

As for the investigation of the KBR noise, the ASD of the KBR deviations for one arc are shown in Figure 8.30 for the results with different high frequency noise levels σ_{hf} (from Fig. 8.23) and the results with no ACC noise in Figure 8.31 (from Fig. 8.25 and 8.28) for 6h and 2h arc length.

The high frequency part of the deviations is not affected by the high frequency noise σ_{hf} of the accelerometer. It is governed by the slope of the KBR range-rate noise. The other side of the spectrum, the low frequencies, are affected by the high frequency ACC noise σ_{hf}. With decreasing σ_{hf} the negative slope for the low frequencies is shifted parallelly downwards. As seen before in the degree difference plot, from σ_{hf} = 1e-10 m/s^2 further reduction does not have an influence anymore, here as well.

Just omitting the ACC noise completely (Fig. 8.31), gives a further reduction of the low frequency content of the range-rate deviations if no calibration is estimated or the arc length is higher (6h). In that case the ASD of the deviations is close to the ASD of the initially generated KBR noise (cf. Fig. 6.29). The result with the short arc length

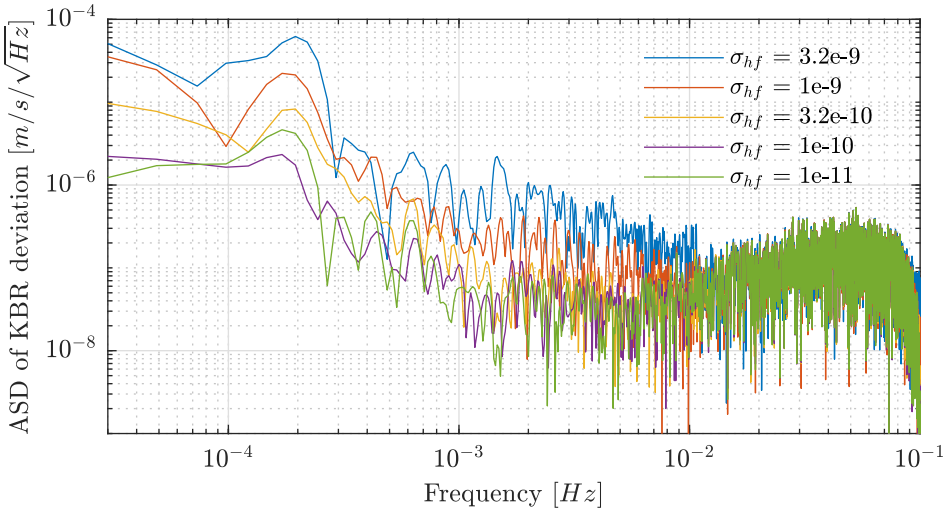

Figure 8.30: ASD of range-rate deviation for Const_lf ACC noise model for different σ_{hf} with 6h arc length. With KBR noise level $\sigma_{hf,KBR}$ = 1e-6 m, arc 26.

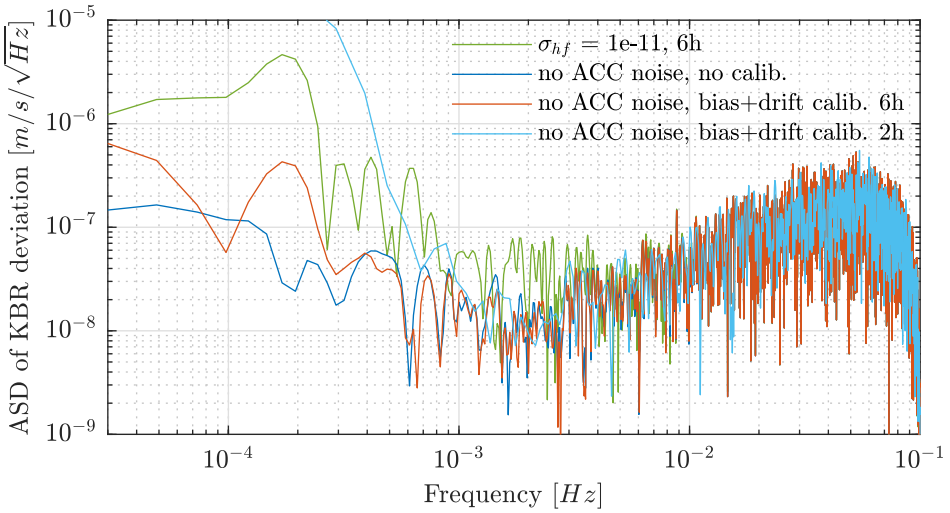

Figure 8.31: ASD of range-rate deviation for solutions with no ACC noise and different accelerometer calibrations and as reference the result for σ_{hf} = 1e-11 from the previous figure. KBR noise level $\sigma_{hf,KBR}$ = 1e-6 m, arc 26.

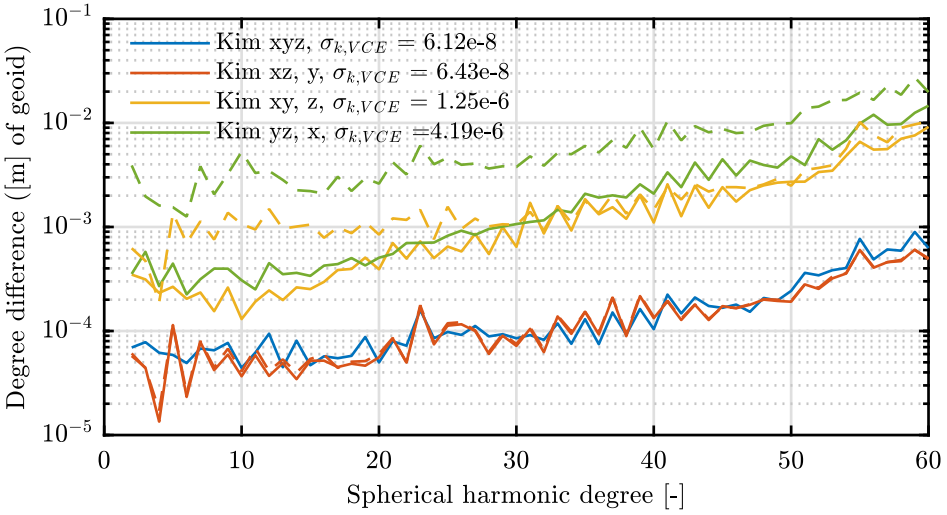

Figure 8.32: Degree difference with respect to the true gravity field for different ACC noise models of the three accelerometer axis. KBR noise level $\sigma_{hf,KBR}$ = 1e-6 m. The estimated KBR weighting factors and standard deviations $\sigma_{k,VCE}$ for each solution are given in the plot. The dashed lines show solutions with a constant weighting of σ_k = 5e-8

.

of 2h shows much higher amplitudes in the low frequency domain. This has also been observed for the parametrization analysis in the ASD in Figure 8.18. For the ACC noise model with σ_{hf} = 1e-10 m/s^2 and 2h arc length the curves (light blue) look about the same. Hence, the observed bigger deviations in the low frequency range originate from the error of the fast changing parametrization for the short arc length. Thus, the high frequency ACC noise has more or less no effect in this frequency range because it is then governed by the error of the calibration.

8.5.2 Sensitivity of Different Axes

Based on the Kim ACC noise model (Fig. 6.31), which utilizes a different noise model for the accelerometer y-axis, the influence of the three axes is investigated. Therefore the model for the accelerometer y-axis with a higher noise is applied to the different axes subsequently.

The results of this experiment are shown in Figure 8.32. The first result (blue) is obtained using the lower noise model Kim x,y for all three axes (Kim xyz). For the other three results, the higher noise model is applied to each axis, respectively. The VCE weighting of each solution is given in the plot. It confirms the already seen trend that a lower ACC noise increases the KBR range-rate weighting. The dashed lines in that plot show the results for constant KBR weighting σ_k = 5e-8 as reference, demonstrating that the automatic VCE weighting works well and the results are not a weighting issue.

The solution with the the lower ACC noise on all three axis (blue) is about the same as for the original Kim model with a less sensitive y-axis (red). The sensitivity of the cross-track axis, which for the GRACE formation is pretty much aligned with the accelerometer y-axis, is not as important than along-track and radial axes. This is the reason why the accelerometer is mounted in the satellite that way.

With the higher noise model applied to the z-axis (yellow), the solution decreases about one order of magnitude for the higher degrees and a bit less for the lower degrees. The result for a lower sensitivity of the x-axis (green) is about the same and tendentially

Table 8.1: Set constant scale factors $\vec{s}$ (the true values are 1)

	GRACE A	GRACE B
x	0.9912	0.9885
y	0.9856	0.9987
z	0.99631	0.9926

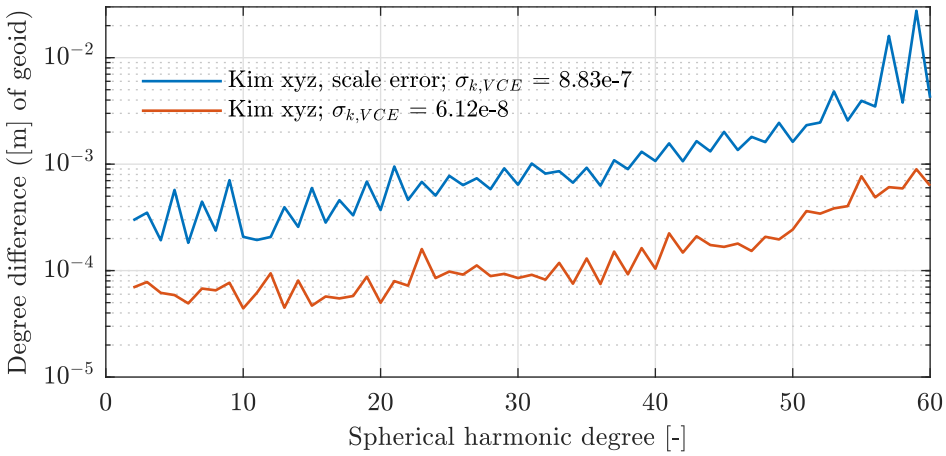

Figure 8.33: Degree difference with respect to the true gravity field for the Kim xyz ACC noise model with slightly wrong ACC scale $\vec{s}$. KBR noise level $\sigma_{hf,KBR}$ = 1e-6 m. The estimated KBR weighting factors and standard deviations $\sigma_{k,VCE}$ for each solution are given in the plot.

.

even more worse. Thus along-track and radial directions are decisive for the resulting GFR solution.

8.5.3 Sensitivity of Scale Factor

The scale factor of the accelerometer calibration $\vec{s}$ has a strong influence for the real GRACE data processing. Small differences have a remarkable effect on the resulting gravitational fields (eg. Sec. 7.8 and Fig. 7.59). Here this is again investigated in the simulation. Therefore a constant scale is added to the accelerometer model in each axis. The defined constant scale factors for both satellites deviate just slightly from the true values of one. The set values for the three axes are given in Table 8.1. Their deviation is a little smaller than for the GRACE data (see eg. Tab. 7.2).

The experiment is conducted with the Kim xyz ACC noise model. The result is shown in Figure 8.33 in terms of degree differences for the solution with scale error and the reference solution with no scale error. The difference of the resulting solution is surprisingly big, especially for the higher degrees (nearly one order of magnitude). This is much more than expected from GRACE data processing (cf. Fig. 7.59).

The influence on the ASD of the range-rate deviations is shown later together with the other ACC models in Figure 8.36.

8.5.4 Further Accelerometer Models

In Section 6.3.2 further accelerometer models from the literature are introduced. Their intrinsic noise models are given in Figure 6.31. The GFR results with these models in

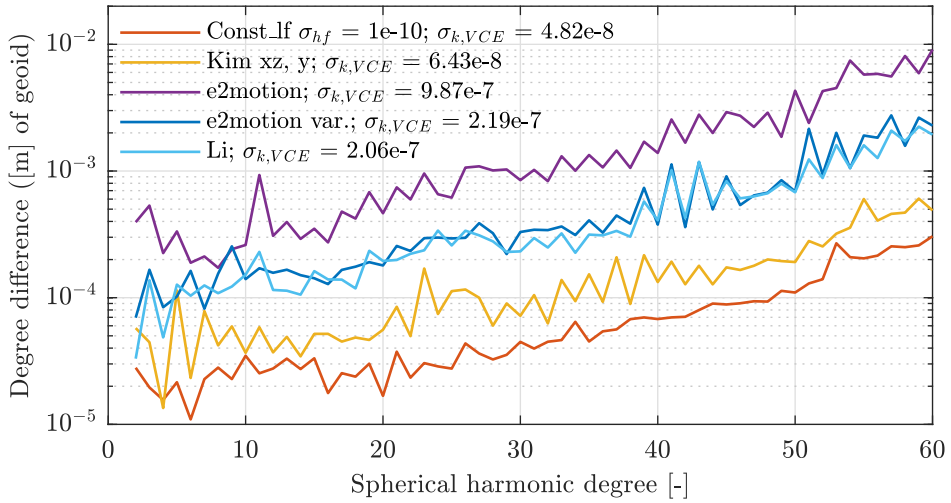

Figure 8.34: Degree difference with respect to the true gravity field for 6h arc length for different literature ACC noise models (see eg. Fig. 6.31). KBR noise level $\sigma_{hf,KBR}$ = 1e-6 m. The estimated KBR weighting factors and standard deviations $\sigma_{k,VCE}$ for each solution are given in the plot.

terms of degree difference with respect to the true gravity field are shown in Figure 8.34 for bias plus drift parametrization with 6h arc length. Again, the VCE standard deviations $\sigma_{k,VCE}$ are given in the plot. The previous result from the Const_lf model with σ_{hf} = 1e-10 is shown again as reference.

Compared to the Const_lf model, the obtained results with all other models are worse. Even though, besides the Kim model, they have a lower high frequency noise. Here again it turns out that the mid and low ACC noise frequencies limit the GFR accuracy. For the Const_lf, e2motion and e2motion var. models, the negative slope of the mid to low frequencies in the ASD model is just slightly shifted, but results in a difference of about an order of magnitude in the gravitational field accuracy, respectively.

The difference between the Li model and the e2motion var. model is just the increasing amplitude of the high frequencies in the Li model. For the GFR solution this has no influence, the results are pretty much the same. Considering the previous analysis, this can be explained by the much higher influence of the lower ACC frequency noise level and the accelerometer calibration, which is the limiting factor, here. For example the variation of the high frequency noise in Figure 8.23 with eg. σ_{hf} = 1e-9 m/s^2 results in a better result than the Li model.

The same ACC models are processed with the arc length of 2h. The results look surprisingly different. They are shown in Figure 8.35 as degree difference. Especially the solutions utilizing the ACC models with higher low and mid frequency noise (e2motion, e2motion var. and Li) drastically improve with the shorter arc length. The e2motion and Li solutions reach the same accuracy than the Const_lf model with σ_{hf} = 1e-10. The accelerometer calibration error of the e2motion var. solution is about the same as for the Const_lf model (shown in Fig. 8.29).

This shows the importance of an appropriate parametrization, adjusted with respect to the noise characteristics of the involved data. Considering the previous results with the const_lf ACC model with different high frequency noise levels and no ACC noise model, it can be concluded, that the solutions are either limited by the increasing error of the accelerometer calibration with small arc lengths or by the mid frequency noise in the accelerometer data. A stable estimation of a higher order acclerometer

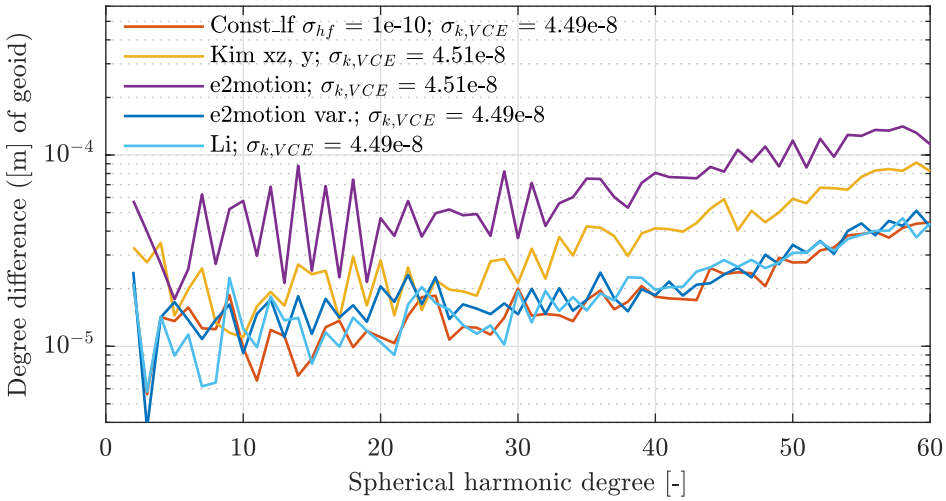

Figure 8.35: Degree difference with respect to the true gravity field for 2h arc length for different literature ACC noise models (see eg. Fig. 6.31). KBR noise level $\sigma_{hf,KBR}$ = 1e-6 m. The estimated KBR weighting factors and standard deviations $\sigma_{k,VCE}$ for each solution are given in the plot.

calibration with longer arc lengths would be desirable to exploit the full accuracy of the inter-satellite ranging.

The ASD of the resulting KBR range-rate deviations is shown for one arc in Figure 8.36 for the results of the 6h arc length parametrization and in Figure 8.37 for the 2h arc lengths investigation. The deviation in the high frequency domain is completely determined by the range-rate noise, as seen before.

For the 6h arc length case, the rather bad solutions with the e2motion var. and e2motion ACC noise models and also the solution with the scale error, a distinct jump at about 10^{-2} Hz occurs. The investigation before showed that the high frequency noise results in a shift of the negative slope to higher frequencies (cf. Fig. 8.30 and 8.31), the effect of the high mid frequency ACC errors is rather a jump, rising that slope upwards.

For the more optimal arc length of 2h (Fig. 8.37), the results are much smoother and show a distinctly lower deviation in the mid frequencies. Compared to the results in terms of degree differences, the curves are a little closer together, but the better solutions show also slightly lower range-rate deviations in the mid frequencies.

In general, the mid frequency noise has a much stronger effect on the gravity field solution than the high frequency noise. This is reasonable, because the very high frequency noise may average out and is attenuated by the integration of the acceleration. The very low frequency noise does not affect the higher degrees of the gravitational field so much and is counteracted by the accelerometer calibration. The mid frequency noise can not be counteracted so easily by calibration. A high order calibration function would need to be determined, which may not be accurate, considering the problems of an appropriate bias plus drift determination and the unacceptable results already for a second order calibration function.

The error of the accelerometer scale has a similar effect than the inappropriate calibration of the mid frequency ACC noise (6h arc length). This is because it is a permanent error that is affecting the complete frequency band.

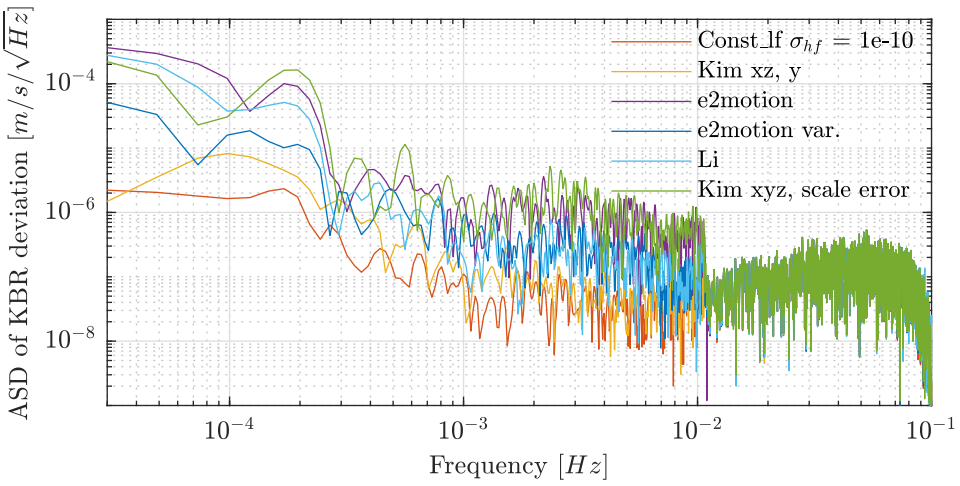

Figure 8.36: ASD of range-rate deviation from GFR with the different literature ACC noise models for 6h arc length. KBR noise level $\sigma_{hf,KBR}$ = 1e-6 m, arc 26.

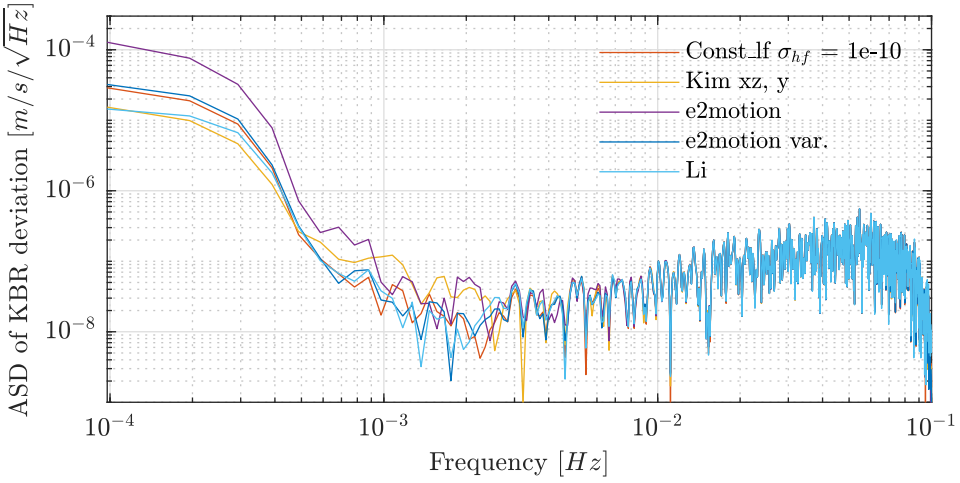

Figure 8.37: ASD of range-rate deviation from GFR with the different literature ACC noise models for 2h arc length. KBR noise level $\sigma_{hf,KBR}$ = 1e-6 m, arc 26.

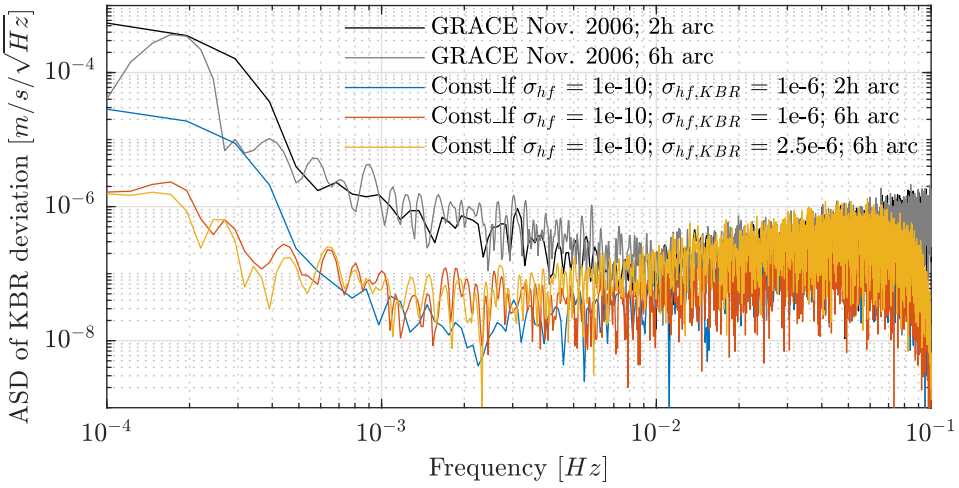

Figure 8.38: Comparison of ASD of range-rate deviations from GFR with the different ACC and KBR noise models and arc lengths and real GRACE results.

8.5.5 Comparison to GRACE Results

The results from the previous two subsections can be compared to the processing of the real GRACE data. The ASD of the GRACE range-rate deviations has been shown eg. in Figure 7.38 for one arc in November 2006. In Figure 8.38 this (black) is compared to the previously shown results in terms of the ASD of the KBR range-rate deviations.

For this comparison it has to be mentioned, that for the real GRACE data processing some more effects are influencing the resulting gravity field and range-rate ASD, which are not considered in the simulation. These are mainly not completely correct background gravity models and a minor effect from averaging the time dependent gravitational field over a certain period, like one month. Furthermore the simulation results in this chapter are based on the analysis of just 12 days of data, compared to around 30 days used for the monthly GRACE solutions.

In the comparison (Fig. 8.38) the high frequency noise in the deviations with the used default KBR range-rate model with $\sigma_{hf,KBR}$ = 1e-6 m seems to be a little to low (red). With $\sigma_{hf,KBR}$ = 2.5e-6 m (yellow) the simulations agrees quite well with the real data in the high frequency range.

The arc length does not have such big importance for the GRACE results in terms of the range-rate deviations (the black and gray curves for 2h and 6h arc length are very close). For the lower frequencies the differences are bigger. Theoretically, the differences could be dissolved for example by using the Const_lf ACC noise model with σ_{hf} = 3.2e-9 m/s^2 (cf. Fig. 8.30). But such a high high-frequency noise level is definitely not realistic. It also could be dissolved using the e2motion var. ACC model with the non-optimal arc length of 6h (Fig. 8.36), which exhibits a higher mid frequency noise. The higher mid frequency ACC noise has the same effect on the ASD of the range-rate deviations. However, for the GRACE processing the arc length and parametrization had been optimized (cf. Sec. 7.2), thus this is not likely the explanation. Therefore, the difference might be rather explained by the mentioned background model errors. Hence some gravitational signal content is still present in the residuals in this frequency band of the real data. Furthermore, a slightly wrong scale factor has the same effect on the ASD, as well (cf. Fig. 8.36), which definitely can not be ruled out for the GRACE processing. The higher low frequency amplitudes may be most probably a combination of these factors.

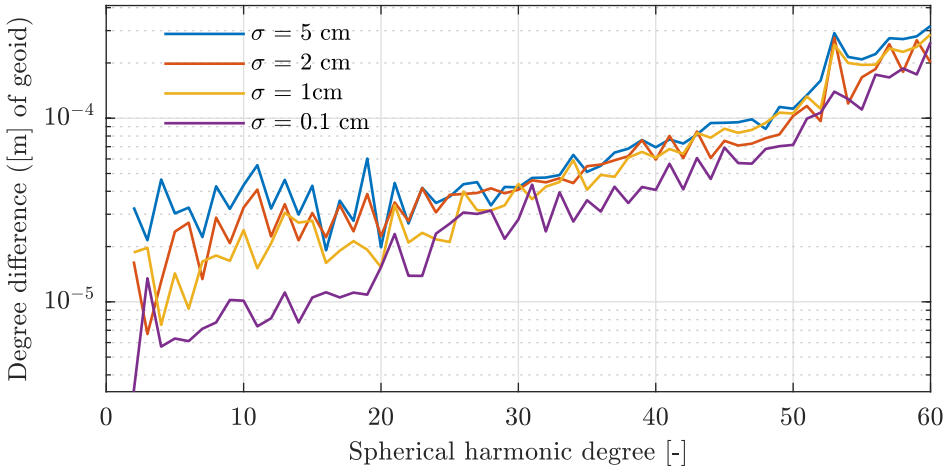

Figure 8.39: Degree difference for different GNV noise levels with respect to the true gravity field. For 6h arc length, ACC and KBR noise level $\sigma_{hf,ACC}$ = 1e-10 m/s^2 and $\sigma_{hf,KBR}$ = 1e-6 m, respectively.

8.6 GNV Noise

The influence of the GNV or KOS noise (for the simulation there is no difference between both) is investigated for noise levels with standard deviations of σ = 5, 2, 1, and 0.1 cm. The GNV noise is modeled as white Gaussian noise (cf. Sec. 6.3.3). The default ACC and KBR noise levels with $\sigma_{hf,ACC}$ = 1e-10 m/s^2 and $\sigma_{hf,KBR}$ = 1e-6 m are utilized. Agian, the VCE weighting approach is used. The determination of the GNV weighting factors, and hence the variances of the noise σ_g, works exact to about three digits for the perfect white Gaussian noise. The weighting of the KBR data is pretty constant for all cases (σ_k = 4.8e-8).

The results are shown in Figure 8.39 in terms of degree difference with respect to the true gravity field. Especially the lower degrees are comparably sensitive to the absolute GNV position observation. Thus, as expected, the lower degrees, up to about 20, show an improvement with decreasing GNV noise level. Furthermore, at least for the lowest GNV noise level, the higher degrees slightly improve as well. This is not only a direct effect of the lower GNV noise level, but also of a better accelerometer calibration. The accelerometer calibration is much more sensitive to the absolute position observation, than the relative range-rate and is primarily determined by this observation. Therefore, the lower GNV noise level allows for a better accelerometer calibration, which in turn increases the quality of the higher degrees of the gravitational field slightly. This statement is not in contrast to the previous Section 8.5 where the low frequency errors of the accelerometer calibration were not found to be the primarily limiting factor, because the improvement of the higher degree is not that big here. Furthermore, considering the noise level of 0.1 cm is at least one order of magnitude better than for the best investigated and estimated orbit solutions for GRACE.

The acclerometer calibration is depicted in Figure 8.40 for the GNV noise levels of 2 cm and 0.1 cm. In (a) and (c) the true noise and the negative of the estimated calibration for each axis is shown. In (b) and (d) the differences between the true and estimated calibration is shown, respectively. The RMS of the differences for each axis are given in the plots, as well.

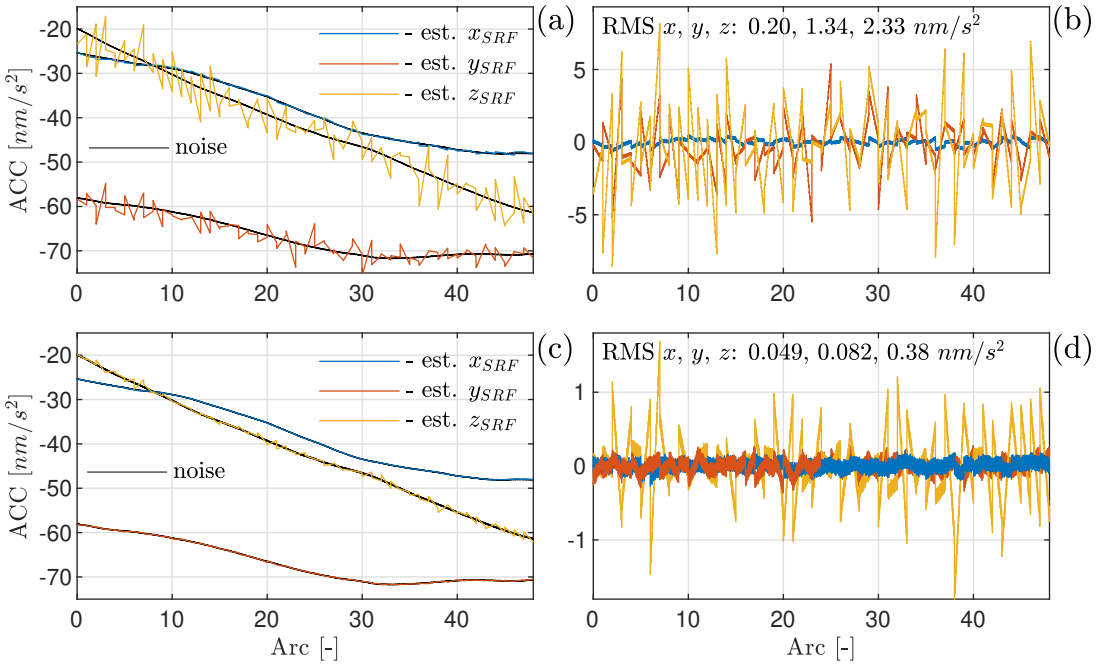

Figure 8.40: Accelerometer calibration for GNV noise levels with standard deviation $\sigma = 2$ cm (a) and 0.1 cm (c). Shown is the true noise and the negative of the estimated (- est.) calibration for each axis. (b) and (d) show the differences between truth and estimated calibration, respectively. The RMS for each axis is given in the plots, as well. For 6h arc length, ACC and KBR noise level $\sigma_{hf,ACC}$ = 1e-10 m/s^2 and $\sigma_{hf,KBR}$ = 1e-6 m, respectively.

In general it shows the known pattern, that the x-axis is the most sensitive and the calibration is distinctly better than y- and z-axes. The differences, and their RMS, show this more qualitatively. But here, an obvious improvement of nearly one order of magnitude is visible for the lower GNV noise level. This is also a reason for the slightly improved higher degrees in Figure 8.39 with a lower GNV noise level.

8.7 SCA Noise

The star camera attitude solution (SCA) model has been elaborated in Chapter 6.3.4. Different processing strategies to compute a SCA solution from the two camera measurements have been investigated and the resulting attitude errors were shown. The different setups are in short: 1. Using just one star camera, 2. Two star camera combination and 3. A Kalman filter attitude solution. In an additional case a misalignment of the star cameras was added.

The influence on the recovered gravitational field is investigated in the following. For all solutions the KBR noise level $\sigma_{hf,KBR}$ = 1e-6 m is utilized with 6h arc length. No accelerometer noise is added and no calibration is estimated. Hence the results show just the sensitivity to the SCA data.

In Figure 8.41 the degree difference with respect to the true gravity field is shown for different SCA setups.

The reference solution with no SCA noise is the best possible solution and limited by the applied KBR and GNV noise. For the analysis one has to keep in mind, that an attitude error is indirect a further accelerometer error (the attitude is just needed to

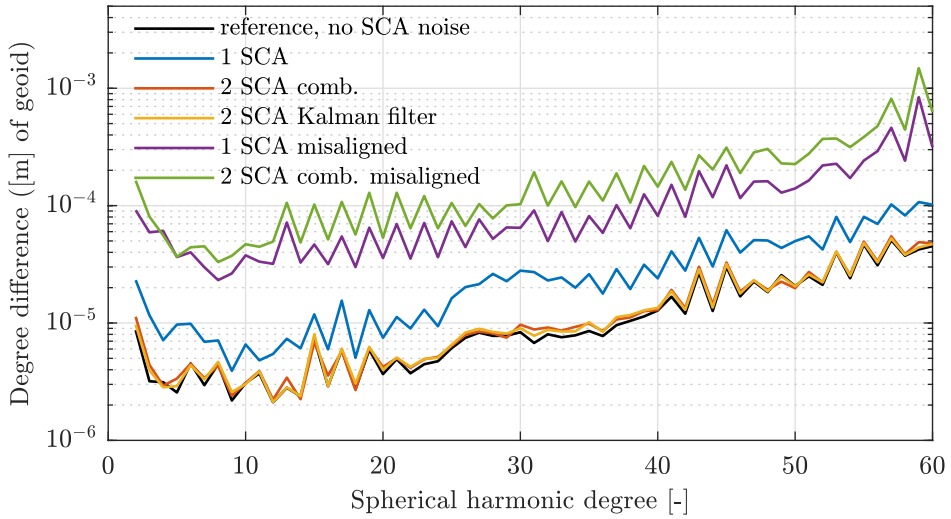

Figure 8.41: Degree difference for different SCA setups with respect to the true gravity field. No ACC noise and no calibration is estimated, 6h arc length, KBR noise level $\sigma_{hf,KBR}$ = 1e-6 m.

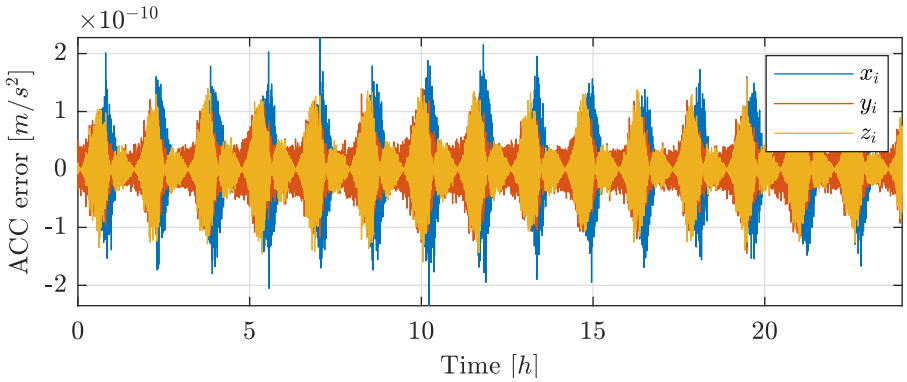

Figure 8.42: Accelerometer error due to SCA model for using just one star camera in inertial frame.

transform the measured ACC data from the actual satellite body frame to the inertial ECI frame).

The gravitational field results with the two combined star camera measurements and the Kalman filter attitude solution are about the same as the reference solution. The attitude error is too small and vanishes in the other noise sources. The result when using just one star camera distinctly deviates from that. Introducing the star camera misalignment drastically decreases the GFR solution quality. Even though the random attitude noise is not much higher than for the one star camera solution (cf. Fig. 6.35 and 6.38), the constant offset has a big influence on the gravitational field. The solution using two misaligned star cameras is even worse.

It is interesting to have a look at the acceleration error due to the attitude error. In Figure 8.42 the ACC error when using just one star camera is shown for one exemplary day. The oscillation is resulting from the time dependent non-gravitational accelerations, which have this frequency (eg. Fig. 6.16). Comparing this error to the results from the high frequency ACC noise model (Fig. 8.23), the error is in a range starting to affect the GFR solutions.

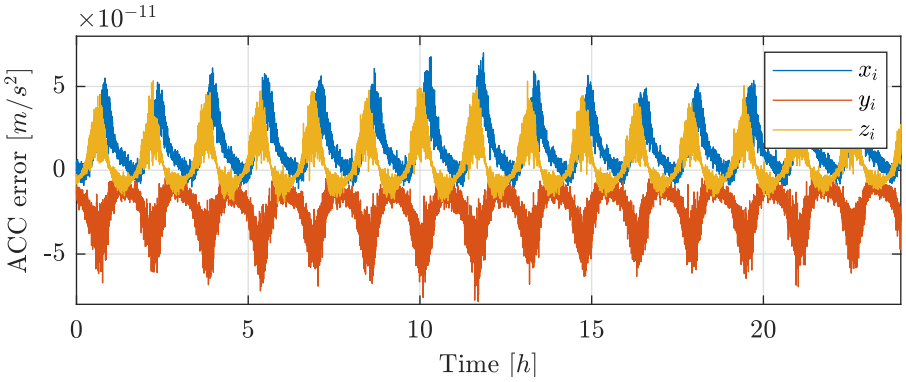

Figure 8.43: Accelerometer error due to SCA model for two combined star cameras with misalignment in inertial frame.

For the attitude solution based on two misaligned star cameras, the ACC error is depicted in Figure 8.43. Surprisingly the magnitude is lower than for the case with just one star camera without misalignment. But due to the constant attitude offset the ACC error does not have a zero mean. This has obviously a big influence on the resulting gravitational field.

Concluding it can be said, that a star camera misalignment should definitely be avoided by calibration in the processing of the attitude solution. Furthermore it could be worth estimating attitude parameters in a GFR and or POD solution for real GRACE data, which is already done in the latest TU Graz GRACE solutions (Ellmer, 2018).

The random star camera error of two combined instruments is so small that it has no influence on the GFR solutions with the used KBR and GNV models. If also considering the investigated accelerometer models, the SCA noise and its effects on the solutions are negligible, even more.

8.8 Thruster

The thruster model is mainly an additional accelerometer model. The firings of the imperfect thusters exert a small force on the satellites, usually in all directions. These are measured by the accelerometers and produce sharp peaks in the accelerometer data. Furthermore, in the L1B processing the accelerometer data are filtered and down-sampled, widening these peaks. For details see Chapter 6.3.6.

In the following the effect of the thruster peaks in the accelerometer data in general, the filtering of the ACC data and an assumed error in sensing the peaks by the accelerometer is investigated for the GFR.

As for the investigation of the SCA noise, no other ACC noise model is applied, thus the influence of the thruster spikes can be observed, separately. The KBR noise level $\sigma_{hf,KBR}$ = 1e-6 m is utilized with 6h arc length and no calibration is estimated.

GFR results for the different thruster effects are shown in Figure 8.44 in terms of degree difference with respect to the true gravitational field. The reference solution with no ACC noise and thruster disturbances demonstrates the best possible solution, limited by the applied KBR and GNV noise.

Adding the peak shaped disturbances in the accelerometer data (blue) already worsen the solution. Even though there is no difference in the forward integration of the simulated

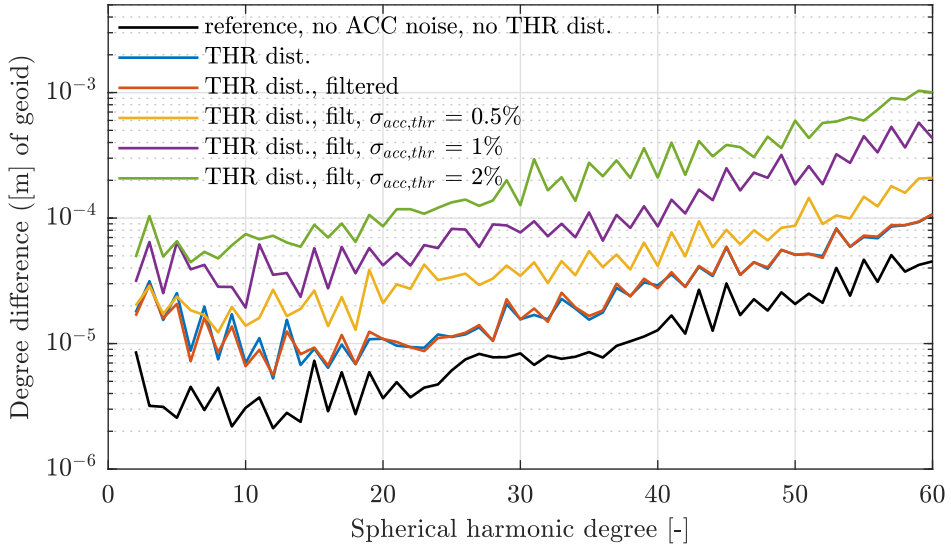

Figure 8.44: Degree difference for different thruster disturbances in the ACC data with respect to the true gravitational field. No further ACC noise model and no calibration is considered, KBR noise level $\sigma_{hf,KBR}$ = 1e-6 m, 6h arc length.

measurement data and the GFR integration, the peaks influence the performance of the estimation process.

The applied CRN-filter in the L1B processing, widening the peaks (cf. Fig. 6.39 and 6.40), has more or less no influence on the solution (red). The blurring of the acceleration on this short time scale, by preserving the magnitude of the total impulse, does not influence the GFR solution. The situation is completely different when an error for sensing the peaks is assumed. For an error of around 0.5% ($\sigma_{acc,thr} = 0.005$) a distinct decrease of the solution is visible (yellow). For 1% and 2% it is even stronger (purple and green). From this results it seems not realistic that the GRACE accelerometers exhibit an error in the dimension of 2% in sensing the thruster impulses. The electrostatic accelerometer test mass controller is fast and may be strong enough to sense these impulses without a significant loss of accuracy. Nevertheless, it is hard to assess this from the available L1B data.

CONCLUSIONS 9

This work dealt with the topic of satellite gravimetry, with the focus on the GRACE concept of low-low Satellite-to-Satellite Tracking (ll-SST). The foundations and the theory of Gravity Field Recovery (GFR) and Precise Orbit Determination (POD), as well as the full satellite simulation and orbit propagation, were elaborated in detail.

In the main part, the data processing in general and the correlations of the different instruments, measurement data and processing choices were investigated and discussed. First this was conducted for the GRACE data processing. Subsequently the investigation was extended to the processing of simulated data of a GRACE-like ll-SST mission. This closed loop simulation approach allowed the investigation of the influence of each single sensor, measurement data, noise model and processing choice, separately, with the truth always as reference. Both results were compared. Furthermore, the GRACE results were compared to solutions from other processing centers.

The work demonstrated the possibilities of a simulation approach to assess and quantify how various effects and instrument characteristics influence the overall mission goal and collected data. A dedicated modeling is a mighty tool to understand correlations in dynamics, processing and data evaluation. The assessment of interactions is often not directly possible when just dealing with real data, especially for a complicated mission with many coupled effects influencing the mission goal like in satellite gravimetry.

Hereafter, this thesis is summarized and the main scientific findings and prominent results are emphasized, mainly following the structure of the thesis. Finally future expansions and applications of the work will be discussed in the Outlook 9.2.

9.1 Summary

In the first four chapters of this thesis the topic of satellite gravimetry was motivated, introduced and the mathematical process from satellite observations to monthly gravitational field solutions was derived and discussed in detail.

After the introduction (Ch. 1), giving a through background of satellite gravimetry and the achievements of the most recent and current missions, the fundamentals of spaceflight mechanics and especially of the gravitational theory, as applied in geodesy, were presented in Chapter 2. The different representations of the gravitational and gravity field were derived and exemplary presented. Being the main focus of this thesis, the GRACE mission, its measurement principles and its instrumentation were elaborated in Chapter 3. The available science data from GRACE were introduced and some inconsistencies highlighted, which need to be considered in the GFR processing.

The theory of dynamic POD and GFR in terms of the classical, variational-equation approach was described and derived in detail in Chapter 4. The parallelization and combination of different observations with different accuracies was emphasized, as both are indispensable for GRACE GFR processing. Also the automatic weighting scheme

by Variance Component Estimation (VCE) was elaborated in this sense. The intention of this rather comprehensive chapter is also to serve as a theoretical reference for the implemented GFR and POD software.

In Chapter 5, dealing with the simulation background, first the implemented numerical integration, substantial for GFR and POD and of cause for the satellite simulation, was evaluated. Different explicit integration methods and options were compared with the use of an arbitrary precision arithmetic implementation of the code. On the one hand side this allowed to assess the general limitations of the usually used double data type for orbit propagation, as well as to assess the accuracy of the solutions and the efficiency of the numerical integrators. The ABM multistep integrator performed best in terms of overall achievable precision and by far in terms of efficiency.

Subsequently the developed non-gravitational force modeling was described in detail. As for Chapter 4, the thorough description of the models aims to serve as a reference for the generic implementation of the models in the software, which is applicable to all kind of satellites and missions.

The simulation of a GRACE-like gravimetry mission was described in Chapter 6. At first, the focus was on the validation of the utilized non-gravitational force models for the GRACE mission. These are indispensable for the generation of simulated accelerometer data, but furthermore, were used for the validation of the GRACE accelerometer data and its calibration. The comparison of modeled and measured non-gravitational accelerations showed a very good accordance for the cross-track and radial directions, which are barely affected by atmospheric drag. The along-track direction exhibit bigger differences, mainly due to deficiencies in the thermosperic density modeling.

Secondly, an attitude control scheme for the simulated GRACE satellites was implemented considering magnetic torquer and attitude thruster actuator models. Comparable characteristics to the GRACE data were obtained. An optimized attitude control scheme for GRACE-FO or future Next-Generation-Gravity-Missions (NGGM) was developed as well, but not explicitly used in this thesis.

For the generation of simulated measurement data, equivalent to GRACE L1B data, models of the instruments were introduced in the third part of the chapter. Different models for the KBR and ACC sensors were introduced to investigate the sensitivity of different noise characteristics on the GFR processing and solutions. The influence of the thruster firings on the accelerometers were modeled with the data from the simulated attitude control. Furthermore, different methods of generating the satellite's attitude solution (SCA) from the erroneous star camera observations were analyzed.

In Chapter 7, finally the GRACE GFR processing was investigated. The investigation revealed a high sensitivity of the solutions towards the weighting and parametrization, especially to the arc length and accelerometer calibration parameters. The partly contradictory parameter choices are also dependent on the epoch and the results differ for different months. Especially for the months with worse data quality, a relatively high weighting of the KBR inter-satellite range-rate observations was mandatory to obtain reasonable results. The automatic VCE weighting approach did not work well for the real data processing because the orbit solution, in terms of GNV or KOS 3d-positions, was relatively weighted too strong. This problem had be encountered before by other processing centers, for instance at CSR. Nevertheless, the relative weighting of $\sigma_g = 0.02$ m and σ_k = 1e-8 m/s for GNV and KBR observations, respectively turned out to

be optimal for nearly all investigated epochs. The analysis of the post-fit deviations and residuals showed that the changing data quality over time would benefit from an additional arc-wise weighting of the observation data.

The aforementioned and utilized optimal weighting resulted in the best overall gravitational field solutions. Nevertheless, the detailed analysis of the accelerometer calibration revealed that the co-estimated accelerometer calibration is far from being best for this weighting and parametrization. Anyway, the physically completely unrealistic calibration resulted in the best overall gravitational field solutions, leading to the second crucial processing choice, the parametrization. For all cases a bias plus drift calibration was found to be advantageous compared to just bias calibration. Together with the rather short arc lengths between 2 to 3 hours, the best results in terms of gravitational field were obtained. The resulting high errors of the calibrated non-gravitational accelerations were found not to influence the resulting gravitational field much, especially not the higher degrees, as long as the mean error was small and the frequency, hence the arc length, was not too small.

These effects could be verified with the closed loop GFR simulation approach, where the true values for all data are always known as reference. Together with the analysis of the range-rate deviations, it was shown that the solutions are especially sensitive to higher non-gravitational acceleration errors in a mid frequency range between around 10^{-3} to 10^{-5} Hz. The lower frequency errors or noise is mainly affecting the lower degrees of the gravitational field solutions.

The estimated calibration was compared for the whole year 2006 with the calibration based on the precise non-gravitational force modeling and the calibration from POD, as used for the data pre-processing. Besides the high variations between the different arcs, the median filtered long term trend of the GFR calibration showed a distinct deviation from the other two calibrations, which are much closer together. The POD calibration accords very well with the references investigated in Wöske et al. (2019).

The processing of the GRACE data over one year revealed that the KBR and GNV deviations or residuals exhibited some longer time scale trends, which lead to the conclusion that the data quality of the observations is varying. The May 2006 solution, with the best quality, showed especially smooth GNV deviations, while for the slightly worse months, clearly a trend in the GNV deviations was visible. This might be an indication for the reason of different solution qualities for the different months. Furthermore it demonstrated that an automatic, arc dependent weighting might be advantageous.

No significant difference could be detected in the solutions when using the dynamic orbit solution (GNV), given with the L1B data, or a kinematic orbit solution (KOS), where the available TU Graz solution was utilized.

It was found that a crucial step to obtain reasonable results for most of the months is a pre-processing of the KBR data. After gaps in the data, the instrument might exhibit a phase shift and the measurement time series is not continuous. Furthermore, after these jumps the data quality may be drastically worsen for up to one day. These jumps are not detectable in the data itself because the overall variation is orders of magnitude bigger. Also in the post-fit deviations or residuals of the GFR it is not detectable, because the estimated gravitational field and parameters are estimated towards the erroneous data. With the POD for both satellites simultaneously, including the KBR measurement as observation, reveals these jumps and the high errors in the KBR residuals. This detection and the subsequent rejection of the affected arcs was a crucial requirement to obtain

reasonable results for most months and hence the annual hydrological gravitational signal. This problem demonstrates the benefit of an arc dependent weighting approach, as well.

The precise non-gravitational force modeling was also utilized for GRACE GFR processing instead of using the measured accelerometer data to validate its capabilities. The results were about one order of magnitude worse than the reference solutions with the accelerometer measurements. The reasons were identified to be the drag modeling, where the thermospheric density is uncertain and the applied drag model is not detailed enough. Furthermore, the sensed disturbances due to the attitude thruster firings, which are detected by the accelerometer, but not included in the modeled non-gravitational accelerations were identified to be crucial. The simulation analysis illuminated the immense effect of erroneous thruster peaks for the GFR processing.

The analysis of the closed loop GFR simulation was presented in Chapter 8. First, the general GFR processing options, mainly weighting and parametrization, as done for the GRACE data processing, were analyzed. Subsequently the sensitivity of the GFR solutions to the different sensors, observations and noise models was investigated.

In contrast to the GRACE data, the automatic VCE weighting approach turned out to work perfectly. Actually the VCE solution was always among the best, independent of all processing choices and sensor models. This raised the question why it did not work for the GRACE processing. It was concluded that most probably the changing data quality over time and outliers in the KBR data are crucial and would need to be considered. Furthermore, the effect of the non white noise of the GNV data is estimated too small and its weighting would need to be decreased manually.

The analysis demonstrated that the weighting of the KBR range-rate is a combined measure of the KBR and ACC data accuracy, as both measurements couple in the range-rate residuals. Therefore the optimal weighting is dependent on both measurement accuracies and hence also on the ACC calibration. Thus the applied accelerometer noise models influence the optimal weighting, as well.

Accelerometer noise models with different noise characteristics in the lower frequency band and high frequency noise were investigated. Therefore, models from the literature and adapted models were considered. With the comparisons of investigations without accelerometer noise and different calibrations, it was found, that the high frequency noise is not that much the limiting factor for the GFR solutions as the mid frequency noise. While the very low noise frequencies are not that decisive for the higher gravitational field degrees, and the low frequency noise may be compensated by an appropriate calibration strategy, it is hard to cancel out the mid frequency noise by calibration. This frequency band contains main parts of the significant gravitational signal and thus is limiting the obtainable precision, decisively.

The known sensitivity of the GFR solutions towards the three accelerometer axes could be confirmed by the simulation. The GFR solution is much more sensitive to the along-track and radial axes than to the cross-track axis, where a much higher noise level could be tolerated. Furthermore, errors in the accelerometer scale factor were found to strongly affect the GFR solutions, as well. This confirms the findings from the GRACE processing, where predefined constant values were used. Thus, this encourages the development of a stable estimation approach of accelerometer scale factors.

The lower degrees of the gravitational field and the accelerometer calibration are highly dependent on the precision of the orbit solution in form of GNV or KOS observation data. The analysis with different GNV noise levels revealed a distinctly improved accelerometer calibration with decreased GNV noise, but which did not have a strong influence on the higher degrees of the estimated gravitational field, as also mentioned before. The very low degree coefficients profit from an increased GNV measurement accuracy.

The attitude solution (SCA), mainly based on the star cameras, is needed to relate the accelerometer measurement to the inertial frame. Different methods to obtain the SCA solution based on a model of the star camera noise characteristic were investigated. It was found, that GFR solutions using SCA data based on the combination of the two star cameras were barely affected by the characteristic star camera error. However, the use of the data from just one star camera had a negative effect on the GFR solution. The introduction of a small star camera misalignment completely changed that picture and the GFR solution was significantly worsened by about an order of magnitude. Thus a proper calibration in the L1B SCA processing is crucial.

9.2 Outlook

As the aim of the the presented work was twofold, split into the GRACE GFR processing and the closed loop GFR simulation, its applications and future expansions are so, as well.

Beginning with the GRACE processing, the analysis has shown that the data quality of GNV and KBR data varies over the time, causing some problems in the current processing and may be limiting the overall precision for some months. Therefore an additional arc wise weighting, using the VCE approach, could be additionally implemented. Furthermore, the local estimation of accelerometer calibration parameters could be enhanced by a condition that the beginning and end points of adjacent arcs need to coincide. This would require that the accelerometer calibration is partly a global estimation parameter, but which would not be a general problem in the implemented framework. The consideration of the KBR range-rate noise characteristic could be considered in the processing in terms of an observation covariance analysis, resulting in a complete weighting matrix.

The results concerning the GFR sensitivity with respect to different senors and processing choices may be used for the improvement of the existing GFR processing strategies, but furthermore for the development of new concepts. Leading to the most prominent application of the GFR simulation: Studies for future gravimetry missions, referred to NGGM, which we already began (eg. Punke, 2019; Wöske and Rievers, 2021). After the GRACE-FO mission no definite plan exists how to continue the gravimetric time series of Earth observation, yet. The closed loop simulation offers the possibility to assess new ideas and measurement concepts to mitigate the problems of the GRACE concept, which were also demonstrated in this thesis. These studies do not necessarily need to aim for a short term implementation, as the main research focus is on right now, but may also guide the path for future developments. With the upcoming development of quantum technologies and the ongoing progress in laser technology and instrument development, like already flight proven instruments on GRACE-FO (Abich et al., 2019) and LISA Pathfinder (Armano et al., 2018), improved instruments for gravimetry are

feasible. To exploit their full potential, optimized mission scenarios with respect to these sensor characteristics, as well as processing and modeling strategies need to be investigated. Furthermore, in regard of recent developments in the satellite sector, this may also include applications with swarms of much smaller satellites or the combination and joint use of data from commercial satellites, which may also carry some additional sensors for gravimetry. This is partly anticipated in the new Collaborative Research Center (CRC) "TerraQ - Relativistic and Quantum-Based Geodesy" where the developed software and tools, as well as the gained expertise of this work will be applied.

Although the simulation approach is already quite realistic, some aspects could be included in the future. First, this would be a model of the non-tidal time varying gravitational signals due to hydrology, ice, and solid Earth (usually referred to as HIS). Furthermore, an error in the applied background models could be implemented in the GFR processing to model the effect that the applied models are not perfect. Especially the ocean tide model is a source of dealiasing errors in the GRACE processing.

The analysis of the GRACE GFR showed that the post-fit GNV and KOS deviations were not exactly white noise, but contained some periodic signal. This might be incorporated in a more realistic noise model of an orbit solution. Maybe these improvements could more clearly verify why the VCE approach did not work as good for the real GRACE processing.

Finally, two applications of the high precision non-gravitational force modeling shall be given. By the subtraction of modeled non-gravitational accelerations from accelerometer data, except atmospheric drag, conclusions on the roughly known thermosperic density can be drawn to enhance respective models. This idea is nearly as old as the GRACE mission and improved since then. It will benefit from the more exact non-gravitational force modeling and insights into the accelerometer calibration in this thesis.

A further utilization is with respect to GRACE-FO. The accelerometer on one satellite was damaged and the crucial ACC data are currently estimated by a transplant from the other satellite's accelerometer. With a model based approach, including the working accelerometer to calibrate the drag model and maybe a few other parameters, the artificial ACC data might be improved. As discussed before, the consideration of thruster spikes is crucial for such an approach, but this holds for the current transplant method, too.

BIBLIOGRAPHY

Abich, K., Abramovici, A., Amparan, B., Baatzsch, A., Okihiro, B. B., Barr, D. C., Bize, M. P., Bogan, C., Braxmaier, C., Burke, M. J., Clark, K. C., Dahl, C., Dahl, K., Danzmann, K., Davis, M. A., de Vine, G., Dickson, J. A., Dubovitsky, S., Eckardt, A., Ester, T., Barranco, G. F., Flatscher, R., Flechtner, F., Folkner, W. M., Francis, S., Gilbert, M. S., Gilles, F., Gohlke, M., Grossard, N., Guenther, B., Hager, P., Hauden, J., Heine, F., Heinzel, G., Herding, M., Hinz, M., Howell, J., and et. al. In-orbit performance of the GRACE Follow-On laser ranging interferometer. *Phys. Rev. Lett.*, 123:031101, 2019. doi: 10.1103/PhysRevLett.123.031101.

Aristoff, J. and Poore, A. Implicit Runge-Kutta methods for orbit propagation. *AIAA/AAS Astrodynamics Specialist Conference*, 2012.

Armano, M., Audley, H., Baird, J., Binetruy, P., Born, M., Bortoluzzi, D., Castelli, E., Cavalleri, A., Cesarini, A., Cruise, A. M., Danzmann, K., de Deus Silva, M., Diepholz, I., Dixon, G., Dolesi, R., Ferraioli, L., Ferroni, V., Fitzsimons, E. D., Freschi, M., Gesa, L., Gibert, F., Giardini, D., Giusteri, R., Grimani, C., Grzymisch, J., Harrison, I., Heinzel, G., Hewitson, M., Hollington, D., Hoyland, D., Hueller, M., and et. al. Beyond the required LISA free-fall performance: New LISA Pathfinder results down to 20 μHz. *Phys. Rev. Lett.*, 120:061101, 2018. doi: 10.1103/PhysRevLett.120.061101.

Baldesarra, M., Brieden, P., Danzmann, K., Daras, I., Doll, B., Feili, D., Flechtner, F., Flury, J., Gruber, T., Heinzel, G., Iran Pour, S., Kusche, J., Langemann, M., Lücher, A., Müller, J., Müller, V., Murböck, M., Naeimi, M., Pail, R., Raimondo, J., Reiche, J., Reubelt, T., Sheard, B., Sneeuw, N., and Wang, X. *e2.motion - Earth System Mass Transport Mission (Square) - Concept for a Next Generation Gravity Field Mission - Final Report of Project "Satellite Gravimetry of the Next Generation (NGGM-D)"*, volume 318 of *DGK, Reihe B*. Verlag der Bayerischen Akademie der Wissenschaften in Kommission beim Verlag C. H. Beck, München, 2014. ISBN 978-3-7696-8597-8.

Bandikova, T., McCullough, C., Kruizinga, G., Save, H., and Christophe, B. GRACE accelerometer data transplant. *ASR*, 64:623–644, 2019. doi: https://doi.org/10.1016/j.asr.2019.05.021.

Barthelmes, F. Definition of functionals of the geopotential and their calculation from spherical harmonic models: Theory and formulas used by the calculation service of the International Centre for Global Earth Models (ICGEM). Scientific technical report STR09/02, revised edition, GeoForschungsZentrum (GFZ), Potsdam, 2013. URL http://icgem.gfz-potsdam.de/theory.

Berry, M. *A Variable-Step Double-Integration Multi-Step Integrator*. PhD thesis, Virginia Polytechnic Institute, State University, 2004.

Bettadpur, S. GRACE technical note 2: Recommendation for a-priori bias & scale parameters for level-1B ACC data (Version 2). Technical report, Center for Space Research, University of Texas, Austin, 2009.

Bettadpur, S. GRACE UTCSR Level-2 processing standards document (for level-2 product release 0005, report no. 327-742). Technical report, Center for Space Research, University of Texas, Austin, 2012a. URL ftp://isdcftp.gfz-potsdam.de/grace/DOCUMENTS/Level-2.

Bettadpur, S. GRACE product specification document. Technical report, Center for Space Research, University of Texas, Austin, 2012b. URL ftp://podaac.jpl.nasa.gov/allData/grace/docs/ProdSpecDoc_v4.6.pdf.

Bettadpur, S. UTCSR Level-2 processing standards document (the interplanetary network progress report no. 327-742). Technical report, Center for Space Research, University of Texas, Austin, 2018. URL ftp://isdcftp.gfz-potsdam.de/grace/DOCUMENTS/Level-2.

Beutler, G., Jäggi, A., Mervart, L., and Meyer, U. The celestial mechanics approach: Theoretical foundations. *Journal of Geodesy*, 84:605–624, 2010.

Bezděk, A. Calibration of accelerometers aboard GRACE satellites by comparison with POD-based nongravitational accelerations. *Journal of Geodynamics*, 50:410 – 423, 2010. doi: 10.1016/j.jog.2010.05.001.

Biancale, R. and Bode, A. Mean annual and seasonal atmospheric tide models based on 3-hourly and 6-hourly ECMWF surface pressure data. Issn 1610-0956, GeoForschungsZentrum (GFZ), Potsdam, 2006.

Bowman, B. R., Tobiska, W. K., Marcos, F. A., Huang, C. Y., Lin, C. S., and Burke, W. J. A new empirical thermospheric density model JB2008 using new solar and geomagnetic indices. In *AIAA/AAS Astrodynamics Specialists Conference*, number 2008-6438, 2008.

Bremer, S. *Entwicklung von Simulations- und Analysemethoden zur Modellierung von Störkräften im Rahmen der Satellitenmission MICROSCOPE*. PhD thesis, University of Bremen, Bremen, Germany, 2018.

Bremer, S., List, M., and Pelivan, I. HPS design document. Technical report, Zentrum für Angewandte Raumfahrttechnik und Mikrogravitation (ZARM), Bremen, Germany, 2013.

Brockmann, J., Zehentner, N., Höck, E., Pail, R., Loth, I., Mayer-Gürr, T., and Schuh, W.-D. EGM TIM RL05: An independent geoid with centimeter accuracy purely based on the GOCE mission. *Geophys. Res. Lett.*, 41:8089–8099, 2014. doi: 10.1002/2014GL061904.

Calabia, A., Jin, S., and Tenzer, R. A new GPS-based calibration of GRACE accelerometers using the arc-to-chord threshold uncovered sinusoidal disturbing signal. *Aerospace Science and Technology*, 45:265 – 271, 2015. ISSN 1270-9638. doi: https://doi.org/10.1016/j.ast.2015.05.013.

Caron, L., Ivins, E., Larour, E., Adhikari, S., Nilsson, J., and Blewitt, G. GIA model statistics for GRACE hydrology, cryosphere, and ocean science. *Geophys. Res. Lett.*, 45:2203 – 2212, 2018. doi: https://doi.org/10.1002/2017GL076644.

Case, K., Kruizinga, G., and Wu, S.-C. GRACE level 1B data product user handbook. JPL D-22027, Jet Propulsion Laboratory, 2010. URL ftp://podaac.jpl.nasa.gov/allData/grace/docs/Handbook_1B_v1.3.pdf.

Dahle, C., Flechtner, F., Murböck, M., Michalak, G., Neumayer, H., Abrykosov, O., and Knig, R. GRACE GFZ level-2 processing standards document for level-2 product release 06 (Tech. Rep. No. 327-743). Technical report, GFZ German Research Centre for Geosciences, Potsdam, 2018. URL ftp://isdcftp.gfz-potsdam.de/grace/DOCUMENTS/Level-2.

Daras, I. and Pail, R. Treatment of temporal aliasing effects in the context of next generation satellite gravimetry missions. *J. Geophys. Res. Solid Earth*, 122:7343–7362, 2017. doi: 10.1002/2017JB014250.

Darbeheshti, N., Wegener, H., Müller, V., Naeimi, M., Heinzel, G., and Hewitson, M. Instrument data simulations for GRACE Follow-On: Observation and noise models. *Earth System Science Data*, 9:833–848, 2017. doi: 10.5194/essd-2017-45.

Darbeheshti, N., Wöske, F., Weigelt, M., Mccullough, C., and Wu, H. GRACETOOLS-GRACE gravity field recovery tools. *geosciences*, 8:350, 2018. doi: 10.3390/geosciences80900350.

Darbeheshti, N., Wöske, F., Weigelt, M., Wu, H., and Mccullough, C. *Comparison of Spacewise and Timewise Methods for GRACE Gravity Field Recovery*, pages 279–315. Springer Geophysics: Geodetic Time Series Analysis in Earth Sciences. Springer Nature, Cham, Switzerland, 2020. doi: 10.1007/978-3-030-21718-1.

Desai, S. Observing the pole tide with satellite altimetry. *J. Geophys. Res.*, 107(C11): 7–1–7–13, 2002. doi: https://doi.org/10.1029/2001JC001224.

Dicati, R. *Satellite Geodesy*, pages 27–57. Stamping the Earth from Space. Springer International Publishing, Cham, Switzerland, 2017. doi: 10.1007/978-3-319-20756-8_2.

Dobslaw, H., Flechtner, F., Bergmann-Wolf, I., Dahle, C., Dill, R., Esselborn, S., Sasgen, I., and Thomas, M. Simulating high-frequency atmosphere-ocean mass variability for dealiasing of satellite gravity observations: AOD1B RL05. *J. Geophys. Res. Oceans*, 118:3704–3711, 2013. doi: https://doi.org/10.1002/jgrc.20271.

Doelling, D., Sun, M., Nguyen, L., Nordeen, M., Haney, C., Keyes, D., and Mlynczak, P. Advances in geostationary-derived longwave fluxes for the CERES synoptic (SYN1deg) product. *Journal of Atmospheric and Oceanic Technology*, 33(3):503–521, 2016. doi: 10.1175/JTECH-D-15-0147.1.

Doornbos, E. *Thermospheric Density and Wind Determination from Satellite Dynamics*. PhD thesis, TU Delft, Delft, The Netherlands, 2011.

Doornbos, E., Klinkrad, H., and Visser, P. Atmospheric density calibration using satellite drag observations. *Advances in Space Research*, 36:515–521, 2005.

Doornbos, E., Den Ijssel, J., Lühr H., M., Förster, and Koppenwallner, G. Neutral density and crosswind determination from arbitrarily oriented multiaxis accelerometers on satellites. *J Spacecr Rockets*, 47(4):580–589, 2010. doi: https://doi.org/10.2514/1.48114.

Dormand, M. and Prince, R. A family of embedded Runge-Kutta formulae. *Journal of Computational and Applied Mathematics*, 6:19–26, 1980.

Drinkwater, M., Floberghagen, R., Haagmans, R., Muzi, D., and Popescu, A. *GOCE: ESA's first Earth Explorer Core mission. In Earth Gravity Field from Space - from Sensors to Earth Sciences*, volume 18 of *Space Sciences Series of ISSI*. Kluwer Academic Publishers, Dordrecht, Netherlands, 2003. ISBN 1-4020-1408-2.

Ellmer, M. *Contributions to GRACE Gravity Field Recovery: Improvements in Dynamic Orbit Integration, Stochastic Modelling of the Antenna Offset Correction, and Co-Estimation of Satellite Orientations*. PhD thesis, Graz University of Technology; Institude of Geodesy, Graz, Austria, 2018.

Elsaka, B., Raimondo, J.-C., Brieden, P., Reubelt, T., Kusche, J., Flechtner, F., Iran Pour, S., Sneeuw, N., and Müller, J. Comparing seven candidate mission configurations for temporal gravity field retrieval through full-scale numerical simulation. *J. Geod.*, 88:31–43, 2014. doi: 10.1007/s00190-013-0665-9.

Famiglietti, J., Lo, M., Ho, S., Bethune, J., Anderson, K., Syed, T., Swenson, S., de Linage, C., and Rodell, M. Satellites measure recent rates of groundwater depletion in California's central valley. *Geophys. Res. Lett.*, 38, 2011. doi: 10.1029/2010GL046442.

Fehlberg, E. Classical fifth-, sixth-, seventh-, and eight-order Runge-Kutta formulas with step-size control. Technical report, NASA-TR-R-287, NASA Marshall Space Flight Center, Huntsville, Alabama, 1968.

Feng, W. and Zhong, M. Global sea level variations from altimetry, grace and argo data over 2005–2014. *Geodesy and Geodynamics*, 6:274–279, 2015. doi: https://doi.org/10.5194/essd-10-1551-2018.

Finlay, C., Maus, S., Beggan, C., and the IAGA team. International geomagnetic reference field: The eleventh generation. *Geophysical Journal International*, 183: 1216–1230, 2010. doi: https://doi.org/10.1111/j.1365-246X.2010.04804.x.

Flechtner, F., Neumayer, K.-H., Dahle, C., Dobslaw, H., Fagiolini, E., Raimondo, J.-C., and Güntner, A. What can be expected from the GRACE-FO laser ranging interferometer for Earth science applications. *Surveys in Geophysics*, 37(2):453–470, 2016.

Folkner, W., Williams, J., Boggs, D., Park, R., and Kuchynk, P. The planetary and lunar ephemerides DE430 and DE431. IPN progress report 42-196, Jet Propulsion Laboratory, California (JPL), 2014.

Forsberg, R., Sørensen, L., and Simonsen, S. Greenland and antarctica ice sheet mass changes and effects on global sea level. *Surv. Geophys.*, 38:89–104, 2017. doi: 10.1007/s10712-016-9398-7.

Fousse, L., Hanrot, G., Lefevre, V., Pelissier, P., and Zimmermann, P. MPFR: A multiple-precision binary floating-point library with correct rounding. *ACM Transactions on Mathematical Software (TOMS)*, 33(2), 2007. doi: doi:10.1145/1236463.1236468.

Franklin, J. Numerical simulation of stationary and non-stationary gaussian random processes. *SIAM Review*, 7:68–80, 1965.

Gauss, C. *Bestimmung des Breitenunterschiedes zwischen den Sternwarten von Göttingen und Altona.* C. F. Gauss Werke, Band IX, 1828.

Goodyear, W. Completely general closed form solution for coordinates and partial derivatives of the two-body problem. *Astronomical Journal*, 70(3):189–192, 1965.

Gottlieb, R. Partials, normalized gravity, gravity gradient torque and magnetic field: Derivation, code and data. NASA contractor report 188243, McDonnell Douglas Space Systems - Houston Division, Houston, Texas, 1993.

Gruber, T., Baldesarra, M., Brieden, P., Danzmann, K., Daras, I., Doll, B., Feili, D., Flechtner, F., Flury, J., Heinzel, G., Iran Pour, S., Kusche, J., Langemann, M., Lücher, A., V., M. J., Müller, M. M., Naeimi, M., Pail, R., Raimondo, J. C., Reiche, J., Reubelt, T., Sheard, B., and Sneeuw, N. *e2.motion - Earth System Mass Transport Mission (Square) - Concept for a Next Generation Gravity Field Mission - Final Report of Project "Satellite Gravimetry of the Next Generation (NGGM-D)"*, volume 318 of *DGK, Reihe B.* Verlag der Bayerischen Akademie der Wissenschaften in Kommission beim Verlag C. H. Beck, München, 2014. ISBN 978-3-7696-8597-8.

Harvey, N. GRACE star camera noise. *Adv. Space Res.*, 58:408–414, 2016. doi: http://dx.doi.org/10.1016/j.asr.2016.04.025.

Hauk, M. and Pail, R. Gravity field recovery using high-precision, high–low inter-satellite links. *Remote Sensing*, 11:537, 2019. doi: doi:10.3390/rs11050537.

Hauk, M. and Wiese, D. New methods for linking science objectives to remote sensing observations: A concept study using single- and dual-pair satellite gravimetry architectures. *Earth and Space Science*, 7, 2020. doi: https://doi.org/10.1029/2019EA000922.

Heinzel, G., Rüdigerand, A., and Schilling, R. Spectrum and spectral density estimation by the Discrete Fouriertransform (DFT), including a comprehensive list of window functions and some new flat-top windows. Technical report, Max-Planck-Institut für Gravitationsphysik, Albert-Einstein-Institut (AEI), Hannover, Germany, 2002.

Herman, J., Presti, D., CodazziA., and Belle, C. Attitude control for GRACE the first low-flying satellite formation. *Proceedings of the 18th International Symposium on Space Flight Dynamics (ESA SP-548), Oct. 11-15, Munich, Germany*, 2004.

Hofmann-Wellenhof, B., Lichtenegger, H., and Wasle, E. *GNSS – Global Navigation Satellite Systems: GPS, GLONASS, Galileo, and more.* Springer Vienna, 2007. ISBN 978-211-73012-6.

Hughes, P. *Spacecraft Attitude Dynamics.* Dover Publications, Inc., Mineola, New York, 2004. ISBN 0-486-43925-9.

Ince, S., Barthelmes, F., Reißland, S., Elger, K., Förste, C., Flechtner, F., and Schuh, H. ICGEM - 15 years of successful collection and distribution of global gravitational models, associated services, and future plans. *Earth System Science Data*, 11(2): 647–674, 2019. doi: 10.5194/essd-11-647-2019.

Jäggi, A. *Pseudo-Stochastic Orbit Modeling of Low Earth Satellites Using the Global Positioning System.* PhD thesis, Astronomical Institute, University of Bern, Bern, Switzerland, 2006.

Jekeli, C. Alternative methods to smooth the Earth's gravity field. 19820014947, Ohio State University, Columbus, OH, USA, 1981. URL https://ntrs.nasa.gov/citations/19820014947.

Jekeli, C. *The Energy Balance Approach*, pages 127–160. Lecture Notes in Earth System Sciences: Global Gravity Field Modeling from Satellite-to-Satellite Tracking Data. Springer, Berlin, Germany, 2017. doi: 10.1007/978-3-319-49941-3.

Jones, B. Orbit propagation using Gauss-Legendre collocation. *AIAA/AAS Astrodynamics Specialist Conference*, 2012.

Jones, B. and Anderson, R. A survry of sympleectic and collocatation integration methods for orbit propagation. *22nd AAS/AIAA Space Flight Mechanics Meeting*, 2012.

Jäggi, A., Meyer, U., Lasser, M., Jenny, B., Lopez, T., Flechtner, F., Dahle, C., Förste, C., Mayer-Gürr, T., Kvas, A., Lemoine, S., J.-M. amd Bourgogne, Weigelt, M., and Groh, A. *International Combination Service for Time-Variable Gravity Fields (COST-G)*. International Association of Geodesy Symposia. Springer, Berlin, Heidelberg, 2020. doi: https://doi.org/10.1007/1345_2020_109.

Kabamba, P. and Girard, A. *Fundamentals of Aerospace Navigation and Guidance*. Cambridge University Press, New York, NY, USA, 2014. ISBN 978-1-107-07094-3.

Kalman, R. A new approach to linear filtering and prediction theory. *Journal of Basic Engineering*, 82(1):35–45, 1960.

Kang, Y., Tapley, B., Bettadpur, S., Ries, J., Nagel, P., and Pastor, R. Precise orbit determination for the GRACE mission using only gps data. *Journal of Geodesy*, 80: 322–331, 2006. doi: 10.1007/s00190-006-0073-5.

Kato, T. and Wöske, F. XHPS design document. Technical report, Zentrum für Angewandte Raumfahrttechnik und Mikrogravitation (ZARM), Bremen, Germany, 2017.

Kato, T., Rievers, B., and List, M. Generic computation method of free-molecular flow effects on space objects. *Trans. JSASS Aerospace Tech. Japan*, 14:105–110, 2016. doi: 10.2322/tastj.14.Pd_105.

Kaula, W. *Theory of Satellite Geodesy*. Blaisdell, Waltham, MA, 1966.

Kim, J. *A Low-Low Satellite-to-satellite Tracking Mission*. PhD thesis, University of Texas at Austin, Austin, TX, USA, 2000.

King-Hele, D. and Merson, R. Use of artificial satellites to explore the Earth's gravity field: Results from Sputnik 2. *Nature*, 182:640–641, 1958.

Klees, R., Liu, X., Wittwer, T., Gunter, B., Revtova, E., Tenzer, R., Ditmar, P., and Winsemius, H., H. Savenije. A comparison of global and regional GRACE models for land hydrology. *Surv. Geophys.*, 29:335–359, 2008. doi: 10.1007/s10712-008-9049-8.

Klinger, B. and Mayer-Gürr, T. The role of accelerometer data calibration within GRACE gravityfield recovery: Results from ITSG-Grace2016. *Advances in Space Research*, 58:1597–1609, 2016. http://dx.doi.org/10.1016/j.asr.2016.08.007.

Knocke, P., Ries, J., and Tapley, B. Earth radiation pressure effects on satellites. *American Institute of Aeronautics and Astronatutics*, 88-4292-CP, 1988. doi: 10.2514/6.1988-4292.

Koch, K. and Kusche, J. Regularization of geopotential determination from satellite data by variance components. *Journal of Geodesy*, 76(5):641–652, 2001.

Kusche, J. Approximate decorrelation and non-isotropic smoothing of time-variable GRACE-type gravity field models. *Journal of Geodesy*, 81:733–749, 2007. doi: https://doi.org/10.1007/s00190-007-0143-3.

Kusche, J. and Springer, A. *Parameter Estimation for Satellite Gravity Field Modeling*, pages 1–31. Lecture Notes in Earth System Sciences: Global Gravity Field Modeling from Satellite-to-Satellite Tracking Data. Springer, Berlin, Germany, 2017. doi: 10.1007/978-3-319-49941-3.

Kvas, A., Behzadpour, S., Ellmer, M., Klinger, B., Strasser, S., Zehentner, N., and Mayer-Gürr, T. ITSG-Grace2018: Overview and evaluation of a new GRACE-only gravity field time series. *JGR Solid Earth*, 124, 2019. doi: https://doi.org/10.1029/2019JB017415.

Landerer, F., Flechtner, F., Save, H., Webb, F., Bandikova, T., Bertiger, W., Bettadpur, S., and et. al. Extending the global mass change data record: GRACE Follow-On instrument and science data performance. *Geophys. Res. Lett.*, 47(12), 2020. doi: https://doi.org/10.1029/2020GL088306.

Lemoine, F., Kenyon, S., Factor, J., Trimmer, R., Pavlis, N., Chinn, D., Cox, C., Klosko, S., Luthcke, S., Torrence, M., Wang, Y., Williamson, R., Pavlis, E., Rapp, R., and Olson, T. The development of the joint NASA GSFC and NIMA geopotential model EGM96. Technical report, NASA Goddard Space Flight Center, Greenbelt, Maryland, 20771 USA, 1998.

Lemoine, F., Klosko, S., Chinn, D., and Cox, C. The development of NASA gravity models and their dependence on SLR. 13th International Workshop on Laser Ranging: Proceedings from the Science Session, 2002. URL https://cddis.nasa.gov/lw13/docs/papers/sci_lemoine_1m.pdf.

Lerch, F., Klosko, S., Wagner, C., and Patel, G. On the accuracy of recent Goddard gravity models. *J. Geophys. Res.*, 90(B11):9312–9334, 1985.

Li, H., Reubelt, T., Antoni, M., and Sneeuw, N. Gravity field error analysis for pendulum formations by a semi-analytical approach. *J. of Geodesy.*, 91:233–251, 2017. doi: 10.1007/s00190-016-0958-x.

List, M., Bremer, S., Rievers, B., and Selig, H. Modelling of solar radiation pressure effects: Parameter analysis for the MICROSCOPE mission. *International Journal of Aerospace Engineering*, 2015. doi: 10.1155/2015/928206. ID 928206.

Liu, X. *Global Gravity Field Recovery From Satellite-to-Satellite Tracking Data With the Acceleration Approach*. PhD thesis, Nederlandse Commissie voor Geodesie Netherlands Geodetic Commission, Delft, The Netherlands, 2008.

Loeb, N., Su, W., Doelling, D., Wong, T., Minnis, P., Thomas, S., and Miller, W. 5.03 - Earth's top-of-atmosphere radiation budget. *Comprehensive Remote Sensing*, 5: 67–84, 2018. doi: https://doi.org/10.1016/B978-0-12-409548-9.10367-7.

Mashtakov, Y., Ovchinnikova, M., Wöske, F., Rievers, B., and List, M. Attitude determination & control system design for gravity recovery missions like GRACE. *Acta Astronautica*, 173:172–182, 2020. doi: doi.org/10.1016/j.actaastro.2020.04.019.

Mayer-Gürr, T. *Gravitationsfeldbestimmung aus der Analyse kurzer Bahnbögen am Beispiel der Satellitenmissionen CHAMP und GRACE*. PhD thesis, University Bonn, Universitäts-und Landesbibliothek Bonn, 2006.

Mayer-Gürr, T., Savcenko, R., Bosch, W., Daras, I., Flechtner, F., and Dahle, C. Ocean tides from satellite altimetry and GRACE. *Journal of Geodynamics*, 59-60:28–38, 2012. doi: https://doi.org/10.1016/j.jog.2011.10.009.

McCullough, C. *Gravity Field Estimation for Next Generation Satellite Missions*. PhD thesis, University of Texas at Austin, Austin, TX, USA, 2017.

Meyer, U., Jäggi, A., and Beutler, G. *The Impact of Attitude Control on GRACE Accelerometry and Orbits*, pages 139–146. Geodesy for Planet Earth: Proceedings of the 2009 IAG Symposium, Buenos Aires, Argentina, 31 August 31 - 4 September 2009. Springer-Verlag, Berlin, Heidelberg, Germany, 2012. doi: 10.1007/978-3-642-20338-1_17.

Mikkola, S. Non-canonical pertubations in symplectic integration. *Celestial Mechanics and Dynamical Astronomy*, 68(3):249–255, 1998.

Montenbruck, O. and Gill, E. *Satellite Orbits*. Springer, Berlin Heidelberg New York, 3rd edition, 2005. ISBN -10 3-540-67280-X.

Montenbruck, O., Steigenberger, P., and Hugentobler, U. Enhanced solar radiation pressure modeling for Galileo satellites. *Journal of Geodesy*, 89(3):283–297, 2015. doi: https://doi.org/10.1007/s00190-014-0774-0.

NASA. GRACE launch press kit. Technical report, National Aeronautics and Space Administration (NASA), 2002. URL https://www.jpl.nasa.gov/news/press_kits/gracelaunch.pdf.

Nerem, R., Lerch, F., Marshall, J., Pavlis, D., Putney, B., Tapley, B., Eanes, R., Ries, J., Schutz, B., Shum, C., Watkins, M., Klosko, S., Chan, J., Luthcke, S., Patel, G., Pavlis, N., Williamson, R., Rapp, R., Biancale, R., and Nouel, F. Gravity model development for TOPEX/POSEIDON: Joint gravity models 1 and 2. *J. Geophys. Res.*, 99:24421–24447, 1994. doi: https://doi.org/10.1029/94JC01376.

O'Keefe, J., Eckeis, A., and R., S. Vanguard measurements give pear-shaped component of Earth's figure. *Science*, 129:565–566, 1959. doi: 10.1126/science.129.3348.565.

Panet, I., Flury, J., Biancale, R., Gruber, T., Johannessen, J., van den Broeke, M. R., van Dam, T., Gegout, P., Hughes, C. W., Ramillien, G., Sasgen, I., Seoane, L., and Thomas, M. Earth system mass transport mission (e.motion): A concept for future Earth gravity field measurements from space. *Surv. Geophys.*, 2012. doi: 10.1007/s10712-012-9209-8.

Petit, G. and Luzum, B. E. IERS conventions (2010). IERS technical note 36, Frankfurt am Main: Verlag des Bundesamts für Kartographie und Geodäsie, 2010.

Philipp, D., Perlick, V., Puetzfeld, D., Hackmann, E., and Lämmerzahl, C. Definition of the relativistic geoid in terms of isochronometric surfaces. *Phys. Rev. D*, 95:104037, 2017. doi: 10.1103/PhysRevD.95.104037.

Philipp, D., Wöske, F., Biskupek, L., Hackmann, E., Mai, E., List, M., Lämmerzahl, C., and Rievers, B. Modeling approaches for precise relativistic orbits: Analytical, lie-series, and pn approximation. *Adv. Space Res.*, 62:921–934, 2018. doi: 10.1016/j.asr.2018.05.020.

Prince, R. and Dormand, J. High order embedded Runge-Kutta formulae. *Journal of Computational and Applied Mathematics*, 7:66–75, 1981.

Punke, T. Examination of next generation gravity mission concepts. Master's thesis, Zentrum für Angewandte Raumfahrttechnik und Mikrogravitation (ZARM), University of Bremen, Bremen, Germany, 2019.

Reigber, C., Balmino, G., Schwintzer, P., Biancale, R., Bode, A., Lemoine, J., König, R., Loyer, S., Neumayer, H., Marty, J., Barthelmes, F., Perosanz, F., and Yuan Zhu, S. A high-quality global gravity field model from CHAMP GPS tracking data and accelerometry (EIGEN-1S). *Geophys. Res. Lett.*, 29:37–1–37–4, 2002. doi: https://doi.org/10.1029/2002GL015064.

Ries, J., Bettadpur, S., Eanes, R., Kang, Y., Ko, U., C., M., Nagel, P., Pie, N., Poole, S., Richter, H., T. Save, and Tapley, B. The development and evaluation of the global gravity model GGM05. CSR-16-02, CSR, the university of Texas at Austin, 2016.

Rievers, B. and Lämmerzahl, C. High precision thermal modeling of complex systems with application to the flyby and Pioneer anomaly. *Annalen der Physik*, 523:439–449, 2011.

Rievers, B., Kato, T., van der Ha, J., and Lämmerzahl, C. Numerical prediction of satellite surface forces with application to Rosetta. 143:1123–1142, 2012.

Rievers, B., List, M., and Bremer, S. Advanced thermal radiation pressure modeling and its benefits for the MICROSCOPE mission. volume 158 of *Adv. Astr. Sci.*, pages 2997–3012, 2016.

Robertson, R. *Highly physical solar radiation pressure modeling during penumbra transitions.* PhD thesis, Department of Aerospace and Ocean Engineering at Virginia Polytechnic Institute and State University, Blacksburg, Virginia, 2015.

Rodell, M., Famiglietti, J., Wiese, D., Reager, J., Beaudoing, H., Landerer, F., and Lo, M.-H. Emerging trends in global freshwater availability. *Nature*, 557:651–659, 2018. doi: https://doi.org/10.1038/s41586-018-0123-1.

Rummel, R., van Gelderen, M., Koop, R., Schrama, E., Sansó, F., Brovelli, M., Migliaccio, F., and Sacerdote, F. *Spherical Harmonic Analysis of Satellite Gradiometry.* Publications on Geodesy, New Series 39. Netherlands Geodetic Commission, Delft, The Netherlands, 1998.

Sakumura, C. GRACE technical note 10: Comparison of degree 60 and degree 96 monthly solutions. CSR-GR-14-01, Center for Space Research, University of Texas, Austin, 2014.

Sakumura, C., Bettadpur, S., and Bruinsma, S. Ensemble prediction and intercomparison analysis of GRACE time-variable gravity field models. *Geophys. Res. Lett.*, 41: 1389–1397, 2014. doi: 10.1002/2013GL058632.

Sasgen, I., Wouters, B., Gardner, A., King, M., Tedesco, M., Landerer, F., Dahle, C., Save, H., and Fettweis, X. Return to rapid ice loss in Greenland and record loss in 2019 detected by the GRACE-FO satellites. *Communications Earth & Environment*, 1(8), 2020. doi: 10.1038/s43247-020-0010-1.

Savcenko, R., Bosch, W., Dettmering, D., and Seitz, F. EOT11a - global empirical ocean tide model from multi-mission satellite altimetry, with links to model results. *PANGAEA*, 2012. doi: https://doi.org/10.1594/PANGAEA.834232. Supplement to: Savcenko, R., Bosch, W. (2012): EOT11a - Empirical Ocean Tide Model from Multi-Mission Satellite Altimetry. Deutsches Geodätisches Forschungsinstitut (DGFI), München, 89, 49 pp, hdl:10013/epic.43894.d001.

Save, H. *Using regularization for error reduction in GRACE gravity estimation.* PhD thesis, University of Texas at Austin, Austin, TX, USA, 2009.

Schmid, H. How to use the FFT and Matlab's pwelch function for signal and noise simulations and measurements. Technical report, University of Applied Sciences Northwestern Switzerland, Institute of Microelectronics (FHNW, IME), 2012.

Seeber, G. *Satellite Geodesy - 2nd completely revised and extended edition.* Walter de Gruyter, Berlin, 2nd edition, 2003. ISBN 3-11-017549-5.

Sentman, L. Free molecule flow theory and its application to the determination of aerodynamic forces. Technical report, Lockheed Missile and Space Co., 1961.

Shampine, L. and Gordon, M. *Computer Solution of Ordinary Differential Equations.* W. H. Freeman and Company, San Francisco, 1975.

Sheard, B., Heinzel, G., Danzmann, K., and Shaddock, D. Intersatellite laser ranging instrument for the GRACE Follow-On mission. *J. Geod.*, 86(12):1083 – 1095, 2012. doi: 10.1007/s00190-012-0566-3.

Shepherd, A., Ivins, E., Rignot, E., and the IMBIE team. Mass balance of the Greenland ice sheet from 1992 to 2018. *Nature*, 579:233 – 239, 2020. doi: https://doi.org/10.1038/s41586-019-1855-2.

Swenson, S. and Wahr, J. Post-processing removal of correlated errors in GRACE data. *Geophys. Res. Lett.*, 33:L08402, 2006. doi: 10.1029/2005GL025285.

Swerling, P. First order error propagation in a stagewise differential smoothing procedure for satellite observations. *Journal of Astronautical Science*, 6:46–52, 1959.

Tapley, B., Ries, J., G., D., Eanes, R., Schutz, B., Shum, C., Watkins, M., Marshall, J., Nerem, R., Putney, B., Klosko, S., Luthcke, S., Pavlis, D., Williamson, R., and Zelensky, N. Precision orbit determination for TOPEX/Poseidon. *J. Geophys. Res.*, 99:24383–24404, 1994. doi: https://doi.org/10.1029/94JC01645.

Tapley, B., Watkins, M., Ries, J., Davis, G., Eanes, R., Poole, S., Rim, H., Schutz, B., Shum, C., Nerem, R., Lerch, F., Marshall, J., Klosko, S., Pavlis, N., and Williamson, R. On the accuracy of recent Goddard gravity models. *J. Geophys. Res.*, 101: 28029–28049, 1996. doi: 10.1029/96JB01645.

Tapley, B., Bettadpur, S., Watkins, M., and Reigber, C. The gravity recovery and climate experiment: Mission overview and early results. *Geophys. Res. Lett.*, 31: L09607, 2004a. doi: http://dx.doi.org/10.1029/2004GL019920.

Tapley, B., Schutz, B., and Born, G. *Statistical Orbit Determination*. Elsevier Academic Press, Berlin, Heidelberg, 2004b. ISBN 0-12-683630-2.

Tapley, B., Ries, J., Bettadpur, S., and Cheng, M. Neutral density measurements from the gravity recovery and climate experiment accelerometers. *J. Spacecr. Rockets*, 44: 1220–1225, 2007. doi: https://doi.org/10.2514/1.28843.

Tapley, B., Watkins, M., Flechtner, F., Reigber, C., Bettadpur, S., Rodell, M., Sasgen, I., Famiglietti, J., Landerer, F., Chambers, P., Reager, J., Gardner, A., Save, H., Ivins, E., Swenson, S., Boening, C., Dahle, C., Wiese, D., Dobslaw, H., Tamisiea, M., and Velicogna, I. Contributions of GRACE to understanding climate change. *Nature Climate Change*, 9:358 – 369, 2019. doi: 10.1038/s41558-019-0456-2.

Theil, S. *Satellite and Test Mass Dynamics Modeling and Observation for Drag-free Satellite Control of the STEP Mission*. PhD thesis, University of Bremen, Bremen, Germany, 2002.

Torge, W. and Müller, J. *Geodesy*. Walter de Gruyter, Berlin/Boston, 4th edition, 2012. ISBN 978-3-11-020718-7.

Touboul, P., Willemont, E., Foulon, B., and Josselin, V. Accelerometers for CHAMP, GRACE and GOCE space missions: Synergy and evolution. *Bollettino di Geofisica ed applicata*, 40(3-4):321–327, 1999.

Touboul, P., Foulon, B., Rodrigues, M., and Marque, J. In orbit nano-g measurements, lessons for future space missions. *Aerospace Science and Technology*, 8:431–441, 2004. doi: http://dx.doi.org/10.1016/j.ast.2004.01.006.

Uebbing, B., Kusche, J., Rietbroek, R., and Landerer, F. Processing choices affect ocean mass estimates from GRACE. *JGR Oceans*, 124:1029 – 1044, 2019. doi: https://doi.org/10.1029/2018JC014341.

Van Helleputte, T., Doornbos, E., and Visser, P. CHAMP and GRACE accelerometer calibration by GPS-based orbit determination. *Advances in Space Research*, 43: 1890–1896, 2009.

Vielberg, K. and Kusche, J. Extended forward and inverse modeling of radiation pressure accelerations for LEO satellites. *Journal of Geodesy*, 94:43(43), 2020. doi: https://doi.org/10.1007/s00190-020-01368-6.

Vielberg, K., Forootan, E., Lück, C., Löcher, A., Kusche, J., and Börger, K. Comparison of accelerometer data calibration methods used in thermospheric neutral density estimation. *Ann. Geophys.*, 36:761–779, 2018. doi: doi.org/10.5194/angeo-36-761-2018.

Visser, T., March, G., Doornbos, E., de Visser, C., and Visser, P. Horizontal and vertical thermospheric cross-wind from goce linear and angular accelerations. *Adv. Space Res.*, 63(10):3139–3153, 2019. doi: https://doi.org/10.1016/j.asr.2019.01.030.

Voss, K. A., Famiglietti, J. S., Lo, M., de Linage, C., Rodell, M., and Swenson, S. C. Groundwater depletion in the Middle East from GRACE with implications for

transboundary water management in the Tigris-Euphrates-Western Iran region. *Water Resources Research*, 49:904–914, 2013. doi: 10.1002/wrcr.20078.

Wahr, J., Molenaar, M., and Bryan, F. Time variability of the Earth's gravity field: Hydrological and oceanic effects and their possible detection using GRACE. *J. Geophysical Research*, 103:30,205–30,229, 1998.

Watkins, M., Wiese, D., Yuan, D.-N., Boening, C., and Landerer, F. Improved methods for observing Earth's time variable mass distribution with GRACE using spherical cap mascons. *JRG Solid Earth*, 120, 2015. doi: 10.1002/2014JB011547.

WCRP Global Sea Level Budget Group. Global sea-level budget 1993–present. *Earth Syst. Sci. Data*, 10:1551–1590, 2018. doi: https://doi.org/10.5194/essd-10-1551-2018.

Weigelt, M. *The Acceleration Approach*, pages 97–126. Lecture Notes in Earth System Sciences: Global Gravity Field Modeling from Satellite-to-Satellite Tracking Data. Springer, Berlin, Germany, 2017. doi: 10.1007/978-3-319-49941-3.

Weigelt, M., van Dam, T., Jäggi, A., Prange, L., Tourian, M., Keller, W., and Sneeuw, N. Time-variable gravity signal in Greenland revealed by high-lowsatellite-to-satellite tracking. *JGR Solid Earth*, 118:3848–3859, 2013. doi: 10.1002/jgrb.50283.

Weinbach, U. and Schön, S. Improved GRACE kinematic orbit determination using GPS receiver clock modeling. *GPS Sol.*, 17:511–520, 2013. doi: 10.1007/s10291-012-0297-1.

Wertz, J. *Spacecraft Attitude Determination and Control*. Kluwer Academic Publishers, Dordrecht, The Netherlands, 1978.

Wielicki, B., Barkstrom, B., Harrison, E., Lee, R., Smith, L., and Cooper, J. Clouds and the Earth's radiant energy system (CERES): An Earth observing system experiment. *Bulletin of the American Meteorological Society*, 77(5):853–868, 1996. doi: 10.1175/1520-0477(1996)077<0853:CATERE>2.0.CO;2.

Wiese, D., Landerer, F., and Watkins, M. Quantifying and reducing leakage errors in the JPL RL05M GRACE mascon solution. *Water Resour. Res.*, 52:7490–7502, 2016. doi: 10.1002/2016WR019344.

Wiese, D., Yuan, D.-N., Boening, C., Landerer, F., and Watkins, M. JPL GRACE mascon ocean, ice, and hydrology equivalent water height release 06 coastal resolution improvement (CRI) filtered version 1.0. ver. 1.0. PO.DAAC. Technical report, Jet Propulsion Laboratory (JPL), CA, USA, 2018. URL http://dx.doi.org/10.5067/TEMSC-3MJC6.

Witchayangkoon, B. *Elements of GPS precise point positioning*. PhD thesis, The University of Maine, 2000.

Wöske, F. and Rievers, B. Evaluation of pendulum NGGM scenarios by full closed-loop simulation. In *EGU General Assembly, EGU21-12257*, 2021. doi: doi.org/10.5194/egusphere-egu21-12257.

Wöske, F., Kato, T., List, M., and Rievers, B. Development of a high precision simulation tool for gravity recovery missions like GRACE. volume 158 of *Adv. Astr. Sci.*, pages 2445–2457, 2016.

Wöske, F., Kato, T., Rievers, B., and List, M. GRACE accelerometer calibration by high precision non-gravitational force modeling. *Adv. Space Res.*, 63:1318 – 1335, 2019. doi: https://doi.org/10.1016/j.asr.2018.10.025.

Wu, H. *Gravity field recovery from GOCE observations*. PhD thesis, Leibniz Universität Hannover, Hannover, Germany, 2017.

Wu, S.-C., Kruizinga, G., and Bertiger, W. Algorithm theoretical basis document for GRACE Level-1B data processing V1.2, GRACE 327-741. JPL D-27672, Jet Propulsion Laboratory, 2006.

Yuan, D. GRACE JPL level-2 processing standards document for level-2 product release 06 (Tech. Rep. No. 327-744). Technical report, Jet Propulsion Laboratory, California Institute of Technology., 2018. URL ftp://isdcftp.gfz-potsdam.de/grace/DOCUMENTS/Level-2.

Zehentner, N. and Mayer-Gürr, T. Precise orbit determination based on raw GPS measurements. *Journal of Geodesy*, 90:275–286, 2016. doi: 10.1007/s00190-015-0872-7.

APPENDIX

A

A.1 Quaternions and Rotations

The attitude of a spacecraft might be represented by quaternions, rotation matrices or Euler angles. In all cases the attitude is defined as the rotation between two reference frames. The different representations have their advantages and disadvantages but are in general equivalent and interchangeable. For space applications and in general for numeric calculations and big amount of data, quaternions are preferred. Quaternions and rotation matrices are not very intuitive or demonstrative, thus attitude is often presented in terms of Euler angles, but which has several disadvantages for computations (eg. Hughes, 2004; Wertz, 1978). In the following the basics of quaternion algebra, its application to rotations, the analogies to rotation matrices and its conversions are shortly described.

The definitions used in this thesis and in the implemented software are based on the representation in Wertz (1978), as also compendiously given in the HPS Design Document (Bremer et al., 2013). It is important to mention, that different notations of a quaternions are used in the literature and software packages.

A.1.1 Quaternion Definitions

A quaternion is generally defined as

$$\vec{q} = iq_1 + jq_2 + kq_3 + q_4, \tag{A.1}$$

where i,j and k are the hyper imaginary numbers to satisfy the conditions

$$\begin{aligned} i^2 = j^2 = k^2 &= -1 \\ ij = -ji &= k \\ jk = -kj &= i \\ ki = -ik &= j. \end{aligned} \tag{A.2}$$

The quaternion is usually expressed as a four dimensional vector, which can be separated in a vectorial and a scalar part

$$\vec{q} = \begin{bmatrix} q_1 & q_2 & q_3 & q_4 \end{bmatrix}^T = \begin{bmatrix} \underline{q} & q_4 \end{bmatrix}^T. \tag{A.3}$$

The already mentioned different notations, refer most commonly only to the position of the non-imaginary component in the vector (here denoted as q_4). It might be the first or last component of the vector, which is just a matter of convenience, but the according mathematical operations need to be adjusted to the definition.

Quaternion Conjugate

Like complex numbers, quaternions have a conjugate which is defined as

$$\vec{q}^{*} = -iq_1 - jq_2 - kq_3 + q_4 \tag{A.4}$$

with * being the conjugate operator.

Quaternion Unit Norm

For the representation of rotations unit quaternions are used. Thus, the identity needs to be always assured

$$\begin{aligned} 1 &= q_1^2 + q_2^2 + q_3^2 + q_4^2 \\ &= \underline{q}\ \underline{q}^T + q_4^2, \end{aligned} \tag{A.5}$$

Quaternion Multiplication

The general quaternion multiplication is defined as

$$\begin{aligned} \vec{q}'' &= \vec{q}\,\vec{q}' \\ &= (q_4 + iq_1 + jq_2 + kq_3)(q_4' + iq_1' + jq_2' + kq_3'). \end{aligned} \tag{A.6}$$

This can also be expressed in vector representation as

$$\begin{aligned} \underline{q}'' &= q_4\ \ \underline{q}' + q_4'\,\underline{q} + \underline{q} \times \underline{q}' \\ q_4'' &= q_4\, q_4' - \underline{q} \cdot \underline{q}', \end{aligned} \tag{A.7}$$

with $\cdot$ being the scalar product and $\times$ being the vector cross product.

A.1.2 Quaternions and Rotations

In the application of quaternions to represent rotations they are also referred to as *Euler symmetric parameters*. A rotation around an axis, defined by the unit vector $[e_1 \quad e_2 \quad e_3]^T$, with the rotation angle ϕ is linked to the quaternion $\vec{q}$ by the following definition

$$\begin{aligned} q_1 &= e_1 \sin\left(\frac{\phi}{2}\right) \\ q_2 &= e_2 \sin\left(\frac{\phi}{2}\right) \\ q_3 &= e_3 \sin\left(\frac{\phi}{2}\right) \\ q_4 &= \cos\left(\frac{\phi}{2}\right). \end{aligned} \tag{A.8}$$

For the rotation between different frames, the following notation is used. Considering two frames i and b, the transformation from frame i to b is given by the quaternion

$$\vec{q}_{i2b} = \vec{q}_i^{\,b}. \tag{A.9}$$

The same rotation can be expressed by a rotation matrix T:

$$T_{i2b} = T_i^b. \tag{A.10}$$

Vector Rotation by Quaternions

The rotation of a vector $\vec{r}_i$ given in frame i, to its representation in frame b by the quaternion $\vec{q}_i^b$ is given by

$$\vec{r}_b = \vec{q}_i^{b\,*}\ \vec{V}_i\ \vec{q}_i^b, \tag{A.11}$$

where $\vec{V} = [\vec{r}_i \quad 0]^T$ is the extended four dimensional vector of $\vec{r}_i$. Equivalently, the rotation using the rotation matrix T_i^b can be performed by matrix vector multiplication

$$\vec{r}_b = T_i^b\ \vec{r}_i. \tag{A.12}$$

The reverse transformation by the quaternion is given by

$$\vec{r}_i = \vec{q}_i^b\ \vec{V}_b\ \vec{q}_i^{b\,*}, \tag{A.13}$$

Hence, it is

$$\vec{q}_i^b = \vec{q}_b^{i\,*}. \tag{A.14}$$

This is similar to rotation matrices where applies

$$T_i^b = T_b^{i\,T}. \tag{A.15}$$

Successive Rotations

For attitude computations and attitude determination and control applications, it is quite useful to execute successive rotations. The standard way is to multiply rotation matrices with each other. For example, the transformation matrix from frame c to a via b can be expressed as

$$A_c^a = A_b^a\ A_c^b. \tag{A.16}$$

With the above definitions, the corresponding quaternion multiplication is

$$\vec{q}_c^a = \vec{q}_c^b\ \vec{q}_b^a. \tag{A.17}$$

Compared to the rotation matrices, the sequence is interchanged.

Conversion of Quaternion to Rotation Matrix

The conversion of the quaternion $\vec{q}$ to the rotation matrix T is given by

$$T = \begin{bmatrix} q_1^2 - q_2^2 - q_3^2 + q_4^2 & 2\,(q_1q_2 + q_3q_4) & 2\,(q_1q_3 - q_2q_4) \\ 2\,(q_1q_2 - q_3q_4) & -q_1^2 + q_2^2 - q_3^2 + q_4^2 & 2\,(q_2q_3 + q_1q_4) \\ 2\,(q_1q_3 + q_2q_4) & 2\,(q_2q_3 - q_1q_4) & -q_1^2 - q_2^2 + q_3^2 + q_4^2 \end{bmatrix}. \tag{A.18}$$

Conversion of Rotation Matrix to Quaternion

The vice versa conversion of a rotation matrix T to a quaternion $\vec{q}$, with T being composed of

$$T = \begin{bmatrix} T_{11} & T_{12} & T_{13} \\ T_{21} & T_{22} & T_{23} \\ T_{31} & T_{32} & T_{33} \end{bmatrix}, \tag{A.19}$$

is obtained in two steps. First the values of q_{1i}, q_{2i}, q_{3i} and q_{4i} are computed by

$$\begin{aligned} q_{1i} &= 0.5\sqrt{1 + T_{11} - T_{22} - T_{33}} \\ q_{2i} &= 0.5\sqrt{1 - T_{11} + T_{22} - T_{33}} \\ q_{3i} &= 0.5\sqrt{1 - T_{11} - T_{22} + T_{33}} \\ q_{4i} &= 0.5\sqrt{1 + T_{11} + T_{22} + T_{33}} \end{aligned} \tag{A.20}$$

Subsequently the components of the desired quaternion $\vec{q}$ are calculated regarding the following conditions:

- $|q_{1i}| > |q_{ji}|$ $(j = 2, 3, 4)$:

$$\begin{aligned} q_1 &= 0.5\sqrt{1 + T_{11} - T_{22} - T_{33}} \\ q_2 &= \frac{0.5\,(T_{12} + T_{21})}{\sqrt{1 + T_{11} - T_{22} - T_{33}}} \\ q_3 &= \frac{0.5\,(T_{13} + T_{31})}{\sqrt{1 + T_{11} - T_{22} - T_{33}}} \\ q_4 &= \frac{0.5\,(T_{23} - T_{32})}{\sqrt{1 + T_{11} - T_{22} - T_{33}}} \end{aligned} \tag{A.21}$$

- $|q_{2i}| > |q_{ji}|$ $(j = 1, 3, 4)$:

$$\begin{aligned} q_1 &= \frac{0.5\,(T_{12} + T_{21})}{\sqrt{1 - T_{11} + T_{22} - T_{33}}} \\ q_2 &= 0.5\sqrt{1 - T_{11} + T_{22} - T_{33}} \\ q_3 &= \frac{0.5\,(T_{32} + T_{23})}{\sqrt{1 - T_{11} + T_{22} - T_{33}}} \\ q_4 &= \frac{0.5\,(T_{31} - T_{13})}{\sqrt{1 - T_{11} + T_{22} - T_{33}}} \end{aligned} \tag{A.22}$$

- $|q_{3i}| > |q_{ji}|$ $(j = 1, 2, 4)$:

$$\begin{aligned} q_1 &= \frac{0.5\,(T_{13} + T_{31})}{\sqrt{1 - T_{11} - T_{22} + T_{33}}} \\ q_2 &= \frac{0.5\,(T_{32} + T_{23})}{\sqrt{1 - T_{11} - T_{22} + T_{33}}} \\ q_3 &= 0.5\sqrt{1 - T_{11} - T_{22} + T_{33}} \\ q_4 &= \frac{0.5\,(T_{12} - T_{21})}{\sqrt{1 - T_{11} - T_{22} + T_{33}}} \end{aligned} \tag{A.23}$$

- $|q_{4i}| > |q_{ji}|$ $(j = 1, 2, 3)$:

$$
\begin{aligned}
q_1 &= \frac{0.5\,(T_{23} - T_{32})}{\sqrt{1 + T_{11} + T_{22} + T_{33}}} \\
q_2 &= \frac{0.5\,(T_{31} - T_{13})}{\sqrt{1 + T_{11} + T_{22} + T_{33}}} \\
q_3 &= \frac{0.5\,(T_{12} - T_{21})}{\sqrt{1 + T_{11} + T_{22} + T_{33}}}
\end{aligned}
\qquad (A.24)
$$

$$
q_4 = 0.5\sqrt{1 + T_{11} + T_{22} + T_{33}}
$$

A.1.3 Euler Angle Representation

The representation of the attitude in terms of Euler angles might be the most descriptive, especially for small angles. The attitude of a frame with respect to a reference frame can be described by three successive rotations of the frame by three angles, referred to as the Euler angles. For these three successive rotations 12 possibilities exists around which axes and in which order is rotated, called the rotation sequence. Therefore, for an unambiguous Euler angle representation, the rotation sequence and which angle describes which rotation must be stated.

In this thesis the Euler angles $\vec{\Theta}$ are defined by the x-y-z rotation sequence, with the three angles φ (roll), θ (pitch) and ψ (yaw), being a rotation around each axes, respectively. Nevertheless, for small rotation angles, the Euler angles for all sequences are very similar.

The conversion from rotation matrices and quaternions to Euler angles can be obtained by the successive multiplication of the rotation matrix or quaternion representing a rotation around the respective axis with the desired angle. For the x-y-z sequence and the quaternion $\vec{q} = [q_1\ q_2\ q_3\ q_4]^T$, the conversion is given by

$$
\begin{aligned}
r_{11} &= -2(q_2 q_3 - q_4 q_1) \\
r_{12} &= q_4^2 - q_1^2 - q_2^2 + q_3^2 \\
r_{21} &= 2(q_1 q_3 + q_4 q_2) \\
r_{31} &= -2(q_1 q_2 - q_4 q_3) \\
r_{32} &= q_4^2 + q_1^2 - q_2^2 - q_3^2
\end{aligned}
\qquad (A.25)
$$

$$
\begin{aligned}
\varphi &= \arctan2(r_{11}, r_{12}) \\
\theta &= \arcsin(r_{21}) \\
\psi &= \arctan2(r_{31}, r_{32})
\end{aligned}
$$

The conversion for the other rotation sequences and the direct conversion from rotation matrix to Euler angles may be found in Wertz (1978) (p. 763 f.).

A.1.4 Time-Derivative of Quaternion

The kinematic equation of rotational motion, as introduced in Equation (2.8), is given by

$$\begin{aligned} \dot{\vec{q}}_i^b &= \frac{1}{2}\, \vec{q}_i^b \; \underline{\omega}_{i,b}^b \\ \Leftrightarrow \dot{\vec{q}}_i^b &= \frac{1}{2}\, \Omega \; \vec{q}_i^b, \end{aligned} \tag{A.26}$$

with the matrix Ω and the extended four dimensional vector $\underline{\omega}_{i,b}^b$ of the angular velocity $\vec{\omega}_{i,b}^b$ being:

$$\Omega = \begin{bmatrix} 0 & \omega_{i,b_z}^b & -\omega_{i,b_y}^b & \omega_{i,b_x}^b \\ -\omega_{i,b_z}^b & 0 & \omega_{i,b_x}^b & \omega_{i,b_y}^b \\ \omega_{i,b_y}^b & -\omega_{i,b_x}^b & 0 & \omega_{i,b_z}^b \\ -\omega_{i,b_x}^b & -\omega_{i,b_y}^b & -\omega_{i,b_z}^b & 0 \end{bmatrix} \quad \text{and} \quad \underline{\omega}_{i,b}^b = \begin{bmatrix} \omega_{i,b_x}^b \\ \omega_{i,b_y}^b \\ \omega_{i,b_z}^b \\ 0 \end{bmatrix}. \tag{A.27}$$

A.2 Spectral Representation and Amplitude Spectral Density (ASD)

Power Spectral Density (PSD) and Amplitude Spectral Density (ASD) are widely used for the analysis and characterization of stochastic processes and noise. For the spectral analysis of periodic and sinusoidal signals, thus with the main interest in characterizing the signal itself, the Power Spectrum (PS) or the Amplitude Spectrum (AS) is usually the representation of choice.

There is often some confusion of the four terms PSD, ASD, PS and AS. Furthermore, there are several methods for their computation, which may result in very different appearances of the results, even though they are correct ASDs or PSDs of the same signal. Therefore the terms are briefly discussed and the computation used throughout this thesis is given here. A comprehensive overview of this topic is for instance given in Heinzel et al. (2002); Schmid (2012).

Generally, the PS of a signal gives the power in each infinitesimal frequency interval, whereas the the PSD gives the power in each infinitesimal frequency interval divided by the width of that interval. The reason or the logic of that definition will be resolved in the following. The power does not need to be an actual physical power in Watt, but is generally identified by the squared signal. Therefore the unit of the PS is $[\cdot^2]$, with $\cdot$ being the unit of the signal, and hence the unit of the PSD is $[\cdot^2/Hz]$. The AS and ASD are simply the square root of the PS and PSD, and hence have the units of the signal itself $[\cdot]$ and of the signal divided by the square root of frequency $[\cdot/\sqrt{Hz}]$, respectively.

$$AS = \sqrt{PS} \qquad \text{and} \qquad ASD = \sqrt{PSD} \tag{A.28}$$

Mathematically, the PS is the Fourier transform of the autocorrelation function of the signal. With a discrete signal $s(t_i)$, using Fast Fourier Transform (FFT), the PS is given by

$$PS_{2s}(f_i) = \frac{|FFT(s(t_i))|^2}{N^2}, \tag{A.29}$$

with N being the number of data samples. The FFT gives a spectrum of negative and positive frequencies, which is symmetrical around zero for real-world signals. PS_{2s} is referred to as two-sided spectrum, where the power is equally distributed over positive and negative frequencies. Usually a one-sided spectrum is used which is

$$PS(f_i) = 2 * PS_{2s}(f_i) \qquad \text{for} \qquad f_i \geq 0. \tag{A.30}$$

Because of the $|\ |^2$ in Equation A.29, the PS is sometimes also referred to as rms spectrum. For elucidation, a sinusoidal signal $s(t)$ with a peak amplitude of $\sqrt{2}*3$ would result in a single peak with height 9 in the PS, or 3 in the AS. For real data processing the frequency resolution or the bin width Δf is limiting the correct visualization of peaks, because a single peak may be present in more than one frequency bin. In general, the total signal power is the integral over all frequency bins. The frequency resolution is

$$\Delta f = \frac{f_s}{N} = \frac{1}{T}, \tag{A.31}$$

with f_s being the sampling frequency and T the total signal length. Thus, with more data samples N, the frequency resolution is increased.

The PSD is a normalization of the PS. This normalization of the PS is very usefull to display stochastic processes and noise, where power and amplitude may be referred to as variance and standard deviation. Assuming a time series of white noise with a variance (i.e. power) σ^2 or standard deviation (i.e. amplitude) σ. Extending this time series of white noise, for instance by a factor of 10, would of cause not change the power or the amplitude of the noise. But in the PS, the same power would be distributed over 10 times more frequency bins because it is white noise and present over the full frequency range. In other words, the frequency resolution Δf of the FFT and the PS is increased. Thereby the signal power in each frequency bin is reduced by a factor of 10 and the resulting PS is lower by a factor of 10. Thus for the representation as PSD, the PS is divided by the frequency resolution giving the same magnitude for all signal length N and sampling frequencies f_s. This makes clear, that it is not possible to visualize signal and noise meaningfully in the same spectral plot. Either the magnitude of the signal or the noise are dependent on the frequency resolution Δf

$$PSD(f_i) = \frac{PS(f_i)}{\Delta f}. \tag{A.32}$$

Usually the computation of the PS or PSD involves applying a window function for the computation of the FFT. Many possibilities doing this exist (eg. Heinzel et al., 2002), which is the main reason that results might look pretty different. The window function reduces the influence of the fact that real signals are usually not periodic i.e, repeat itself eternally, which is implicitly considered by the FFT. For example, if the signal length of a sinusoidal signal is not an exact multiple of the signal's period, the FFT detects a discontinuity. Thus, usually such discontinuities corrupt the PS and PSD estimates. The window function is more or less a weighting of the signal in the time domain which is usually zero at the ends, reducing this effect.

For all ASD plots in this thesis the same computation and the same window function is used. The one-sided PSD of the signal s is computed with Matlab's `pwelch` function

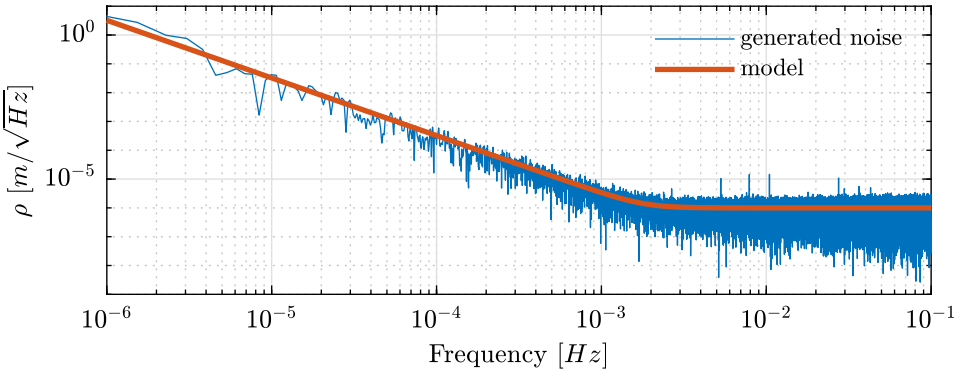

Figure A.1: ASD of the KBR noise model and of the generated noise time series.

using a Hanning window with the length of the signal and the respective sampling frequency of the signal f_s:

```
[pxx,f] = pwelch(s,hanning(length(s)),0,[],f_s)
```

Exemplary the ASD of the KBR noise model is shown in Figure A.1, as it has been shown and discussed in Section 6.3.1 (Fig. 6.27). The standard deviation σ of the white noise in the higher frequencies can be directly read out from the ASD plot, being 10^{-6} m. The amplitude of the lower frequencies is increasing and its standard deviation follows from the plot, as well.

Regarding the Nyquist theorem, stating that the maximal usefull frequency is $f_s/2$, the ASD is limited towards the high frequencies on the right hand side. The low frequencies are limited by the length of the signal N or T, and hence detecting its lowest frequency components by $1/T = f_s/N$. The usage of the windowing may extend this lower bound a little further.